

REPUBLIQUE DU CAMEROUN

Paix-Travail-Patrie

UNIVERSITE DE YAOUNDE I

FACULTE DES SCIENCES

CENTRE DE RECHERCHE ET DE
FORMATION DOCTORALE EN SCIENCES,
TECHNOLOGIES ET GEOSCIENCES

UNITE DE RECHERCHE ET DE
FORMATION DOCTORALE EN
PHYSIQUE ET APPLICATIONS

B.P: 812 Yaoundé

Email: crfd_stg@uy1.uninet.cm



REPUBLIC OF CAMEROON

Peace-Work-Fatherland

THE UNIVERSITY OF YAOUNDE I

FACULTY OF SCIENCE

POSTGRADUATE SCHOOL OF SCIENCE,
TECHNOLOGY AND GEOSCIENCES

RESEARCH AND POSTGRADUATE
TRAINING UNIT FOR PHYSICS AND
APPLICATIONS

P.O. Box: 812 Yaoundé

Email: crfd_stg@uy1.uninet.cm

DEPARTEMENT DE PHYSIQUE

DEPARTMENT OF PHYSICS

LABORATOIRE D'ENERGIE ET SYSTEMES ELECTRIQUES ET ELECTRONIQUES

ENERGY-ELECTRIC AND ELECTRONIC SYSTEMS LABORATORY

**DYNAMICS OF OPTICAL INJECTION
SEMICONDUCTOR LASERS: EFFECTS OF
LANGEVINIAN NOISE SOURCES AND INTEGRATED
RESONANT TUNNELING DIODE DEVICES**

THESIS

Submitted and Defended Publicly in Fulfillment of the Requirements for the Award of a
Doctor of Philosophy/PhD Degree in Physics

Option: Electronic and Electrical Systems

By

ESSEBE EBA David

Registration Number: **11Y726**

Master of Science in Physics

Under the Supervision of

ESSIMBI ZOBO Bernard

Professor,

University of Yaoundé I

Year 2021





DEPARTEMENT DE PHYSIQUE
DEPARTMENT OF PHYSICS

ATTESTATION DE CORRECTION DE LA THESE DE
DOCTORAT/PhD

Nous, Professeurs **BODO Bertrand**, **MBINACK Clément** et Professeur **WOAFO Paul**, respectivement Examineurs et Président du Jury de la thèse de Doctorat/PhD de Monsieur **ESSEBE EBA David** Matricule **11Y726**, préparée sous la direction du Professeur **ESSIMBI ZOBO Bernard**, intitulée : « **DYNAMICS OF OPTICAL INJECTION SEMICONDUCTOR LASERS : EFFECTS OF LANGEVINIAN NOISE SOURCES AND INTEGRATED RESONANT TUNNELING DIODE DEVICES** », soutenue le **Mardi, 21 Décembre 2021**, en vue de l'obtention du grade de Docteur/Ph.D en Physique, Spécialité **Systemes Electriques et Electroniques**, attestons que toutes les corrections demandées par le Jury de soutenance ont été effectuées.

En foi de quoi, la présente attestation lui est délivrée pour servir et valoir ce que de droit.

Fait à Yaoundé le **05 JAN 2022**

Les Examineurs

Pr. **BODO Bertrand**

Pr. **MBINACK Clément**

Le Président du Jury

Pr. **WOAFO Paul**

Le Chef de Département de Physique



Pr. **Njoku Jean-Marie Biemvenu**
Professeur

Dedication

Dedication

*To the memory of my father,
EBA EDOU Pépin Lebref*

and

*Love for my mother
EVINA ESSEBE Jeannette*

Acknowledgments

I wish to express my heartiest gratitude and sincere thanks to my mentor and supervisor at the University of Yaoundé I, Professor ESSIMBI ZOBO Bernard, for proposing the Ph.D. project and accepting me as research student in his group, for his continuous guidance and support. I would also like to thank him for his continuous belief in this works, and for the freedom, he allowed me during this research. I am indebted to him for taking necessary steps for this work to be possible, for his encouragement and his advices.

My sincere gratitude also goes to the members of my thesis jury for all they did to accept to take part to the examination of this work. Thank you all for your suggestions tending to improve this thesis.

I wish to express my sincere gratitude to the University of Yaoundé 1. Especially all the staff of the Department of Physics and most especially to Professor NDJAKA Jean Marie Bienvenu as the Head of Department of Physics, Professor KOFANE Timoléon Crépin, Professor WOAFO Paul, Professor TCHAWOUA Paul, Professor BEN-BOLIE Germain Hubert, who have greatly shaped my scientific mind in the way.

Special thanks go to Professor ELE Pierre, Professor BODO Bertrand, Professor MBINACK Clément, Professor EYEBE FOUDA Jean-Sire Armand, Professor BIYA MOTTO Frédéric, Professor ATANGANA Jacques, and Doctor AYISSI EYEBE Guy for their fruitful discussions and encouragement throughout seminars.

Special thanks go to Doctor MENGUE MENGUE Armand Didier from the University of Buea, for his help and support that contributed to overcome difficulties encountered. I also thank him for his guidance; encouragement and friendship that have made this research project a success.

I am also grateful to the Laboratory of Energy, Electronics and Electrical Systems for useful discussions, seminars and friendly atmosphere. Special thanks go to KANA NGUIMEYA Christian, NGUIMZAP Christian, NDALLA ESSENGUE Gloire, FOLLA KAMDEM Jerome, MAHAMAT LOUFTI Imran, DJEUFA DAGOUMGEI Guy Morgand, and DJAMET Arnaud for the atmosphere of camaraderie, collaboration and friendship in the laboratory of electronics.

Above all, special thanks go to my joyful Mother EVINA ESSEBE Jeannette.

In a personal dimension, how could I forget about the encouragements, the guidance, and the financial assistance of my brother EBA EBA Pepin Lamy during my secondary and high school?

Most at all, I am indebted to my family. I acknowledge you all my brothers and sisters EBA's for your love, supports and encouragements throughout the period of research.

Finally, I would like to express my thanks to all those not mentioned and that by their hard work and kindness made this thesis possible.

Contents

DEDICATION	I
ACKNOWLEDGMENTS.....	II
CONTENTS	IV
LIST OF FIGURES.....	VI
LIST OF TABLES	XI
LIST OF ACRONYMS	XII
ABSTRACT	XV
RÉSUMÉ.....	XVII
GENERAL INTRODUCTION	1
I. LITERATURE REVIEW OF SCLs, RTD DEVICES AND OPTOELECTRONIC OSCILLATORS.....	8
I.1. Introduction.....	8
I.2. Lasers	8
I.2.1. Electromagnetic spectrum.....	8
I.2.2. Basic Elements of Lasers	10
I.2.3. Two-atomic-level Laser System.....	10
I.3. Semiconductor Lasers	11
I.3.1. Rate Equations of SCLs	12
I.3.2. Semiconductor Laser with Optical Injection.....	14
I.3.3. Noise-induced effects in Semiconductor Lasers	14
I.4. RTDs, Electronic and Optical Properties of Semiconductors	16
I.4.1. Heterostructure SC material	16
I.4.2. The Resonant Tunneling Diode.....	17
I.4.3. Original Models of RTD current-voltage.....	19
I.5. Optoelectronic Oscillators.....	23
I.5.1. Optoelectronic devices	23
I.5.2. RTD based optoelectronic oscillators.....	23
I.6. Conclusion.....	27
II. MATERIALS AND NUMERICAL METHODS	28
II.1 Introduction.....	28

II.2. Fourier Transformations	28
II.2.1. Noise in Frequency domain	28
II.2.3. Langevin Equation and Langevin Noise	29
II.3. Analysis and Characteristic Descriptions for Nonlinear Systems.....	31
II.3.1. Reduction methods.....	31
II.3.2. Low-dimension projections	31
II.3.3. Polynomial Approximation.....	31
II.3.4. Time series	32
II.3.5. Power spectrum.....	33
II.3.6. Phase portrait	33
II.3.7. Poincaré section	34
II.3.8. Stability Analysis Methods: Bifurcation and Lyapunov Calculations	35
II.3.9. Simulink Analysis Method and Numerical Simulations	42
II.4. Model of Optical Injection SCL	44
II.5. Model of RTD-OISCL Integrated Circuit.....	45
II.5.1. Dimensionless Equations of RTD-OISCL Model.....	47
II.6. Conclusion	48
III. RESULTS AND DISCUSSIONS	50
III.1. Introduction	50
III.2. Noise Induced Effects in Optical Injection SCLs	50
III.2.1. Noise Characteristics and Discussions	52
III.2.2. Relative Intensity and Frequency Noises of OISCL.....	57
III.3. Stability Analysis of RTD-LD Integrated Systems	65
III.3.1. Linear stability and Routh-Hurwitz criteria.....	65
III.4. Dynamics of RTD-OISCL Systems	72
III.4.1. Bifurcation Diagrams and Route to Chaos	72
III.4.2. Chaotic multiscroll, infinite scroll and Simulink implementation.....	76
III.5. Conclusion.....	95
GENERAL CONCLUSION.....	97
APPENDIX.....	100
Bibliography	101
LIST OF PUBLICATIONS	110

List of Figures

Figure 1. Low-loss transmission windows of silica fibres in the wavelength regions near 1.3 and 1.55 μm [2].....	1
Figure 2. Semiconductor laser diodes modules [9, 10].....	3
Figure 3. Simulated dynamics the photon number and carrier inversion showing damped oscillations toward a steady state (relaxation oscillations). Dynamics is limited to spiralling relaxation flows in the phase plane (right) [16].	5
Figure 4. Chaos in laser diode: (a) Optical feedback from an external mirror, (b) Optical injection from a master to a slave laser diode. (c) External current modulation applied to a laser diode. (d) Optoelectronic feedback by reinjecting a delayed and amplified signal from a photodiode that measures the laser output [16].....	5
Figure I.1. The EM spectrum is divided for maser and laser depending upon the wavelengths of the radiation. Visible light refers to optical rang that occupies the smaller window ranging from 400nm to 700nm wavelength [32].	9
Figure I.2. Basic elements of a laser system.....	10
Figure I.3. Interactions light material: (a) Absorption, (b) Spontaneous emission and (c) Stimulated emission. ..	11
Figure I.4. The basic working principles of semiconductor laser diode. The absorption (a) of a photon results in the generation of an electron-hole pair. The recombination of an electron-hole pair results in the spontaneous emission (b) of a photon. Electron-hole recombination can generate the stimulated emission (c) of an identical photon [39].	12
Figure I.5. Scheme of optical injection. The SL is subjected to optical injection by the ML. Unidirectional coupling is ensured by an optical isolator.....	14
Figure I. 6. Rectangular potential barrier and particle wave function	17
Figure I.7. Tunneling Diode I-V characteristic. When a reverse bias voltage, the current becomes extremely large	17
Figure I.8. (a) Diagram of a DBQW band profile formed by InGaAs/AlAs semiconductor compounds (bottom). (b) Resonant tunneling process. (d) Typical DBQW-RTD room-temperature current-voltage characteristic exhibiting NDR [28].	18
Figure I.9. (a) Evolution diagram of a DBQW RTD band profile formed at bias. (b) Typical DBQW-RTD room-temperature current-voltage characteristic exhibiting negative differential conductance.....	19
Figure I.10. RTD experimental I-V curves and numerical fitting InGaAs/AlAs semiconductor compounds using Schuman et al. model [28].	22
Figure I.11. I-V characteristic of NDR device provided by: (a) a nine-order polynomial, (b) a six-order polynomial and (c) a cubic polynomial resulting from the Schulman et al. model of Eq. (I.16).	23
Figure I.12. NDR oscillator (a) and electrical equivalent circuit of the RTD b(i) with its I-V characteristic providing the NDR region b(ii)	24
Figure II.1. Free-noise signal (a) and noisy signal (b)	29

Figure II.2. Time series of an artificial neural system showing chaotic behavior [70].	33
Figure II.3. Lorenz attractor [74].	34
Figure II.4. Poincaré map of an n -th order autonomous system. Γ : n -dimensional trajectory, Σ : $(n - 1)$ -dimensional hyperplane [11]	35
Figure II.5. Local bifurcations. Pitchfork bifurcation diagrams; (i) Pitchfork supercritical, (ii) Pitchfork subcritical and (iii) Bifurcation condition for flows. (b) Saddle-node bifurcation diagrams; (i) Saddle-node supercritical, (ii) Saddle-node subcritical and (iii) Bifurcation condition for flows. (c) Transcritical bifurcation diagrams; (i) Supercritical, (ii) Subcritical and (iii) Bifurcation condition for flows. (d) Hopf bifurcation diagrams; (i) Hopf Supercritical, (ii) Hopf Subcritical and (iii) Bifurcation condition for flows. (e) Period-Doubling bifurcations. In the bifurcation diagrams, solid (dashed) lines indicate stable (unstable) structures.	37
Figure II.6. (a) A homoclinic orbit (continuous line) connecting a saddle point P to itself. (b) Two heteroclinic orbits (continuous line) defining a homoclinic cycle connecting saddle points P_1 and P_2 . Dashed line: other close trajectories [68].	38
Figure II.7. Schematic illustrations of several different types of equilibrium points and their nearby trajectories in 2-D continuous-time dynamical systems. The real part of the dominant eigenvalue determines the overall stability of the equilibrium point (top) [85]	40
Figure II.8. Superimposition of the bifurcation diagram and the LE spectrum. This shows the coincidence of the accumulation point with the switch in the LE from negative to positive. The strong 3-period in the chaotic region is also echoed by the negative LE in the chaotic region [89].	42
Figure II.9. Simulink library browser	43
Figure II.10. Equivalent circuit of the optoelectronic novel RTD-OISCL optoelectronic oscillator	46
Figure II.11. Equivalent Diagram of the normalized RTD-OISCL integrated circuit	47
Figure III.1. RIN of ML as function of frequency; (a) when $\gamma_{inj} = 0.5$ for several bias current conditions (1) $J_{inj} = 2J_{thinj}$, (2) $J_{inj} = 2.5J_{thinj}$, (3) $J_{inj} = 4J_{thinj}$ and (4) $J_{inj} = 12J_{thinj}$; (b) when $J_{inj} = 2J_{thinj}$, for several value of EGC (1) $\gamma_{inj} = 0.00$, (2) $\gamma_{inj} = 0.25$ (3),(4) $\gamma_{inj} = 0.5$,(4) $\gamma_{inj} = 0.65$,(5) $\gamma_{inj} = 0.99$	55
Figure III.2. FN of the master laser as a function of frequency: (a) when $\gamma_{inj} = 0.45$ for several bias current conditions; (b) when $J_{inj} = 2J_{thinj}$ for several values of EGC	56
Figure III.3. Variation of linewidth with injection current ratio. Curves show the rapid narrowing of linewidth with increasing current ratio that is obtained by decreasing (a) SEF, (b) EGC and (c) LEF.	57
Figure III.4. Eliminating 1/f noise. RIN variation for injection rates of (a) -20 dB and (b) 40 dB when phase fluctuations of the ML are considered, and (c) -20 dB and (d) 40 dB when phase fluctuations are neglected.	62
Figure III.5. Effects of increasing ML current on the slave RIN spectrum for the injection rates of (a) 40 dB and (b) -20 dB.	63
Figure III.6. Slave laser FN for (a) some values of current and (b) some values of EGC	64
Figure III.7. Frequency variation of FN of the slave laser, with the following injection parameters: $\Delta\omega = -20\text{GHz}$, $k_{inj} = 1 \times 10^{-1}$, $S_0 = 10^{-2}(S_{inj})_0$, $J_{inj} = 2.5(J_{inj})_{th}$ (a) when the master laser and slave laser EGCs' change; (b) when the slave laser EGC is fixed.	64

- Figure III.8.** Influence of EGC and other parameters on RIN. (a) When EGC of the master laser is fixed to 0.55; (b) when the EGCs of both ML and SL change 65
- Figure III.9.** (a) Unlocked and locked regions for $\gamma=0.65$, $\gamma=0.8$ and $\gamma=0.9$; (b) Range of fixed optical phase ψ_0 for $\Delta\Omega$ situated in locked region..... 67
- Figure III.10.** The range of stable phases given by (III.47)-(III.48): (a) Under weak injection, stable phases regions are limited by pairs of curves inside $-\pi/2 < \psi_0 < \pi/2$ and $-\pi < \psi_0 < 0$ for the limits of EGC, $\gamma \approx 0$ and $\gamma \approx 1$ respectively. (b) Under strong injection, the boundary of stable phase is limited only by $-\pi/2 < \psi_0 < \pi/2$ blue and red lines correspond to $\gamma \approx 0$ and $\gamma \approx 1$ respectively. 68
- Figure III.11.** Stability boundaries calculated from the Routh-Hurwitz stability criterion given by Eq.(III.52) for the first minor (a), the second minor (b), the third minor (c), the fourth minor (d) and the fifth minor (e) of the Hurwitz matrix. The intersecting figure (f) shows that there exists a shrunk region which satisfies Routh conditions..... 70
- Figure III.12.** Bifurcation diagrams of laser driving current (a) and photons density (b) versus external frequency f_{in} showing the replication of chaotic and nonchaotic regions when EGC γ is fixed to **0.5**, **Vdc = 1.145 V** and **Vac = 130 mV**..... 73
- Figure III.13.** Bifurcation diagram of photons density $s(t)$ when effective gain coefficient γ is varying $\gamma \in [0.1, 0.99]$, for $k_{inj} = 2 \times 10^{-3}$, **Vdc = 1.145 V** and **Vac = 180 mV**, $f_{in} = 1.3 \text{ GHz}$ and $\Delta\omega = 2 \text{ GHz}$ 73
- Figure III.14.** The bifurcation diagram of the driving current (a) and the laser normalized photon number (b) when the parameter **Vac** is varying from 0 to 2V both at bias of 1.145V, with $f_{in} = 1.5 \text{ GHz}$, when the laser diode operating without frequency detuning and with $\gamma = 0.75$ and $k_{inj} = 0.001$ 74
- Figure III.15.** Bifurcation diagram of photons density $s(t)$ when effective gain coefficient γ is varying $\gamma \in [0.1, 0.99]$, for $k_{inj} = 2 \times 10^{-3}$, **Vdc = 1.145 V** and **Vac = 180 mV**, $f_{in} = 1.3 \text{ GHz}$ and $\Delta\omega = 2 \text{ GHz}$ 74
- Figure III.16.** Time series analysis for electrical driving current (top panels) laser carrier density (middle panels) and optical output (lower panels) when RF perturbed (**Vac = 100 mV**). The laser exhibits relaxation oscillations without AC perturbation (a) and chaotic signals adding AC voltage (b) and (c). Nevertheless, it always attempts to emulate driving current time repetitions..... 75
- Figure III.17.** Limit cycles of the driven semiconductor laser in photon-carrier (s-n) for different values of EGC γ when $\Delta\omega = 2 \text{ GHz}$, $k_{inj} = 2 \times 10^{-3}$ at the amplitude voltage equal to **180 mV**. The laser behaves like semiconductor laser with optical feedback. 76
- Figure III.18.** (a) Birth of multiscroll chaotic attractors in s-n phase plane of LD from period-2 attractor ($\gamma = 0.99$), period-3 attractor ($\gamma = 0.9$) period-4 attractor ($\gamma = 0.8$), period-5 chaotic attractor ($\gamma = 0.6$) to multiscroll chaotic attractors ($\gamma = 0.1$ and $\gamma = 0.099$) and (b) 3D phase portrait of multiscroll chaotic attractors for $\gamma = 0.099$, when $\Delta\omega = 30 \text{ GHz}$ 77
- Figure III.19.** The formation of infinite-scroll attractor: (a) Two-scroll attractor ($t = 1,000$), (b) Five-scroll attractor ($t = 3,000$) and (c) Forty one-scroll attractor with eight laminar phases ($t = 20,000$). 78
- Figure III.20.** Lyapunov exponents' dynamics of infinite-scroll of system (4.9) with the same fixed parameters as in Fig. III.17 79

- Figure III.21.** Simulink implementation scheme of RTD-LD hybrid optoelectronic oscillator. 80
- Figure III.22.** (a) Simulink observations referring to formation of Infinite-scroll attractor: the projection on $\psi - n$ plane from XY Graph3 given for the simulating time show three-scroll a(i) $t = 2,226$, four-scroll a(ii) $t = 2,410$, five-scroll a(iii) $t = 3,000$ and six-scroll a(iv) $t = 3,360$ attractors. Projections of chaotic attractor from Simulink simulation in (b) current-voltage,(c) light-voltage and (d) carrier-photons plane from XY Graph1, XY Graph2 and XY Graph4 respectively when $r = 6.65$, $\gamma = 0.7$, $v_{dc} = 1.145$, $v_{ac} = 0.1441$ and $k = 0.020637$ 80
- Figure III.23.** Current-voltage (I-V) characteristics of RTD corresponding to $S1 \approx S2$ (a), $S1 < S2$ (b) and $S1 > S2$ (c). 81
- Figure III.24.** Influence of areas of RTD current-voltage (I-V) characteristics on driven laser dynamics values of the EGC. a-When $S1 \approx S2$: a(i) Three-scroll chaotic attractor, a(ii) Two-scroll attractor and a(iii) One-scroll attractor. b- When $S1 < S2$: b(i) relaxation dynamics, b(ii) non-oscillatory dynamics and b(iii) crisis. c- When $S1 > S2$, the system generates periodic limit cycles whatever the value of γ : c(i), c(ii), and c(iii). 82
- Figure III.25.** DC bias control of system dynamics (1): (a) and (b) bifurcation diagrams of electrical driving current and optical output, respectively 82
- Figure III.26.** Bifurcation diagrams' of windows of NDR region with the indication of antimonotonicity and reverse period-doubling scenario created with the smooth variation of v_{dc} for some specific value of the parameter r . (a) period-4 bubbles $r = 9$, (b) period-8 bubbles $r = 8$, (c) period-16 bubbles $r = 7.5$, (d) period-32 bubbles $r = 7.4$, (e), (f) and (g) chaotic bubbles $r = 7.35$ and $r = 6.68$ in (f) and (g) respectively and stable states occur for $v_{dc} \in [2.39, 2.4]$ when the EGC $\gamma = 0.976$. (h) Bifurcation diagrams extension in NDR for $2.32 \leq v_{dc} \leq 2.4$ showing chaos control. 84
- Figure III.27.** Sensitivity to initial conditions as the coexistence of two different outputs in laser phase oscillations where red line correspond to ICs $(x_0, 0.0300, 0, s_0, n_0, \psi_0)$ and blue line for $(x_0, 0.0305, 0, s_0, n_0, \psi_0)$. 86
- Figure III.28.** Phase portraits of coexisting of N-scroll with M-scroll hyperchaotic attractors by adjusting the initial conditions. (a) Coexisting 4-scroll with 2-scroll attractors, (b) coexisting 3-scroll with 1-scroll attractors, (c) coexisting 5-scroll with 3-scroll attractors, (d) coexisting two 1-scroll attractors, (e) coexisting 5-scroll with 1-scroll attractors, (f) coexisting 5-scroll with 1-scroll disconnected attractors. 87
- Figure III.29.** Bifurcation diagram of coexisting multiscroll attractors of a variable ψ with increasing the resistance r showing a controllable number of scroll in the system (III.38) 88
- Figure III.30.** Control of dynamic evolution from the coexisting N-scroll with M-scroll hyperchaotic attractors to a single one-scroll and to periodic limit cycle. (a) Coexisting 6-scroll with 9-scroll hyperchaotic attractors. (b) Coexisting 2-scroll with 5-scroll hyperchaotic attractors, (c) coexisting 2-scroll with 4-scroll hyperchaotic attractors, (d) coexisting 1-scroll with 2-scroll hyperchaotic attractors, (e) coexisting two disconnected single scroll attractors (f) coexisting two connected single scroll into one scroll, (g) coexisting two connected quasi-periodic torus, (h) periodic limit cycle 89
- Figure III.31.** Square – wave bursting. (i) Time series of optical output $s(t)$ and its corresponding (ii) phase portraits in the light-voltage $(s - x)$ planes. (a) Periodic BOs for $\gamma = 0.11$, (b) Periodic BOs for $\gamma = 0.5$ and (c) spiking trains for $\gamma = 0.9$ 91
- Figure III.32.** (a) Time series of chaotic oscillations for voltage $x(t)$ current $y(t)$, carrier density $n(t)$ and optical output $s(t)$ and corresponding phase portraits in the (a) voltage-current $(x - y)$ and (b) carrier-photon $(n - s)$ planes. The solid red line in (b) corresponds to cubic nonlinear of RTD-LD $I - V$ curve 92

Figure III.33. a(i)-b(i) Time series of simple periodic MMO in voltage and optical output respectively and its corresponding phase portraits in the a(ii) current-voltage and b(ii) 3D carrier-voltage-photon projection. . 92

Figure III.34. Optical time series for the sequence of $[15^3, 15^4 \times 2]$ MMO after two MMOIBs for $r = 5$, $v_{ac} = 100$, $\omega = 1.2566 \times 10^8$, $\varepsilon = 0.00035$ and $\gamma = 0.97$ 93

Figure III.35. Bifurcation diagram for $r = 6$, $v_{ac} = 0.110$, $\omega = 0.01\pi \times 10^9$, $0.0000 < \varepsilon < 0.0008$ and $\gamma = 0.97$ with successive $1^0 \rightarrow 2^0 \rightarrow 2^1 \rightarrow 3^0 \rightarrow 3^1 \rightarrow 3^2 \rightarrow 3^3 \rightarrow 4^2 \rightarrow 4^3 \rightarrow 4^4 \rightarrow 4^5 \rightarrow 4^6 \rightarrow 4^7 \rightarrow 4^8$ sequence intervals of MMOs. 93

Figure III.36. Evolution of MMOs with variations of overall resistance when $\gamma = 0.98$; $f_{in} = 0.93GHz$; $\varepsilon = 0.0035$. (a) MMOIBs $[15^3, 15^4 \times 2]$, (b) 15^4 MMOs, (c) 11^{10} MMOs, (d) 7^0 MMOs, (e) 1^0 MMOs and (f) steady state similar to period-1 oscillations 94

Figure III.37. Transient chaos in (a) electrical and (b) optical outputs. Corresponding power spectrum (c) and (d) projection of chaotic transient attractor (bleu trace) and period-1 limit cycle (red trace) in voltage-light plane 95

List of Tables

Table II.1. Polynomial approximation functions of the RTD current-voltage model.....	32
Table II.2. Description of standard RTD-OISCL OEO equations parameters and values used in numerical simulations.....	48
Table III.1. The equilibrium point and their stability evaluated from system typical control parameters values.....	71

List of Acronyms

- AC:** *Alternating Current*
- CB :** *Conduction Band*
- CD :** *Compact Disk*
- CMOS :** *Complementary Metal Oxide Semiconductor*
- CW:** *Continuous Wave*
- DBQW:** *Double Barriers Quantum Well*
- DC:** *Direct current*
- DFT :** *Discrete Fourier Transformation*
- DH :** *Double Heterostructure*
- DVD:** *Digital Video Disk*
- EAM :** *Electroabsorption Modulator*
- E/O:** *Electrical-to-Optical*
- EDFA:** *Erbium Doped Fiber Amplifier*
- EGC:** *Effective Gain Coefficient*
- EM:** *Electromagnetic*
- FFT:** *Fast Fourier Transformation*
- FN:** *Frequency Noise,*
- FT:** *Fourier Transformation*
- GRASER:** *Gamma-Ray Amplification by Stimulated Emission of Radiation*
- FWHM:** *Full-Width-Half-Maximum*
- HIC:** *Hybrid Integrated Circuit*
- IC:** *Initial Condition*
- IR:** *Infrared*
- LAN:** *Local Access Networks*
- LAO:** *Large Amplitude oscillation*
- LASER:** *Light Amplification by Stimulated Emission of Radiation*
- LD:** *Laser Diode*
- LE:** *Lyapunov Exponent*
- LED:** *Light Emitting Diode*
- LEF:** *Linewidth Enhancement Factor*
- LPE:** *Liquid-Phase Epitaxy*

MASER: *Microwave Amplification by Stimulated Emission of Radiation*

MATLAB: *Matrix Laboratory*

MBE: *Molecular-Beam Epitaxy*

ML: *Master Laser*

MMO: *Mixed-Mode Oscillations*

MMOIB : *MMO-Incrementing Bifurcation*

MOCVD: *Metal-Organic Chemical Vapor Deposition*

MW : *Microwave*

NDR: *Negative Differential Resistance*

ODE: *Ordinary Differential Equation*

O/E: *Optical to Electrical*

OEIC: *Optoelectronic Integrated Circuit*

OEO: *Optoelectronic Oscillator*

OEVCO: *Optoelectronic Voltage Controlled Oscillator*

OEHO: *Optoelectronic Hybrid Oscillator*

OILD: *Optically Injected Laser Diode*

OISCL: *Optically Injected Semiconductor Laser*

OW: *Optical Wave*

PD : *Photodetector/Photodiode*

PDR : *Positive Differential Resistance*

PDR1 : *first Positive Differential Resistance*

PDR2 : *second Positive Differential Resistance*

QN: *Quantum Noise*

QW: *Quantum Well*

RFO: *Resonance Frequency Oscillation*

RIN: *Relative Intensity Noise*

RK: *Runge-Kutta*

RK4: *Fourth-order Runge-Kutta*

RLC : *Resistor-Inductor-Capacitor*

RTD: *Resonant Tunneling Diode*

SAO: *Small Amplitude Oscillation*

SCL: *Semiconductor Laser*

SEF: *Spontaneous Emission Factor*

SL: *Slave Laser*

SNR: *Signal to Noise Ratio*

TD: *Tunneling Diode*

UV: *Ultraviolet*

VB: *Valence Band*

VCO: *Voltage controlled oscillator*

VdP: *Van der Pol*

VPE: *Vapor-Phase Epitaxy*

Abstract

The nonlinear dynamic research in laser physics, especially in semiconductor lasers (SCLs) is still growing rapidly since the emergence of first laser diodes (LD). These SCLs are of paramount importance in optical data processing and optical communications. This Thesis studies the nonlinear dynamics of optical injection semiconductor lasers (OISCLs) by focusing on noise effects, its control and suppression using modified SCLs rate equations. Lasers exhibit spontaneous emission phenomenon, which is stochastic and, then a noise induced-effect. We treated noise influence in laser by adding the Langevin noises in laser rate equations. As results, we showed the method of avoiding and eliminating the $1/f$ noise, which requires a master laser (ML) with lower phase fluctuations. We optimized the relative intensity noise (RIN) in the low-frequency region (up to relaxation frequency around 1GHz) and reduced the level of intensity noise and the frequency noise (FN) when the OISCL is controlled by a new control parameter so-called effective gain coefficient (EGC) among many other parameters. We also developed a modified formula of laser full-width-half-maximum (FWHM) leading to an ideal laser linewidth modulated by the EGC in addition to the Henry factor. Next, we integrated it in an electrical oscillator based on resonant tunneling diode (RTD) in order to study the induced-nonlinear dynamics. We showed that either stabilities or instabilities of SCLs are enhanced by optoelectronic integration with an RTD. The EGC allows the restriction of locked optical phase leading to the stability control. The DC voltage, the parameter r (the resistance of the DC biasing circuit) and the EGC were control parameters in the central of these works: We observed that stable points are achieved, when the RTD is biased in the NDR either by smoothly increasing the DC voltage or by increasing r while the EGC is decreasing. Nevertheless, the system has widely generated unstable oscillations. Various rich forms of dynamical behaviors have been observed including generation of chaos, hyperchaos and multistability with coexistence of N-scrolls and M-scrolls attractors due to cooperative dynamics between electrical excitation and optical injection in SCL. We achieved the route to chaos via cascade period doubling sequences termed Feigenbaum scenario in addition to the reversal period doubling cascade named antimonotonicity and, the OISCL exhibited furthermore strange attractors such as chaotic multiscroll attractors and an infinite scroll attractor. We used the parameter r and DC voltage to control multistability and chaos. Lastly, in optical domain, the system has revealed bursting oscillations (BOs), mixed mode

oscillations (MMOs), square-wave BOs modulated by the EGC, and mixed mode incrementing bifurcation (MMOIBs) relevant in the description of brain neuron activity.

Keywords: *Semiconductor laser, optical injection, effective gain coefficient, optoelectronic oscillators, resonant tunneling diode, multistability, chaos, mixed mode oscillations.*

Résumé

La recherche en dynamique non linéaire en physique des lasers, en particulier dans les lasers à semi-conducteurs continue de croître sans cesse depuis l'avènement des premières diodes laser. Ces lasers à semi-conducteur sont d'une importance primordiale dans les traitements optiques de données et les communications optiques. Cette thèse étudie la dynamique non linéaire des lasers à semi-conducteur à injection optique en se concentrant sur les effets du bruit, son contrôle et sa suppression à partir des équations modifiées des lasers à semi-conducteur. Comme résultats, nous avons montré une méthode d'élimination du bruit $1/f$ qui exige un laser maître avec de faibles fluctuations de phase optique. Nous proposons de méthodes d'amélioration du spectre du bruit d'intensité en basses fréquences (jusqu'à la fréquence de relaxation autour de 1 GHz) et de réduction des bruits d'intensité et de fréquence lorsque le laser est contrôlé par un nouveau paramètre de contrôle appelé coefficient de gain effectif parmi tant d'autres paramètres. Nous avons également développé une nouvelle formulation de la longueur à mi-hauteur donnant une largeur de raie laser idéale modulée par le coefficient de gain effectif en plus du facteur Henry. Dans la suite, nous avons intégré ce laser dans un oscillateur électrique à base de diode à résonance tunnel dans le but d'étudier sa dynamique nonlinéaire. Les résultats ont montré que la stabilité du laser à semiconducteur est améliorée par l'intégration optoélectronique avec une diode à résonance tunnel et que le coefficient de gain effectif permet la restriction de la phase optique de verrouillage et donc le contrôle de stabilité. La tension continue, le paramètre r (la résistance globale du circuit) et le coefficient de gain effectif étaient des paramètres de contrôle au centre de ces travaux : nous avons découvert que des points d'équilibre stables sont atteints dans la zone de résistance négative soit en augmentant progressivement la tension de polarisation, soit en augmentant la résistance r pendant que le coefficient de gain effectif diminue. Il est à noter que le système a généré de multiples oscillations instables. Diverses riches dynamiques nonlinéaires ont été observées, notamment la génération du chaos, de l'hyperchaos et la multistabilité avec la coexistence des attracteurs N-scrolls et M-scrolls en raison de la dynamique coopérative (interférence) entre l'excitation électrique et l'injection optique du laser à semi-conducteur. La route vers le chaos était observée via des séquences de doublement de période en cascade (scenario de Feigenbaum) en plus de la cascade de doublement de période inverse appelé antomonotonie et, le laser a révélé en outre des attracteurs étranges tels que des attracteurs chaotiques multiscroll et un attracteur infinite-scroll. Nous avons utilisé le paramètre r (la résistance globale du circuit)

et la tension de polarisation pour contrôler la multistabilité et le chaos. Enfin, dans le domaine optique, le système a révélé une dynamique éclatante à partir d'un point de bifurcation, des oscillations en mode mixte, des oscillations éclatantes à ondes carrées modulées par le coefficient de gain effectif et une bifurcation incrémentielle en mode mixte pertinentes dans la description de l'activité neurale du cerveau.

Mots clés : *Laser à semi-conducteur, injection optique, coefficient de gain effectif, oscillateurs optoélectroniques, circuit, diode tunnel résonante, multiscroll, oscillations en mode mixte.*

General Introduction

Lasers communications systems utilize optical waves as carriers to transport signals through optical fibers to remote locations, taking the advantages of optical fibers low loss, light weight, high capacity, high security and immunity to electromagnetic interferences [1]. This technology is beginning to be used in local access networks (LAN) to provide private users ultra-wideband digital communications. Nowadays, major communications in cities and metro areas are evolving in the replacement of copper-wire based networks with fiber-optic networks. Moreover, the worldwide matrix optic-fibers network that connects continents and communities enables sharing information quicker than ever due to the electrical-to-optical (E/O) conversion enabled by semiconductor lasers (SCLs). This way of higher-speed information transmission at ultrahigh-speed rates through optical fibers should not be possible without the advent revolution of the laser diodes (LDs) as well as the use of pump Erbium Doped Fiber Amplifiers (EDFAs). In addition, standard and long distance communication networks use the second (1.33 μm of wavelength) and the third (1.55 μm of wavelength) windows silica optical fiber respectively (see Figure 1). As the second window is without dispersion, the interest of the third is the low absorption. The no dispersion and low absorption windows of silica optical fiber correspond to the LDs wavelength spectrum.

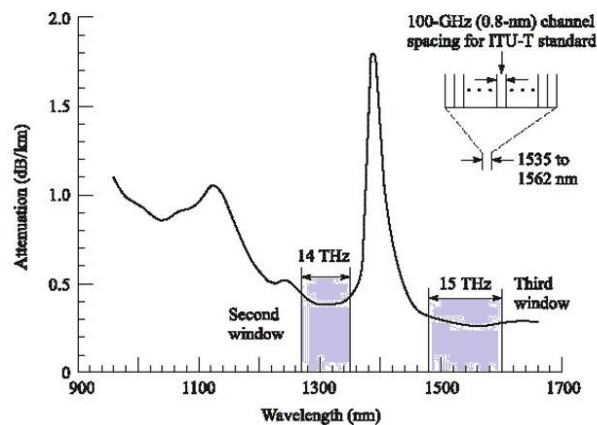


Figure 1. Low-loss transmission windows of silica fibres in the wavelength regions near 1.3 and 1.55 μm [2]

Today, offering improvement to light-wave, more reliable, small size and most cheaply manufactured transmitter equipment with information transmission securely is likely the more severe trend in communications and information technologies. Since optoelectronic oscillators

(OEOs) can significantly simplify and increase the capacity of photonic systems, they have attracted great attention in recent years. Generating pure high frequency signals using simple, low-phase noise, efficient, and low cost oscillators are being considered as major requirements for next generation photonic communication systems. In a special way, OEOs based on resonant tunneling diode (RTD) integrated with a laser diode (LD) can operate at ultrahigh frequency systems. The RTD feature in addition enhances the optoelectronic characteristics. It reduces power consumption and offers significant improvements in the modulation/detection performance and functionality due to its wide bandwidth negative differential resistance (NDR) region, capable of producing electrical oscillations up to 831 GHz [3] or above 1 THz [4 - 6]; this allows the RTD to be the fastest purely electronic devices operating at room temperature.

Emergence of Semiconductor Lasers

Much notable scientific accomplishments related to the emergence of laser magnify the demonstration of the first laser built by T.H. Maiman in ruby crystal in 1960 at Hughes Research Labs. This ruby crystal laser leads to much exaltation each celebration of laser's birthday. However, in many ways, laser technological impact had been quick really ignited by the successive and almost simultaneous demonstrations of SCL in 1962 by four independent groups of researchers. Today almost six decades – the year 2022 will be the 60th birthday of SCL – are passed that the first demonstrations of laser emission in homostructure GaAs semiconductor p-n junction had been reported [7, 8]. The first semiconductor laser diode worked in cryogenic temperature, releases pulsed wave and claims high-pulsed working current. The introduction of the heterostructure SCL led to great advancement and raised an important field named optoelectronics. The emergence of heterostructure LD gave promise in the production of continuous wave (CW) lasers, low threshold lasers operating at room temperature. Therefore, the race to obtain different type of lasers then started. Today, LDs are more reliable means, more rugged constructions (completely solid state), and very convenient means, cost-effective of developing lasers coherent light. SCLs are massively produced in very compact and small size similar to electronic components such as transistors (see Figure 2).

Even though material processing, cutting material and welding require high-power lasers, nowadays, SCLs are the most spread used lasers. For example in printers, bare-code reader, for motion and smoke sensing, lighting for projectors, to measure distance for road or between cars, write/read ability of compact and digital video disks (CDs and DVDs) players. So, communications and plenty applications make LDs necessary for today's electronic technology.

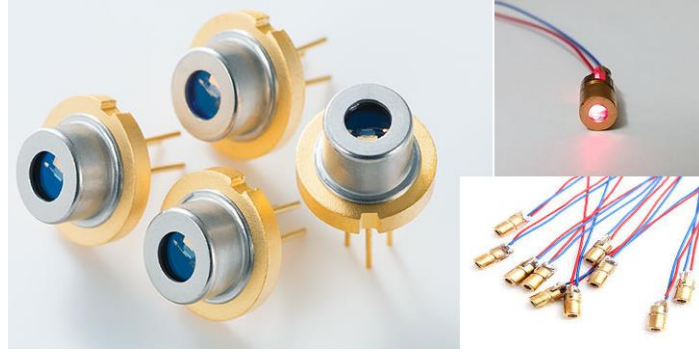


Figure 2. Semiconductor laser diodes modules [9, 10]

Chaos in Semiconductor Lasers Systems

In the beginning of the early 1900s, many researchers were awarded of the existence of complex dynamics in well-defined systems [11]. In 1913, a prominent French mathematician Poincaré noted for the first time the sensitivity to initial conditions (ICs) in some former nonlinear complex systems and defined the unpredictability concept. First, irregular pulsations and dynamical instabilities have been observed in the early stage of the development of the first laser. When lasers with erratic output have been firstly reported, the lack of knowledge of what would later be termed “chaos” made it be unexplained either wrongly be attributed to noise. Since chaotic dynamical systems are described by, a set of determinist equations and irregularity induced by chaos is different from that from random fluctuations due to stochastic process. In 1960-1963s, this situation changed when Lorenz discovered irregular pulsing with a remarkable feature in a nonlinear system with only three variables [12]: the Lorenz Eqs. (1). Lorenz equations for fluid convection is a description model for the atmospheric flow. The observation of the sensitivity to ICs in this system according to Poincaré prediction leaded Lorenz to provide the existence of chaos and to introduce the interesting *Butterfly effect* in the theory of chaos.

$$\begin{cases} \frac{dx(t)}{dt} = \sigma [y(t) - x(t)] \\ \frac{dy(t)}{dt} = \rho x(t) - y(t) - x(t)y(t) \\ \frac{dz(t)}{dt} = x(t)y(t) - \beta z(t) \end{cases} \quad (1)$$

In Eqs. (1), x represents the intensity of the convection, y represents the difference of temperature between the ascending and descending currents, and z is proportional to the distortion of the vertical temperature profile from linearity. Lorenz was led to choose $\rho = 28$, $\sigma = 10$ and $\beta = 8/3$. It has been shown that at least three independent variables (i.e. three degrees of freedom) are necessary to observe deterministic chaos [13].

In 1975 the field of laser physics and chaos theory emerged due to the discovery of a striking analogy [14] between the Lorenz equations and Maxwell-Bloch equation as formulated by Haken modelling the dynamics of light-matter interactions assuming a unidirectional ring laser containing a homogeneously broadened medium [11, 15]. These equations of motion are derived using a semi-classical approach, considering the resonant field inside the laser cavity as a macroscopic variable interacting with a two-level system [14]. Assuming exact resonance between the atomic line and the cavity mode, three coupled non-linear differential equations for the field, polarization, and population inversion of the medium for the so-called Lorenz-Haken [15] model given in Eqs. (2).

$$\begin{cases} \frac{dE(t)}{dt} = \kappa [E(t) + 2CP(t)] \\ \frac{dP(t)}{dt} = -P(t) + E(t)D(t) \\ \frac{dD(t)}{dt} = -\wp [D(t) + 1 + P(t)E(t)] \end{cases}, \quad (2)$$

where $E(t)$ represents the electric field in the laser cavity having a decay constant k ; $P(t)$ is the polarization of this field; $D(t)$ is the population difference having a decay constant. Both κ and \wp are scaled with respect to the polarization relaxation rate, and $2C$ is the pump rate required for obtaining the lasing effect. The model of Lorenz-Haken equations for a laser model is equivalent to Lorenz equation [11].

Later, chaos theory had revealed that, nonlinear systems with high dimension enough might bifurcate to more complex dynamical behaviors and chaos. Since optical material and device such as lasers are nonlinear systems due to the nature of electromagnetic field, nonlinear theory applies to SCLs and, laser equations can be in general, classified as the Lorenz system [11]. Semiconductor laser is one of the first working lasers. However, this semiconductor laser and others semiconductor devices are still very important for developing nowadays equipment. LDs uniquely possess property that makes them sensitive to electrical and optical perturbations (such as optical injection and optical feedback), direct modulating current. Sensitivity of SCL makes it easily be integrated with other optical device or with electrical component in optoelectronic integrated circuits (OEICs) with great potential applications. This unique property of LDs enables them also a high potential such as frequencies up to several GHz or THz achieving high-speed techniques and more sophisticated and chaotic systems in a less space. Chaos is one of the most used tools for today's encryption research problems. In the first view, semiconductor LD is a

damped nonlinear oscillator and is therefore limited to a spiralling flow toward a steady-state so-called relaxation oscillation as depicted in Figure 3.

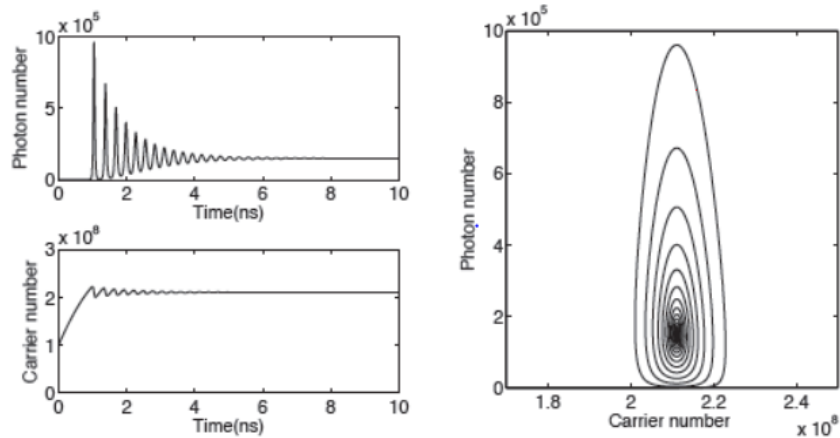


Figure 3. Simulated dynamics the photon number and carrier inversion showing damped oscillations toward a steady state (relaxation oscillations). Dynamics is limited to spiralling relaxation flows in the phase plane (right) [16].

Lorenz explanations of chaos opened many configurations to perform the feature of nonlinear systems. For instance, in optoelectronics, optical feedback [Figure 4(a)], optical injection [Figure 4(b)], current modulation [Figure 4(c)] and optoelectronic feedback [Figure 4(d)] are usually used in LD chaotic-based systems in order to achieve chaos.

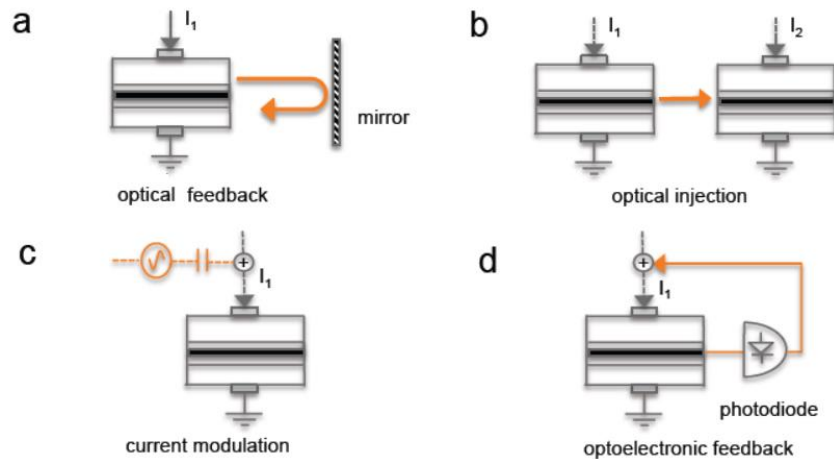


Figure 4. Chaos in laser diode: (a) Optical feedback from an external mirror, (b) Optical injection from a master to a slave laser diode. (c) External current modulation applied to a laser diode. (d) Optoelectronic feedback by reinjecting a delayed and amplified signal from a photodiode that measures the laser output [16].

Motivation and Objective of the Thesis

The radio frequency (RF) resonator-based oscillator technology cannot match all advantages of photonic systems. Therefore, a great search has been achieved in OEO configurations capable to generate complex and ultra-pure RF carriers in both electrical and optical domains. Several OEO

systems have been proposed over last few years, including photonic oscillators based on InP monolithic oscillators [17], using either direct modulated semiconductor lasers and optical/optoelectronic injection schemes [18] or electrical oscillators to drive the SCLs [19 - 21]. However, these configurations either are too complex with several components or do not meet all the photonic RF systems OEO requirements [22].

An ideal OEO should involve the generation of ultra-pure RF signals in both electrical and optical domains with its operation being controlled by both electrical and optical injected signals. In 1996, Yao et al. proposed an OEO configuration that close match these requirements, capable to produce ultra-pure microwave signals [23]. However, such configuration is quite complex, containing an optical fiber delay line several kilometers long, a wide-band Mach-Zehnder modulator to modulate non-linearly a semiconductor laser continuous-wave coherent light beam, a preamplified photodiode, a narrow microwave RF filter and a microwave amplifier.

The fastest purely electronic device operating at room temperature is the RTD. Resonant tunneling diodes are nanoelectronic semiconductor structures with wide bandwidth NDR region capable of producing electrical oscillations up to several hundred of GHz [3] or some THz. When RTD is integrated within optoelectronic devices such as optical waveguides and LDs, they can enhance optoelectronic characteristics [24, 25]. Recently demonstrated optoelectronic voltage controlled oscillators (OEVCOs) and optical controlled RF oscillators based on the hybrid integration of an RTD with a laser diode (RTD-LD) and a RTD with a photoconductive have shown especial interest in OEOs [26].

The main investigation of this thesis to the technology innovation is the proposal of a novel OEO based on the integration of RTDs with optical injection semiconductor lasers. An alternative option to mainstream in innovative devices to integration of optical injection semiconductor lasers dynamics. Extending of the system dimension and bringing high dimension chaos complexity in RTD-LD integrated circuit systems is our main goal. In our study, mostly in concordance with recent works of Figueiredo and al. [27, 28], we use the model of semiconductor laser developed in 2011 by Mengue and Essimbi to be integrated with RTD oscillator. This model of semiconductor laser's rate equations inspired from Lang and Kobayashi model is mainly described by a novel control parameter named the effective gain coefficient (EGC). In addition, as most of tunneling devices, RTDs are nanoelectronic semiconductor structures exhibiting a negative differential resistance (NDR) region. Nevertheless, Schuman and other models giving mathematical description of its I-V characteristics are usually complex and difficult to be used for theoretical analysis of RTD-based systems. A simplified model of the RTD was proposed as a polynomial function of the third order with interesting results [29 - 31].

In this thesis, the investigation of noise-induced effects in optical injection semiconductor laser is achieved by using the Langevin approach. The first aim of this work is thus to estimate several means to reduce, eliminate and control noise that penalizes the performance of optical injection systems. A comparison with previously published results is also presented.

On the other hand, we initiate an optoelectronic oscillator by integrating this semiconductor laser in resonant tunneling diode electrical oscillator. We introduce the polynomial model for current-voltage characteristic of **RTD** and analyze the stability and nonlinear dynamics of the novel **RTD-LD** optoelectronic oscillator.

Outline of Thesis

There are three chapters in this thesis altogether, starting by the General Introduction dedicated to semiconductor lasers and chaos in laser systems. The rest of the thesis is organized as follows: The Chapter **I** presents the Literature Review of Semiconductor Lasers, Resonant Tunneling Diode and Optoelectronic Integrated Circuits. The Chapter **II** is dedicated to the material and tools such as analytical and main numerical approaches used throughout. This chapter also includes laser equations and the class of optoelectronic hybrid oscillator (**OEHO**) that guided us through this work. Chapter **III** provides the obtained results and of the proposed models and their corresponding discussion by using tool provided in Chapter **II**. Finally, this thesis ends with a General Conclusion and gives outlooks of future works in **RTD-Optical Injected SCL**.

Chapter I

LITERATURE REVIEW OF SCLs, RTD DEVICES AND OPTOELECTRONIC OSCILLATORS

I.1. Introduction

SCLs and RTDs are semiconductor optoelectronic devices and, semiconductor operation depends on the one hand on its structure and in the other hand on the external stimuli to which it is subjected. This Chapter is divided into four sections. The first Section presents the basic working principle of laser by considering the interaction between electromagnetic (EM) radiation and material in a two-level energy atomic system. An overview of accomplishments in SCLs, particularly, OISCL with the effective gain coefficient as new control parameter and, origins of noise in SCLs are given in the second Section. The third Section is devoted to the general background on heterostructure semiconductor devices. This Section also provides description of RTD and some current-voltage characteristic models. The last section addresses a brief overview of OEOs based on RTD-LD integrated circuits.

I.2. Lasers

The L.A.S.E.R. would not been made without an understanding that “light is a form of electromagnetic radiation” as discovered by Max Planck, and described by quanta theory. The quanta theory marked the revolutionary point in physics that it inspired up-and-coming physicists such as Albert Einstein. In 1917, Albert Einstein postulated the key phenomenon that makes laser working: the stimulated emission. That is, the word laser is an acronym, which stands for *Light Amplification by Stimulated Emission of Radiation*. Does the word “light” includes all EM radiations of any frequency? We answer to this question in the next subsection I.2.1.

I.2.1. Electromagnetic spectrum

The EM spectrum goes from radio wave to gamma-wave; through microwaves (MW), IR-waves, visible-light, UV-waves, gamma rays and X-rays successively. All these radiations are similar that they all move at 299792458 – approximately 3×10^8 – meters per second: the speed of light in the vacuum commonly denoted by c ($c \approx 3 \times 10^8 \text{ m/s}$). However, their frequencies (their wavelengths or their energies) are all different. Therefore, there is a fullness of lasers, working at

any frequency: IR-lasers, Visible-lasers, UV-laser, X-lasers, and Gamma-lasers. A “laser” emitting radio wave or MW is a MASER (*microwave amplification by stimulated emission of radiation*) instead of as shown in Figure I.1. Nevertheless, there are four great categories of lasers: solids state lasers, gas lasers, dye lasers and semiconductor lasers due to the nature of gain medium.

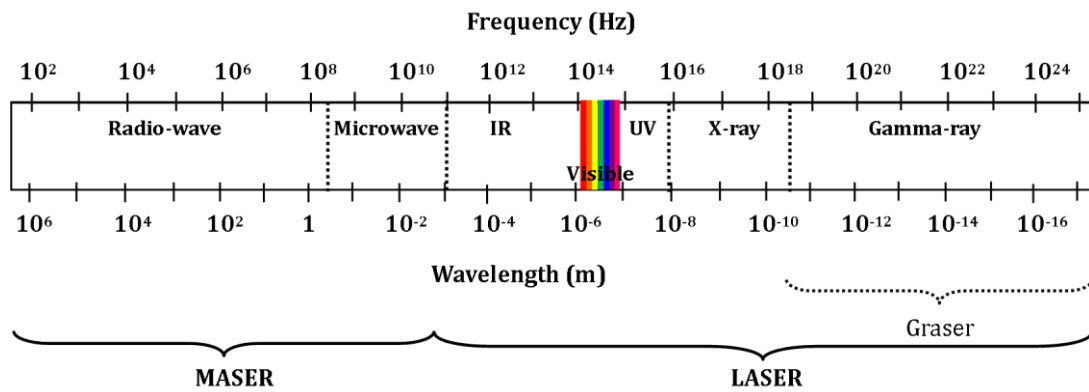


Figure I.1. The EM spectrum is divided for maser and laser depending upon the wavelengths of the radiation. Visible light refers to optical rang that occupies the smaller window ranging from 400nm to 700nm wavelength [32].

Early in 1953, in an unpublished manuscript, John von Neumann firstly suggested that, a sufficient injection of carriers in the p - n junction of semiconductor could generate stimulated emission of incident radiation [8]. For our better knowledge, this suggestion should be the first concept of the laser. One year later i.e. in 1954, C.H. Townes, J. Zeiger and graduate student J. P. Gordon demonstrated the first maser based on the prediction of A. Einstein. This device is called maser because it was a coherent source of MW. In 1958, they analyzed the possibility of the maser to generate and amplify EM radiation over the optical (visible) rang and near optical rang by stimulated emission. When that maser operating in optical rang was imagined, Gordon G. (in 1957) coined the acronym of laser rather than *optical maser*, which is now obsolete [33, 34]. In 1960, inspired by Schawlow and Town, T. H. Maiman built the first laser using ruby crystal ($Al_2O_3 : Cr$) as gain medium and pumped by a lamp flash at Hughes Research Laboratories [35, 36]. This laser produced a red beam of light at 694nm [35]. In 1964 C. H. Town, N. G. Basov and A. M. Prokhorov were awarded the Nobel Prize in Physics for their fundamental works in the field of quantum electronics, which led to the construction of oscillator and amplifier based in maser and laser principle.

The laser can be regarded as one of the most invention of the twentieth century that made live new technology fields such as optical storage information, optical communications, and medical applications, among many others [35].

I.2.2. Basic Elements of Lasers

A laser medium, a laser resonant cavity and a pumping mechanism are three key components in a laser [35], as shown in Figure I.2. The laser medium, which can be a gas, a fiber, a solid-state material or a semiconductor, is inserted into the laser cavity that consists of a pair of mirrors. The laser medium provides light amplification. The pumping energy is applied to the laser medium via a flash lamp (as in this first ruby laser), a laser light (for example in optically pumped lasers), or an electric current (in semiconductor laser for instance). The plane-parallel mirrors form the resonant cavity. The reflectivity of one mirror is 100% (the total reflector mirror), while that of the one other (the partial reflector mirror) is purposely made lower so amplified light inside the cavity will come out of the lower reflective mirror.

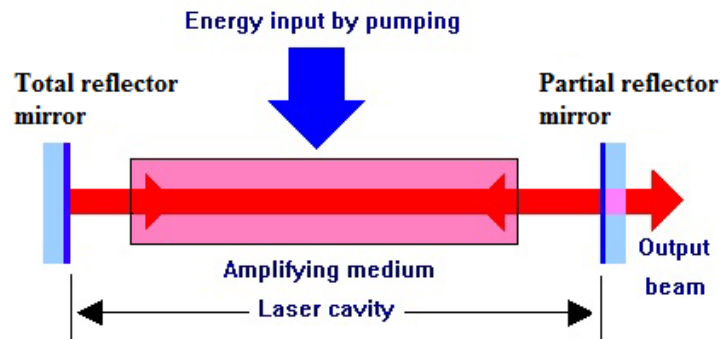


Figure I.2. Basic elements of a laser system

I.2.3. Two-atomic-level Laser System

The laser working principle is best understood by considering a hypothetical two-level atomic system and interaction between EM radiation and material. In this subsection, we consider the two-level atomic system to describe the laser working.

Absorption, spontaneous emission, and stimulated emission are the three basic processes through which EM radiation can interact with the matter. Under normal conditions, all material absorbs light. Let us consider the two-level atomic system with E_1 and E_2 the lower level and the upper level energies respectively. Through the absorption process, a photon of energy $E = \hbar\omega = E_2 - E_1$ is absorbed, while an electron is transferring from lower level to upper level. In general, when an electron is in an excited energy level (the upper level in two-level system), it must eventually decay to the lower level, emitting a photon of energy $\hbar\omega$. This process is called *spontaneous emission*, and, the radiation is emitted in arbitrary direction of propagation and phase (polarization). The average time of electron is called constant of spontaneous emission or spontaneous emission lifetime denoted by τ . On the other hand, if an incident photon happens to

pass by whose energy is approximately $\hbar\omega$, there is a probability that the incident photon induces the electron to make a downward transition. Therefore, a photon is emitted at exactly the same wavelength, in exactly the same direction, and exactly the same phase as the incident photon. This even is called *stimulated emission*. Absorption, spontaneous emission and stimulated emission are illustrated in Figure I.3 for a two level energy system.

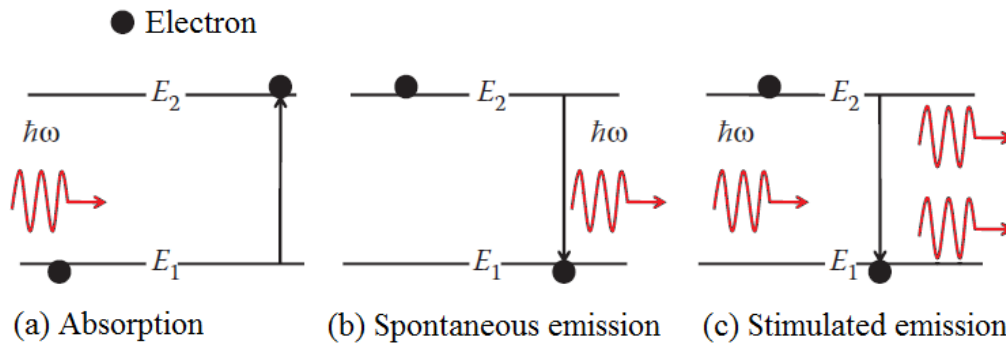


Figure I.3. Interactions light material: (a) Absorption, (b) Spontaneous emission and (c) Stimulated emission.

I.3. Semiconductor Lasers

Early the maser manufacturing, in 1953, John von Neumann sketched out an idea for producing stimulated emission in semiconductors, his proposal was not published until 30 years after his death [8, 37, 38]. In 1962, four groups of persons working independently announced almost at the same time the invention of the first semiconductor LD in the homostructure GaAs semiconductor. The race for the production of semiconductor lasers was then launched. Nevertheless, all those first LDs were wide-area homostructure devices, which operated only at cryogenic temperature and driven above the threshold by powerful current pulses [38].

A SCL can be considered as a system containing two energy levels populated by electrons (carriers). This optoelectronic device consists of a p-n junction (a diode) with an active region where electrons and holes recombine. When this diode is forward biased by electric source such as a battery, electrons from n-region and holes from p-region cross the junction and it can result absorption, spontaneous emission and/or stimulated emission (see Figure I.4).

LD is the more efficiency and reliable lasers that exist and find multiple applications in science and technology due to unique properties that make them be different to other lasers [40 - 42]:

- High conversion efficiency;
- Low power consumption;
- Small size (the typical length of a semiconductor laser is 0.25 mm);
- Low cost;

- High frequency modulation (more than 10 GHz);
- Long service life;
- Wide range of emission wavelengths.

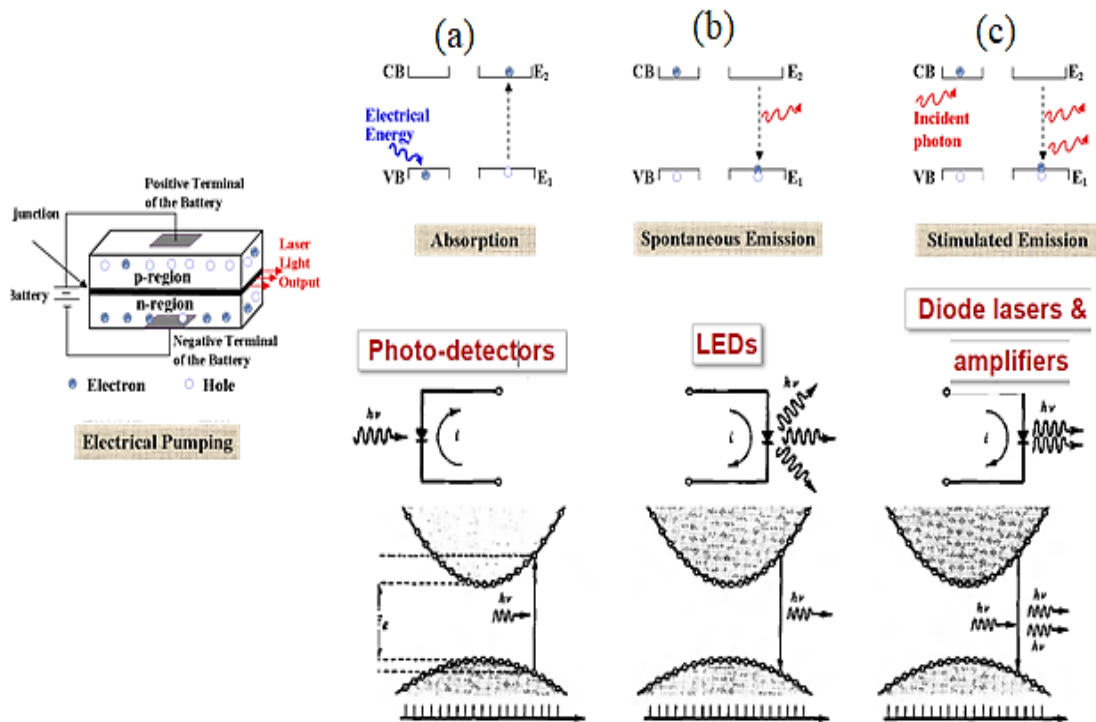


Figure I.4 . The basic working principles of semiconductor laser diode. The absorption (a) of a photon results in the generation of an electron-hole pair. The recombination of an electron-hole pair results in the spontaneous emission (b) of a photon. Electron-hole recombination can generate the stimulated emission (c) of an identical photon [39].

Nowadays, the LDs cover a wide range of application in different areas. From industry to military applications and scientific fields, the role and the use of SCLs is clearly highlighted [43]. One of the most outstanding uses of semiconductor lasers are for light sources for optical fiber communication systems, designed to transmit a huge amount of information at long distances. They are also widely used for optical data storage in CDs, DVDs and Blu-ray systems. Other domains in which SCLs have found important great potential applications are optical medicine, material processing, metrology, spectroscopy, air pollution, etc. Nowadays, SCLs they are become ubiquitous granted application devices such as portable pointers [44].

In addition, the two summarized main physics properties differences between SCLs and other lasers are the low reflectivity of the internal mirrors in the laser cavity [11].

I.3.1. Rate Equations of SCLs

All dynamical systems evolve in time. The temporal dynamics of SCLs can be described by using a set of coupled ordinary differential equations (ODEs), where the main three physical variables are the laser photon density, the carrier density and the laser optical phase in the medium. When

the laser injection pumping current I is below the laser threshold I_{th} the spontaneous emission predominates and the LD emits as simple light emitting diode (LED) and it outputs incoherent light emission (see Figure I.4(b)). Above the threshold, the transparency condition is satisfied and the p-n junction to become active and, the population inversion is established. Then if the injection carrier is higher enough, the stimulated recombination exceeds the absorption and the active region become the gain medium. Then the p-n diode junction emits coherent light emission. The carrier density in laser cavity is commonly denoted by $N(t)$ while photon density is denoted by $S(t)$. The Eq. (I.1) gives the linear gain $g(N)$ of SCL.

$$g(N) = Gn(N - N_0) \quad (\text{I.1})$$

with N_0 The carriers at the transparency.

Eqs. (I.2) give the classical coupled nonlinear ODEs of LD for photon density and carriers explicitly in the form:

$$\begin{cases} \frac{dN(t)}{dt} = J - \frac{N(t)}{\tau_s} - g(N)S(t) \\ \frac{dS(t)}{dt} = g(N)S(t) - \frac{S(t)}{\tau_{ph}} + R_{sp}(t) \\ \frac{d\phi(t)}{dt} = \frac{1}{2} \alpha \left[g(N)S(t) - \frac{S(t)}{\tau_{ph}} \right] \end{cases} \quad (\text{I.2})$$

Furthermore, the variables $N(t)$, $S(t)$ and $\phi(t)$ are carrier density, photon density and optical phase respectively. The pumping current density $J = \eta_i I / q \mathcal{G}$; I is pump current; q is electron charge; η_i is efficiency; \mathcal{G} is active region; N / τ_s is the recombination of carriers; $g(N)S$ takes into account the stimulated emission and absorption; S / τ_{ph} represents the cavity losses and R_{sp} is the spontaneous emission term. Here, τ_{ph} is the photon lifetime and τ_s the carrier lifetime. In Eqs. (I.2), the phase is not coupled with the other equations. Therefore, even though the system (I.2) is described by three variables, it behaves stably. In general, according to laser rate equations, one has three class of laser: the Class A lasers governed by only one rate equation and characterized by no oscillations dynamics. The Class B lasers described by two rate equations generating transient relaxation oscillations. Finally, the Class C lasers governed by three rate equations for carrier density, photon density and the macroscopic atomic polarization [11].

In first point of view, SCLs are class B lasers. However, a SCL with an external perturbation such as optical feedback and optical injection current modulation can display chaotic output.

I.3.2. Semiconductor Laser with Optical Injection

Optical injection consists to subject a laser call slave laser (SL) to external optical beam from the other laser named master laser (ML) as depicted in Figure I.5. Optical injection introduces an extra degree of freedom in laser the perturbed laser is a candidate to chaos [11].

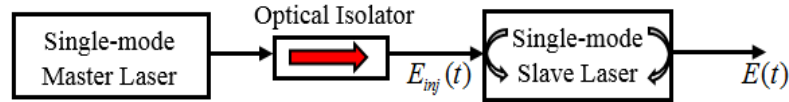


Figure I.5. Scheme of optical injection. The SL is subjected to optical injection by the ML. Unidirectional coupling is ensured by an optical isolator

Before 2012s', it have been known to the scientific community that, the important control parameters of OISCL's dynamics were the frequency detuning between the master and slave lasers, the LEF (the α -parameter) and the injection strength from the master to the slave [11]. Lang and Kobayashi are pioneers to adopt in 1980 the differential equations of field to describe the OISCL. In 2011s' and the beginning of 2012s', Mengue and Essimbi developed and proposed a novel model equations of OISCLs described by (I.3) and (I.4) and resulting from the modification of Lang and Kobayashi equations [45].

$$\frac{dE(t)}{dt} = \frac{1}{2} \frac{1}{(1+\gamma)} [1 - \gamma(1 - j\alpha)] \left\{ (N(t) - N_0) - \frac{1}{\tau_p} \right\} E(t) + \frac{k_{inj}}{\tau_{in}^*} E_{inj} e^{[\psi(t) - \varphi_{inj}(t)]} \quad (I.3)$$

$$\frac{dN(t)}{dt} = J - \frac{N(t)}{\tau_r} - \left\{ \frac{1}{\tau_p} + G_N (N(t) - N_{th}) \right\} E_0^2(t) \quad (I.4)$$

here, the parameter γ called the EGC had been defined as it appears in the effective time of flight in the laser cavity where the round-trip time inside the laser cavity is τ_{in} . $E(t) = E_0(t)e^{-j\phi(t)}$; with $E_0(t)$ the amplitude of the complex field relates to the photon density S by the relation $S(t) = |E_0(t)|^2$. $\psi(t) = \varphi(t) - \Delta\omega$ is the phase difference between the internal and the injected fields; τ_p is the photon lifetime; τ_r is electron-hole recombination time; G_N the modal gain; E_{inj} is the injected field amplitude. The model of Eqs. (I.3-I.4) reveals the existence of a fourth control parameter of LDs dynamics – the EGC – [45 - 48].

I.3.3. Noise-induced effects in Semiconductor Lasers

The noise term is important to describe lasers operating in optical communication links and sensing applications. In contrast to deterministic chaos, which obeys to temporal deterministic mathematical equations, noise is defined as an irregular temporal waveform from stochastic process. Noise cannot be described by a set of nonlinear equations. Instead, the behavior of noise can sometimes be described by a set of differential equations driven by a sequence of random numbers as stochastic terms (see Chapter III).

LDs systems are intrinsically nonlinear and operate in real world, which are naturally noisy environments. LDs include themselves intrinsic fluctuations and stochastic variations in optical beam. Under certain circumstances, an extra dose of noise can in fact help rather than hinder the performance of some devices [35]. In a single-frequency laser, there are intensity noise – amplitude noise – and phase noise. The phase noise is strongly assimilated to frequency noise (FN) which refers to the enhancement of laser linewidth due the Henry factor involved in SCLs. In SCLs, origins of noise in lasers can be separated into two main groups: the quantum noise (QN) and technical noise, which is particularly induced by the quantum effects of spontaneous emission. Technical noises are resulting from excess noise. For example from pumping current fluctuation (due to random carrier generation and recombination), optical injected light from pumping laser, vibrations of laser resonator, or from temperature fluctuations (thermal noise). Since noise cannot be eliminated, techniques of noise reduction consist to minimize noise level until the signal to noise ratio (SNR) given by Eq. (I.5) admitted. For this purpose, the performance of the system may then be judged from the SNR that shall be as large as possible.

$$SNR = \frac{\text{Signal Power}}{\text{Noise Power}} \quad (\text{I.5})$$

In practices, the laser output is detected by a high-speed photo receiver, which plays the role of E/O converter signal over time and sets into frequency domain for a certain angular frequency ω with a fast Fourier transformation (FFT). From this analysis, the relative noise level to the average direct current (DC) signal power called relative intensity noise (RIN) is measured to describe the instability level of systems. Alternatively, the RIN is the ratio of spectral density for photons noise component ($\delta\tilde{S}(\omega)$) and the average power of the laser output as expressed by equation (I.6). The derivation of RIN of OISCLs will be better explained in Chapter III.

$$RIN = \frac{|\delta\tilde{S}(\omega)|^2}{\bar{S}^2} \quad (\text{I.6})$$

For this purpose, one of famous ways for effective reduction of RIN level is that the laser parameters involved in RIN affecting its level should be known and adjusted [49].

I.4. RTDs, Electronic and Optical Properties of Semiconductors

In this section, we present certain creative advancements that had improved optical transitions in semiconductor devices.

I.4.1. Heterostructure SC material

Homostructure materials limited the performance of early LD and semiconductor devices. The advent of heterostructure material provided an opportunity to manufacture efficient electronic and optoelectronic devices from very sufficiently thin-films. Most heterostructures have an active region with a few nanometers thick. The two famous current methods of growth for nanometer heterostructure devices are metal-organic chemical vapor deposition (MOCVD) and Molecular-beam epitaxy (MBE) [50, 27]. Nowadays, semiconductor with layered heterostructures can be tailored to the present-day electronic and optoelectronic devices' needs. In 2000, Kroemer and Alferov were awarded and shared the Nobel Prize in Physics for the creative proposal of double heterostructure (DH) semiconductor that improves homostructure laser (and so on) and used in high-speed and optoelectronics.

I.4.1.1. Potential Barrier and Tunneling Effect

Classical theory of physics predicts that, a particle of energy E , travelling towards a potential barrier of height U_0 , will not be able to overcome the barrier, been reflected, unless it has a kinetic energy, sufficiently enough to pass through the top of the barrier. In contrast to Classical Physics, the development of Quantum Mechanics in the first few decade of the 20th century predicted that the particle has a finite probability to be transmitted or to tunnel through the barrier: one talks to tunneling effect. Considering the potential barriers illustrated in Figure I.6, the wavefunction $\Psi(x)$ of the particle moving through the x -axis direction is required to be continuous at the barrier, while satisfying the Schrödinger equation in the form of Eq. (I.7).

$$-\frac{\hbar^2}{2m} \frac{\partial^2 \Psi(x)}{\partial x^2} = (E - U_0) \Psi(x) \quad (\text{I.7})$$

Heterostructure junction namely Esaki's original TD was made out of a high impurity level germanium p-n junction with a very thin depletion region where the valence band of the p-type material and the conduction band of the n-type material nearly overlapped.

In 1958, Leo Esaki, working at Tokyo Tsushin Kogyo (now known as Sony Corporation) reported at the International Conference of Solid State Physics in Brussels on a new diode which exhibited "negative resistance". The diode that he invented was named the Esaki or TD due to the quantum

mechanical effect called tunneling effect that the device exhibits. This tunneling effect in TD gives rise to the NDR region in the V-I characteristic.

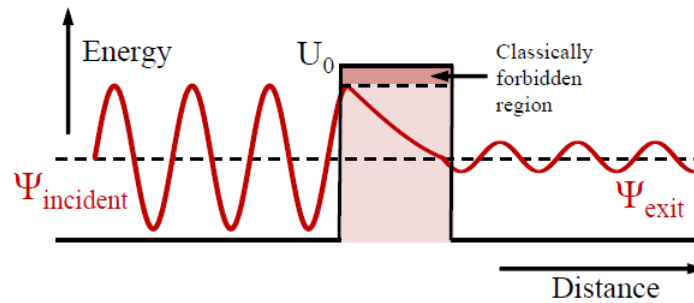


Figure I. 6. Rectangular potential barrier and particle wave function

Tunneling diodes provide the same functionality as Complementary Metal Oxide Semiconductor (CMOS) transistors. Nevertheless, from a practical perspective, these early TDs suffered from being used in control circuits, and did not offer any advantages as price was concerned, compared to the transistor [35]. When the reverse bias voltage is applied, this causes unfortunately a large reverse-bias tunneling current [Figure I.7]. This makes TDs difficult to be controlled.

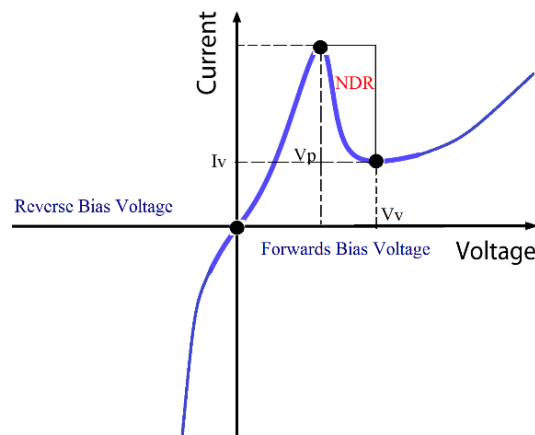


Figure I.7. Tunneling Diode I-V characteristic. When a reverse bias voltage, the current becomes extremely large

I.4.2. DBQW and the Resonant Tunneling Diode

This section presents a description of a particular form of TDs, which is the RTD. We explain the theory of RTDs' operation starting by tunneling effect in potential barrier. The N-shape current-voltage (I-V) characteristic models of RTD resulting from the nonlinear transport of charge across the double barrier quantum well (DBQW) are discussed for the purpose of nonlinear dynamics study of the RTD-based systems.

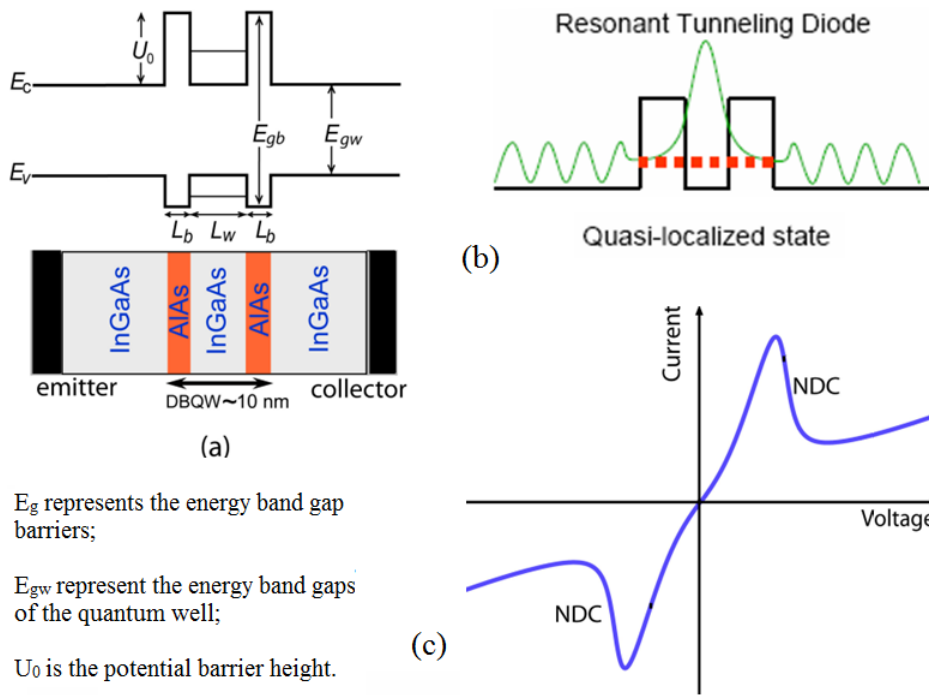


Figure I.8. (a) Diagram of a DBQW band profile formed by InGaAs/AlAs semiconductor compounds (bottom). (b) Resonance tunneling process. (c) Typical DBQW-RTD room-temperature current-voltage characteristic exhibiting NDR [28].

A typical RTD consists of DBQW as predicted by Bohm, and latter Iogansen discussed the possibility of resonant transmission of an electron through double barriers formed in semiconductor crystals [28]. From Figure I.8 (a), it can be seen that, the RTD structure is formed with a symmetric series of ...wide/narrow/wide/narrow/wide/... band gaps semiconductor materials. For the DBQW the structure to become a RTD, the emitter and the collector contact (two terminals) must be highly doped semiconductor for electrical connections. The electron in the well can *cross* or *tunnel* through barriers. When the well is of an appropriate thickness, the energies transmission in the structure approaches 100% – theoretically, a probability transmission equal to 1 is possible – [27]. This corresponds to the resonant tunneling. Chan, Esaki and Tsu predicted the unique tunneling phenomenon in RTD in 1974 for an AlGaAs/GaAs DBQW diode – the RTD –. Fundamentally, tunneling through QW is a very fast process and RTD devices have emerged as one of the most important testing grounds for modern theories of transports in physics. In addition, RTDs are central to the development of new types of semiconductor nanostructures. Recent advances in the technologies of heterostructure semiconductor alloys have stimulated a great deal of interest in theoretical essential to design and fabricate modern high-speed electronic and optoelectronic nanometric devices semiconductor superlattices, SCLs and DBQW-RTDs. It then seems obvious that the RTD is an improving of the TD functions. Indeed, the symmetric structure of RTDs induces equal magnitudes in I-V characteristic for the forward and reverse bias as depicted in Fig. I.8 (b) and (c). When a high reverse bias is applied to TDs, there is a very high

leakage current. The symmetrical structure of RTDs makes way that when reverse and forward bias voltages are applied, the very high leakage current presented in TDs I-V characteristic be eliminated (see Fig. I.8 (c)) and then, the RTDs appear as the rectifier of TDs.

Figure I.9 (a) and (b) illustrate how the applied bias affects the band structure and tunneling current. With zero bias (ii), the bands are flat, the conduction band electrons to the left of the barrier do not have an available bound state in the well to make electrons tunnel into, and no current will flow. (ii), the conduction band electrons have lined up with the lowest bound state inside the well, tunneling will start and a current will flow. The peak current (I_p) with its corresponding peak voltage (V_p) appear, (iii) the incident electrons are now above the bound state and the current will reduce to the valley current (I_v) with corresponding valley voltage (V_v). The current will then increase rapidly above V_v . The nonlinear process of charges' transport across the DBQW substructure of RTD give rise to the NDR across the DBQW substructure. In practical applications, the RTD is wonderful quantum electronic device because it is one of the few quantum transport devices that operate at room temperature [28]. In addition, the N-shape NDR of RTDs is used to make apparently to be adapted as a switching devices and high frequency oscillators. The RTDs' capability to operate as an oscillator has great interest in many topics of nonlinear dynamics. Furthermore, RTD is widely study for transport in quantum devices. Low ohmic contact reported in RTDs and short transit times lead RTDs to operate at higher frequencies.

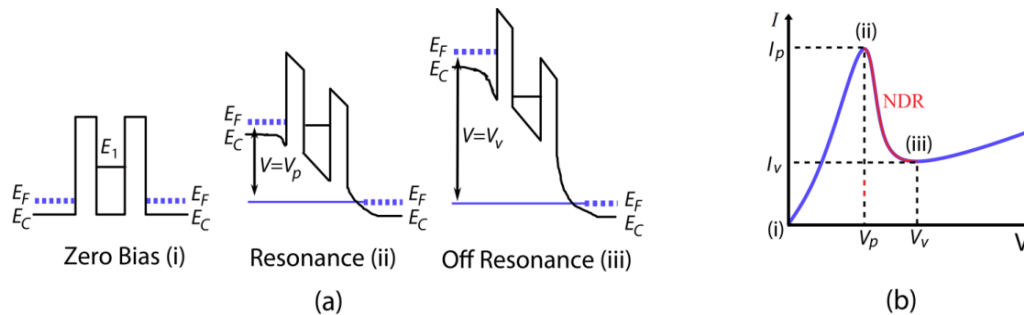


Figure I.9. (a) Evolution diagram of a DBQW RTD band profile formed at bias. (b) Typical DBQW-RTD room-temperature current-voltage characteristic exhibiting negative differential conductance.

I.4.3. Original Models of RTD current-voltage

The resonance state in RTD gives rise to the NDR resulting via quantum tunneling effect. The N-shape feature of the RTD I-V curve is attracting for modeling, designing and studying dynamics of RTD systems. Many approaches have been proposed for numerical and analytical simulations of RTDs in order to model the N-shape characteristic of RTD with best concordance with experiment measures. The more famous mathematics models can be found in Refs [51] and [52]. Among these methods, many of them calculates the first transmission probability function (coefficient) and deduce the I-V characteristic of the RTD. The others methods do not calculate

the transmission coefficient explicitly [52]. In addition, these models include continuous functions such as, trigonometric, exponential and logarithmic function or polynomial. In this section, we present the model from Yan et al. group, the model of Brown et al. group and that of Schulman et al. In addition, we focus on the one most quasi-physical relevant model of Schulman et al. From this model, we deduce resulting ninth order, six order and simple cubic polynomial fitting models. These polynomial models fit well with the N-shape of RTD I-V and then, will be the central of our investigations throughout Chapter III.

1.4.3.1. Model of Yan et al

This model is totally empirical and biased on the observations of most I-V measures. Yan et al. divided the experimental I-V characteristic of RTD in three parts: the positive differential resistance (PDR) from 0 V to V_p , the NDR region from V_V of V_p and the diode like exponential behavior. The total current from Yan et al. model is given by the sum of tunnel and diode like exponential currents $I_{Tp}(V)$ and $I_D(V)$ respectively (Eq. I.8). In addition, Gaussian or exponential function can be used to model $I_{Tp}(V)$ in PDR and NDR (see ref. [52] for explanations). The model of Yan et al. is widely used on SPICE software [53, 54].

$$I_{RDT}(V) = I_{Tp}(V) + I_D(V) \quad (\text{I.8})$$

Brown and Schulman models derived from Lorentzian approximation of transparency. These models are physical basic.

1.4.3.2. Brown et al. Model

The group of Brown developed their model biased on fitting parameters to be used in SPICE for the simulations of integrated circuits. This model is described by equation (I.9) [51]. The coefficients $C_i (i = 1:6)$ are fitting parameters which are functions of V_{peak} and I_{peak} ($c_i (i = 1:4)$) and V_{valley} and I_{valley} ($c_i (i = 4:6)$).

$$I_{RDT}(V) = f \left\{ c_1 V [\tan^{-1}(c_2 V + c_3) - \tan^{-1}(c_2 V + c_4) + c_5 V^m + c_6 V^m] \right\} \quad (\text{I.9})$$

1.4.3.3. Schulman et al. model

An exact expression for the tunneling current in a RTD is given by from the Tsu-Esaki formula [equation (I.10)]:

$$J = \int_0^{\infty} T_v(E_z, V) S(E_z, V) dE_z \quad (\text{I.10})$$

here, $T_v(E_z, V)$ is the transmission probability (transmission coefficient) and $S(E_z)$ is the electron supply functions, and E_z is the electron energy component due to electron momentum in the direction perpendicular to the RTD barriers. In the Schulman et al. I-V model the resonant tunneling current derived from equation (I.8) is expressed within the nonzero temperature, Fermi-Dirac statistics and the transmission coefficient $T_v(E_z, V)$ approximated by a Lorentzian function [27] as in Eq. (I.10)

$$J = \frac{em^*kT}{2\pi^2\hbar^3} \int_0^{\infty} T_v(E_z, V) \ln \left(\frac{1 + e^{(E_F - E)/kT}}{1 + e^{(E_F - E - eV)/kT}} \right) dE_z \quad (\text{I.11})$$

the m^* is the effective mass approximation, k the Boltzmann constant, T the temperature, E_F the Fermi energy level, T_V the transmission, E the energy of electron. This current is reduced to the formula [equation (I.12)]:

$$J = \frac{em^*kT\Gamma}{4\pi^2\hbar^3} \ln \left(\frac{1 + e^{(E_F - E_r - E)/kT}}{1 + e^{(E_F - E_r - eV)/kT}} \right) \left[\frac{\pi}{2} + \tan^{-1} \left(\frac{E_r - \frac{eV}{2}}{\frac{\Gamma}{2}} \right) \right] \quad (\text{I.12})$$

where $E_r = E + eV / 2$.

The formulation (I.12) is usually generalized in the parametric form to reproduce the peak and the NDR part. The Eq. (I.13) gives the fitting parameters and therefore Eq. (I.12) is transformed as presented in (I.14) [27]:

$$A = \frac{em^*kT\Gamma}{4\pi^2\hbar^3}, \quad B = E_F, \quad C = E_r, \quad n_1 = e/2, \quad D = \frac{\Gamma}{2} \quad (\text{I.13})$$

$$J_{RTD} = A \ln \left(\frac{1 + e^{(B - C - n_1 V)/kT}}{1 + e^{(B - E_r - n_1 V)/kT}} \right) \left[\frac{\pi}{2} + \tan^{-1} \left(\frac{C - n_1 V}{D} \right) \right] \quad (\text{I.14})$$

Like in the empirical model of Yan group, the valley current is included by using the diode-like exponential model which corresponds to the no-resonant term $-I_{NR}(V)$ – equation (I.15).

Finally, the total current in the RTD given by Shulman et al. model is in the form of equation (I.16) [27]:

$$J_{NR}(V) = H \left(e^{n_2 eV/kT} - 1 \right) \quad (\text{I.15})$$

$$I = I_{RT} + I_{NR} = f \left\{ A \ln \left(\frac{1 + e^{(B-C-n_1V)/kT}}{1 + e^{(B-E_r-n_1V)/kT}} \right) \left[\frac{\pi}{2} + \tan^{-1} \left(\frac{C-n_1V}{D} \right) \right] + H \left(e^{n_2eV/kT} - 1 \right) \right\} \quad (\text{I.16})$$

here, the parameter f is a scale factor used to take into account for the RTD area. Figure I.10 presents the RTD experimental I-V curves and numerical fitting InGaAs/AlAs semiconductor compounds using Schuman et al. model [28]. The fitting parameters are given as follows: $A=3800A.cm^2$, $B=068V$, $C=1035V$, $C=0088V$, $H=4515cm^2$, $n_1=0862$, $n_2=0.12$; assuming a temperature of operation $T=300K$ and a multiplying factor $f=2 \times 10^6 cm^2$ [28]. We can see a very good agreement between the experiment and Schuman model in Figure I.10.

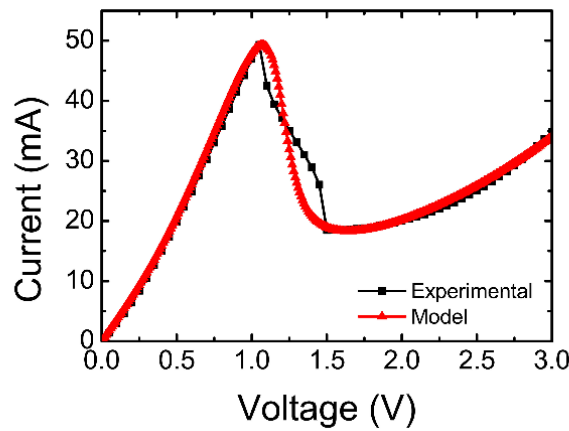


Figure I.10. RTD experimental I-V curves and numerical fitting InGaAs/AlAs semiconductor compounds using Schuman et al. model [28].

I.4.3.4. Polynomial approximations of the N-shape

The formalism of the numerical fitting presented here is special useful for circuit design due to the flexibility and small effort necessary to fit experimental data and to incorporate additional effects when desired. Taking advantage of the relative good description of the RTD DC I-V characteristic presented here, the Schulman et al. I-V model has been included together with an RTD equivalent circuit by Romeira et al. to model alternating current (AC) excited RTD systems. The complexity of Yan et al, Brown et al. and Schuman et al. models makes them difficult for certain analytical and numerical simulations [53]. This leads to many researchers to use empirical fits. For N-shape, several fits have been used such as multiple discrete devices (diodes, switches, current sources, resistors, and capacitors) [53, 55]. Trigonometric functions and Polynomial fits are very easy of working even though high order polynomials are need for good fits. However, it is easy to fit the N-shape of RTD by a simple polynomial order. In Figure I.11, we plot the derivative ninth, sixth and finally cubic polynomial fitting parameters from the Schulman et al. model. We can see a very good agreement between the experiment and Schuman model. So

polynomial approximation of the resonant tunneling diode **NDR** I-V characteristics will be used in the following chapters.

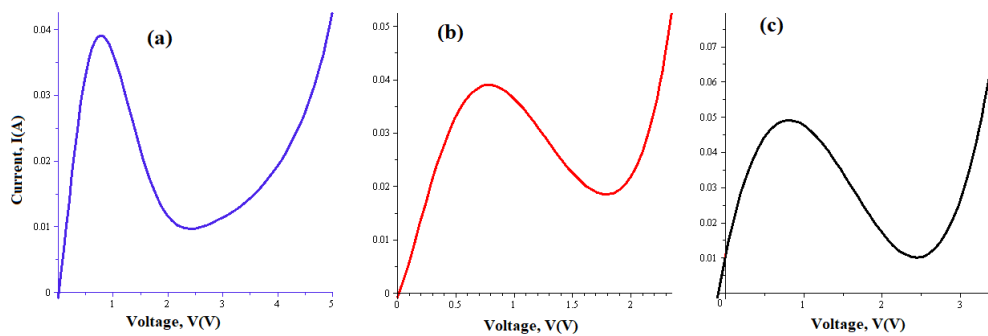


Figure I.11. I-V characteristic of NDR device provided by: (a) a nine-order polynomial, (b) a six-order polynomial and (c) a cubic polynomial resulting from the Schulman et al. model of Eq. (I.16).

I.5. Optoelectronic Oscillators

As the demand for high-speed signal transmission is increasing, optoelectronic oscillator **OEO** grows in popularity. An **OEO** is a system that combines optical device such as a laser and electronic devices. **LD** is an excellent convertor of electrical pumping current to optical signal. Revolutions of **SCL** has leded an important sub-phonic field named optoelectronic. **OEOs** are photonic systems commonly used in optical fiber communications and in wide variety of lasers application areas. Optoelectronic is a sub-photonics field based on the quantum mechanical effect of light on electronic materials. In this subsection, we review optoelectronic oscillators. We focus on **OEOs** based on **RTD-LD** coupling.

I.5.1. Optoelectronic devices

Optoelectronic devices are **E/O** or **O/E** transducers, or instruments that use such devices in their operation. These devices consist of different predominantly direct band gap semiconductors alloys lying on substrates with barriers and well regions that release quantum mechanical effects. Today, there exist plethora of optoelectronic devices include sources such as **LEDs**, **LDs**, photodetectors (**PDs**), optical amplifiers and optical modulators. With optoelectronic devices, one can emit while other can detect or control light. Optoelectronic devices have high efficiency, high speed, and low dispersion (in microwave frequency regime).

I.5.2. RTD based optoelectronic oscillators

The nonlinear characteristic of **RTD** has been intensively used for analogue nonlinear systems such as the **VdP** oscillator, Liénard Systems, Bonhoeffer– **VdP** oscillators, and **RTD** has great

promise as an oscillator and high frequency threshold (trigger) device. An overview of recent investigations related to the dynamics of optoelectronic systems consisting by **RTD** coupled with optical devices such as **EAM**, **PD** and **LD** is reported in this section. First, we start presenting the **RTD** electrical system as a Liénard oscillator [28, 56, 62, 65, 130].

I.5.2.1. NDR Oscillator

Figure I.13 shows the typical topology of an **NDR** device oscillator such as **TD** or **RTD** based circuit. The parameter R_b is the resistance of the **DC** biasing circuit. It is used to represent the contact resistance and some other losses that appear during the manufacturing process; L_b is the bias line inductance and C_n is the capacitance of the **NDR** device when biasing in the **NDR** region. The **NDR** device itself can be modeled as a voltage-controlled current source $I(V) = f(V)$, which represents the **DC** I-V characteristic of the **RTD**. It has been already mentioned that different mathematical models provide generic representation of the N-shape so that those models have been intensively used in nonlinear analysis of circuits containing **NDR** such as **VdP** and Duffing oscillators. **NDR** equations have applications in many areas of sciences and engineering.

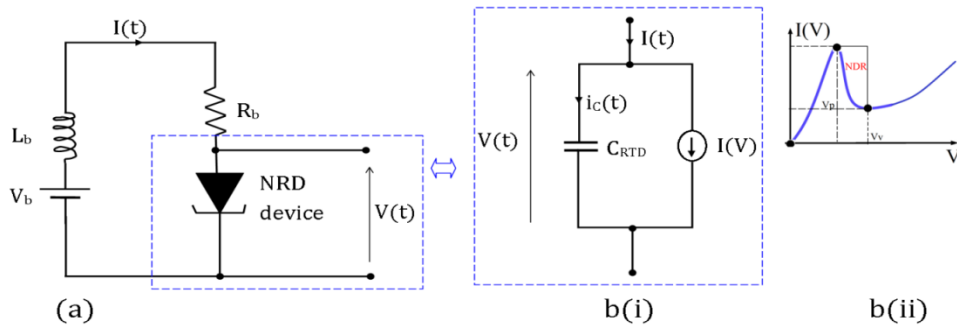


Figure I.12. NDR oscillator (a) and electrical equivalent circuit of the RTD b(i) with its I-V characteristic providing the NDR region b(ii) [28]

The dynamics of the **DC** biased **NDR** device (**RTD**) circuit [Figure I.12] is given by the set of equations (I.17).

$$\begin{cases} \frac{dV(t)}{dt} = \frac{1}{C_{RTD}} [I(t) - I(V)], \\ \frac{dI(t)}{dt} = \frac{1}{L_b} [V_b - R_b I(t) - V(t)], \end{cases} \quad (\text{I.17})$$

here, $I(t)$ is the temporal entering current in the **NDR** active region device while $V(t)$ is the voltage across the **RTD**. Algebraic transformations of Eq. (I.17) reveals that this **NDR** oscillator can be

regarded as a most generalized Liénard's oscillator described by the second-order differential equation (I.18) bellows:

$$\frac{d^2V(t)}{dt^2} + \frac{1}{L_b} \left(R_b + \frac{L_b}{C_{RTD}} \frac{d}{dV} I_{RTD}(V) \right) \frac{dV(t)}{dt} + \frac{1}{L_b C_{RTD}} (V(t) + R_b I_{RTD}(V) - V_b) = 0 \quad (\text{I.18})$$

If we set two voltage-controlled functions $h(V)$ and $g(V)$ as follows [Eqs. (I.19) and (I.20) respectively].

$$h(V) = \frac{1}{L_b} \left(R_b + \frac{L_b}{C_{RTD}} \frac{d}{dV} I_{RTD}(V) \right) \quad (\text{I.19})$$

$$g(V) = \frac{1}{L_b C_{RTD}} (V(t) + R_b I_{RTD}(V) - V_b) \quad (\text{I.20})$$

where $h(V)dV(t)/dt$ is the damping factor and $g(V)$ the nonlinear force, the second order equation (I.18) can be given in the form of normalized Liénard equation (I.21).

$$\frac{d^2x(t)}{dt^2} + h(x) \frac{dx(t)}{dt} + g(x) = 0 \quad (\text{I.21})$$

Obviously, the rescale parameter x denotes the normalized voltage across the RTD. Moreover, so, equation (I.21) is the equal to the normalized VdP equation if $h(x) = \mu(x^2 - 1)$ and $g(x) = \omega_0^2 x$; where ω_0 is the natural frequency of the VdP oscillator [56]. The equation (I.21) lets us understand that, the NDR devices-based circuit belongs to the general class of VdP oscillator well known as Liénard's oscillation [62-65].

In RTD-LD oscillator, the RTD is series connected with the LD. So, the numerical calculation of the current from solving Liénard's oscillator is used to drive the laser dynamics.

I.5.2.2. RTD-OEO oscillators innovations

The mid-1980's has known by the popularization of nanoelectronics. The continuing miniaturization of the conventional CMOS technology faces increasing technological difficulties such as quantum effect. Due to the pioneering work on resonant tunneling effect and improvement of semiconductor material properties by artificial heterostructure semiconductor, semiconductor QWs and superlattices grew using MBE or MOCVD technique, RTD is placed to overcome difficulties that faced conventional nanoscale transistors. Since then, nanoelectronics was championed by several groups for the exploration of new opportunities for circumventing the limit on the downscaling of conventional transistors and integrated circuits. The RTD has become a

research focus in nanoelectronics for its promise as a primary nanoelectronic device for both analog and digital applications [57]. Significant accomplishments have been achieved in terms of RTD integration with optical device, dynamics, modeling, fabrication technology, and circuit design and applications. The RTD-based OEOs have been widely studied, and plenty of research papers have been written on various aspects of this seemingly simple device.

In 2001, J M L Figueiredo, C.N. Ironside et al [58] proposed the resonant tunneling diode electroabsorption modulator (RTD-EAM) by on their previous works from Refs.[59, 60]. This RTD-EAM uses the NDR of RTD to switch an electric field in an optical waveguide modulating light transmission via the Franz-Keldysh effect [61]. Few years after, the resonant tunneling diode-laser diode (RTD-LD) OEO consisting by a DBQW-RTD integrated in the same chip as the semiconductor LD has been reported intensively [28]. This RTD-LD hybrid integrated circuit (HIC) is an OEO described by a Liénard oscillator where the NDR of RTD acts as an electronic amplifier that drives the LD [62]. The RTD-LD HIC have is a cornerstone of many works in RTD-LD OEOs nowadays [63]. On other side, RTD optical-waveguide (OW) has been used as voltage controlled oscillator (VCO). In addition, RTD-OEOs functions include generation, amplification, and distributions of RF carriers, clocks recovery, carrier recovery, modulation and demodulation and frequency synthesis among many others. The RTD integrated with a PD, connected in series with a LD and an optical fiber delay line operates in the time-delayed dynamical systems (RTD-PD-LD delayed systems) leads to improving RTD system furthermore. In addition to the self-sustained current and optical oscillations, chaos [64], self-synchronizations [65], ultrahigh spectral purity microwave generation for sensing and telecommunication networks and noise induced neuron-like pulsing behavior, close-to-noise reduction and so on [66] among others.

RTD-LD HICs offer many advantages not due to the introduction of an external modulating additional degree of freedom in SCLs, in addition, it demonstrates possible performance enhancement of nonlinear dynamics of the laser. In such a situation, the LD is modulated directly by the current output from the RTD electrical oscillator and the LD becomes “a driven nonlinear system” with interesting richness in various dynamics. The RTD provides a nonmonotonic current-voltage (I-V) characteristic with NDR. This nonmonotonic curve allows RTDs systems operating in either a pulsing regime (when biased in PRDs regions) or a self-oscillatory regime (when biased in NDR region). In addition, the single-mode OISCL rate equations (I.3) and (I.4) are driven by modulating current from Liénard equation (I.18). In such a situation we shall ensure that the laser threshold current lies between the RTD peak and valley currents ($I_{peak} > I_{th} > I_{valley}$), then the optical output of the laser will switch off (on) as the RTD voltage is increased (decreased).

I.6. Conclusion

This Chapter aimed to give general background in semiconductor laser, resonant tunneling diode devices and optoelectronic oscillator based on [RTD-LD](#) integrations. In this matter, the chapter has been drawn up into four main parts. Firstly, the working principle of laser was given by assuming a two-level atomic system this was followed by the general background and advances in semiconductor lasers technologies. In addition, general rate equation describing the dynamics of classical laser diode was emphasized. Moreover, in this section, a novel model of [OISCL](#) that the dynamics includes the [EGC](#) as a new control parameter is pointed up as well as an overview of noise-induced effects in semiconductor laser was also provided. At the end, breakthroughs in semiconductor are highlighted mainly the emergence of heterostructure semiconductor, [RTDs](#) features, optical properties of semiconductor material, and optoelectronic oscillator based on [RTD-LD](#) hybrid integrations.

Chapter II

MATERIALS AND NUMERICAL METHODS

II.1 Introduction

After the general review on [SCLs](#), [RTDs](#) models and [RTD-LD](#) optoelectronic oscillators in outline and in Chapter I, we proceed to describe here, sometimes from a mathematical point of view and in simple terms, numerical methods and analytical models of optical injection [SCLs](#), [RTDs](#) materials and initiate a novel [RTD-LD](#) optoelectronic integrated circuit. These numerical and analytical methods shall be applied to these systems in the next Chapter III to the study the Langevin noise induced effects in the [OISCLs](#) model, the analysis of the linear stability of the novel [RTD-LD](#) optoelectronic integrated system and its chaotic dynamics.

II.2. Fourier Transformations

In analysis, the Fourier transformation ([FT](#)) is an extension, for non-periodic functions. All signal $x(t)$ can be represented as a set of superposition of periodic components, which are always expressed in terms of elementary functions (cosine or sine). The determination of the relative amplitudes of these components constitutes the goal of the Fourier analysis. Whatever the kind of the signal, we study the power spectrum, which represents the distribution of the power throughout the frequencies components, and the power spectrum is simply the Fourier transform.

II.2.1. Noise in Frequency domain

In signal processing, noise is a general term for unwanted modifications that a signal may suffer during capture, storage, transmission, processing, or conversion. Let us for instance call $x(t)$ the dependent time variable that can be either $S(t)$, $N(t)$ or $\psi(t)$ be equal to [\(II.1\)](#)

$$x(t) = x_0 + x_1 \sin(\omega t) + \delta p(t) \quad (\text{II.1})$$

From this relation, we have a signal with free-noise and that with noise induced effects in [Fig. II.1 \(a\)](#) and [\(b\)](#) respectively. The evaluation of the square root of the autocorrelation $\sqrt{\langle \delta x(t)^2 \rangle}$ enables the information about noise fluctuations from the variable $x(t)$.

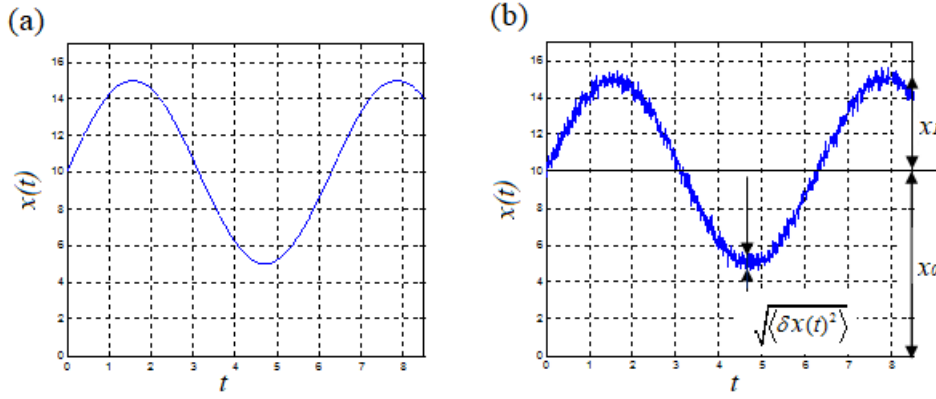


Figure II.1. Free-noise signal (a) and noisy signal (b)

However, this autocorrelation is not easy to be carried out in time domain. In addition, the best interpretation of noise requires frequency analysis i.e. the FT. The Fourier transformation of the fluctuation quantity $\delta x(t)$ is :

$$\tilde{\delta x}(\omega) = \int_{-\infty}^{+\infty} \delta x(t) e^{-j\omega t} dt \quad . \quad (\text{II.2})$$

The inverse transform is

$$\delta x(t) = \int_{-\infty}^{+\infty} \tilde{\delta x}(\omega) e^{j\omega t} d\omega \quad \text{i.e.} \quad \tilde{\delta}(\omega) = \int_{-\infty}^{+\infty} \delta x(t) e^{-j\omega t} dt \quad . \quad (\text{II.3})$$

The Eq. (II.4) defines the power spectral density of the fluctuation $\delta x(t)$ in term of the FT.

$$S_{xx}(\omega) = \left\langle \left| \tilde{\delta x}(\omega) \right|^2 \right\rangle = \left\langle \tilde{\delta x}(\omega) \tilde{\delta x}^*(\omega) \right\rangle \quad (\text{II.4})$$

Here, the term $\tilde{\delta x}^*(\omega)$ is the complex conjugate of the fluctuation $\tilde{\delta x}(\omega)$.

The total energy of the fluctuation signal $\delta x(t)$ can be infinite. Therefore, it is better to works with signal power and not with signal energy. The power spectral density of the fluctuation signal $S(\omega)$ is related to the autocovariance function by the Wiener Khinchin theorem. It is the FT of the autocorrelation. Noise amplitude is better evaluated in the frequency; this is the useful of the power spectral density. As aforementioned, the best explanation of noise requires its frequency domain investigation. In the frequency domain, the fluctuation (the small perturbation) spectrum $\delta x(\omega)$ is defined in a manner similar to the variance in the time domain. It describes the power in a frequency range of 1 Hz. So, frequency components of $\delta x(t)$ are defined by the FT as followed in equation (II.2).

II.2.3. Langevin Equation and Langevin Noise

In Physics, a Langevin equation (II.5) is a stochastic differential equation describing the Brownian motion of small particle in a fluid due to collision with surrounding molecules in thermal motion.

$$m \frac{dv(t)}{dt} = -m\gamma v(t) + F_v(t) \quad (\text{II.5})$$

$F_v(t)$ is the Langevin noise source. It originates from the random effects [11]. Statistical methods are needed to characterize and investigate the effects of these noises. As stochastic and random nature, Langevinian noise sources have zero means value given by equation (II.6). In addition, its time correlation being short enough, the equation (II.7) defines the correlation between two Langevinian noises sources.

$$\langle F_v(t) \rangle = 0 \quad (\text{II.6})$$

$$\langle F_{v_i}(t) F_{v_j}(t') \rangle = 2D_{v_i v_j} \delta(t-t') \quad (\text{II.7})$$

$D_{v_i v_j}$ is the coefficient of diffusion which is not easy to derivate [11]. The Langevin method for the evaluation of noise down to evaluating the spectral density of noise correlation strengths $\langle F_{v_i}(t) F_{v_j}(t') \rangle$ between the various Langevin noise sources. These correlation strengths depend on the parameter of the system [67].

Applying the FT in Eq. (II.8), we can find that

$$(\gamma + j\omega) \tilde{\delta}v(\omega) = \tilde{F}_v(\omega) / m \quad (\text{II.8})$$

From this equation, it is clear that the spectral density of the variable v from the Langevin equation depends to the correlations strength of Langevinian noise sources as set in Eq. (II.9).

$$S_{vv}(\omega) = \frac{\langle \tilde{F}_v(\omega) \tilde{F}_v^*(\omega) \rangle}{m^2(\gamma^2 + \omega^2)} \equiv \frac{D_{vv}}{m^2(\gamma^2 + \omega^2)} \quad (\text{II.9})$$

The term D_{vv} is a constant which depends to the system parameters. For instance, for Brownian motion of particles: $D_{vv} = 2\gamma m K_B T$; with K_B the Boltzmann constant and T the absolute temperature.

The Fourier transformation method of analysis shall be used in Chapter III to derivate the spectral density of RIN and FN of optical injection semiconductor lasers for the autocorrelations of photon density and optical phase respectively.

II.3. Analysis and Characteristic Descriptions for Nonlinear Systems

II.3.1. Reduction methods

From the theoretical point of view, the study of complex nonlinear systems requires the analytical or, in general, numerical solutions of a differential equation for many different ICs and experimental conditions [68, 69]. In many cases, this can be an excessively large quantity of information to handle or understand. Therefore, methods or techniques for reducing the amount of information or the number of degrees of freedom, in such a way that the basic features of the dynamical evolution be retained, are very useful in these cases. The most often-used reduction methods are the low-dimension projections, the adiabatic elimination of variable, and the expansion of Taylor, the representations of the reduced nonlinear functions such as polynomial approximation in the ways that the values and derivatives can be computed efficiently.

II.3.2. Low-dimension projections

In laser experiments, only the temporal evolution of some of the dynamic variables can be detected. This corresponds to observe only a projection of the orbit in the phase space on the subspace defined by these variables. The dynamic features of the system characterizing the time evolution can be observed on any one of these variables. For instance, it is sufficient to look at only one variable to obtain evidence for a stationary, periodic or chaotic time evolution.

Based on this fact, in the next part a way of characterizing a dynamic behavior from a time series on any variable of the system is presented.

II.3.3. Polynomial Approximation

The approximation of a given function by a polynomial is an efficient tool in many problems arising in applied mathematics. In this section, $F(V)$ in Eq. (I.16) is the function to be approximated by a polynomial function. For this purpose, we use the `cftool` command of Matrix Laboratory (MATLAB). Here, we approximate the function in Eq. (I.16) with simpler functions by starting by a polynomial of high degree (degree nine) to a low-degree polynomial (cubic polynomial function). The objective is to make an accuracy of the N-shape of the RTD current-voltage characteristic. Mainly to reproduce the NDR region of the RTD. The MATLAB `cftool` command often performs these operations in a simple way such that the result is as close to the actual function as possible. We have displayed in Fig. I.11, a nine-degree, a five degree and a cubic polynomial functions that approximates the function in Eq. (I.16). Mathematical expressions and values of parameters that are extracted from numerical calculations are in Table. II.1. Indeed, it has already been shown that the last relation $F(V) = BV(V - a)(V - b)$ contains the basic

passive and active phenomena and threshold behaviors of the RTD although there are different model to describe the RTD as we showed in Chapter I (Sect. I.4.3). Therefore, the RTD should well also be described by polynomial function with interesting results for these purposes [29 - 31].

Table II.1. Polynomial approximation functions of the RTD current-voltage model

Schulman model	$F(V) = A \ln \left(\frac{1 + e^{(B-C-n_1V)/kT}}{1 + e^{(B-E_r-n_1V)/kT}} \right) \left[\frac{\pi}{2} + \tan^{-1} \left(\frac{C-n_1V}{D} \right) \right] + H(e^{n_2eV/kT} - 1)$ $A = 6.8 \times 10^{-3}; B = 0.085; C = 0.1346; D = 0.0104; q = 1.602 \times 10^{-19}$ $H = 1.411 \times 10^{-3}; T = 300; k_B = 1.38 \times 10^{-23}; n_1 = 0.1252; n_2 = 0.0182$
Nine degree polynomial	$F(V) = -k_0 + k_1(100V) + k_2(100V)^2 + k_3(100V)^3 + k_4(100V)^4 + k_5(100V)^5 + k_6(100V)^6 + k_7(100V)^7 + k_8(100V)^8 + k_9(100V)^9$
Five degree polynomial	$F(V) = -k_0 + k_1(100V) + k_2(100V)^2 + k_3(100V)^3 + k_4(100V)^4 + k_5(100V)^5$
Cubic function	$F(V) = BV(V-a)(V-b)$

II.3.4. Time series

In mathematics, a time series is a series of data points indexed (or listed or graphed) in time order. Most commonly, a time series is a sequence taken at successive equally spaced points in time. Thus, it is a sequence of discrete-time data. Time series are used in statistics, signal processing, chemistry, econometrics, finances engineering astronomy, communications engineering and largely in any domain of applied science and engineering which involves temporal measurements such as physics. For example the Fig. II.2 showing numerical simulations of an artificial neural model [70] presents changes of dynamics of the system in time.

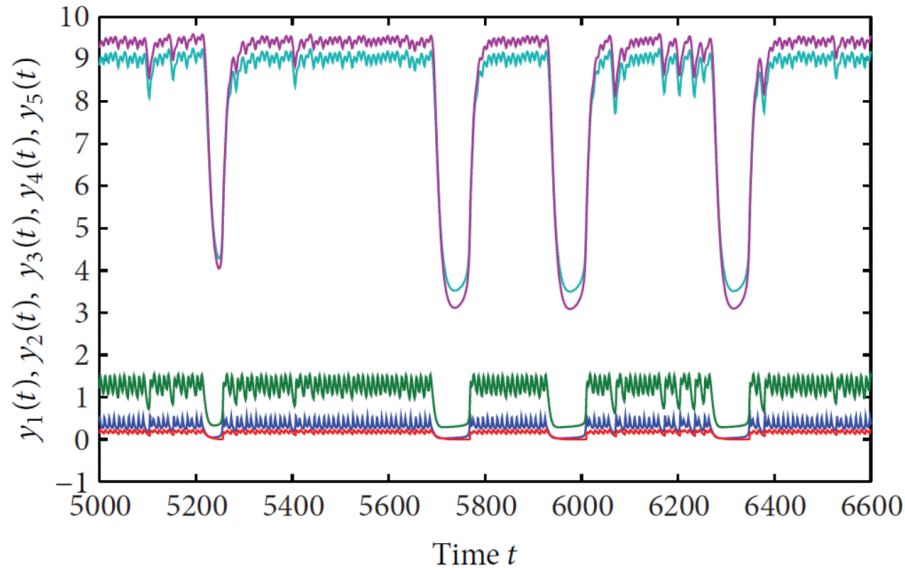


Figure II.2. Time series of an artificial neural system showing chaotic behavior [70].

II.3.5. Power spectrum

Before beginning the nonlinear properties analysis of time series, it is important to know if the phenomenon to study is periodic, quasi-periodic or chaotic. Proving the existence of periodic or chaotic solutions by bifurcations theory is not easy (sometimes expensive) when the phase space is of the high dimension. We can use the indirect ways, often additional among them, which are time series and power spectra. We mention in addition that, for dynamics analysis, it has not been necessary for us to write the fast Fourier transform (FFT) program, it already exists [MATLAB](#) package in the packages. This [MATLAB](#) function computes the discrete Fourier transform (DFT) of x using a [FFT](#) algorithm.

II.3.6. Phase portrait

Sometimes, it is not always possible to observe difference between different responses of a variable of system (or for different systems) with slight change using time series. For this purpose, the phase portraits analysis is an efficient tool to distinguish nonlinear systems dynamical behaviors. The phase space of a dynamical system is a mathematical space with orthogonal coordinate directions representing each of the variables needed to specify the instantaneous state of the system. A phase map may be constructed in several ways. For the Lorenz system, for example, the state of the system can be described by three variables x , y , and z and parameters σ , r , and b as in [11, 12]. The Lorenz system gives an excellent instance of what named strange attractors [71 - 73]. As in Fig. II.3, we can see a beautiful butterfly-shaped attractor on which a trajectory starting from any initial point will come back to the near neighbourhood of the initial point but never precisely repeat it. An important feature of the phase portrait is that two trajectories will never

cross each other. This non-crossing property derives from the fact that both past and future states of a deterministic system are uniquely determined by the system state at a given time. A crossing of trajectories inevitably introduces ambiguity into past and future states and contradicts the assumed uniqueness of the trajectory. However, a projection of a higher dimensional space onto a plane might show apparent crossings which do not represent actual interactions. The phase portraits for the periodic, quasi-periodic, and chaotic time variations in general can appear to be a limit cycle, a torus, and a strange attractor, respectively, as shown in [11].

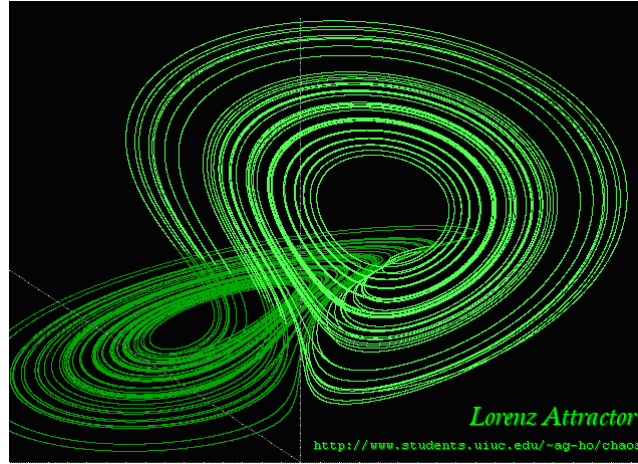


Figure II.3. Lorenz attractor [74].

II.3.7. Poincaré section

The Poincaré map or Poincaré section is a classical technique for analyzing a dynamical system. It is also a useful tool for understanding the characteristics of nonlinear systems. The trajectory, or orbit, of an object X is sampled periodically, as indicated by Fig. II.4. For an n -dimensional trajectory Γ , take an $(n-1)$ -dimensional hyperplane Σ transverse to the trajectory at X_0 . The rate of change for the object emanating from X_0 is determined for each intersection of its orbit with the hyperplane Σ , as shown by X_1, X_2, \dots at the following transversings. The Eq. (II.10) defines the Poincaré map P .

$$X_{k+1} = P(X_k) = PP(X_{k-1}) = P^2(X_{k-2}) \quad (\text{II.10})$$

In the Eq. (II.10), k is an integer. The Poincaré map replaces the continuous dynamical system into a discrete map, which is much easier to deal with mathematically. This set of discrete values can then be used to analyze the long-term stability of the system. With the Poincaré map, one can dramatically reduce the data number that is especially necessary in the experiments. As demonstrated in [11, 68], one can easily distinguish among the periodic, quasi-periodic, and chaotic variations from the appropriate Poincaré maps. In particular, the Poincaré map for chaotic systems exhibits remarkable features. The map does not result in a simple geometrical structure

and, when it is magnified, the fine structure resembles the gross one. Namely, the system trajectory has a fractal structure.

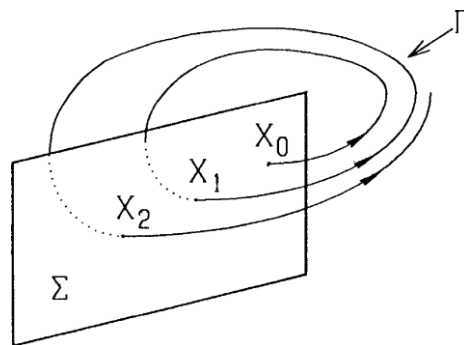


Figure II.4. Poincaré map of an n -th order autonomous system. Γ : n -dimensional trajectory, Σ : $(n - 1)$ -dimensional hyperplane [11]

II.3.8. Stability Analysis Methods: Bifurcation and Lyapunov Calculations

Both in Bifurcation analysis and in Lyapunov spectrum, one observes the dynamics evolution of the system for the change of a certain parameter.

II.3.8.1. Bifurcation Diagrams

Continuous dynamical systems that involve differential equations mostly contain parameters. It can happen that a slight variation in a parameter can have significant impact on their solution. The main questions are that how to continue equilibria and periodic orbits of dynamical systems with respect to a parameter? How to predict qualitative changes in system's behavior (bifurcations) occurring at these equilibrium points [75, 76]? This is why of the use of bifurcation analysis.

Bifurcation analysis is a powerful method for studying the steady-state nonlinear dynamics of systems as it allows one to identify in a systematic way where dynamics of interest exist in parameter space. This tool makes possible to generate 'maps of solutions' in an efficient way that provide valuable insight into the overall dynamic behavior of a system and potentially to influence the design process [77] as functions of the relevant system parameters. In particular, regions of multistability can be identified in this way (as it will be shown in Chapter III Section III.4). In many ways, at a bifurcation, the local stability properties of equilibria, periodic orbits or other invariant sets changes. It is useful to divide bifurcations into two principal classes: Local bifurcations and Global bifurcations.

Local bifurcations – can be analyzed entirely through changes in the local stability properties of equilibria, periodic orbits or other invariant sets as parameters cross through critical thresholds. For instance, as shown in Fig. II.5, local bifurcations include:

- **Pitchfork bifurcation** (see Fig. II.5 (a)). In the supercritical version of this bifurcation, a fixed point loses its stability as it produces two new stable fixed points when a control parameter is varied (see Fig. II.5 a(i)). In its subcritical form, (see Fig. II.5 b(i)), the bifurcation occurs as a fixed point collides with the unstable branches of two previously existent fixed points. It is important to mention that this and other types of bifurcation only appear in dynamical systems with an appropriate symmetry (reflection invariance in this case).
- A **saddle node bifurcation** or tangent bifurcation (see Fig. II.5 (b)) is a collision and disappearance of two equilibria in dynamical systems. In autonomous systems, this occurs when the critical equilibrium has one zero eigenvalue. This phenomenon is also called fold or limit point bifurcation [75].
- A **Transcritical bifurcation** (see Fig. II.5 (c)) occurs when one stable and one unstable steady states collide at the bifurcation point and exchange their stability.
- A **Hopf bifurcation**, also called a Hopf or Poincare-Andronov-Hopf bifurcation (see Fig. II.5 (d)) is a local bifurcation in which a fixed point of a dynamical system loses stability as a pair of complex conjugate eigenvalues of linearization around the fixed point cross the imaginary axis of the complex plane.
- At a **period-doubling bifurcation** (see Fig. II.5 (e)), a periodic orbit loses its stability and a periodic orbit with twice the period emerges; a single Floquet multiplier -1 characterizes this [77].

Global bifurcations – occur when 'larger' invariant sets, such as periodic orbits, collide with equilibria. This causes changes in the topology of the trajectories in the phase space, which cannot be confined, to a small neighbourhood, as is the case with local bifurcations. In fact, the changes in topology extend out to an arbitrarily large distance (hence 'global'). Examples of global bifurcations include:

- **Homoclinic bifurcation** in which a limit cycle collides with a saddle point [78] (see Figure II.6 (a)). Homoclinic bifurcations can occur supercritically or subcritically. The variant above is the "small" or "type I" homoclinic bifurcation. In 2D, there is also the "big" or "type II" homoclinic bifurcation in which the homoclinic orbit "traps" the other ends of the unstable and stable manifolds of the saddle. In three or more dimensions, higher codimension bifurcations can occur, producing complicated, possibly chaotic dynamics.

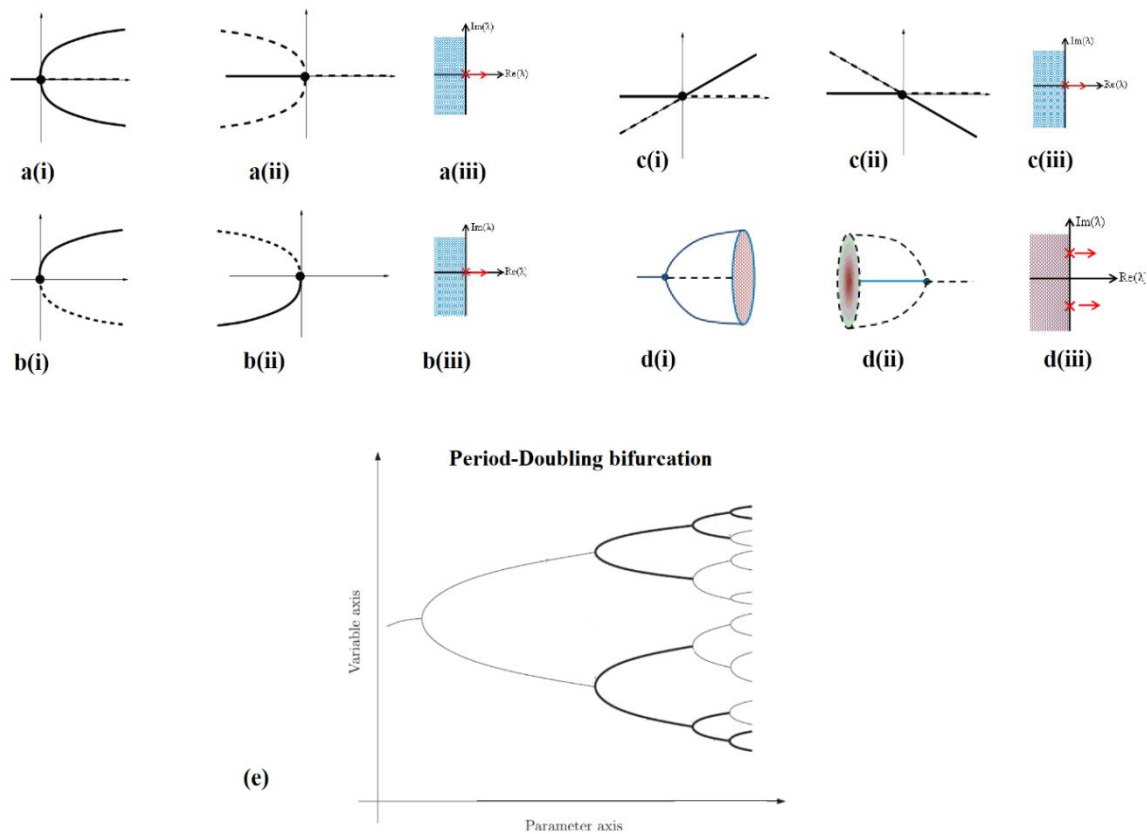


Figure II.5. Local bifurcations. Pitchfork bifurcation diagrams; (i) Pitchfork supercritical, (ii) Pitchfork subcritical and (iii) Bifurcation condition for flows. (b) Saddle-node bifurcation diagrams; (i) Saddle-node supercritical, (ii) Saddle-node subcritical and (iii) Bifurcation condition for flows. (c) Transcritical bifurcation diagrams; (i) Supercritical, (ii) Subcritical and (iii) Bifurcation condition for flows. (d) Hopf bifurcation diagrams; (i) Hopf Supercritical, (ii) Hopf Subcritical and (iii) Bifurcation condition for flows. (e) Period-Doubling bifurcations. In the bifurcation diagrams, solid (dashed) lines indicate stable (unstable) structures.

- **Heteroclinic bifurcation** in which a limit cycle collides with two or more saddle points; they involve a heteroclinic cycle [79] (see Figure II.6 (b)). Heteroclinic bifurcations are of two types: resonance bifurcations and transverse bifurcations. Both types of bifurcation will result in the change of stability of the heteroclinic cycle. At a resonance bifurcation, the stability of the cycle changes when an algebraic condition on the eigenvalues of the equilibria in the cycle is satisfied. This is usually accompanied by the birth or death of a periodic orbit. A transverse bifurcation of a heteroclinic cycle is caused when the real part of a transverse eigenvalue of one of the equilibria in the cycle passes through zero. This will also cause a change in stability of the heteroclinic cycle.
- **Infinite-period bifurcation** in which a stable node and saddle point simultaneously occur on a limit cycle [80]. As the limit of a parameter approaches a certain critical value, the speed of the oscillation slows down and the period approaches infinity. The infinite-period bifurcation occurs at this critical value. Beyond the critical value, the two fixed points

emerge continuously from each other on the limit cycle to disrupt the oscillation and form two-saddle points.

— *Blue-sky catastrophe* in which a limit cycle collides with a nonhyperbolic cycle.

Global bifurcations can also involve complicated sets such as chaotic attractors.

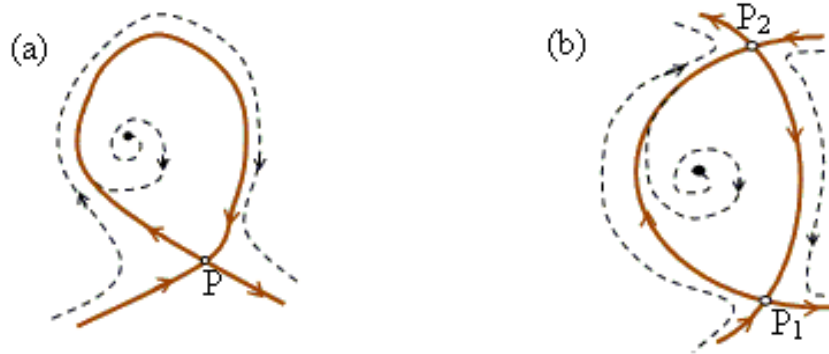


Figure II.6. (a) A homoclinic orbit (continuous line) connecting a saddle point P to itself. (b) Two heteroclinic orbits (continuous line) defining a homoclinic cycle connecting saddle points P_1 and P_2 . Dashed line: other close trajectories [68].

In general, the plot of a bifurcation diagram is obtained by sampling and plotting local extrema of a variable for a parameter change. From the plot of the maxima and minima of a variable, we obtain a map for the parameter. The map is called a bifurcation diagram or a chaotic bifurcation diagram. From this plot, we can see for instance stable fixed point, periodic oscillations (P-n), period doubling or chaotic oscillations occur for the change of a control parameter in Fig. II.5 (e). Period-doubling bifurcation also called Feigenbaum scenarios [68] is not the only chaotic route, but other routes for chaotic evolutions exist depending on the configuration of systems and chaos parameters, for example, quasi-period doubling bifurcations and intermittent chaotic bifurcations. A bifurcation diagram is important to know how the dynamics of a system change for the parameters. We can make similar plots of bifurcation diagrams for the change of the parameters for any chaotic systems and know the chaotic evolution route of the system output [11] or a mean of chaos control as shown in Fig. II.8 (a).

II.3.8.2. Lyapunov Methods

The Lyapunov methods are the most useful and general approaches for stability analysis of nonlinear systems [81-84]. The Linearization method around equilibrium point and the analysis of eigenvalues of the Jacobian matrix only draws conclusion about the stability of the system in the boundary equilibrium points or equilibrium manifolds. For the point of view of nonlinear dynamics, the Lyapunov method based on Lyapunov exponent is the main tool.

Equilibria, Eigen value and Routh Criteria

Let us consider a nonlinear system whose differential equations are in vector notation (II.11)

$$\dot{x}(t) = f(x(t); M) \quad (\text{II.11})$$

where $x = (x_1(t), x_2(t), x_3(t), \dots, x_n(t))^T$ is the state space vector, $f = (f_1, f_2, f_3, \dots, f_n)^T$, M is the set of parameters, $(\dots)^T$ indicates transpose.

To analyze the stability of the system around equilibria, we apply a small signal analysis. Using small perturbation $\delta x(t)$, the variable $x(t)$ is written as follows $x(t) = x_0 + \delta x(t)$. Therefore, the equations for small derivations δx from the trajectory $x(t)$ are (II.12)

$$\delta \dot{x}(t) = J_{ki}(x(t); M) \delta x(t), \quad k = i = 1, 2, \dots, n \quad (\text{II.12})$$

where J_{ki} is the Jacobian matrix of the system of the form (II.13)

$$J_{ki} = \partial f_j / \partial x_i = \begin{bmatrix} \partial f_1 / \partial x_1 & \cdot & \cdot & \cdot & \partial f_1 / \partial x_n \\ \cdot & \cdot & \cdot & \cdot & \cdot \\ \cdot & \cdot & \cdot & \cdot & \cdot \\ \cdot & \cdot & \cdot & \cdot & \cdot \\ \partial f_n / \partial x_1 & \cdot & \cdot & \cdot & \partial f_n / \partial x_n \end{bmatrix} \quad (\text{II.13})$$

The equilibria x_0 of the system can be tracking by solving the equation (II.14)

$$f(x(t); M) = 0 \quad (\text{II.14})$$

To study the stability analysis of the system (II.11), the Jacobian matrix (II.13) is used in such a way that one analyse the eigenvalue λ_i resulting from the characteristic polynomial Eq. (II.15)

$$E(\lambda) = \det(J_{ki} - \lambda I_n) = 0, \quad (\text{II.15})$$

where I_n is the matrix identity. According to the Routh-Hurwitz theorem, the necessary and sufficient conditions for fixed point to be stable is that all eigenvalues have negative real parts. This is interpreted according to the systematic illustrations [85] in Figure II.7. The Routh-Hurwitz criterion leads the characteristic polynomial (II.15) to be in the form of Eq. (II.16).







	Stable $Re(\lambda_i) < 0$	Unstable $Re(\lambda_i) > 0$	Lyapunov Stable $Re(\lambda_i) = 0$
Real eigenvalues	Stable point 	Unstable point 	Neural point 
Complex conjugate eigenvalues	Stable spiral focus 	Unstable spiral focus 	Neural center 

Figure II.7. Schematic illustrations of several different types of equilibrium points and their nearby trajectories in 2-D continuous-time dynamical systems. The real part of the dominant eigenvalue determines the overall stability of the equilibrium point (top) [85]

$$E(\lambda) = a_0\lambda^n + a_1\lambda^{n-1} + a_2\lambda^{n-2} + \dots + a_{n-2}\lambda^2 + a_{n-1}\lambda + a_n \tag{II.16}$$

In addition, the Hurwitz matrix from (II.17) is given by the following equation.

$$H = \begin{pmatrix} a_1 & a_3 & a_5 & \dots & \dots & \dots & 0 & 0 & 0 \\ a_0 & a_2 & a_4 & & & & \vdots & \vdots & \vdots \\ 0 & a_1 & a_3 & & & & \vdots & \vdots & \vdots \\ \vdots & a_0 & & \ddots & & & 0 & \vdots & \vdots \\ \vdots & 0 & & & \ddots & & a_n & \vdots & \vdots \\ \vdots & \vdots & & & & \ddots & a_{n-1} & 0 & \vdots \\ \vdots & \vdots & & & & & a_{n-2} & a_n & \vdots \\ \vdots & \vdots & & & & & a_{n-3} & a_{n-1} & 0 \\ 0 & 0 & 0 & \dots & \dots & \dots & a_{n-4} & a_{n-2} & a_n \end{pmatrix} \tag{II.17}$$

In the same way, according to the Routh-Hurwitz theorem, the necessary and sufficient conditions for all roots to have negative real parts is if and only if all the principal minors of the Equation (II.17) are positive; with $a_0 > 0$. These tools will be used for the study of the stability of the novel RTD-LD system in the middle part of the Chapter III.

Lyapunov Exponents

Lyapunov exponents (LEs) estimate the rate of divergence of nearby trajectories, a key component of chaotic dynamics. The computation of LE is a key component of chaotic dynamics [86]. The basic idea of the Lyapunov exponent is to measure the average rate [87] of the divergence for the neighboring trajectories on the attractor. The direction of the maximum divergence or convergence locally changes on the attractor. The motion must be monitored at each point along

the trajectory. Therefore, a small sphere is defined, whose center is a given point on the attractor and whose surface consists of phase points from nearby trajectories. As the center of the sphere and its surface points evolve in time, the sphere becomes an ellipsoid with the principal axes in the directions of the contraction and the expansion [11]. The average rates of the expansion or the contraction along the principal axes are the Lyapunov exponents. The exponent is positive for a chaotic state, zero or negative for periodic state. Chaotic state generates sensitivity to ICs [88] i.e. trajectories initially very close together will, on the average, diverge, such that after a time dependent on the size of the exponent, there will be no relationship between them [89].

Usually, the Lyapunov exponent or Lyapunov characteristic exponent of a dynamical system is a quantity that characterizes the rate of separation of infinitesimally close trajectories $x(t)$ and $x_0(t)$ in phase space. The general idea is to evaluate the average of their separation with close initial conditions. Let $x(t)$ be the time series variable of system and $\delta x(t) = x(t) - x_0(t)$ a smallest separation vector such that $x(t)$ and $x(t) + \delta x(t)$ be close trajectories. The Eq. (II.18) defines the quantity that measures this separation so-called LEs.

$$\delta x(t) = \delta x(0)e^{\lambda t} \quad (\text{II.18})$$

with $\delta x(0)$ the tiny initial separation condition. From that relation, if the LE is negative, the system exhibits convergence otherwise saying, it is insensitive to initial condition and therefore nonchaotic. On the other hand, if the LE is positive, the separation between close trajectories is growing exponentially rapid and, the system lead sensitivity to ICs i.e. the system is chaotic. In mathematical strict sense, the dynamical system of vectors $x_i(t)$ should be written with that small derivation in terms of Jacobian matrix and the simplest relation defining the LEs is as follows [90, 91].

$$\lambda_i = \lim_{t \rightarrow \infty} \left(\frac{1}{t} \right) \log \frac{\|\partial x_i(t)\|}{\|\partial x_i(0)\|} \quad (\text{II.19})$$

There are some important points related to the Lyapunov exponents as discussed follows. Fourth-order Runge-Kutta method shall be used in Chapter III to compute these LEs.

- (1) For a chaotic system, at least one of the Lyapunov exponents must be positive to allow the sensitive dependence on the ICs. For instance, according to bifurcation diagram, LEs spectrum of the Belousov-Zhabotinsky oscillator depicted in Fig. II.8 (b) (form [89]) shows periodic and chaotic state of the variable x .

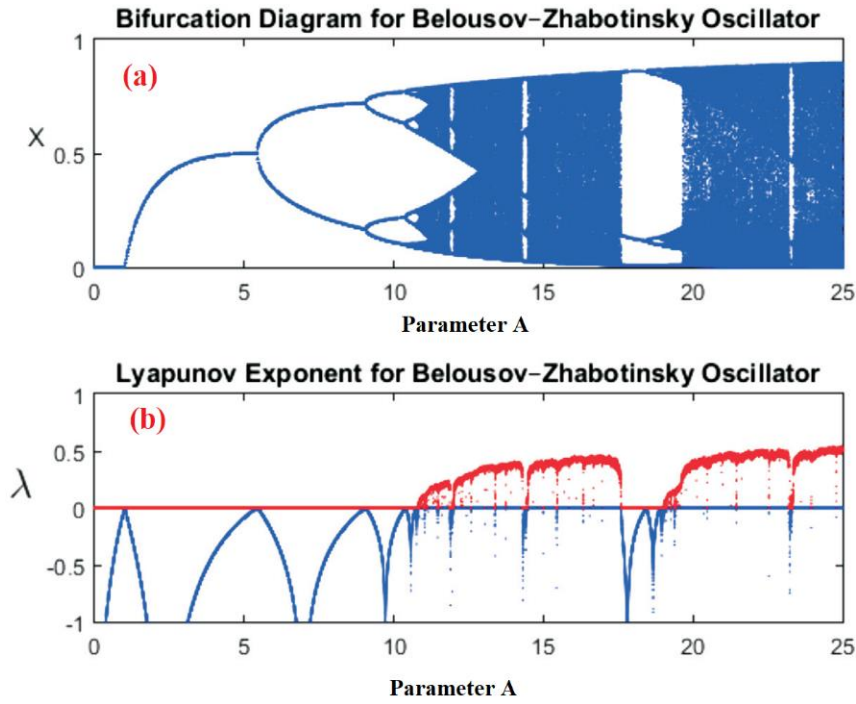


Figure II.8. Superimposition of the bifurcation diagram and the LE spectrum. This shows the coincidence of the accumulation point with the switch in the LE from negative to positive. The strong 3-period in the chaotic region is also echoed by the negative LE in the chaotic region [89].

- (2) According to the definition of the **LEs**, a small volume V in the phase space will change in time such that a dissipative chaotic system, the sum of all the **LEs** must be negative, i.e.

$$\sum_i \lambda_i < 0.$$

- (3) If we order $\lambda_j (j=1, 2, \dots, n)$ as $\lambda_1 < \lambda_2 < \dots < \lambda_n$, then the Lyapunov dimension D_L is computed according to Kaplan-Yorke conjecture as follows

$$D_L = j + \frac{\lambda_1 + \lambda_2 + \dots + \lambda_j}{|\lambda_{j+1}|} \quad (\text{II.20})$$

In Eq. (II.20), j , is the number of **LEs** which gives a positive sum, but adding λ_{j+1} would

make the sum negative, i.e. $\sum_{i=1}^j \lambda_i > 0$ and $\sum_{i=1}^{j+1} \lambda_i < 0$.

II.3.9. Simulink Analysis Method and Numerical Simulations

II.3.8.2. Simulink Analysis

Simulink is a graphical front end to **MATLAB**. Simulink tool offers a visual approach to the differential equation setup. The Simulink library browser contains a plethora of components. We

will restrict ourselves to the **Integrator** block (highlighted in Fig. II.9) under the **Continuous** Library and various blocks in the **Math Operations**, **User-Defined Functions**, **Sinks** and **Sources** library.

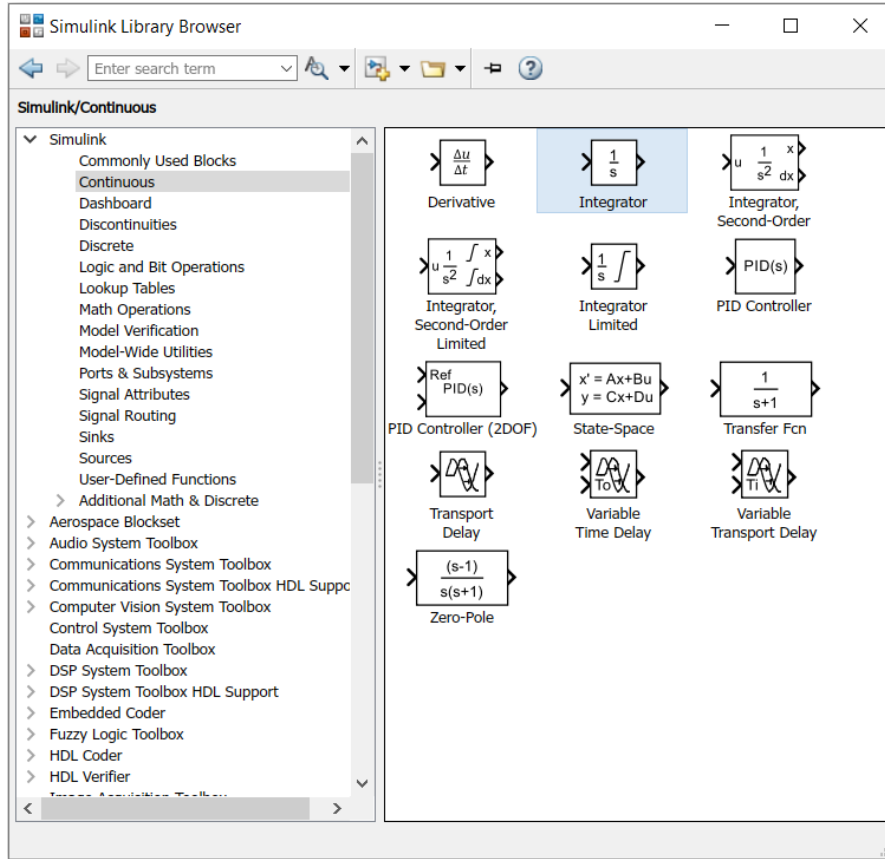


Figure II.9: Simulink library browser

II.3.8.2. Fourth-order Runge-Kutta Method

Runge-Kutta (RK) formula are among the oldest and the best understood schemes in numerical analysis. RK method continues to be a source of active research [92-94]. Runge-Kutta methods have been one of the robust methods for numerical integration of first order ODEs. Consider the general form of equation (II.11) in the form an initial value problem be specified as follows:

$$\frac{dx}{dt} = f(t, x), \quad x(t_0) = x_0. \tag{II.21}$$

Here, x is an unknown function (scalar and vector) of time t . The function f and initial conditions t_0 and x_0 are given. The vectors f and x are given by Eqs. (II.22) and (II.23) respectively.

$$x(t) = (x_1(t), x_2(t), \dots, x_n(t)) \tag{II.22}$$

$$f(t, x) = (f_1(t, x), f_2(t, x), \dots, f_n(t, x)) \tag{II.23}$$

Consider a step-size $h > 0$. With **RK** methods, we numerically solve (II.22) at $t = t_0 + h$. The general of **RK** methods given by Eq. (II.25) [95, 94].

$$x_{n+1} = x_n + h \sum_{i=1}^s b_i k_i, \quad (\text{II.24})$$

where

$$\begin{aligned} k_1 &= f(t_n, x_n) \\ k_i &= f\left(t_n + hc_i, x_n + h \sum_{j=1}^{i-1} a_{ij} k_j\right), \\ c_i &= \sum_{j=1}^{i-1} a_{ij}, \quad 2 \leq i \leq s \end{aligned} \quad (\text{II.25})$$

Each value k_i can then be calculated in sequence for order of **RK** method, for the fourth-order explicit Runge-Kutta (**RK4**). A similar but classical **RK4** is often known as:

$$x_{n+1} = x_n + \frac{1}{6} h (k_1 + 2k_2 + 2k_3 + k_4),$$

where

$$\begin{aligned} k_1 &= f(t_n, x_n) \\ k_2 &= f\left(t_n + \frac{1}{2}h, x_n + \frac{1}{2}hk_1\right) \\ k_3 &= f\left(t_n + \frac{1}{2}h, x_n + \frac{1}{2}hk_2\right) \\ k_4 &= f(t_n + h, x_n + hk_3) \end{aligned} \quad (\text{II.26})$$

This **RK4** method is what we use in our numerical integration in this thesis.

II.4. Model of Optical Injection SCL

In this Section, we review the model of the **OISCL** developed by Mengue and Essimbi and set it in term of photon density $S(t)$, carrier density $N(t)$ and the optical phase $\psi(t)$. The system is schematically depicted in the configuration of Figure I.5; Chap I; which consists of two **LDs** where one receives an optical beam from another. To analyze noise contribution, in addition to Langevinian noise source for each variable, we also take into account spontaneous emission contribution. Eqs. (II.27) and (II.28) give the model equations **OISCLs** developed by Mengue [68].

$$\frac{dE(t)}{dt} = \frac{1}{2} \frac{1}{(1+\gamma)} \left[1 - \gamma(1 - j\alpha) \right] \left\{ (N(t) - N_0) - \frac{1}{\tau_p} \right\} E(t) + \frac{k_{inj}}{\tau_{in}^*} E_{inj} e^{[\psi(t) - \varphi_{inj}(t)]} \quad (\text{II.27})$$

$$\frac{dN(t)}{dt} = J - \frac{N(t)}{\tau_r} - \left\{ \frac{1}{\tau_p} + G_N(N(t) - N_{th}) \right\} E_0^2(t) \quad (\text{II.28})$$

here, the parameters are better explained in [68]. By using the notation of the complex field inside the cavity of the SL as $E(t) = E_0(t)e^{-j\phi(t)}$, the amplitude $E_0(t)$ and the phase $\phi(t)$ of the field, one obtains the set of rate Eqs. (II.27-28) which is also deterministic. Nevertheless, we assume the master phase to be variable. On one hand, we have $d\phi(t)/dt = d\psi(t)/dt + \Delta\omega$. By using the relation $E(t) = E_0(t)e^{-j\phi(t)}$, we have the relation $dE_0(t)/dt - jE_0(t).d\phi(t)/dt$. In addition, when the real terms and complex term are kept separated, the equation (II.27) can be rewritten in the form Eqs. (II.29) and (II.30).

$$\frac{d}{dt} E_0(t) = \frac{1}{2} \frac{(1-\gamma)}{(1+\gamma)} \{G_N(N(t) - N_{th})\} E_0(t) + \frac{k_{inj}}{\tau_{in}^*} E_{inj} \cos(\psi(t) - \varphi_{inj}(t)) \quad (\text{II.29})$$

$$-E_0(t) \left[\frac{d}{dt} \psi(t) + \Delta\omega \right] = \left[\frac{1}{2} \frac{\gamma\alpha}{(1+\gamma)} \{G_N(N(t) - N_{th})\} E_0(t) + \frac{k_{inj}}{\tau_{in}^*} E_{inj} \sin(\psi(t) - \varphi_{inj}(t)) \right] \quad (\text{II.30})$$

Using the relationship between the amplitude $E_0(t)$ of the complex field inside the cavity and the photon density as i.e. $E_0^2(t) \equiv S(t)$, one has equation (II.31) [96]. These rate equations of SCL will be a main folder of the central of our study in the first section of the Chapter III.

$$\begin{aligned} \frac{d}{dt} S(t) &= \frac{(1-\gamma)}{(1+\gamma)} [G_N(N(t) - N_{th})] S(t) + 2 \frac{k_{inj}}{\tau_{in}^*} \sqrt{S_{inj} S(t)} \cos[\psi(t) - \varphi_{inj}(t)] \\ \frac{d}{dt} \psi(t) &= \frac{1}{2} \alpha \frac{\gamma}{(1+\gamma)} [G_N(N(t) - N_{th})] - \frac{k_{inj}}{\tau_{in}^*} \sqrt{\frac{S_{inj}}{S(t)}} \sin[\psi(t) - \varphi_{inj}(t)] - \Delta\omega \\ \frac{d}{dt} N(t) &= J - \frac{N(t)}{\tau_r} - \left\{ \frac{1}{\tau_p} + [G_N(N(t) - N_{th})] \right\} S(t) \\ \psi(t) &= \varphi_{inj}(t) - \Delta\omega t \end{aligned} \quad (\text{II.31})$$

here, parameters are already well defined in Section I.3.2.

II.5. Model of RTD-OISCL Integrated Circuit

LDs are very sensitive to external perturbations such as optical injection, optical feedback, optoelectronic feedback or electrical current modulation. Such perturbations induce instabilities in laser operations. In recent years, RTD electrical circuits have been intensively used as driving

circuit for SCLs. This is due to the wide range of RTD's NDR region. The incorporations of RTD with a LD leads additional degree of freedom in laser dynamics as well as it induce instabilities in laser.

In this Section, we initiate and we report on a novel hybrid integrated RTD-LD circuit consisting of separated RTD and optical injection LD two Chips. The LD is the model of optical injection SCL described in Section II.4. Therefore, this optoelectronic system consists of two main parts: the electrical subsystem and the optical subsystem that converts the electrical energy into optical energy. The equivalent lumped circuit of the system used here is shown in Figure II.10. The output voltage $V(t)$ across the capacitance C and the electrical current $I(t)$ flowing in the inductor L describe the electrical dynamics of this system. The resistor R is the overall resistance due to ohmic contacts. The circuit a forced Liénard oscillator. Since the series connection of the RTD with the SCL preserves the shape of RTD's current-voltage I - V characteristic [65], we use the function $F(V)$ in cubic presented in Table II.1 to model a mathematical representation of current-voltage characteristic of RTD-OISCL whose graphic is given in Fig. I.11(c). B , a and b being positive constants (see Table II.1).

Using Kirchhoff's roles to the circuit presented in Fig. II.10, we obtain the set of first order ordinary differential equations (II.32) giving the current modulation of the LD; $I(t)$ and the voltage $V(t)$ across RTD-OISCL series connected (for simplicity, we could also admit RTD-LD instead of RTD-ILD).

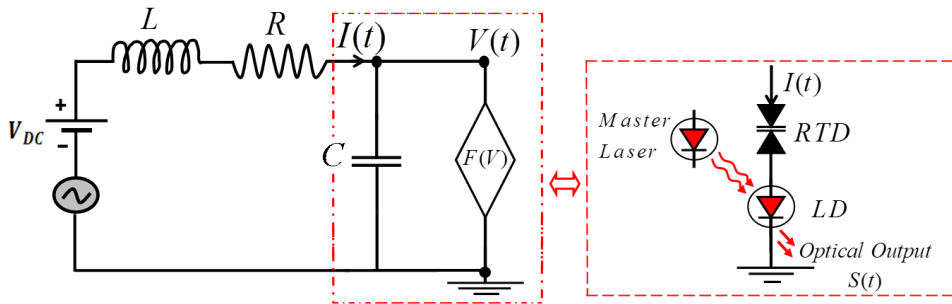


Figure II.10. Equivalent circuit of the optoelectronic novel RTD-OISCL optoelectronic oscillator

$$\begin{cases} \frac{dV(t)}{dt} = \frac{1}{C} [I(t) - F(V)], \\ \frac{dI(t)}{dt} = \frac{1}{L} [V_{dc} - RI(t) - V(t) + V_{ac} \sin(2\pi f_{in}t)]. \end{cases} \quad (\text{II.32})$$

The electrical current flowing in the active region is used to drive the laser Eq. (II.31). For this purpose, the relation $J(t) = \eta_i I(t)/q\vartheta$ relates the relationship between the pumping parameter

$J(t)$ and the driving current $I(t)$. Here, η_i is the optical efficiency, the ϑ the volume of laser active region and q the electric charge of an electron.

II.5.1. Dimensionless Equations of RTD-OISCL Model

For simplification purposes, we normalize Eqs. (II.33) - (II.37) as follows:

$$x(t) = V(t) / V_0 \tag{II.33}$$

$$y(t) = I(t) / I_0 \tag{II.34}$$

$$z(t) = 2\pi f_{in} t \tag{II.35}$$

$$n(t) = N(t) / N_{th} \tag{II.36}$$

$$s(t) = S(t) / S_0 \tag{II.37}$$

where variables are rescaled by the mean of constant values of optoelectronic system as: $V_0 = 1 V$, $I_0 = 1 A$, $N_{th} = N_0 + 1/(G_N \tau_p)$, $S_0 = N_{th} \tau_p / (G_N \tau_s)$. The coupled rate equations corresponding to dimensionless quantities $(x, y, z, n, s, \psi)^T$ for the dimensionless rescaling time variable $\tau = \omega_0 t$ are given as follows after resetting $\tau = t$ by equation (II.38) [97].

$$\begin{cases} \dot{x}(t) = m^{-1} [y(t) - f(x)] \\ \dot{y}(t) = m [v_{dc} - ry(t) - x(t) + v_{ac} \sin(z(t))] \\ \dot{z}(t) = \Omega_{in} \\ \dot{n}(t) = \gamma_0 \left[\frac{1}{i_{th}} y(t) - n(t) - \frac{n(t) - \delta}{1 - \delta} s(t) \right] \\ \dot{s}(t) = 2G_0 (\gamma^{-1} - 1) (n(t) - 1) s(t) + 2\gamma k \sqrt{s(t)} \cos(\psi(t)) \\ \dot{\psi}(t) = \alpha G_0 (n(t) - 1) - \gamma k \frac{1}{\sqrt{s(t)}} \sin(\psi(t)) - \Delta\Omega \end{cases} \tag{II.38}$$

In the last folders of Chapter III, we shall use the normalized Eq. (II.38), whose the equivalent diagram is as follows in Fig. II.11 to carry out its dynamics analysis.

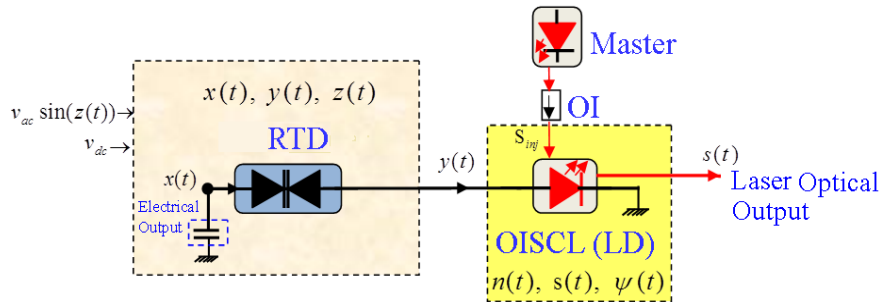


Figure II.11. Equivalent Diagram of the normalized RTD-OISCL integrated circuit

The normalized parameters are defined by $m = \sqrt{L/C}$, $\gamma_0 = 1/\omega_0\tau_r$ and $\Omega_{in} = 2\pi f_{inj}/\omega_0$ is the normalized frequency of external AC perturbation, $G_0 = \omega_0 G$ with G the normalized differential gain [45], $\omega_0 = 1/\sqrt{LC}$ is the dimensionless natural angular-frequency of forced RTD circuit, $\Delta\Omega = \frac{\Delta\omega}{\omega_0}$ and $k = \frac{k_{inj}}{\omega_0\tau_{in}}\sqrt{\frac{S_{inj}}{S_0}}$ refer to normalized frequency detuning and injection strength respectively. Without lack to generality and for simplification, we choose $S_{inj} = S_0$. Analytical and numerical calculations are performed throughout the above dimensionless normalized rate coupled equations describing an OHEO oscillator. The Table II.2 gives the parameters values of the system (II.38).

Table II.2. Description of standard RTD-OISCL OEO equations parameters and values used in numerical simulations

Symbol	Description	Value
L	Inductance	8.0 nH
C	Capacitance	5.6 pF
R	Overall resistance of due to connections	6.65 Ω
V_{ac}	Alternating voltage	Variable
V_{dc}	Direct voltage bias	Variable
\mathcal{G}	Laser active region volume	$10^{-16} m^{-3}$
τ_r	Carrier lifetime	2.0 ns
τ_p	Photon lifetime	2.0 ps
G_N	Differential gain coefficient	$8.1 \times 10^{-13} m/s$
N_{th}	Carrier density at threshold	$1.7173 \times 10^{24} m^{-3}$
γ	Effective gain coefficient	Variable
k_{inj}	Optical injection strength	Variable
α	Linewidth enlargement factor	6
$\Delta\omega$	Frequency detuning	Variable

II.6. Conclusion

In this chapter, we have firstly presented FT as the method that allows the interpretation of signal in frequency domain. In addition, the Langevin approach for analysis of noise effects in dynamical systems was given. Moreover, the method of reduction consisting of polynomial approximation of the RTD current-voltage characteristic was also provided. For stability and chaos studies, bifurcation analysis and Lyapunov methods (eigenvalues, Lyapunov spectrum and Routh-Hurwitz criterion) were presented as efficient tools. On the other hand, we have presented Simulink environment for visual approach to the differential equation setup and Runge-Kutta methods for

numerical simulations of ODEs. In the last folder, we modified the OISCL rate equations in terms of photon density, carrier density and developed a novel model of OEOs based on this laser model and RTD integration.

The Chapter III shall therefore give and discuss the main results from those models using each of these methods and models.

Chapter III

RESULTS AND DISCUSSION

III.1 Introduction

After the presentation of different materials, numerical and analytical methods and models of rate equations in Chapter II, we will present in this chapter the main collected results. This chapter proceeds as follows: In Section III.2, we consider the novel SCL rate equations (II.31). These equations are treated using the Langevin approach and FT in order to investigate the noise induced effect, and the influence of parameters in noise level especially the EGC. In Section III.3, we study the stability analysis of the OEO described by equations (II.38) according to Routh-Hurwitz criterion and Lyapunov methods, with the help of the polynomial approximation of RTD. The Section III.4 studies the nonlinear dynamics of the novel RTD-LD OEO. We use the fourth-order Runge-Kutta method to solve numerically the normalized system (II.38). In addition, we analyze the system through time series, phase portraits and bifurcation diagrams. The Lyapunov exponent calculation is performed by using a program of Wolf et al. [98].

III.2. Noise Induced Effects in Optical Injection SCLs

Noise induced effects have an important role in the performance of SCLs. It is capable of exciting intriguing behaviors modifying laser dynamics. Optical injection technique opens a rich variety of dynamical behavior in SCL optics. This technique significantly improves the performance of slave lasers, leading to several benefits for many applications including optical communications, microwave signal generation and all-optical signal processing. However, these SCLs systems are likely to generate noise due to intrinsic and extrinsic mechanisms, such as spontaneous emission, carrier recombination, etc., which tend to decrease the performance of optical emission, manifesting themselves in the form of RIN, FN and widening of laser linewidth [2, 99, 100]. Several investigations have proposed the possibility of reducing the noise level in classical model of SCLs [11, 101-106]. In the first folder of this chapter, we consider the novel SCL rate equations (II.31). These equations are treated using the Langevin approach. For this purpose, we shall use small-signal analysis and the FT to examine laser noise in frequency domain and propose the methods of noise reduction that consist on an appropriate variation of laser parameters especially the EGC.

By including Langevinian noise sources for each variable in addition to the temporal spontaneous emission term $R_{sp}(t) = \beta_{sp} \xi N(t) / \tau_r$, the Eqs. (II.31) become (III.1).

$$\begin{aligned}
 \frac{d}{dt} S(t) &= \frac{(1-\gamma)}{(1+\gamma)} [G_N(N(t) - N_{th})] S(t) + 2 \frac{k_{inj}}{\tau_{in}^*} \sqrt{S_{inj} S(t)} \cos[\psi(t) - \varphi_{inj}(t)] + R_{sp}(t) + F_S(t) \\
 \frac{d}{dt} \psi(t) &= \frac{1}{2} \alpha \frac{\gamma}{(1+\gamma)} [G_N(N(t) - N_{th})] - \frac{k_{inj}}{\tau_{in}^*} \sqrt{\frac{S_{inj}}{S(t)}} \sin[\psi(t) - \varphi_{inj}(t)] - \Delta\omega + F_\psi(t) \\
 \frac{d}{dt} N(t) &= J - \frac{N(t)}{\tau_r} - \left\{ \frac{1}{\tau_p} + [G_N(N(t) - N_{th})] \right\} S(t) + F_N(t) \\
 \psi(t) &= \varphi_{inj}(t) - \Delta\omega t
 \end{aligned} \tag{III.1}$$

In these equations, $\psi(t) = \varphi_{inj}(t) - \Delta\omega t$ is the phase difference between the internal and the injected fields; $\Delta\omega t$ is the frequency detuning; S_{inj} is the injected photon number from the ML; β_{sp} is the factor of spontaneous emission coupled to the laser mode; ξ is the confinement factor; the functions $F_x(t)$ ($x=S, N$ or ψ) are the Langevin noises sources. The rest of parameters are already defined in Sect. (II.4).

Let us redefine the variable $x(t)$ be equal to S, N or ψ with the mean value x_0 as described with the following equation (III.2) while the spontaneous emission contribution is given by equation (III.3):

$$x(t) = x_0 + \delta x(t) \tag{III.2}$$

$$R_{sp}(t) = (R_{sp})_0 + \left(\frac{\partial R_{sp}}{\partial N} \right)_0 \delta N(t) \tag{III.3}$$

The Langevin terms $F_S(t)$ and $F_\psi(t)$ are random noise due to the quantum effects of spontaneous emission of light while the term $F_N(t)$ is the noise source induced by random generation and recombination of carriers. They all originate from the random or shot noise effects [11] and noise effects need to be analyzed using statistical methods. We assume the correlation time of noise less than the photon and the carrier lifetime τ_p and τ_r respectively. As stochastic and random nature, Langevinian noise sources have zero means value and Eqs. (II.6-II.7) summarize their properties.

The Eqs. (III.4) and (III.5) give the Fourier Transformation of Eqs. (III.2) and (III.3) respectively while Eqs. (III.6) relate the frequency components of Langevin noises by taking into account their properties from (II.6).

$$x(t)(x = S, N, \psi) = x_0 + \int_{-\infty}^{\infty} \tilde{\delta}x(\omega)e^{j\omega t} d\omega \quad (\text{III.4})$$

$$R_{sp}(t) = (R_{sp})_0 + \left(\frac{\partial R_{sp}}{\partial N} \right)_0 \int_{-\infty}^{\infty} \tilde{\delta}N(\omega)e^{j\omega t} d\omega \quad (\text{III.5})$$

$$F_x(t)(x = S, N, \psi) = \int_{-\infty}^{\infty} \tilde{F}_x(\omega)e^{j\omega t} d\omega \quad (\text{III.6})$$

III.2.1. Noise Characteristics and Discussions

The inspection of the above equations (III.1) shows that, these equations explicitly involve the ML parameters: the emitted power related to photons density $S_{inj}(t)$ and the optical field related to optical phase $\varphi_{inj}(t)$. Therefore, the slave will be directly affected by noise emission from the master. Thus, the determination of the spectra characteristics of the slave will be possible unless those of the ML are known firstly.

III.2.1.1. Master Laser noises

The ML is described by the same equations as slave but without optical injection parameters, we set $S_{inj} = 0$ in (III.1) for this purpose. For much understanding, we adopt the notation *inj* to designate the master and assume that master and slaver lasers are identical. Taking into account Eqs. (III.4), (III.5) and (III.6), and according to the fact that the Langevin noise sources have zero means values, we treat the problem by linearization and we neglect second-order fluctuations. In addition, we separate continuous and fluctuating terms. In addition, applying FTs, we obtain the following equations (III.7), (III.8) and (III.9):

$$(S_{inj})_0 = \left(J_{inj} - \frac{N_{th_{inj}}}{\tau_{r_{inj}}} \right) \tau_{p_{inj}} = (J_{inj} - J_{th_{inj}}) \tau_{p_{inj}} \quad , \quad (\text{III.7a})$$

$$(\varphi_{inj})_0 = 0 \quad , \quad (\text{III.7b})$$

$$(N_{inj})_0 = N_{th_{inj}} \quad , \quad (\text{III.7c})$$

$$(R_{sp_{inj}})_0 = \frac{\beta_{sp_{inj}} \xi_{inj} (N_{inj})_0}{\tau_{r_{inj}}} \quad , \quad (\text{III.7d})$$

$$\begin{bmatrix} \delta\tilde{S}_{inj}(\omega) \\ \delta\tilde{N}_{inj}(\omega) \end{bmatrix} = \begin{bmatrix} j\omega + m_{11} & m_{12} \\ m_{21} & j\omega + m_{22} \end{bmatrix}^{-1} \begin{bmatrix} \tilde{F}_{S_{inj}}(\omega) \\ \tilde{F}_{N_{inj}}(\omega) \end{bmatrix}, \quad (\text{III.8})$$

$$\delta\tilde{\varphi}_{inj}(\omega) = \frac{1}{j\omega} \left\{ m_{32} \delta\tilde{N}_{inj}(\omega) + \tilde{F}_{\varphi_{inj}}(\omega) \right\}, \quad (\text{III.9})$$

where the matrix elements m_{ij} ($i, j = 1; 2$) 's are depending on the parameters of the **ML** and on continuous terms expressed in Eqs. (III.8) and given by

$$m_{11} = 0, \quad m_{12} = - \left\{ \frac{(1 - \gamma_{inj})}{(1 + \gamma_{inj})} G_{N_{inj}}(S_{inj})_0 + \left(\frac{\partial R_{sp_{inj}}}{\partial N_{inj}} \right)_{(N_{inj})_0} \right\}, \quad m_{21} = 1 / \tau_{p_{inj}}, \quad m_{22} = 1 / \tau_{r_{inj}} + G_{N_{inj}}(S_{inj})_0,$$

$$m_{32} = \frac{1}{2} \alpha_{inj} \frac{\gamma_{inj}}{(1 + \gamma_{inj})} G_{N_{inj}}.$$

The parameter $(S_{inj})_0$ and $(N_{inj})_0$ are the steady state average values inside the **ML** given in (III.7).

Here, $\delta\tilde{S}_{inj}(\omega)$, $\delta\tilde{N}_{inj}(\omega)$, $\delta\tilde{\varphi}_{inj}(\omega)$, $\tilde{F}_{S_{inj}}(\omega)$, $\tilde{F}_{N_{inj}}(\omega)$ and $\tilde{F}_{\varphi_{inj}}(\omega)$ are the **FTs** of time functions corresponding to the fluctuation terms $\delta S_{inj}(t)$, $\delta N_{inj}(t)$, $\delta\varphi_{inj}(t)$, $F_{S_{inj}}(t)$, $F_{N_{inj}}(t)$ and $F_{\varphi_{inj}}(t)$ respectively. Using Cramer's rule, we find the spectral densities for photon density, carrier density and phase density given by Eq. (III.10)-(III.13).

$$\begin{aligned} \langle |\delta\tilde{S}_{inj}(\omega)|^2 \rangle &= \frac{1}{|\Delta(\omega)|^2} \left[(\omega^2 + m_{22}^2) \langle |\tilde{F}_{S_{inj}}(\omega)|^2 \rangle + m_{12}^2 \langle |\tilde{F}_{N_{inj}}(\omega)|^2 \rangle \right. \\ &\quad \left. - 2m_{22}m_{12} \langle \tilde{F}_{S_{inj}}(\omega) \tilde{F}_{N_{inj}}(\omega)^* \rangle \right] \end{aligned} \quad (\text{III.10})$$

$$\langle |\delta\tilde{N}_{inj}(\omega)|^2 \rangle = \frac{1}{|\Delta(\omega)|^2} \left(m_{21}^2 \langle |\tilde{F}_{S_{inj}}(\omega)|^2 \rangle + \omega^2 \langle |\tilde{F}_{N_{inj}}(\omega)|^2 \rangle \right) \quad (\text{III.11})$$

$$\langle |\delta\tilde{\varphi}_{inj}(\omega)|^2 \rangle = \frac{1}{\omega^2} \left\{ \frac{1}{|\Delta(\omega)|^2} m_{32}^2 \left(m_{21}^2 \langle |\tilde{F}_{S_{inj}}(\omega)|^2 \rangle \right) + \langle |\tilde{F}_{\varphi_{inj}}(\omega)|^2 \rangle \right\} \quad (\text{III.12})$$

$$|\Delta(\omega)|^2 = (m_{12}m_{21} + \omega^2)^2 + \omega^2 m_{22}^2. \quad (\text{III.13})$$

Equations (III.10)-(III.13) reveal that the spectral characteristics of the **ML** can be determined unless the spectral densities of Langevin noise sources are known. Following the formulas given in [101] and according to some change mentioned, diffusion coefficient associated with each noise

sources can be expressed by taking their correlation as in Eq.(II.10) and in Ref. [107]. Among these, Langevin terms are given such as:

$$\begin{aligned} \langle |\tilde{F}_{S_{inj}}(\omega)|^2 \rangle &= 2R_{sp_{inj0}} S_{inj0} \\ \langle |\tilde{F}_{\varphi_{inj}}(\omega)|^2 \rangle &= \frac{R_{sp_{inj0}}}{2S_{inj0}} \\ \langle \tilde{F}_{S_{inj}}(\omega)\tilde{F}_{\varphi_{inj}}(\omega)^* \rangle &= 0 \end{aligned} \quad (III.14)$$

$$\begin{aligned} \langle |\tilde{F}_{N_{inj}}(\omega)|^2 \rangle &= 2 \left(R_{sp_{inj0}} S_{inj0} + \frac{N_{th_{inj}}}{\tau_{S_{inj}}} \right) \\ \langle \tilde{F}_{S_{inj}}(\omega)\tilde{F}_{N_{inj}}(\omega)^* \rangle &= -2R_{sp_{inj0}} S_{inj0} \\ \langle \tilde{F}_{N_{inj}}(\omega)\tilde{F}_{\varphi_{inj}}(\omega)^* \rangle &= 0 \end{aligned} \quad (III.15)$$

Equations (III.9), (III.10), (III.14), (III.15) and (I.6) lead to the Eq. (III.16) giving the RIN of master laser:

$$RIN_{inj} = \frac{2(R_{sp_{inj}})_0}{(S_{inj})_0} \times \frac{\omega^2 + m_{22}^2 + m_{12}^2 \left(1 + \frac{N_{th_{inj}}}{\tau_{S_{inj}} R_{sp_{inj0}} (S_{inj})_0} \right) + 2m_{12}m_{22}}{(m_{12}m_{21} + \omega^2)^2 + \omega^2 m_{22}^2}, \quad (III.16)$$

where m_{12} , m_{21} and m_{22} are already defined.

We assume the following numerical values for the laser parameters as in Table II.2. In addition, $J_{th} = 8.5865 \times 10^{32} \text{ m}^{-3} \text{ s}^{-1}$, $\xi = 0.2$ and other parameters used are found on figure captions. The Fig. III.1(a) shows the variation of RIN variation of the ML (free-running laser) for some values of bias current, and figure III.1(b) presents the RIN when EGC changes. The RIN exhibits a resonance phenomenon at the resonance frequency. This will be easier to see by the presence of peaks on illustrative curves, when increasing the injection current from 1.5 to 12 times the threshold current (figure III.1 (a)). This RIN spectrum shows the characteristic of flat white noise in the low-frequency regime due to the small amplitude of the intensity fluctuation. In the high-frequency regime, the spectra exhibit the well-known carrier-photon resonance peak around the resonance frequency. The peaks show that the laser is affected by the natural resonance of electron and photon populations [108]. The increase in current is associated with an increase in the relaxation oscillation peaks. The fact that the photon number and carrier number in the laser cavity are random variables makes that noise intensity different from that of a white noise spectrum. Similar results have been obtained by numerical simulations or observed in experiments [106].

Moreover, when the laser is operating above the threshold (see figure III.1 (b)), varying the EGC values reveals a significant diminution of RIN spectra at low frequency from $-110\text{dB}\cdot\text{Hz}^{-1}$ to $-175\text{dB}\cdot\text{Hz}^{-1}$ when EGC changes from 0.99 to 0.1. According to Ref. [11], this noise level is allowed in communication systems for EGC values less than or equal to 0.75 for a bias current of twice the threshold. If we need to reduce the RIN level we must increase the current. Particularly around the resonance frequencies whose values depend also on the EGC values, the RIN spectra are the same. However, with the same current bias, it is also possible to reduce the RIN level through EGC values (see figure III.1 (b) curves (1), (2) and (3)). Over the resonance frequency oscillation (RFO), the convergence of all RIN spectra observed when EGC changes is very quick, unlike the values when the current changes. The peak of intensity noise is reduced by around $25\text{dB}\cdot\text{Hz}^{-1}$ with the frequency oscillation, which shifts by about 0.65 GHz when the EGC value is fixed in figure III.1 (a) (see curves (1)–(5)). In addition, in figure III.1 (b) this decrease is only pronounced at the lower frequency (lower than the RFO).

The frequency noise in time domain is given from the relationship between the frequency and angular frequency (the phase) i.e. $2\pi f(t) = d\varphi(t) / dt$. Therefore, in accordance with equation (III.12)-(III.15), the Eq. (III.17) gives the ML frequency noise $FN_{inj} = \langle |\tilde{f}_{inj}(\omega)|^2 \rangle$ as:

$$FN_{inj} = \frac{(R_{sp_{inj}})_0}{8\pi^2 (S_{inj})_0} \left\{ 1 + \frac{4m_{32}^2 m_{21}^2 [(S_{inj})_0]^2}{(m_{12}m_{21} + \omega^2)^2 + \omega^2 m_{22}^2} \right\} \quad (\text{III.17})$$

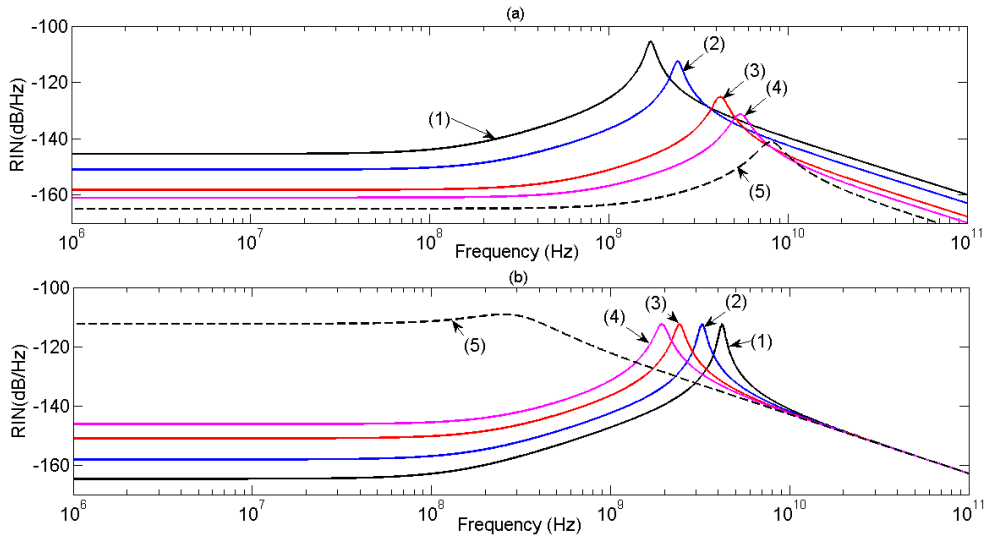


Figure III.1. RIN of ML as function of frequency; (a) when $\gamma_{inj} = 0.5$ for several bias current conditions (1) $J_{inj} = 2J_{th_{inj}}$, (2) $J_{inj} = 2.5J_{th_{inj}}$, (3) $J_{inj} = 4J_{th_{inj}}$ and (4) $J_{inj} = 12J_{th_{inj}}$; (b) when $J_{inj} = 2J_{th_{inj}}$, for several value of EGC (1) $\gamma_{inj} = 0.00$, (2) $\gamma_{inj} = 0.25$ (3),(4) $\gamma_{inj} = 0.5$ (4) $\gamma_{inj} = 0.65$, (5) $\gamma_{inj} = 0.99$.

The simulated results of the FN are illustrated in figure III.2 with the same intrinsic parameters' values as those used for RIN in Fig. III.1. Figure III.2 (a) shows that, for an injection-current-ratio just above unity, the FN spectra are flat. Above and far above unity, the spectra reveal the RFO around 1 GHz and 10 GHz when the EGC is fixed. If we keep the current constant and change, the EGC the variation becomes the same as with the RIN (see Fig. III.2 (b)).

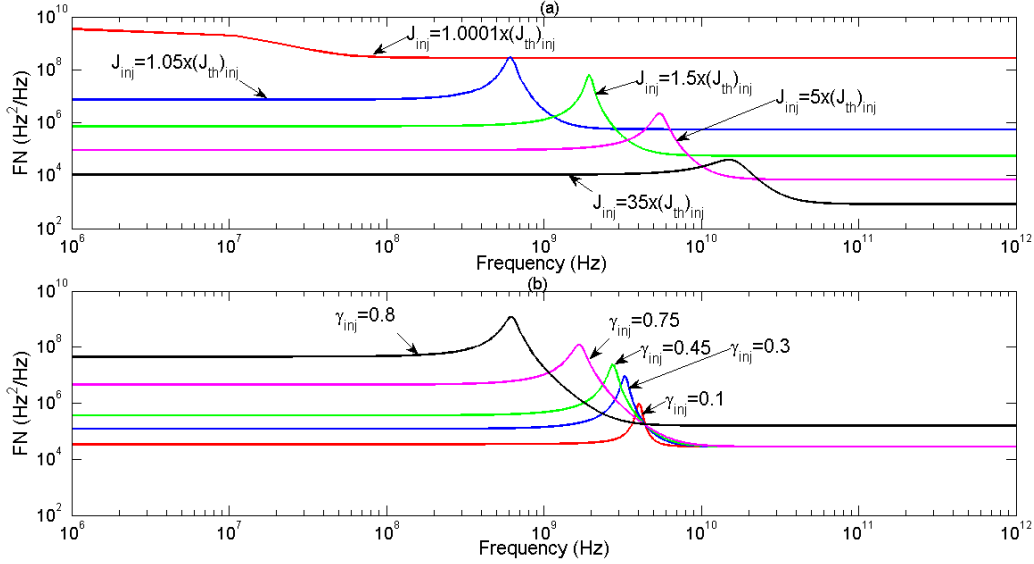


Figure III.2. FN of the master laser as a function of frequency: (a) when $\gamma_{inj} = 0.45$ for several bias current conditions; (b) when $J_{inj} = 2J_{th_{inj}}$ for several values of EGC.

The FWHM is derived from the FN. Because of the Lorentzian shape of electrical field, the spectral linewidth is evaluated from the low frequency from the FN as $\Delta f = 2\pi FN(\omega = 0)$ [11, 99]. Using (III.12) and (III.17) the FWHM becomes:

$$\begin{aligned} \Delta f_{ini} &= \frac{(R_{sp_{inj}})_0}{8\pi^2 (S_{inj})_0} \left[1 + \alpha_{inj}^2 \left(\frac{\gamma_{inj}}{1 - \gamma_{inj}} \right)^2 \right] \\ &= \frac{(R_{sp_{inj}})_0}{8\pi^2 (J_{inj} - J_{th_{inj}}) \tau_{p_{inj}}} \left[1 + \alpha_{inj}^2 \left(\frac{\gamma_{inj}}{1 - \gamma_{inj}} \right)^2 \right] \end{aligned} \quad (III.18)$$

It is well known that the linewidth of SCL is larger than that ordinary laser that has an almost LEF α , which value is few units [101]. Due to the EGC range values, equation (III.18) shows and induced modulation of the FWHM by the means of EGC (see [45 - 48] for the mean EGC), which leads to a more significant reduction of the laser linewidth. Indeed, the relationship $\alpha_{inj}^2 (\gamma_{inj} / (1 - \gamma_{inj}))^2 < \alpha_{inj}^2$ remains valid as long as $0 < \gamma_{inj} < 0.5$. The formula (III.18), known as a Schawlow–Townes formula is one of the main points of in this Chapter. This formula is designated as the modified Schawlow–Townes formula due to the fact that, the EGC parameter leads to a

narrower laser linewidth by decreasing **EGC** values. Figure III.3 plots the corresponding result for the **FWHM**. Figure III.3 (a) depicts the variation of the linewidth with bias current ratio ($J_{inj} / J_{th_{inj}}$) for some value of **SEF**, and figure III.3 (b) shows the variations of linewidth with **EGC**. In recent years, the main way to reduce the **FWHM** was to reduce the **LEF** or **SEF** (Figure III.3 (a) and (c)). Now, we show that the **FWHM** can also be controlled with the help of the **EGC** (Figure III.3 (b)). Therefore, the **EGC** plays a similar role to the **SEF**, avoiding an abrupt increase in **FWHM** near the threshold [107]. Thus, figure III. 3(b) shows that the decrease in **EGC** leads to a route to the ideal laser linewidth.

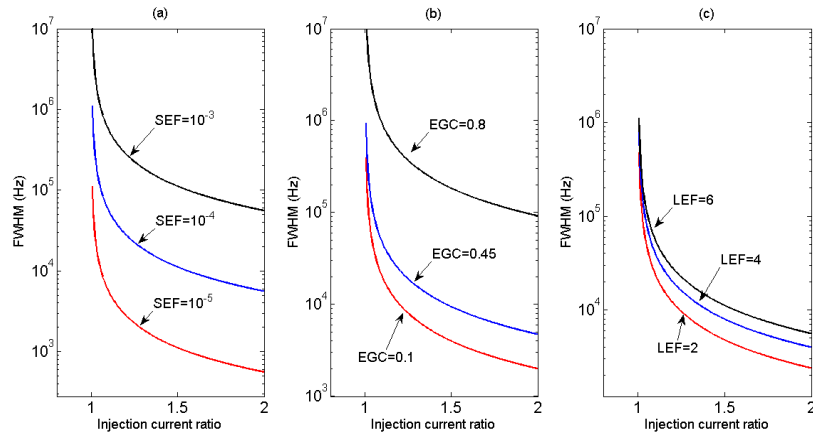


Figure III.3. Variation of linewidth with injection current ratio. Curves show the rapid narrowing of linewidth with increasing current ratio that is obtained by decreasing (a) **SEF**, (b) **EGC** and (c) **LEF**.

We mention addition that, according to figures III.1 (b) and III.3, we should pay more attention to the conditions of getting a narrow linewidth by ensuring to maintain the **RIN** and **FN** levels lower. Thus, to avoid an increase in **FN** and **RIN** spectra while keeping a narrow linewidth, this requires to the **EGC** to stay at a level lower than 0.8.

III.2.2. Relative Intensity and Frequency Noises of OISCL

In this section we derivated mathematical expression for **RIN** and **FN** of the optical injection semiconductor lasers implying small-signal analysis around the steady state $(S_0, \bar{N}, \psi_0)^T$, linearization and **FT** of equation (II.1) successively. Similar to the section II.2.1, after linearization, **FT** and arrangement, the steady state points are given by the implicit expressions (III.19) while the fluctuations terms are obtained as solutions of the equation (III.20).

$$\psi_0 = -\tan^{-1}\left(\frac{\alpha\gamma}{1-\gamma}\right) + \sin^{-1}\left[-\frac{\Delta\omega\tau_{in}^*}{k_{inj}}\left(\frac{S_0}{(S_{inj})_0}\right)^{1/2} \frac{1}{\sqrt{1+(\alpha\gamma/(1-\gamma))^2}}\right],$$

$$S_0 = \frac{J - \bar{N} / \tau_r}{1 / \tau_p + G_N (\bar{N} - N_{th})}, \quad (III.19)$$

$$\bar{N} = N_{th} - 2 \frac{1 + \gamma}{G_N (1 - \gamma)} \frac{k_{inj}}{\tau_{in}^*} \left(\frac{(S_{inj})_0}{S_0} \right)^{1/2} \cos(\psi_0).$$

$$\begin{bmatrix} \delta \tilde{S}(\omega) \\ -2S_0 \delta \tilde{\psi}(\omega) \\ \delta \tilde{N}(\omega) \end{bmatrix} = \begin{bmatrix} j\omega + b_{11} & b_{12} & b_{13} \\ -b_{12} & j\omega + b_{22} & b_{23} \\ b_{31} & 0 & j\omega + b_{33} \end{bmatrix}^{-1} \begin{bmatrix} \tilde{f}_s(\omega) \\ \tilde{f}_N(\omega) \\ \tilde{f}_\psi(\omega) \end{bmatrix}. \quad (III.20)$$

here, the parameters $b_j (i, j = 1; 2)$ are depending on the parameters of both master and slave lasers and expressed as follows:

$$b_{11} = - \left(\frac{1 - \gamma}{1 + \gamma} G_N (\bar{N} - N_{th}) + \frac{k_{inj}}{\tau_{in}^*} \left(\frac{(S_{inj})_0}{S_0} \right)^{1/2} \cos(\psi_0) \right), b_{12} = - \frac{k_{inj}}{\tau_{in}^*} \left(\frac{(S_{inj})_0}{S_0} \right)^{1/2} \sin(\psi_0),$$

$$b_{13} = - \left(\frac{1 - \gamma}{1 + \gamma} G_N S_0 + \left[\frac{\partial R_{sp}}{\partial N} \right]_{\bar{N}} \right), b_{21} = -b_{12} = \frac{k_{inj}}{\tau_{in}^*} \left(\frac{(S_{inj})_0}{S_0} \right)^{1/2} \sin(\psi_0),$$

$$b_{22} = \frac{k_{inj}}{\tau_{in}^*} \left(\frac{(S_{inj})_0}{S_0} \right)^{1/2} \cos(\psi_0), b_{23} = \alpha \frac{\gamma S_0}{1 + \gamma} G_N, b_{31} = \frac{1}{\tau_p} + G_N (\bar{N} - N_{th}), b_{33} = \frac{1}{\tau_r} + G_N S_0.$$

The parameter is S_0 the steady-state average values inside the **SL** given in (III.19) while $(S_{inj})_0$ is that of the **ML**. In the other hand, the functions \tilde{f}_s , \tilde{f}_N and \tilde{f}_ψ expressed in Eqs. (III.21)- (III.23) are equivalent to the total fluctuations of photon density, carrier density and optical phase respectively inside the slave laser cavity:

$$\tilde{f}_s(\omega) = \tilde{F}_s(\omega) + S_0 b_{22} \frac{\delta \tilde{S}_{inj}(\omega)}{S_{inj_0}} - 2S_0 \delta \tilde{\varphi}_{inj}(\omega), \quad (III.21)$$

$$\tilde{f}_N(\omega) = \tilde{F}_N(\omega) \quad (III.22)$$

$$\tilde{f}_\psi(\omega) = -2S_0 \left(\tilde{F}_\psi(\omega) + \frac{1}{2} b_{12} \frac{\delta \tilde{S}_{inj}(\omega)}{S_{inj_0}} + b_{22} \delta \tilde{\varphi}_{inj}(\omega) \right), \quad (III.23)$$

where S_0 , \bar{N}_0 and ψ_0 are average values for photon density, carrier density and optical phase of SL respectively. The fluctuations components $\delta\tilde{S}(\omega)$, $\delta\tilde{\psi}(\omega)$ and $\delta\tilde{N}(\omega)$ are obtained as solution of equation (III.20). After arrangement we get Eqs. (III.24)-(III.27):

$$\delta\tilde{S}(\omega) = \left\{ -\left[b_{22}b_{33} - \omega^2 + j\omega(b_{22} + b_{33}) \right] \tilde{f}_S(\omega) + \left[b_{12}b_{33} + j\omega b_{33} \right] \tilde{f}_\psi(\omega) + \left[-b_{12}b_{23} + b_{13}b_{22} + j\omega b_{13} \right] \tilde{f}_N(\omega) \right\} \div \tilde{Y}(\omega), \quad (\text{III.24})$$

$$\delta\tilde{\psi}(\omega) = \frac{1}{2S} \left\{ -\left[b_{11}b_{23} + b_{13}b_{12} + j\omega b_{23} \right] \tilde{f}_N(\omega) \right\} + \left[b_{12}b_{33} + b_{23}b_{31} + j\omega b_{12} \right] \tilde{f}_S(\omega) + \left[b_{11}b_{33} - b_{31}b_{13} - \omega^2 + j\omega(b_{33} + b_{11}) \right] \tilde{f}_\psi(\omega) \right\} \div \tilde{Y}(\omega), \quad (\text{III.25})$$

$$\delta\tilde{N}(\omega) = \left\{ \left[b_{22}b_{31} + j\omega b_{31} \right] \tilde{f}_S(\omega) - \left[b_{31}b_{12} \right] \tilde{f}_\psi(\omega) - \left[b_{11}b_{22} + b_{12}^2 - \omega^2 + j\omega(b_{22} + b_{11}) \right] \tilde{f}_N(\omega) \right\} \div \tilde{Y}(\omega), \quad (\text{III.26})$$

with

$$\tilde{Y}(\omega) = \left\{ -b_{31}b_{12}b_{23} + b_{31}b_{13}b_{22} - b_{12}^2b_{33} - b_{11}b_{22}b_{33} + (b_{11} + b_{22} + b_{33})\omega^2 \right\} + j \left\{ \omega^3 + \omega(b_{31}b_{13} - b_{12}^2 - b_{11}b_{33} - b_{11}b_{22} - b_{22}b_{33}) \right\}. \quad (\text{III.27})$$

We need to know the cross-correlations and correlations of functions \tilde{f}_S , \tilde{f}_N and \tilde{f}_ψ function in order to express the RIN and the FN of slave. For simplification, Yabre et al. [109] assumed that the Langevin noise sources \tilde{F}_S , \tilde{F}_ψ and \tilde{F}_N are not to be correlated with photon density $\delta\tilde{S}_{inj}(\omega)$ and optical phase $\delta\tilde{\varphi}_{inj}(\omega)$ fluctuations of the ML, which are given as the solution of equation (III.10) and (III.12). From the equation (III.24), the power spectral density for intensity and phase noise can be obtained as follows:

$$\begin{aligned} \langle |\delta\tilde{S}(\omega)|^2 \rangle &= \left\{ \left[(b_{22}b_{33} - \omega^2)^2 + \omega^2 (b_{22} + b_{33})^2 \right] \langle |\tilde{f}_S(\omega)|^2 \rangle \right. \\ &\quad + \left[b_{12}^2b_{33}^2 + \omega^2b_{33}^2 \right] \langle |\tilde{f}_\psi(\omega)|^2 \rangle \\ &\quad + \left[(b_{13}b_{22} - b_{12}b_{23})^2 + \omega^2b_{13}^2 \right] \langle |\tilde{f}_N(\omega)|^2 \rangle \\ &\quad + 2(\omega^2 - b_{22}b_{33})(b_{13}b_{22} - b_{12}b_{23}) \langle \tilde{f}_S(\omega)\tilde{f}_N(\omega)^* \rangle + \\ &\quad + 2b_{12}b_{33}(\omega^2 - b_{22}b_{33}) \Re \left[\langle \tilde{f}_S(\omega)\tilde{f}_\psi(\omega)^* \rangle \right] + \\ &\quad + 2b_{12}b_{23}(b_{13}b_{22} - b_{12}b_{23}) \langle \tilde{f}_\psi(\omega)\tilde{f}_N(\omega)^* \rangle \left. \right\} \div |\tilde{Y}(\omega)|^2 \end{aligned} \quad (\text{III.28})$$

$$\begin{aligned}
\langle |\delta\tilde{\psi}(\omega)|^2 \rangle &= \frac{1}{4S_0^2 |\tilde{Y}(\omega)|^2} \left\{ \left[(b_{12}b_{33} + b_{23}b_{31})^2 + \omega^2 b_{12}^2 \right] \langle |\tilde{f}_S(\omega)|^2 \rangle \right. \\
&+ \left[(b_{11}b_{33} - b_{31}b_{13} - \omega^2)^2 + \omega^2 (b_{11} + b_{33})^2 \right] \langle |\tilde{f}_\psi(\omega)|^2 \rangle \\
&+ \left[(b_{11}b_{23} + b_{13}b_{12})^2 + \omega^2 b_{23}^2 \right] \langle |\tilde{f}_N(\omega)|^2 \rangle \\
&+ 2(b_{12}b_{33} + b_{23}b_{31})(b_{11}b_{33} - b_{31}b_{13} - \omega^2) \Re \left[\langle \tilde{f}_S(\omega) \tilde{f}_\psi(\omega)^* \rangle \right] \\
&- 2(b_{12}b_{33} + b_{23}b_{31})(b_{11}b_{23} + b_{13}b_{12}) \langle \tilde{f}_S(\omega) \tilde{f}_N(\omega)^* \rangle \left. \right\} \quad (\text{III.29})
\end{aligned}$$

Using the expressions of \tilde{f}_S , \tilde{f}_ψ , \tilde{f}_N and according to $\delta\tilde{S}_{inj}(\omega)$, $\delta\tilde{N}_{inj}(\omega)$ and $\delta\tilde{\varphi}_{inj}(\omega)$, we obtained spectral density of slave fluctuation as

$$\langle |\tilde{f}_S(\omega)|^2 \rangle = 2R_{sp_0} S_0 - \frac{4R_{sp_{inj_0}} S_0^2 m_{21} m_{32} b_{12} b_{22}}{|\Delta(\omega)|^2} + S_0^2 b_{22}^2 \frac{\langle |\delta\tilde{S}_{inj}(\omega)|^2 \rangle}{S_{inj_0}^2} + 4S_0^2 b_{12}^2 \langle |\delta\tilde{\varphi}_{inj}(\omega)|^2 \rangle, \quad (\text{III.30})$$

$$\langle |\tilde{f}_\psi(\omega)|^2 \rangle = 4S_0^2 \left(\frac{R_{sp_0}}{2S_0} + \frac{2R_{sp_{inj_0}} m_{21} m_{32} b_{12} b_{22}}{|\Delta(\omega)|^2} + \frac{1}{4} b_{12}^2 \frac{\langle |\delta\tilde{S}_{inj}(\omega)|^2 \rangle}{S_{inj_0}^2} + b_{22}^2 \langle |\delta\tilde{\varphi}_{inj}(\omega)|^2 \rangle \right), \quad (\text{III.31})$$

$$\langle |\tilde{F}_N|^2 \rangle = 2 \left(R_{sp_0} S_0 + \frac{\bar{N}_0}{\tau_r} \right), \quad (\text{III.32})$$

$$\langle \tilde{F}_S(\omega) \tilde{F}_N(\omega)^* \rangle = -2R_{sp_0} S_0, \quad (\text{III.33})$$

$$\langle \tilde{F}_N(\omega) \tilde{F}_\psi(\omega)^* \rangle = 0, \quad (\text{III.34})$$

where

$$\begin{aligned}
\Re \left\{ \langle \tilde{f}_S(\omega) \tilde{f}_\psi(\omega)^* \rangle \right\} &= -2(S_0)^2 \left[\frac{2R_{sp_{inj_0}} m_{21} m_{32}}{|\Delta(\omega)|^2} (b_{22}^2 - b_{12}^2) \right. \\
&\left. + \frac{1}{2} b_{12} b_{22} \frac{\langle |\delta\tilde{S}_{inj}(\omega)|^2 \rangle}{S_{inj_0}^2} - 2b_{22} b_{12} \langle |\delta\tilde{\varphi}_{inj}(\omega)|^2 \rangle \right]. \quad (\text{III.35})
\end{aligned}$$

Using the definition of the [RIN](#) and substituting we find the following relation:

$$\begin{aligned}
RIN = & \frac{2R_{sp_0}}{S_0 |\tilde{Y}(\omega)|^2} \left\{ \left[1 - \frac{S_0}{2R_{sp_0}} \left(\frac{4R_{sp_{inj_0}} m_{21} m_{32} b_{12} b_{22}}{|\Delta(\omega)|^2} + b_{22}^2 RIN_{inj} + 4b_{12}^2 \left(\frac{2\pi}{\omega} \right)^2 FN_{inj} \right) \right] \times \right. \\
& \left. \left[(b_{22} b_{33} - \omega^2)^2 + \omega^2 (b_{22} + b_{33})^2 \right] + \right. \\
& \left. + \left[b_{12}^2 b_{33}^2 + \omega^2 b_{33}^2 \right] \left[1 + \frac{2S_0}{R_{sp_0}} \left(\frac{2R_{sp_{inj_0}} m_{21} m_{32} b_{12} b_{22}}{|\Delta(\omega)|^2} + \frac{1}{4} b_{12}^2 RIN_{inj} + b_{22}^2 \left(\frac{2\pi}{\omega} \right)^2 FN_{inj} \right) \right] \right\} \quad (III.36) \\
& + \left[1 + \frac{\bar{N}}{\tau_r R_{sp_0} S_0} \right] \left[(b_{13} b_{22} - b_{12} b_{23})^2 + \omega^2 b_{13}^2 \right] - 2(\omega^2 - b_{22} b_{33})(b_{13} b_{22} - b_{12} b_{23}) \\
& - \frac{2b_{12} b_{33} S_0}{R_{sp_0}} (\omega^2 - b_{22} b_{33}) \left[\frac{2R_{sp_{inj_0}} m_{21} m_{32}}{|\Delta(\omega)|^2} (b_{22}^2 - b_{12}^2) + \frac{1}{2} b_{12} b_{22} RIN_{inj} - 2b_{22} b_{12} \left(\frac{2\pi}{\omega} \right)^2 FN_{inj} \right]
\end{aligned}$$

From the previous definition giving the expression of frequency noise following Eq. (III.17), the Eq. (III.37) gives the FN for optical injection SCLs.

$$\begin{aligned}
FN = & \frac{\omega^2}{16\pi^2 S_0^2 |\tilde{Y}(\omega)|^2} \left\{ 2 \left(R_{sp_0} S_0 + \frac{\bar{N}_0}{\tau_r} \right) \left[(b_{11} b_{23} + b_{13} b_{12})^2 + \omega^2 b_{13}^2 \right] + \right. \\
& 4R_{sp_0} S_0 (b_{12} b_{33} + b_{23} b_{31})(b_{11} b_{23} + b_{13} b_{12}) + \\
& \left[(b_{12} b_{33} + b_{23} b_{31})^2 + \omega^2 b_{12}^2 \right] \times \left[2R_{sp_0} S_0 - \frac{4R_{sp_{inj_0}} S_0^2 m_{21} m_{32} b_{12} b_{22}}{|\Delta(\omega)|^2} + \right. \\
& \left. + S_0^2 b_{22}^2 RIN_{inj} + \frac{16\pi^2 S_0^2 b_{12}^2}{\omega^2} FN_{inj} \right] + 4S_0^2 \left[(b_{11} b_{33} - b_{31} b_{13} - \omega^2)^2 + \omega^2 (b_{33} + b_{11})^2 \right] \times \\
& \left(\frac{R_{sp_0}}{2S_0} + \frac{2R_{sp_{inj_0}} m_{21} m_{32} b_{12} b_{22}}{|\Delta(\omega)|^2} + \frac{b_{12}^2}{4} RIN_{inj} + \frac{4\pi^2 b_{22}^2}{\omega^2} FN_{inj} \right) + \\
& - 4S_0^2 (b_{12} b_{33} + b_{23} b_{31})(b_{11} b_{33} - b_{31} b_{13} - \omega^2) \times \\
& \left. \left[\frac{2R_{sp_{inj_0}} m_{21} m_{32}}{|\Delta(\omega)|^2} (b_{22}^2 - b_{12}^2) + \frac{b_{12} b_{22}}{2} RIN_{inj} - \frac{8\pi^2 b_{22} b_{12}}{\omega^2} FN_{inj} \right] \right\} \quad (III.37)
\end{aligned}$$

Both Eq. (III.36) and Eq. (III.37) reveal that the RIN and FN depend to the master laser noise (the functions RIN_{inj} and FN_{inj} derived from the equations (III.16) and (III.17) respectively). This evidences the optical injection noise induced-effects.

III.2.2.1. Influence of Optical Injection in RIN Spectra

As aforementioned, ML noises affect the SL emission (see for instance Eqs. (III.36) and (III.37)). Owing to the large number of parameters involved in these expressions, in addition, for reducing the level of frequency noise and intensity noise, only parameters that can significantly affect noise

levels shall be considered. The choice of these parameters and especially of the EGC can be best understood through RIN and FN spectra by turning to the next figures for SL relative intensity and frequency noises. Figures III.4 (a) and (b) show the abrupt decrease of intensity noise with the appearance of two relaxation peaks. That decreasing is similar to the shot noise limit in ref. [107] or to the famous “1/f noise”. The first peak corresponds to the free-running laser relaxation frequency (dotted lines). We can observe that all these peaks are at exactly the same relaxation frequency as those of the optically injected laser (solid lines). However, for an injection rate of -20dB (figures III.4 (a) and (c)), at all frequencies both RIN spectra are higher than the free-running noise level. Near the RFO and above it, these levels are reduced to more than 5dB/Hz, compared to the master levels. At RFO, the reduction is more than 10dB. Nevertheless, we can establish from figure III.4 (d) that for an injection rate of 40 dB the slave RIN level is above that of the ML for all frequencies. In those conditions, the intensity fluctuation from the SL is greatly enhanced by the optical injection from the ML. Finally, a second peak has appeared as in Ref. [109]. That peak can be understood regarding Eq. (III.36) and in connection with the fact that the noise characteristics of the ML are included in the determination of the SL noise in the stable-locking condition.

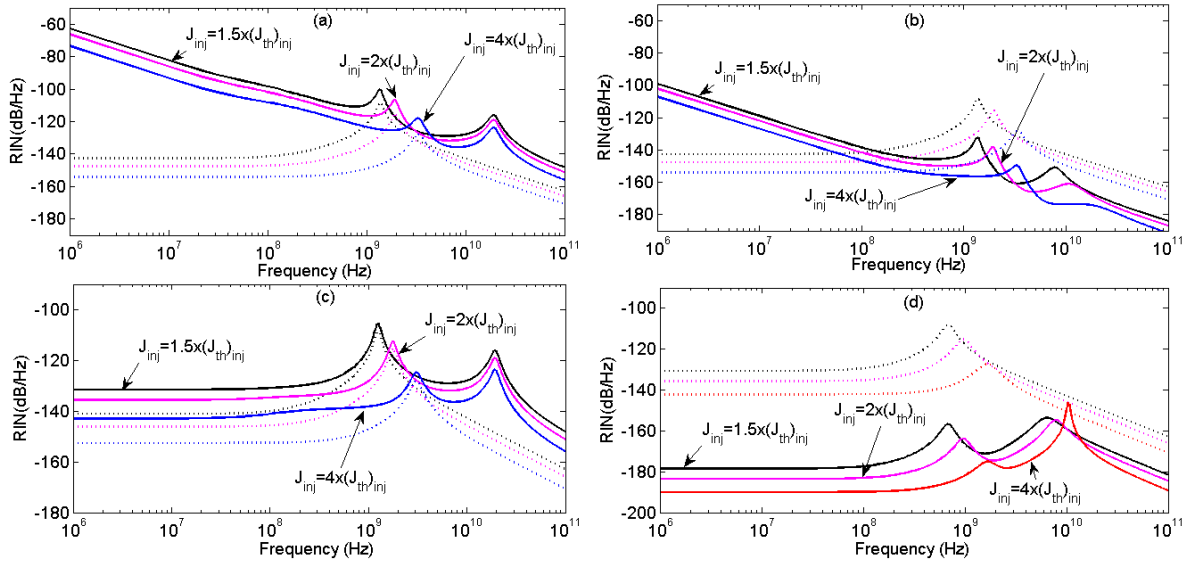


Figure III.4. Eliminating 1/f noise. RIN variation for injection rates of (a) -20 dB and (b) 40 dB when phase fluctuations of the ML are considered, and (c) -20 dB and (d) 40 dB when phase fluctuations are neglected.

Eliminating 1/f noise in RIN spectrum

1/f noise is low frequency noise for which the noise power is inversely proportional to the frequency. The sources of 1/f noise are still widely debated and much research is still being done in this area. 1/f noise can be a limit to achieving the best performance in precision measurement applications since this type of noise cannot be filtered out. To avoid the 1/f noise observed in RIN

spectrum, we may need here more careful choice of parameters involved and also supposed for simplicity that, the ML phase fluctuations are small enough to be taking into account. The term $\delta\tilde{\varphi}_{inj}(\omega)$ from equation (III.21) could be neglected. Figs. III.4 (c) and (a) show the effects of neglecting the contribution of optical phase noise from the ML in SL. The frequency spectra show an almost flat profile at lower frequencies whatever the injections rate $(S_{inj})_0 / S_0$. Figure III.4 (a) is the main important case of intensity noise reduction. Indeed, we have a little more than 40dB reduction in the RIN spectrum compared to the free-running slave. Nevertheless, we pay attention to the choice of the physical parameter values by supposing that slave and master lasers can be almost identical and keeping the SCL linewidth narrow. Then, we restrict ourselves to work on these conditions: injection parameters are to be $S_{inj0} / S_0 \in]-4dB \ 45dB[$, and EGC in the ranges $]0 \ 0.88[$ and $]0.4 \ 0.99[$ for the ML and SL respectively. In these conditions, the bias current of the SL is greater than or equal to twice its threshold current. Exact values of the main parameters are given in the captions. When the master bias current is increasing, the RIN decreases. However, when that current reaches five times the threshold current (for a 40dB injection parameter) and ten times (for a -20 dB injection parameter) (see figures III.5 (a) and (b) respectively) or above, the stochastic dynamics of the slave change. The RIN and FN spectra become very interesting. We can observe clearly the gradual disappearance of the first relaxation peak. The intensity spectrum of the slave behaves almost identically to that of the ML (see figure (III.5)). That fact is supported by the SL frequency noise in figure III.6(a) where we also have the gradual disappearance of the first relaxation peak corresponding to the SL when $J_{inj} = 12 \times J_{inj_{th}}$ and in figure III.6 (b) for $\gamma = 0.45$. These observations indicate that the ML parameters and noise could lead to a drastic change in the characteristic of the SL noise spectrum.

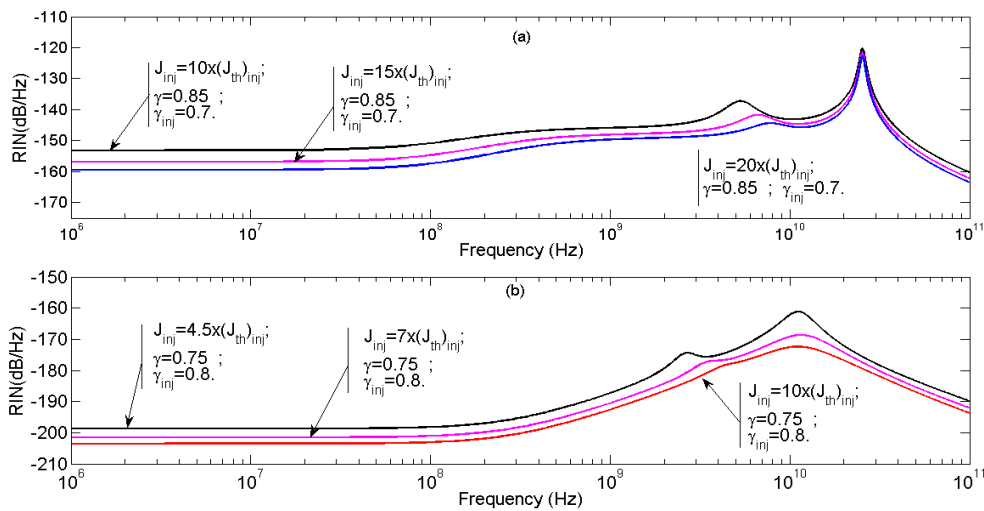


Figure III.5. Effects of increasing ML current on the slave RIN spectrum for the injection rates of (a) 40 dB and (b) -20 dB.

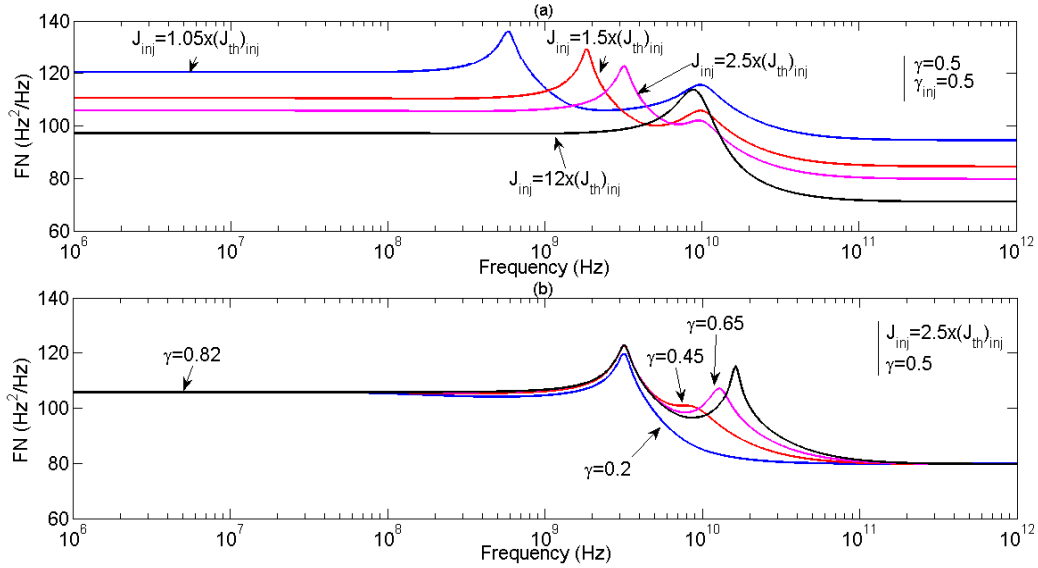


Figure III.6. Slave laser FN for (a) some values of current and (b) some values of EGC.

Figures III.7 and III.8 show the effect of EGC on the FN and RIN spectra when the ML and SL bias currents and other injection parameters are fixed. By increasing the EGC of the slave, the FN is reduced. Sometimes, if the master laser EGC becomes near unity, the master laser FN takes the lead and noise also becomes more intense in RFO (figure III.7 (a) for $\gamma = 0.3$; $\gamma_{inj} = 0.99$). Figure III.7 (b) presents the effect of the master laser EGC on FN when the slave laser EGC is fixed; it causes a reduction in FN when the master laser EGC is decreasing. When $\gamma_{inj} = 0.55$, whatever $\gamma > 0.3$, we have dual pronounced peaks in noise spectra (figure III.8 (a)). However, the level easily decreases at low frequencies and displays convergence after RFO by increasing EGC of the slave laser when EGC of the master laser is fixed (see figure III.8 (b)).

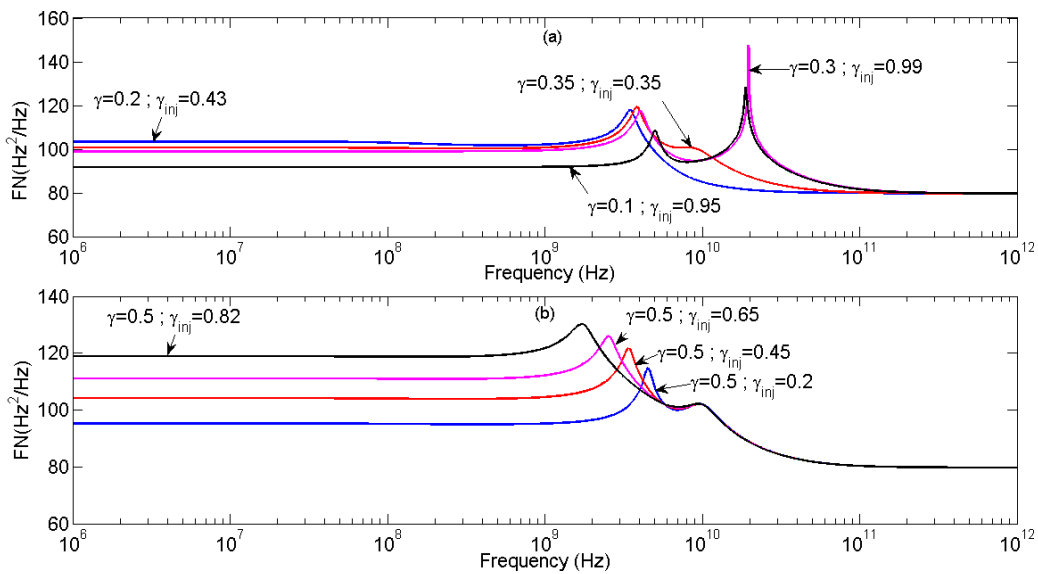


Figure III.7. Frequency variation of FN of the slave laser, with the following injection parameters: $\Delta\omega = -20\text{GHz}$, $k_{inj} = 1 \times 10^{-1}$, $S_0 = 10^{-2}(S_{inj})_0$, $J_{inj} = 2.5 (J_{inj})_{th}$ (a) when the master laser and slave laser EGCs change; (b) when the slave laser EGC is fixed.

The RIN and FN profiles show that stochastic behavior of the SL can be identical to that of a free-running laser or injected laser by the adapted choice of EGC values. Indeed for small variations of EGC, the RIN spectrum presents a very new particular stochastic dynamics: for $0.65 \leq \gamma \leq 0.69$, the profiles present dips at points A and B (see figure III.8 (b)) at low frequencies (before resonance), which are connected with the change of RIN sign observed in [12].

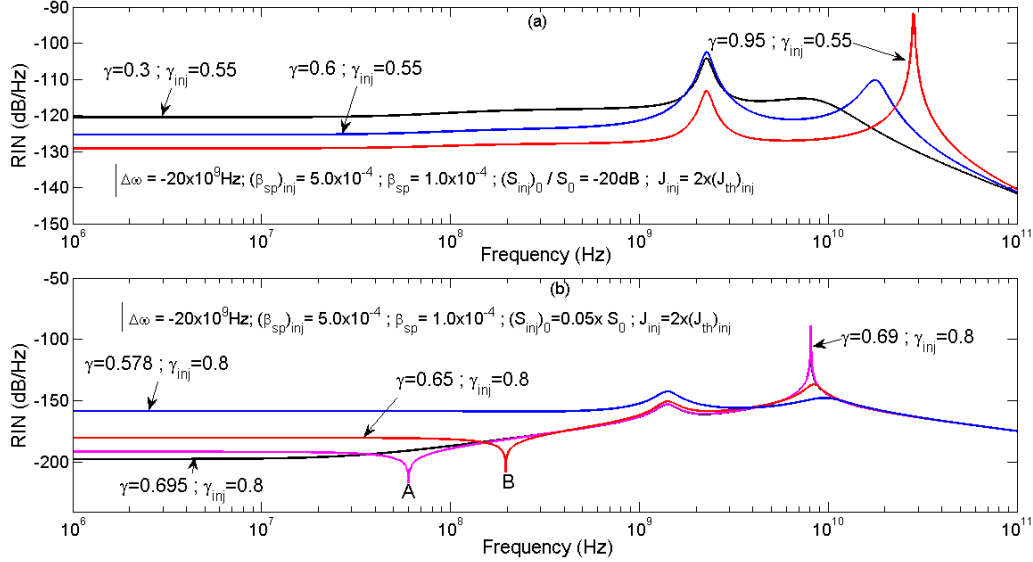


Figure III.8: Influence of EGC and other parameters on RIN. (a) When EGC of the master laser is fixed to 0.55; (b) when the EGCs of both ML and SL change

III.3. Stability Analysis of RTD-LD Integrated Systems

In previous Section III.2, we have reported a noise characterization in new modified rate equations of optical injection SCLs. Through EGC and other laser control parameters, it was proved that this model of lasers could be placed as a candidate for optoelectronic applications due to induced noise level modulation by the EGC and injection parameters. In this section, we use this OISCL monolithically integrated with a RTD in a setup a novel class of OEIC described in Section II.5 by Eqs. (II.38), for stability's analysis purposes and investigate the role of the EGC. In several investigations related to the RTD-LD integration, the nonlinearity of RTD have been widely modeled by mathematical representations of Brown or that of Schulman. In addition, polynomial models have also shown their great usefulness in NDR oscillators. The purpose of this section is to analysis of this innovate OEHO. We shall therefore provide a brief investigation of the stability analysis of this OEHO using Routh-Hurwitz criterion through eigenvalues and Lyapunov exponents' calculations.

III.3.1. Linear stability and Routh-Hurwitz criteria

This section uses Routh-Hurwitz criteria and the first Lyapunov method of eigenvalues for the purpose of stability analysis of the novel optoelectronic oscillator (II.38).

III.3.1.1. Steady states and phase locking regions

Steady states are starting points for the determination of stabilities properties of nonlinear dynamical system. In steady states solutions, this OEO operates with constant electrical and optical outputs. The steady-state solutions $(x_0, y_0, z_0, n_0, s_0, \psi_0)^T$ are obtained by setting the differential terms of equation (II.38) to zero as follows

$$m^{-1}[y_0 - f(x_0)] = 0 \quad (\text{III.38})$$

$$m[v_{dc} - ry_0 - x_0 + v_{ac} \sin(z_0)] = 0 \quad (\text{III.39})$$

$$\Omega_{in} = 0 \quad (\text{III.40})$$

$$\gamma_0 \left(\sigma y_0 - n_0 - \frac{n_0 - \delta}{1 - \delta} s_0 \right) = 0 \quad (\text{III.41})$$

$$2G_0\beta(n_0 - 1)s_0 + 2\gamma k \sqrt{s_0} \cos(\psi_0) = 0 \quad (\text{III.42})$$

$$\alpha G_0(n_0 - 1) - \gamma k \frac{1}{\sqrt{s_0}} \sin(\psi_0) - \Delta\Omega = 0 \quad (\text{III.43})$$

Solving (III.38)-(III.43), we obtained steady state for electrical voltage and current given by two implicit relations. Obviously Eq. (III.40) shows that the system (II.38) must be free to external AC excitation during the determination of steady-state solutions; $z_0 = 0$.

$$f(x_0) + x_0 - v_{dc} = 0 \quad (\text{III.44})$$

$$y_0 = f(x_0) \quad (\text{III.45})$$

So, knowing x_0 and y_0 , and solving equations (III.41)-(III.43), we obtain a cubic equation enabling the determination of LD carrier steady state n_0 in equation (III.46).

$$A_3(\Delta n_0)^3 + A_2(\Delta n_0)^2 + A_1(\Delta n_0) + A_0 = 0 \quad (\text{III.46})$$

The coefficients A_0 , A_1 , A_2 and A_3 are defined by

$$A_0 = -(\Delta\Omega)^2 (\sigma y_0 - 1) + \gamma^2 k^2, \quad A_1 = \frac{\gamma^2 k^2}{1 - \delta} + (\Delta\Omega)^2 + 2\alpha G_0 \Delta\Omega (\sigma y_0 - 1),$$

$$A_2 = -\alpha^2 (G_0)^2 (\sigma y_0 - 1) - \beta^2 (G_0)^2 (\sigma y_0 - 1) - 2\alpha G_0 \Delta\Omega, \quad A_3 = \alpha^2 (G_0)^2 + \beta^2 (G_0)^2.$$

with $\sigma = 1 / I_{th}$ and $\beta = 1 - \gamma$ is the mean of EGC [45].

The steady state for the photon density photon density are then given by the following equations

$$s_0 = (\sigma y_0 - n_0)(1 - \delta) / (n_0 - \delta) \tag{III.47}$$

$$\psi_0 = -\arctan(\alpha / \beta) + \sin^{-1} \left(-\Delta\Omega \sqrt{s_0} / \gamma k \sqrt{1 + (\alpha / \beta)^2} \right) \tag{III.48}$$

Since the stability of an OISCL is considered theoretically with an emphasis on the understanding of the locked phase [110], photon and carrier number curves for regions within and outside stable locking are presented on the EGC limits. From the relation $S(t) = (E_0(t))^2$, it is obvious that s_0 must always be a positive value i.e. $\sigma y_0 > n_0$. Numerical calculation of shows that this condition are satisfied if and only if the frequency detuning is less or equal to 2GHz i.e. $\Delta\Omega \leq 0.41952$. In addition, according to the boundary of sine function, the necessary condition for optical locking requires the following relation $\Delta\Omega = \pm (\gamma k / \sqrt{s_0}) \sqrt{1 + (\alpha / \beta)^2}$. For constant biased laser, is has been found in ref [46] that all the points situated in space $(\Delta\Omega, \pm \gamma k / \sqrt{s_0})$ inside two curves are in locking region.

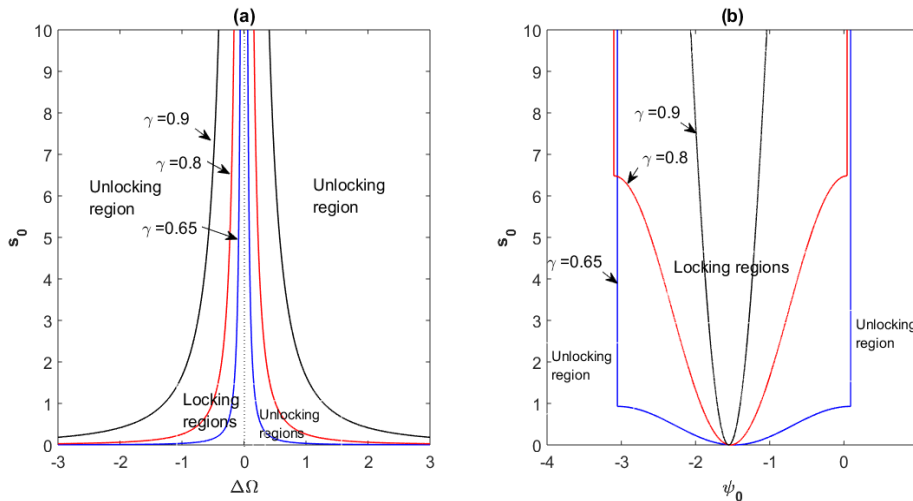


Figure III.9. (a) Unlocked and locked regions for $\gamma=0.65$, $\gamma=0.8$ and $\gamma=0.9$; (b) Range of fixed optical phase ψ_0 for $\Delta\Omega$ situated in locked region.

However, for the described driven OISCL, the condition $\Delta\Omega \leq 0.41952$ is added to insure that the photon number s_0 should be positive. Then possible locking regions can be found as presented in Figure III.9 (a), it is shown that the locking region extends when the EGC increases from a certain value.

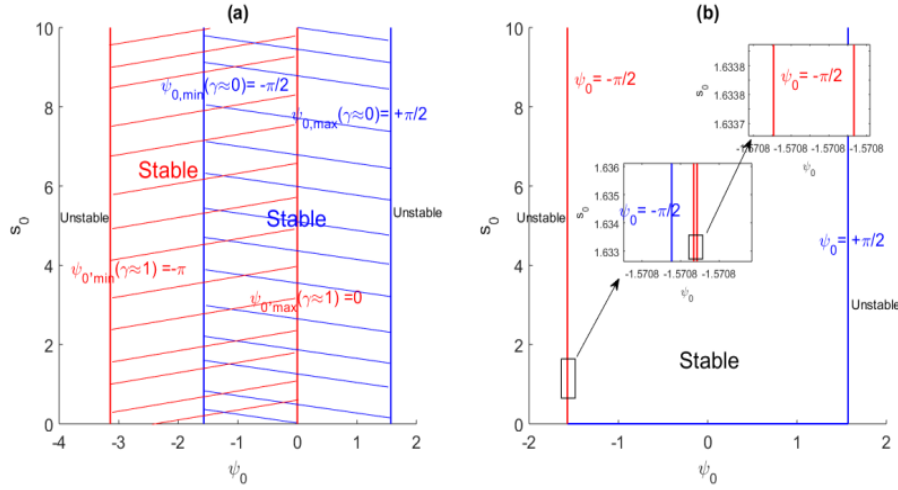


Figure III.10. The range of stable phases given by (III.47)-(III.48): (a) Under weak injection, stable phases regions are limited by pairs of curves inside $-\pi/2 < \psi_0 < \pi/2$ and $-\pi < \psi_0 < 0$ for the limits of EGC, $\gamma \approx 0$ and $\gamma \approx 1$ respectively. (b) Under strong injection, the boundary of stable phase is limited only by $-\pi/2 < \psi_0 < \pi/2$ blue and red lines correspond to $\gamma \approx 0$ and $\gamma \approx 1$ respectively.

From the figure III.9 (b), almost all possible values of ψ_0 are negative. That number should be larger as γ decreasing. In other hand, under weak injection strength $\psi_{0,\max,\min} = \pm\pi/2 - \arctan(\alpha/\beta)$. In addition, under strong injection $\psi_{0,\max,\min} = \pm\pi/2$. These results are similar to that in [111]. As $\beta = \gamma^{-1} - 1$, the stable phase condition at the boundaries of EGC γ will be such that, when $\gamma \approx 1$ and $\psi_{0,\min,\max}(\gamma \rightarrow 1) = -\pi$ or 0 . In figure III.10, different regions of stable phase for the limited cases of EGC values are plotted with accuracy by numerically solving of (III.47)-(III.48) under weak injection strength figure III.10 (a) and strong injection strength in figure III.10 (b).

III.3.1.1. Linear stability Analysis

We have already introduced the steady states points in the subsection II.3.1.1. Here, we consider the dynamics of the optoelectronic hybrid system governed by the set of normalized differential equations (II.38) in the form of equation (II.11). We treat the problem around the steady point by using the small signal analysis method. According to the Eq. (II.13), the relation (III.49) gives the Jacobian matrix of the system (II.33) at the equilibrium point. The function $f'(x_0) = B_0(3x_0^2 - 2(a+b)x_0 + ab)$.

$$J = \begin{bmatrix} -m^{-1}f'(x_0) & m^{-1} & 0 & 0 & 0 & 0 \\ -m & -mr & mv_{ac} & 0 & 0 & 0 \\ 0 & 0 & 0 & 0 & 0 & 0 \\ 0 & \gamma_0\sigma & 0 & -\gamma_0\left(1 + \frac{s_0}{1-\delta}\right) & -\gamma_0\left(\frac{n_0-\delta}{1-\delta}\right) & 0 \\ 0 & 0 & 0 & 2\beta G_0 s_0 & 2G_0\beta(n_0-1) + \frac{\gamma k}{\sqrt{s_0}}\cos(\psi_0) & -2\gamma k\sqrt{s_0}\sin(\psi_0) \\ 0 & 0 & 0 & \alpha G_0 & \frac{\gamma k}{2(s_0)^{3/2}}\sin(\psi_0) & -\frac{\gamma k}{\sqrt{s_0}}\cos(\psi_0) \end{bmatrix} \quad (\text{III.49})$$

The Routh-Hurwitz criterion leads the characteristic polynomial of the Eq. (III.49) to be in the form of Eq. (III.50).

$$E(\lambda) = \lambda \left(a_0\lambda^5 + a_1\lambda^4 + a_2\lambda^3 + a_3\lambda^2 + a_4\lambda + a_5 \right) \quad (\text{III.50})$$

In the following, we calculate the eigenvalues λ of J and interpret according to the systematic illustrations [85] in Figure II.7. Different results to determine the stability of the equilibrium point X_0 for given control parameters' values are gathered in Table III.1. Each equilibrium point has at least two complex-conjugate eigenvalues. For appropriate pick of control parameters, there exist stable fixed points. For instance, when the RTD is biased in PDR2, the whole system should be positive so that stable fixed points A_1 and A_2 on the Table III.1 have x_0 and n_0 values which effectively belong to the shrunk stable region too close to the line A on in Fig. III.11 (f). Therefore, it is obviously to point out that stable fixed points A_1 and A_2 belong to stable phase locking regions from Fig. III.9. In addition, for complex dynamical analysis study, three main control parameters have been used to control the whole stability of the system namely the DC voltage, the parameter r and the ECG. So, stable points are achieved when the RTD is biased in the NDR. In the other hand, the Eq. (III.51) gives the Hurwitz matrix associated to Eq. (III.50). In the same way, from the Routh-Hurwitz criterion, the equilibrium point X_0 is stable if and only if all the principal minors of (III.51) are positive. Since the coefficient $a_0 = 1$, (with the respect of notes in Chap. II, Eq. (II.17)), this implies the following Routh-Hurwitz criterion stable locked solutions condition Eqs. (III.51).

The implementation results of Eq. (III.52) in Maple software is given in Figure III.11. Note that, according to (III.52) the stable region corresponding to the frequency detuning in locking region

shall be given from voltage-carrier steady states ($x_0 - n_0$) as all states can be connected [Eqs. (III.43) - (III.48) and (III.50) - (III.52)].

$$H = \begin{bmatrix} a_1 & a_0 & 0 & 0 & 0 \\ a_3 & a_2 & a_1 & a_0 & 0 \\ a_5 & a_4 & a_3 & a_2 & a_1 \\ 0 & 0 & a_5 & a_4 & a_3 \\ 0 & 0 & 0 & 0 & a_5 \end{bmatrix} \quad (III.51)$$

$$\begin{cases} a_1 > 0 \\ a_1 a_2 - a_3 > 0 \\ a_1 a_2 a_3 - (a_1)^2 a_4 - (a_3)^2 + a_5 a_1 > 0 \\ a_1 a_2 a_3 a_4 - a_1 (a_2)^2 a_5 + 2 a_1 a_4 a_5 - (a_1 a_4)^2 - (a_3)^2 a_4 + a_2 a_3 a_5 - (a_5)^2 > 0 \\ a_5 > 0 \end{cases} \quad (III.52)$$

From Fig. III.11 (a) to III.11 (e) we illustrate the Routh condition for the first minor, the second minor, the third minor, the forth-minor and the fifth minor from the Hurwitz matrix (III.51) respectively. The figure III.11 (f) illustrates the superposition of aforementioned figures corresponding to all combined parts of Eq. (III.52). It is obvious to observe that, Fig. III.11 (f) does not display a wide intersecting region that satisfies Eq. (III.52). Nevertheless, it exists a shrunk region where the system has stable fixe points; this tiny region is circumscribed by a stability boundary denoted by the line **A** in figure III.11 (f). Thereby, the study reveals a shrunk area of the system from which nonlinear dynamics can be undertaken as attraction basin and a sea of points in which the system drops to instability.

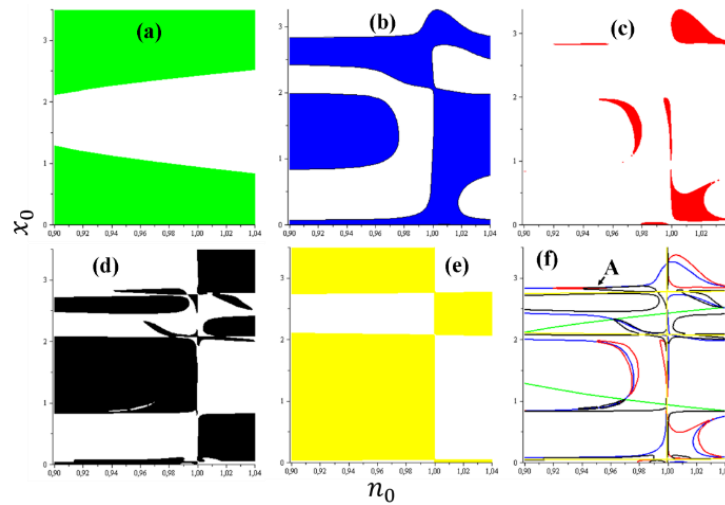


Figure III.11. Stability boundaries calculated from the Routh-Hurwitz stability criterion given by Eq.(III.52) for the first minor (a), the second minor (b), the third minor (c), the forth minor (d) and the fifth minor (e) of the Hurwitz matrix. The intersecting figure (f) shows that there exists a shrunk region which satisfies Routh conditions.

Table III.1. The equilibrium point and their stability evaluated from system typical control parameters values

Current-voltage region		Values of (r, γ)	Equilibrium point $(x_0, y_0, z_0, n_0, s_0, \psi_0)$	Type of equilibrium point $\lambda_i (i = 1, 2, 3, 4, 5 \text{ or } 6)$		
NDR	$v_{dc} = 1.2$	(9, 0.97)	(0.8489, 0.039011, 0, 7.647, 0.00024732, 1.5708)	$\lambda_{1,2} = 0.0641886 \pm 0.98513i$; $\lambda_3 = 0$; $\lambda_{4,5} = 6.2539 \pm 0.11939i$; $\lambda_6 = -0.10458$	Unstable focus	
	$v_{dc} = 2.37$	(9, 0.97)	(1.2648, 0.031829, 0, 6.24, 0.00014793, 1.5708)	$\lambda_{1,2} = 0.4276 \pm 0.7481i$; $\lambda_3 = 0$; $\lambda_{4,5} = 4.9301 \pm 0.157903i$; $\lambda_6 = -0.10446$	Unstable focus	
	$v_{dc} = 2.38$	(9, 0.97)	(2.3781, 0.00021143, 0, 0.0083898, 0.19646, -1.5708)	$\lambda_{1,2} = -0.0050058 \pm 0.97296i$; $\lambda_3 = 0$; $\lambda_{4,5} = -0.94053 \pm 0.08050596i$; $\lambda_6 = -0.06555$	Stable focus	
	$v_{dc} = 2.359$	(11.5, 0.95)	(2.3558, 0.00036306, 0, 0.037318, 0.25232, -1.5708)	$\lambda_{1,2} = -0.00023928 \pm 0.95598i$; $\lambda_3 = 0$; $\lambda_{4,5} = -1.5402 \pm 0.18637i$; $\lambda_6 = -0.043516$	Stable focus	
	$v_{dc} = 2.37$	(9, 0.976)	(2.3781, 0.00021143, 0, 0.008407, 0.19638, -1.5708)	$\lambda_{1,2} = -0.0050058 \pm 0.97296i$; $\lambda_3 = 0$; $\lambda_{4,5} = -0.79592 \pm 0.27131i$; $\lambda_6 = 0.022979$	Unstable Focus	
		(9, 0.9)	(2.3781, 0.00021143, 0, 0.008407, 0.19638, -1.5708)	$\lambda_{1,2} = -0.0050058 \pm 0.97296i$; $\lambda_3 = 0$; $\lambda_{4,5} = -0.96952 + 0.24848i$; $\lambda_6 = -0.0075571$	Stable focus	
		(9, 0.8)	(2.3781, 0.00021143, 0, 0.008407, 0.19638, -1.5708)	$\lambda_{1,2} = -0.0050058 + 0.97296i$; $\lambda_3 = 0$; $\lambda_{4,5} = -6.8153 + 0.087472i$; $\lambda_6 = -0.072172$	Stable focus	
		(9, 0.65)	(2.3781, 0.00021143, 0, 0.0074539, 0.20071, -1.5708)	$\lambda_{1,2} = -0.0050058 \pm 0.97296i$; $\lambda_3 = 0$; $\lambda_{4,5} = -13.015 + 0.057095i$; $\lambda_6 = -0.07251$	Stable focus	
	PDR2	$v_{dc} = 2.8$	(6.68, 0.5)	$A_1 = (2.7664, 0.0050225, 0, 0.92163, 0.069603, -1.5708)$	$\lambda_{1,2} = -0.72469 \pm 0.83547i$; $\lambda_3 = 0$; $\lambda_4 = -0.37477$; $\lambda_5 = -1.2257$; $\lambda_6 = -1.7413$	Stable focus
			(6.68, 0.8)	$A_2 = (2.7664, 0.0050225, 0, 0.92067, 0.07074, -1.5708)$	$\lambda_{1,2} = -0.72469 \pm 0.83547i$; $\lambda_3 = 0$; $\lambda_4 = -0.901153$; $\lambda_{5,6} = -0.15062 \pm 0.47136i$	Stable focus

III.4. Dynamics of RTD-OISCL Systems

This section is devoted to the study of dynamical behavior of the novel RTD-LD integrated circuit (II.38). The normalized system is numerically solved using MATLAB and RK4 method. Phase portraits shall be sets of projections of the space variables $(x, y, n, s, \psi)^T$ in the 2D and/or 3D. The LE calculation is performed by using a program of Wolf et al. [98]. We will achieve the route to chaos and chaos control for specific control parameters using a collection of bifurcation diagrams. Phase portraits will show the occurrence of strange attractors. Moreover, we shall use bifurcation diagrams to control chaos. In addition, we shall treat the system (II.38) in term of fast-slow system and investigate the rate of timescale system in order to discuss the ratio of slow and fast timescales parameter.

III.4.1. Bifurcation Diagrams and Route to Chaos

The SCL in Eq. (II.38) being perturbed by an external periodic AC voltage with frequency f_{in} and an optical injection signal characterized by the injection strength parameters k_{inj} , γ or S_{inj} according to semiconductor LD here used model, we propose to use an RTD driver oscillator parameter f_{in} and the laser EGC parameter γ as control parameters the OEO (II.38). The Fig. III.12 plots bifurcation diagrams of LD driving current corresponding to normalized current; $y(t)$ parameter (Fig. III.12 (a)) and photon density in Fig. III.12 (b) with the variation of f_{in} respectively. It is found that these bifurcation diagrams present chaotic regions separated by quiescent regions when f_{in} is moving from around 0GHz to 2.35GHz maintaining the EGC constant at 0.5, $V_{dc} = 1.145 V$ and $V_{ac} = 150mV$. Chaotic regions are known as unsynchronized windows and quiescent regions describe a possible synchronization between driving current and laser emission corresponding to period-n oscillations [112]. It is also found that the nature of driving current is emulated by laser photon number through accurate replications of different windows corresponding to bifurcation diagrams in frequency domain. Therefore, we also highlight this fact using series evolutions stood for Figure III.16. The bifurcation diagram of laser output with increasing EGC is presented in Figure III.13 for $f_{in} = 1.3GHz$. According to certain values of EGC as depicted in Figure III.13, it is clearly shown that the laser evolves from chaotic dynamical behavior for $\gamma \leq 0.37$ to periodic orbits. For instance, when γ equal to 0.4, 0.6 or near 0.8 as presented by zooming in Figure III.13 and far near to 0.97 EGC values. However, there are narrower chaotic regions between periodic windows. According to bifurcation diagrams in Fig. III.12 and Fig. III.13, the parameters f_{in} and the EGC γ can be used as to control chaotic dynamics.

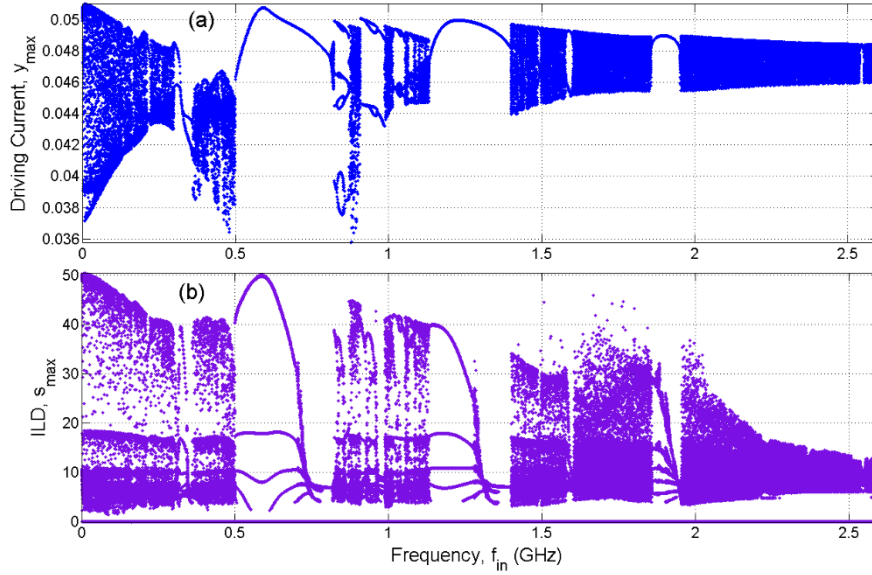


Figure III.12. Bifurcation diagrams of laser driving current (a) and photons density (b) versus external frequency f_{in} showing the replication of chaotic and nonchaotic regions when EGC γ is fixed to **0.5**, $V_{dc} = 1.145$ V and $V_{ac} = 130$ mV.

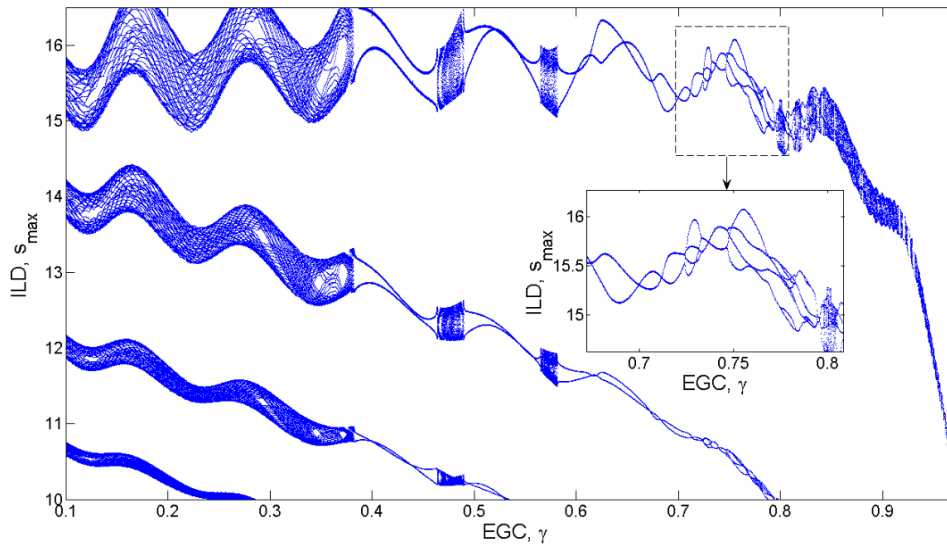


Figure III.13. Bifurcation diagram of photons density $s(t)$ when effective gain coefficient γ is varying $\gamma \in [0.1, 0.99]$, for $k_{inj} = 2 \times 10^{-3}$, $V_{dc} = 1.145$ V and $V_{ac} = 180$ mV, $f_{in} = 1.3$ GHz and $\Delta\omega = 2$ GHz.

In addition, bifurcation diagrams depicted in Figure III.14 show that the amplitude of the periodic perturbation V_{ac} also allows the control of chaos. Therefore, various dynamics that bifurcation diagrams reveal leads to choose f_{in} , γ and V_{ac} like control parameters whose numerical values are given on different captions.

When the parameter r is used as bifurcation parameter varying from 5 to 7, the bifurcation diagram of the electronic output $x(t)$ and optical output $s(t)$ in Figure III.15 (a) and (b) display the Feigenbaum scenario namely: period-2, period-4, period-8 oscillations to chaos. By increasing the

parameter r , system (II.38) undergoes a cascade four-period-doubling bifurcation to chaos for $5.6 \leq r \leq 5.82$. By further increasing the parameter r from 6 to 6.3, the system evolves from a reverse cascade four-periods doubling bifurcation to period-2 oscillations. In $6.3 \leq r \leq 6.45$ window, we observe chaos and at least eight-periods doubling to chaos and reversely. A period-1 oscillation occurs beyond $r \approx 6.7$.

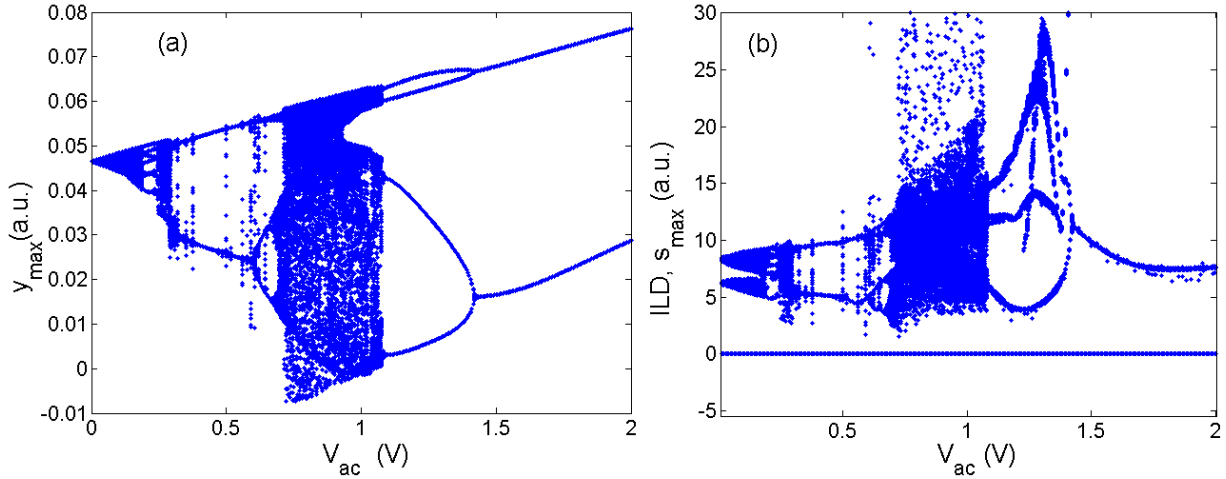


Figure III.14. The bifurcation diagram of the driving current (a) and the laser normalized photon number (b) when the parameter V_{ac} is varying from 0 to 2V both at bias of 1.145V, with $f_{in} = 1.5\text{GHz}$, when the laser diode operating without frequency detuning and with $\gamma = 0.75$ and $k_{inj} = 0.001$.

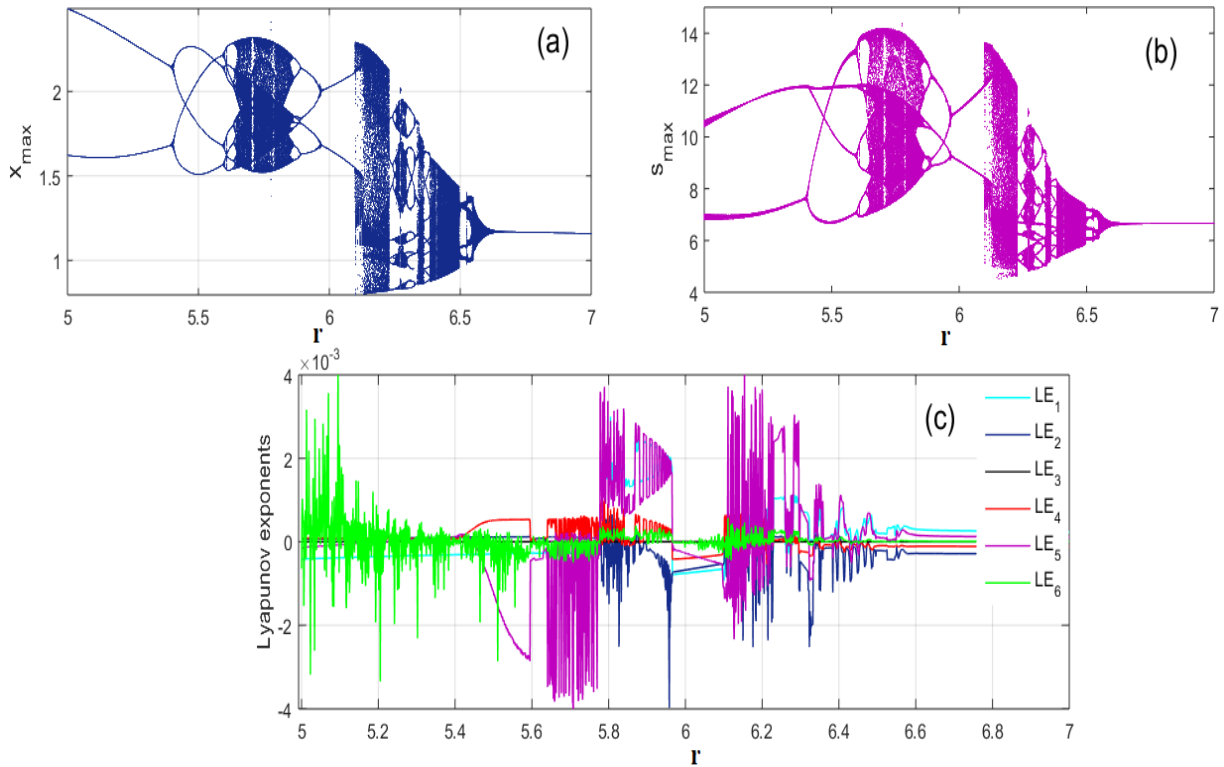


Figure III.15. Bifurcation diagram of photons density $s(t)$ when effective gain coefficient γ is varying $\gamma \in [0.1, 0.99]$, for $k_{inj} = 2 \times 10^{-3}$, $V_{dc} = 1.145\text{V}$ and $V_{ac} = 180\text{mV}$, $f_{in} = 1.3\text{GHz}$ and $\Delta\omega = 2\text{GHz}$.

The corresponding **LEs** spectrum is plotted in Figure III.15 (c) and one can observe two major windows of resistor values ($5.8 \leq r < 6$ and $6.1 < r < 6.6$) corresponding to the generation of hyperchaos with at least two positive **LEs**.

Electro-Optical Conversion and Limit Cycles

In **OEOs**, the driving oscillatory current $I(t)$ information is converted into optical output via the laser in order to be coupled to conventional channel such as optical fiber until its extraction at the receiver.

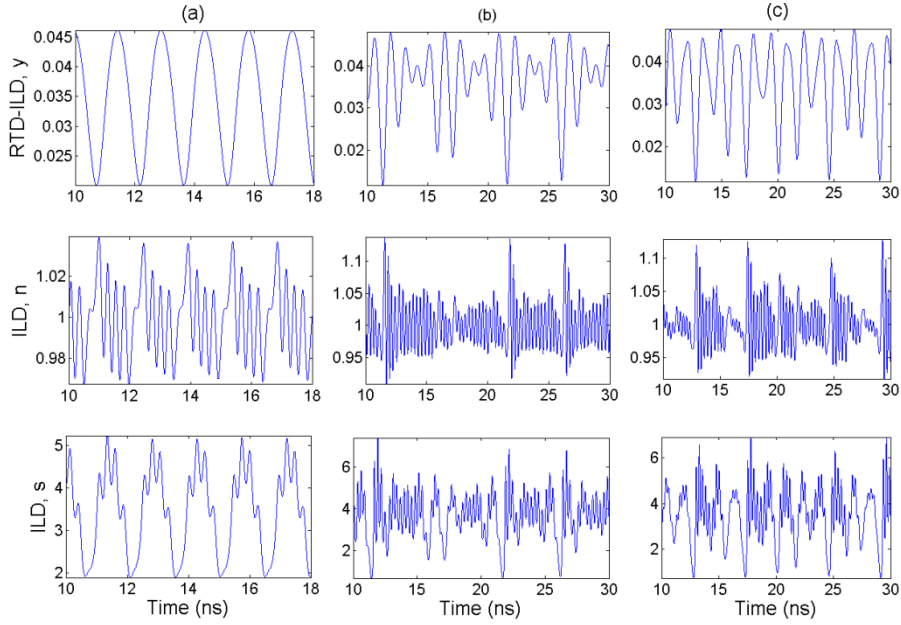


Figure III.16. Time series analysis for electrical driving current (top panels) laser carrier density (middle panels) and optical output (lower panels) when RF perturbed ($V_{ac} = 100 \text{ mV}$). The laser exhibits relaxation oscillations without AC perturbation (a) and chaotic signals adding AC voltage (b) and (c). Nevertheless, it always attempts to emulate driving current time repetitions.

In Figure III.16, time series evolutions of driving current and optical outputs are presented when **EGC** is fixed to 0.65, without frequency detuning, for $k_{inj} = 0.0078$, $V_{dc} = 1.145 \text{ V}$ and $V_{ac} = 120 \text{ mV}$, in addition for certain values of f_{in} mainly $f_{in} = 0 \text{ GHz}$ (Fig. III.16 (a)), $f_{in} = 0.42 \text{ GHz}$ (Fig. III.16 (b)), and $f_{in} = 1.9 \text{ GHz}$ (Fig. III.16 (c)). It appears conspicuous to observe for laser emissions, carriers and photons evolutions emulate the driving current (y variable), confirming the earlier mentioned fact that the **RTD** current waveforms directly modulate the **OISCL** even when laser outputs are chaotic (Fig. III.16 (b) and (c)). The emulation phenomenon means that **LD** rationally converts electrical signal into optical signal.

With particular values of injection and **AC** voltage excitation, corresponding to injection strength $k_{inj} = 2 \times 10^{-3}$ for frequency $f_{in} = 1.3 \text{ GHz}$, at $V_{dc} = 1.145 \text{ V}$ bias, we reproduce some dynamical behaviors of the **LD** through phase portraits limit cycles in Figure III.17 for certain

values of EGC, namely $\gamma = 0.99$, $\gamma = 0.9$, $\gamma = 0.75$, $\gamma = 0.4$, $\gamma = 0.3$ and $\gamma = 0.25$. We notice that a period-1 oscillation occurs when $\gamma = 0.99$ and a period 2 close $\gamma = 0.9$. When EGC $\gamma = 0.75$ and $\gamma = 0.4$, the laser displays a period 3 and a period-6 attractors respectively. The dynamics becomes chaotic as long as γ is decreasing from 0.41 to 0.1. According to the bifurcation diagram depicted in Fig. III.13, we clearly observe the chaos control in laser oscillations in Fig. III.17. In these conditions, γ -variations carry away a route to chaos like those displayed in certain optical feedback systems.

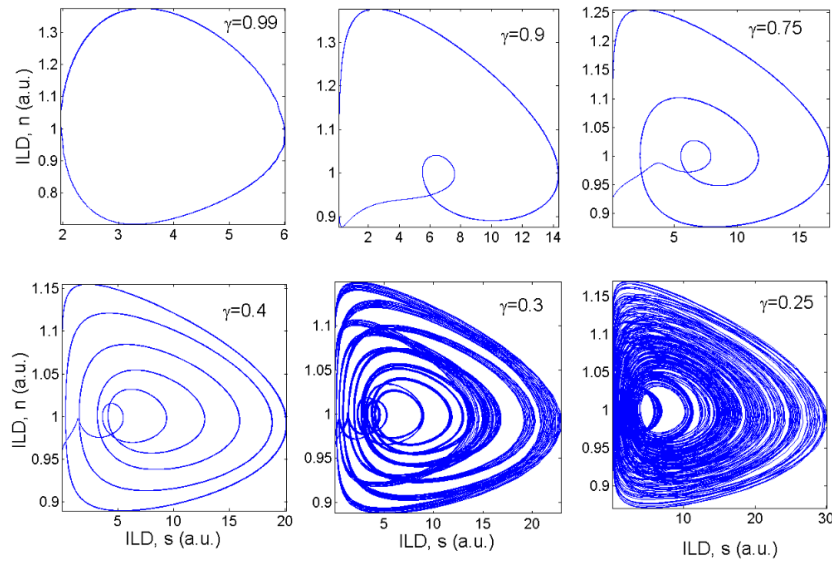


Figure III.17. Limit cycles of the driven semiconductor laser in photon-carrier (s-n) for different values of EGC γ when $\Delta\omega = 2$ GHz, $k_{inj} = 2 \times 10^{-3}$ at the amplitude voltage equal to 180 mV. The laser behaves like semiconductor laser with optical feedback.

III.4.2. Chaotic multiscroll, infinite scroll and Simulink implementation

There is not, nonchaotic systems that can exhibit multiple scrolls or infinite scroll attractors. Multiscroll attractors can be found either the system is chaotic or hyperchaotic. Especially, the multiple scroll chaotic/hyperchaotic systems with more than single-scroll or double-scroll attractors present more complex dynamical behavior with potential applications in engineering [113], [114] and fields such as encryption chaos, secure communication, neural network and laser design [113]. Higher numbers of scroll or infinite-scroll systems have infinitely many saddle equilibrium due to trigonometric functions implied onto their equations. If the number of scroll depends to calculating time, the system is classified as infinite-scroll system. Nowadays, very few works are devoted to study infinite-scroll system. For example, Sachin Bhalekar has proposed a complex pendulum equation [115] that exhibits infinite-scroll attractor and F. Li and C. Yao use jerks system circuits to generated hyperchaotic attractors with very higher number of scroll or infinite-scroll [116].

III.4.2.1. Generation of multiscroll chaotic attractors

Here, the frequency detuning shifts from 2GHz to 30GHz, while other parameter values are constant as from Fig. III.17. The LD outputs strange attractors values of EGC as presented in Figure III.18. A paramount result of this coupled system the emergence of novel multiscroll chaotic attractors rarely observed in semiconductor lasers dynamics which appear through a scenario of 2-period attractor, 3-period attractor and multiscroll chaotic attractor in the photon-carrier phase plane by decreasing the EGC. In Fig. III.18 (b), we stand for the 3D projection (s, n, ψ) of a multiscroll attractor near to the upper limit value of EGC ($\gamma = 0.099$).

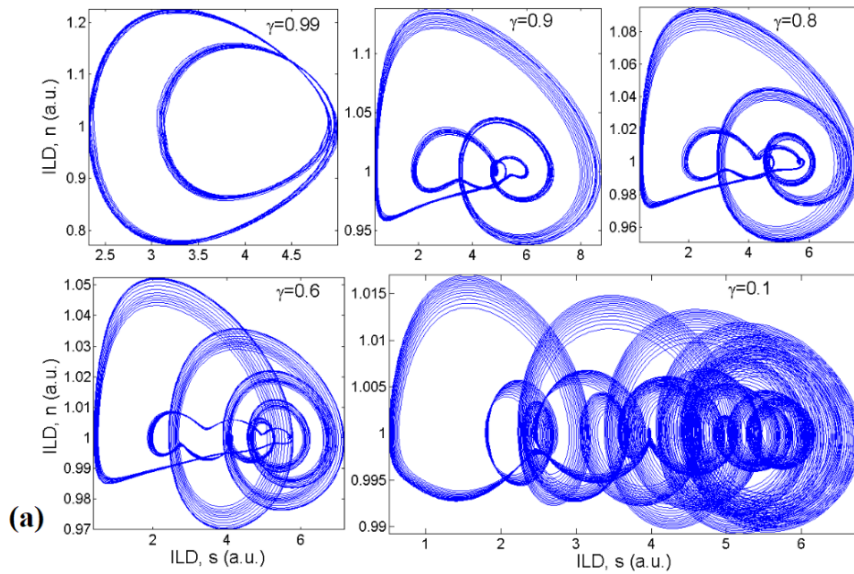


Figure III.18. (a) Birth of multiscroll chaotic attractors in s-n phase plane of LD from period-2 attractor ($\gamma = 0.99$), period-3 attractor ($\gamma = 0.9$) period-4 attractor ($\gamma = 0.8$), period-5 chaotic attractor ($\gamma = 0.6$) to multiscroll chaotic attractors ($\gamma = 0.1$ and $\gamma = 0.099$) and (b) 3D phase portrait of multiscroll chaotic attractors for $\gamma = 0.099$, when $\Delta\omega = 30$ GHz.

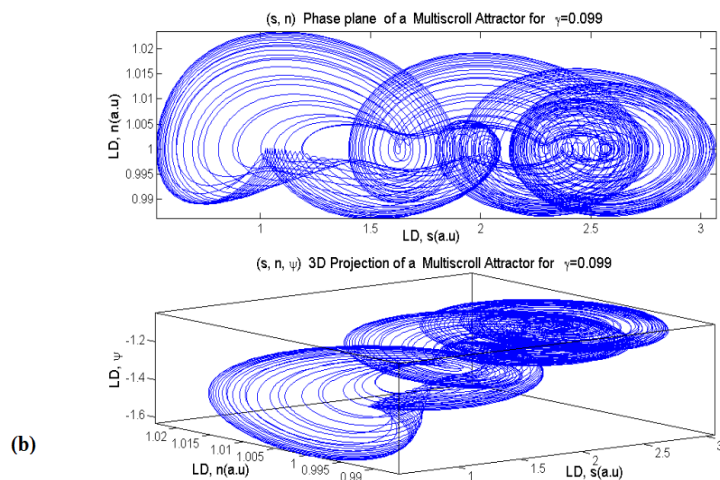


Figure III.18 (End). (b) 3D phase portrait of multiscroll chaotic attractors for $\gamma = 0.099$, when $\Delta\omega = 30$ GHz.

III.4.2.2. Infinite scroll and Simulink implementation of RTD-LD oscillator

In this section, we furthermore use the RK4 method in the system (II.38) to generate the infinite scroll attractor and verify its effectiveness using MatLab/Simulink implementation. We set the

parameters as $m = 0.0264$, $r = 6.65$, $\gamma = 0.68$, $\sigma \approx 196$, $\delta = 0.1512$, $v_{dc} = 1.145$ and $v_{ac} = 0.1441$; the system (II.38) being under relative strong external optical injection $k = 0.020637$. We choose the normalized time varying. After an initial transient, the solution settles into irregular a non-periodic oscillation that never repeats exactly in time. The trajectories in phase diagram when the optical phase $\psi(t)$ is plotted against the carrier density $n(t)$ in Fig. III.19 show that, an attractor which the number of scroll that increases while the calculating time increasing. The optical phase values upgrade and the number of attractor scrolls infinitely grows. With this framework, the system depicts two-scroll attractor in Fig. III.19 (a) for ($t=1,000$), five-scroll attractor Fig. III.19 (b) for ($t=3,000$) and forty one-scroll attractor in Fig. III.19 (c) for ($t=20,000$). We notice that scrolls are interspersed to laminar phases that firstly appear after the fifteen scroll, as the time evolves they erratically appear and after a relative long time their appearance becomes flat before falling again. This aforementioned study proves that it refers to a so-called an infinite-scroll chaotic attractor therein the number of generated scrolls depend to time calculation and the non-periodic reproduction of infinite-scroll as the time evolves in regard to laminar phases. Therefore, the system (II.38) generates an infinite-scroll attractor. Indeed, the transformation $M(x_0, y_0, z_0, n_0, s_0, \psi_0) \rightarrow M(x_0, y_0, z_0, n_0, s_0, \psi_0 + 2k\pi)$ is an invariant in this system since trigonometric functions involved in optical phase give rise to infinitely many equilibrium points that provide infinite-scroll attractor. Here, where $k = 0, \pm 1, \pm 2, \pm 3, \dots$). Nowadays, infinite-scroll attractor is not mostly reported in nonlinear dynamical systems for the best knowledge of the authors.

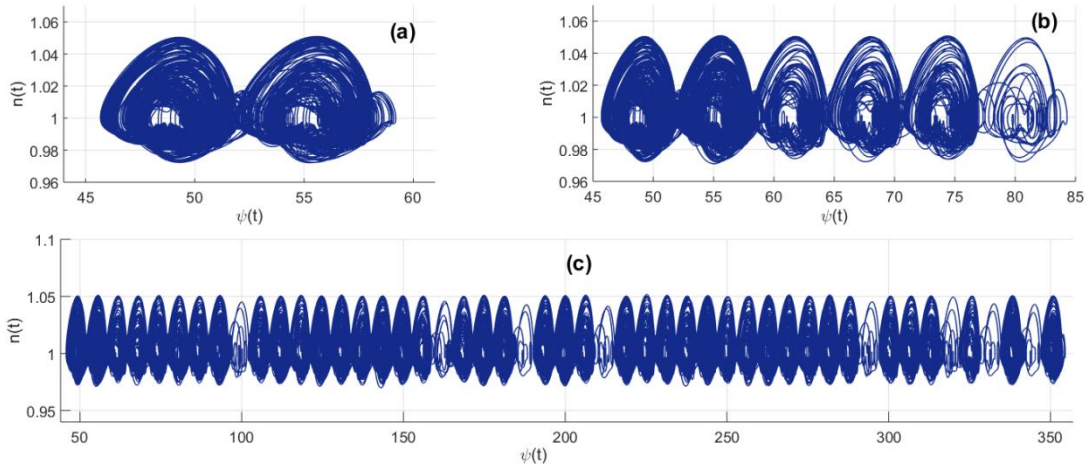


Figure III.19. The formation of infinite-scroll attractor: (a) Two-scroll attractor ($t = 1,000$), (b) Five-scroll attractor ($t = 3,000$) and (c) Forty one-scroll attractor with eight laminar phases ($t = 20,000$).

We recall in addition that, according to refs. [117] and [118], the number of scroll increases the complexity of the systems; it is useful that this number be stabilized to a fixed number. This fact is possible to be carried out by choosing $\gamma > 0.68$ when others parameters are fixed as indicated

above or by decreasing the optical injection parameter k . Let us mention in addition that, the chaotic behavior of the infinite-scroll attractor is confirmed in respect to the frame of Lyapunov exponent dynamics. As depicted in Fig. III.20, we have at least one positive LE; so, the infinite-scroll attractor generated by the system (II.38) is chaotic.

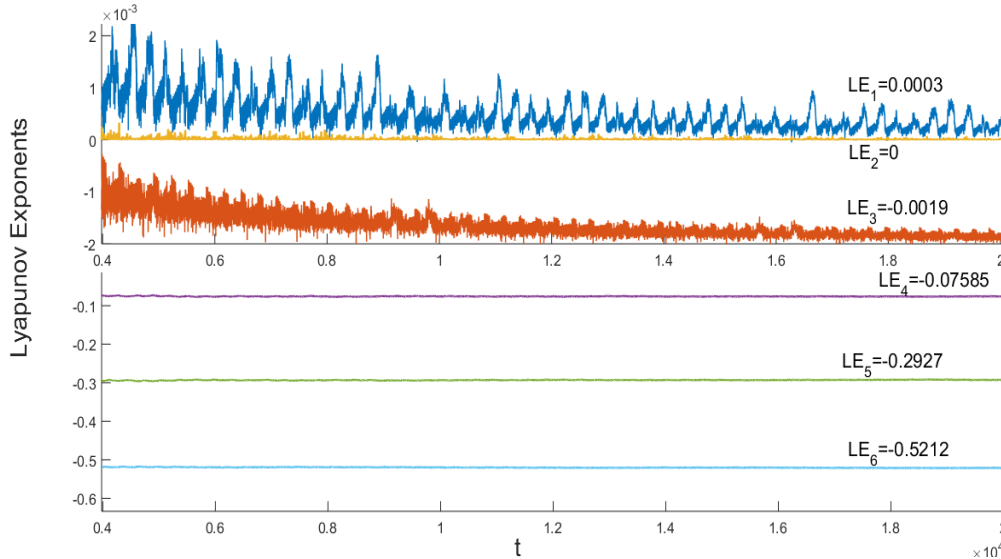


Figure III.20. Lyapunov exponents’ dynamics of infinite-scroll of system (4.9) with the same fixed parameters as in Fig. III.17

The Simulink implementation is used in addition in normalized system (II.38). A complex scheme, resulting from this system is designed in a chip simply by selecting essentially small building blocks of Simulink such as multipliers, gains, summations, constants, functions and integrators is depicted in Fig. III.21. The behavior of (II.38) through Simulink scheme is investigated for same parameter values as in Fig. III.19 approves the formation and the effectivity of the infinite scroll chaotic attractor in the plane from XY Graph3 is depicted in Fig. III.22 (a) showing a three scroll attractor for $t=2,226$, a four scroll for $t=2,410$, a five scroll attractor for $t=3,000$ and a six scroll attractor for $t=3,360$ in Fig. III.22 (ii) to (iv) respectively. In addition, the number of scrolls generated increases by the time of implementation. The Simulink observations confirm the RK4 numerical simulation results and the effectivity of generating the infinite scroll attractor. In addition, Fig. III.22 (b), (c) and (d) depict the current-voltage, the light-voltage (optoelectronic) and the carried-photon projection of the chaotic attractors respectively.

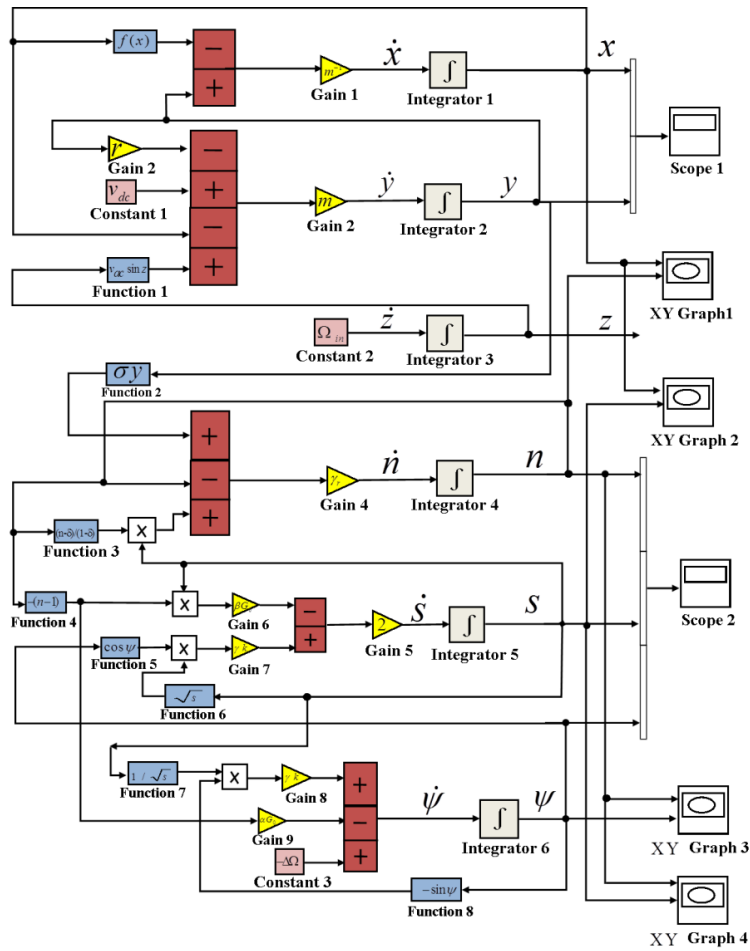


Figure III.21. Simulink implementation scheme of RTD-LD hybrid optoelectronic oscillator.

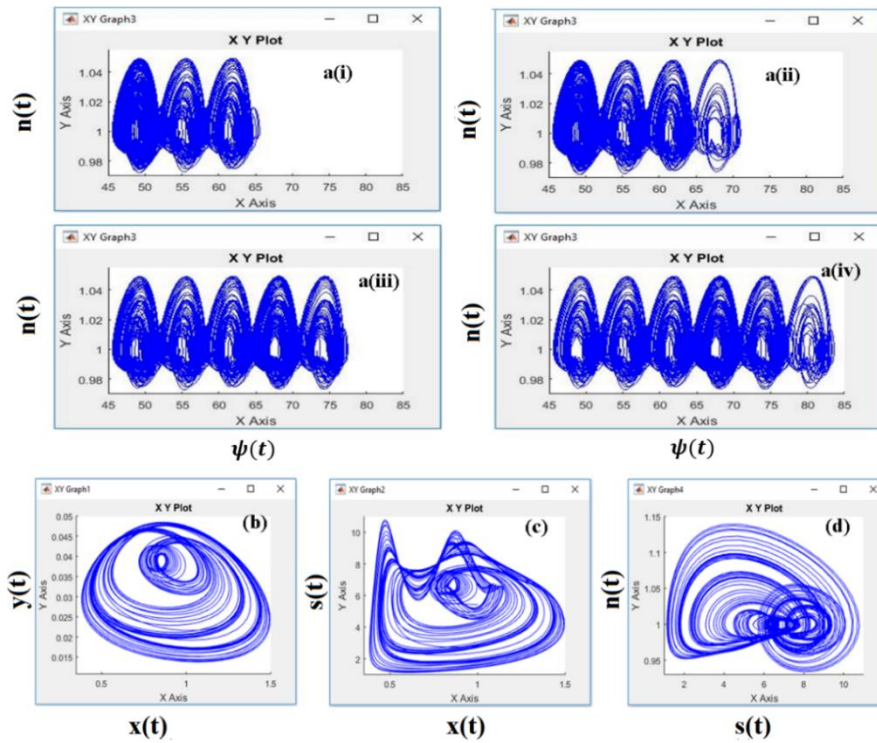


Figure III.22. (a) Simulink observations referring to formation of Infinite-scroll attractor: the projection on $\psi - n$ plane from XY Graph3 given for the simulating time show three-scroll a(i) $t = 2,226$, four-scroll

a(ii) $t = 2,410$, five-scroll a(iii) $t = 3,000$ and six-scroll a(iv) $t = 3,360$ attractors. Projections of chaotic attractor from Simulink simulation in (b) current-voltage,(c) light-voltage and (d) carrier-photons plane from XY Graph1, XY Graph2 and XY Graph4 respectively when $r = 6.65$, $\gamma = 0.7$, $v_{dc} = 1.145$, $v_{ac} = 0.1441$ and $k = 0.020637$.

Influence of the RTD I-V areas in the dynamics

Throughout the previous section, areas between the RTD current-voltage characteristic and the V-axis i.e. S_1 and that above i.e. S_2 were chosen to be almost equal. Here, we shall compare the dynamical behaviour of the system for three different cases; when $S_1 \approx S_2$, $S_1 < S_2$ and $S_1 > S_2$. It is important to show the function $F(V) = BV(V - a)(V - b)$ has an invariance by changing a-parameter to b-parameter. The Figure III.23 depicts different shape of RTD V-I $S_1 \approx S_2$ in Fig. III.23 (a), $S_1 < S_2$ in Fig. III.23 (b) and finally when $S_1 > S_2$ in Fig. III.23 (c). We use in addition the EGC γ as bifurcation parameter in order to magnify the influence of the areas S_1 and S_2 in the system (II.38). When $S_1 \approx S_2$, the Fig. III.24 (a) shows that the complexity of (II.38) decreases while γ is increasing. For instance, the laser exhibits a three-scroll chaotic attractors for $\gamma = 0.6$ in Fig. III.24 a(i), two-scroll attractor for $\gamma = 0.75$ in Fig. III.24 a(ii), and fails down unto one-scroll attractor for $\gamma = 0.9$ in Fig. III.24 a(iii). However, in the case $S_1 < S_2$ we can observe relaxation dynamics for $\gamma = 0.6$ in Fig. III.24 b(i), a non-oscillatory dynamics for $\gamma = 0.75$ in Fig. III.24 b(ii), and crisis when $\gamma = 0.9$ in Fig. III.24 b(iii). When $S_1 > S_2$, the system generates merely periodic limit cycles whatever the value of the EGC γ as depicted in Fig. III.24 c(i), Fig. III.24 c(ii) and Fig. III.24 c(iii).

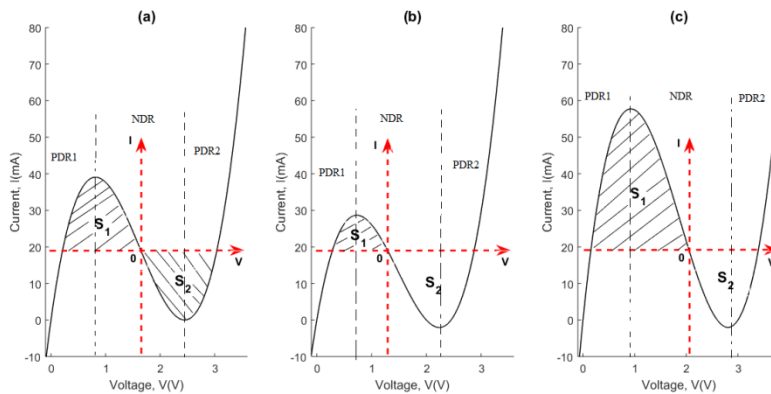


Figure III.23. Current-voltage (I-V) characteristics of RTD corresponding to $S_1 \approx S_2$ (a), $S_1 < S_2$ (b) and $S_1 > S_2$ (c).

We have found important to highlight that as one of the area S_1 gradually increasing the system evolves from chaos to periodic dynamics as depicted from Fig. III.24 (a) and Fig. III.24 (d). Nevertheless a more careful observation of Fig. III.23 reveals that the overall shape of RTD

current-voltage characteristics is not changed but everything suggests that a shift in the axes has occurred.

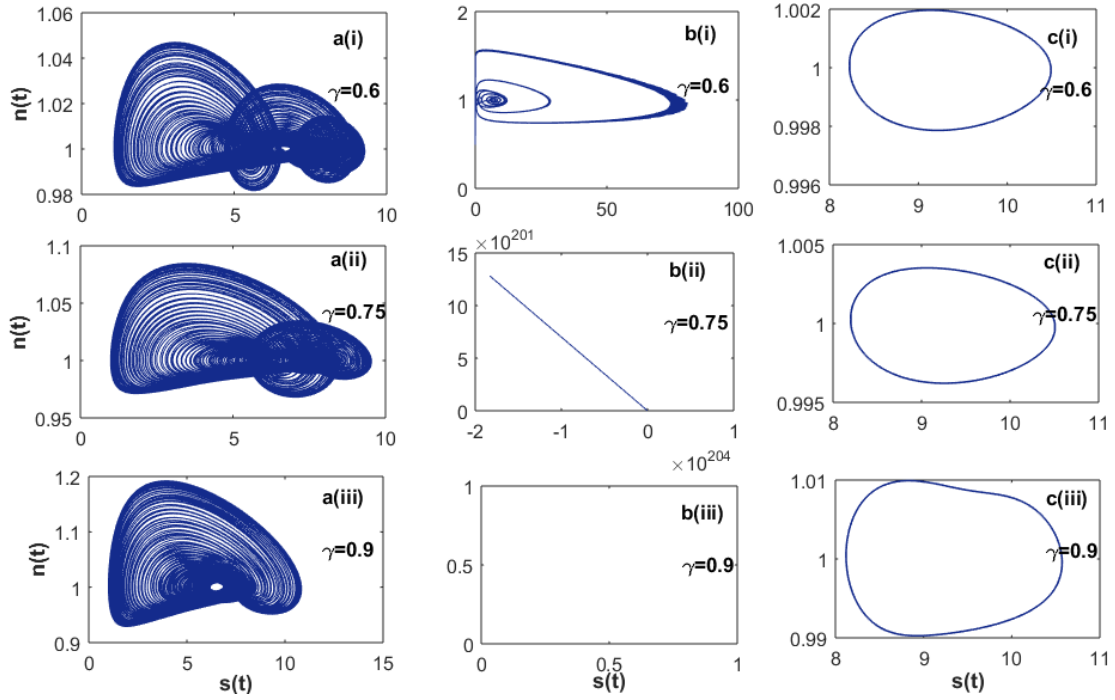


Figure III.24. Influence of areas of RTD current-voltage (I-V) characteristics on driven laser dynamics values of the EGC. a-When $S_1 \approx S_2$: a(i) Three-scroll chaotic attractor, a(ii) Two-scroll attractor and a(iii) One-scroll attractor. b- When $S_1 < S_2$: b(i) relaxation dynamics, b(ii) non-oscillatory dynamics and b(iii) crisis. c- When $S_1 > S_2$, the system generates periodic limit cycles whatever the value of γ : c(i), c(ii), and c(iii).

Therefore, interestingly the voltage biased and other system parameters could be adjusted to get a desired dynamics such as chaos, hyperchaos or periodic oscillations resulting from each of the investigated cases namely $S_1 \approx S_2$, $S_1 < S_2$ and $S_1 > S_2$ according to the threshold characteristics of the semiconductor laser. For instance, the bifurcation diagram shows that periodic and aperiodic oscillations occur in electrical current in Fig. III.25 (a), and in optical output given by Fig. III.25 (b) if the system is biased in the NDR of the RTD.

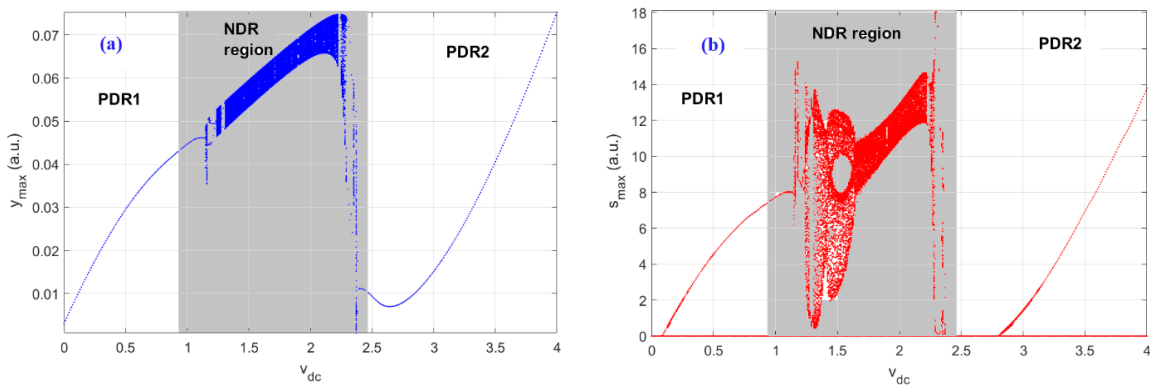


Figure III.25. DC bias control of system dynamics (1): (a) and (b) bifurcation diagrams of electrical driving current and optical output, respectively

When the DC bias is beyond the NRD region i.e. onto one of the PDR1 or PDR2, the dynamical behavior becomes periodic. However, the system could exhibit either slight chaotic or periodic windows in NDR region. This sticks out the relevance of DC polarisation on the chaos control in optoelectronic systems [119].

Antimonotonicity and Chaos Control

One of the most common chaos scenario have been shown to be period-doubling cascades. In most chaotic systems, this phenomenon appears without its destruction [120]. This phenomenon has been reported in many literatures, such as VdP oscillator, Duffing oscillator, Chua circuit, a fourth-order nonlinear autonomous hyperchaotic RLC circuit, Jerk systems [121, 122]. In this section, we will demonstrate that the system (II.38) generates the creation of period doubling cascade to chaos followed by their annihilation via period-doubling bifurcation. This property is an interesting phenomenon in nonlinear dynamics termed by antimonotonicity and no observed in most nonlinear systems. Fig. III.26 pictures magnified views of bifurcation diagrams in a tin region of the NDR region of the RTD the smooth variations of two control parameters in the $v_{dc} - r$ space. As the DC voltage bias is increased in approximatively, $2.30 < v_{dc} < 2.36$ the phenomenon of antimonotonicity is created. For specific parameters v_{dc} and r , sample results are provided as follows. A period two (P-2) exists in the in the NDR for $v_{dc} = 2.33$. In particular, as the DC voltage is further increased, P-4 bubbles is created for $r = 9$ [see Fig. III.26 (a)], P-8 bubbles is obtained for $r = 8$ [see Fig. III.26 (b)], P-16 bubbles is obtained for $r = 7.5$ and P-32 bubbles is created for $r = 7.4$ [see Fig. III.26 (c) and (d)], respectively]. For $2.335 < v_{dc} < 2.3425$, this period doubling can be destroyed via reverse period-doubling bifurcation sequence as the bifurcation parameter and the system fails in P-2 dynamics for $v_{dc} = 2.36$ for example. In addition, as the parameter r is decreased smoothly, the dynamics of the system becomes more and more complex so that P-32 bubbles inters in chaos and each bubble increases until it connects with others [see Fig. III.26 (e), (f) and (g)]. By further increasing the v_{dc} the system can enter in chaos in undoubling period manner for example for $v_{dc} = 2.365$ and then produced P-1 stable state for example for $2.39 \leq v_{dc} < 2.4$ i.e. this voltage being always in the NDR [see Fig. III.26 (i)-4(j)] according to the Table III.1. The Fig. III.26 illustrates the bifurcation diagrams of x_{max} and s_{max} versus control parameter v_{dc} with perfect indication of chaos scenario. Resulting graphs of LEs are in accordance with these observations. Bier and Bountis [123] demonstrated that the phenomenon of reverse period-doubling cascades could occur when a minimum number of conditions is fulfilled. The main result of the latter was that the system of differential equations must remain invariant to the transformation $x \rightarrow -x$, $y \rightarrow -y$, $z \rightarrow -z$, etc., where x , y , z are state variable of the system. However, Eqs. (II.38) do not remain invariant to the above

transformation. Nevertheless, the phenomenon of antimonotonicity and reverse period-doublings is generated and present as shown in Figs. III.26 showing that the above criterion by Bier and Bountis is not a necessity as in Ref. [124]. Chlouverakis and Adams firstly demonstrated this fact for the best knowledge of the authors in two-section semiconductor lasers subject to optical injection [124].

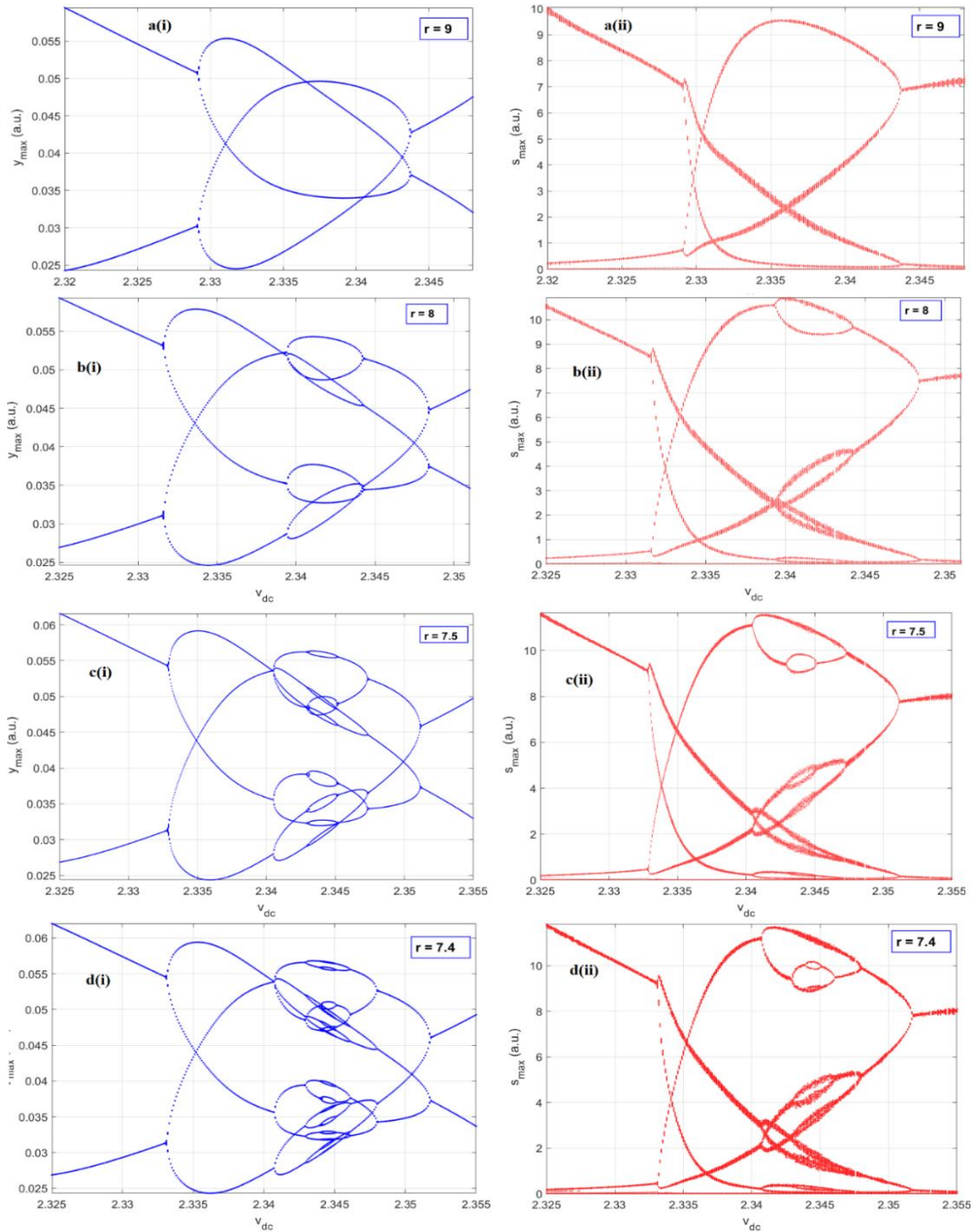


Figure III.26. Bifurcation diagrams' of windows of NDR region with the indication of antimonotonicity and reverse period-doubling scenario created with the smooth variation of v_{dc} for some specific value of the parameter r . (a) period-4 bubbles $r = 9$, (b) period-8 bubbles $r = 8$, (c) period-16 bubbles $r = 7.5$, (d) period-32 bubbles $r = 7.4$.

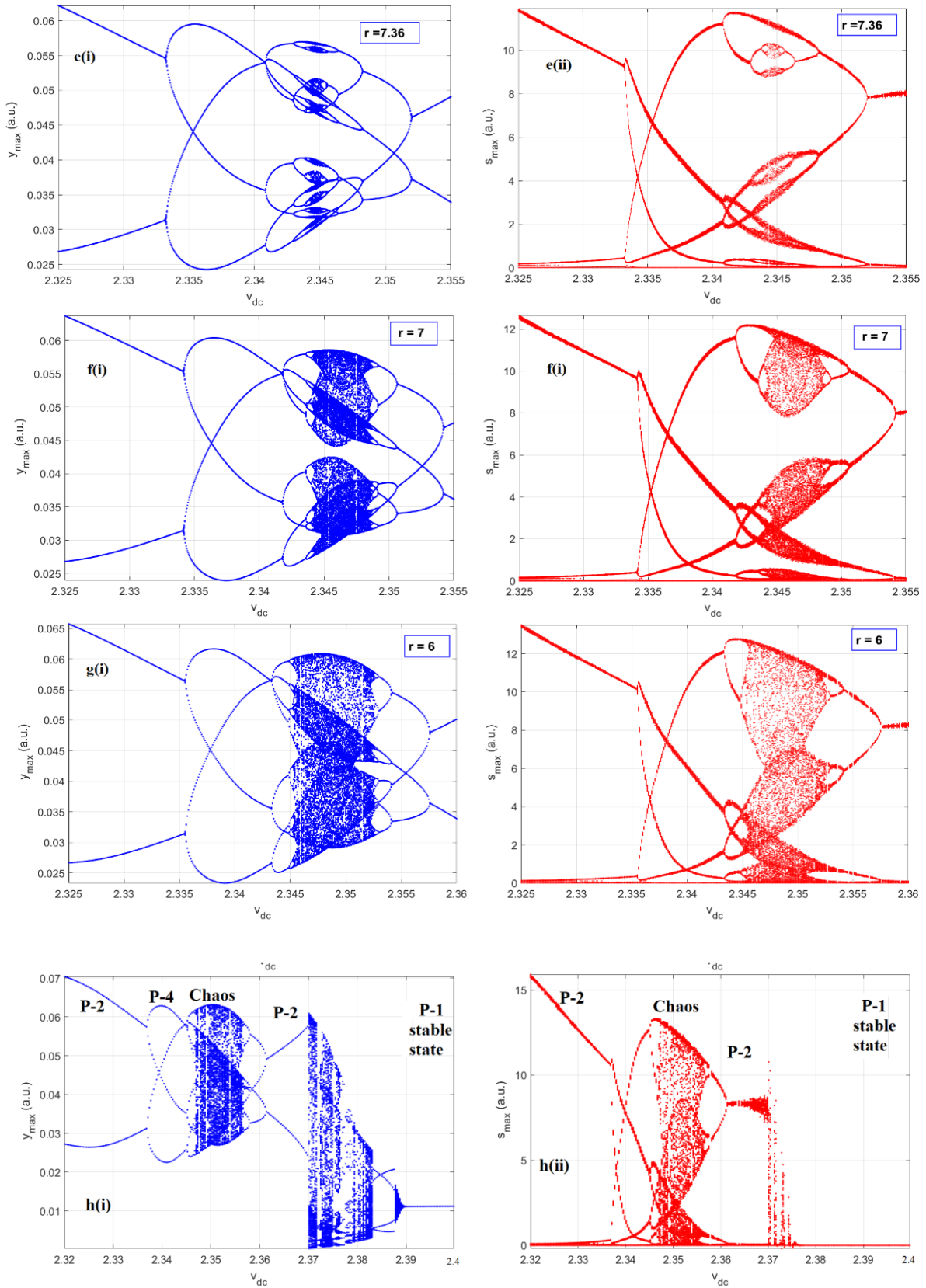


Figure III.26 (End). (e), (f) and (g) chaotic bubbles $r = 7.35$ and $r = 6.68$ in (f) and (g) respectively and stable states occur for $v_{dc} \in [2.39, 2.4]$ when the EGC $\gamma = 0.976$. (h) Bifurcation diagrams extension in NDR for $2.32 \leq v_{dc} \leq 2.4$ showing chaos control.

Multistability and coexisting attractors

The coexistence of two or more attractors in nonlinear system for different initial conditions and fixed other system parameters or for fixed initial condition and different control parameters is known as multistability phenomenon [125, 126]. This means the system is sensitive to initial conditions and can experience different outputs simultaneously. In Figure III.27, the LD's optical phase time series generated from two very close initial conditions $(x_0, 0.0300, 0, s_0, n_0, \psi_0)$ and $(x_0, 0.0305, 0, s_0, n_0, \psi_0)$ are presented. At the beginning, these time series are almost the same, but the difference is increasing after a certain number of iterations $t = 75 \text{ ns}$. Therefore, the system (II.38) has sensitive dependence on ICs caused by coexisting attractors' phenomenon, and then its future behavior cannot be predicted.

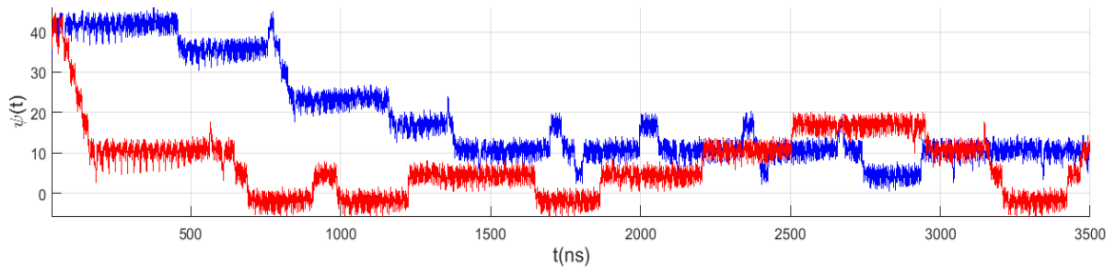


Figure III.27. Sensitivity to initial conditions as the coexistence of two different outputs in laser phase oscillations where red line correspond to ICs $(x_0, 0.0300, 0, s_0, n_0, \psi_0)$ and blue line for $(x_0, 0.0305, 0, s_0, n_0, \psi_0)$.

In addition, by fixing system parameters as follows: $m = 0.0264$; $r = 6.65$; $\gamma_r = 0.1058$; $\sigma = 1/i_{th} \approx 196$; $\delta = 0.1512$; $k = 0.020637$, the coexisting of N-scroll and M-scroll attractors can be found. To display this phenomenon, we arbitrary choose some ICs. In Figure III.28, there appears coexisting 4-scroll with 2-scroll hyperchaotic attractors for $[1, 0.02, 0, -, -, -]^T$ and $[1, 0.025, 0, -, -, -]^T$ in Fig. III.28 (a), coexisting 3-scroll with 1-scroll hyperchaotic attractors for $[1.23, 0.028, 0, -, -, -]^T$ and $[1.25, 0.028, 0, -, -, -]^T$ in Fig. III.28 (b), coexisting 5-scroll with 3-scroll hyperchaotic attractors for $[1.01, 0.028, 0, -, -, -]^T$ and $[1.02, 0.03, 0, -, -, -]^T$ in Fig. III.28 (c), coexisting two 1-scroll attractors for $[1.23, 0.029, 0, -, -, -]^T$ and $[1.01, 0.028, 0, -, -, -]^T$ in Fig. III.28 (d), coexisting 5-scroll with 1-scroll attractors for $[1.01, 0.03, 0, -, -, -]^T$ and $[1.05, 0.03, 0, -, -, -]^T$ in Fig. III.28 (e) and it is found coexisting 5-scroll with 1-scroll disconnected hyperchaotic attractors for $1.01, 0.03, 0, -, -, -]^T$ and $[1.01, 0.04, 0, -, -, -]^T$ Fig. III.28 (f).

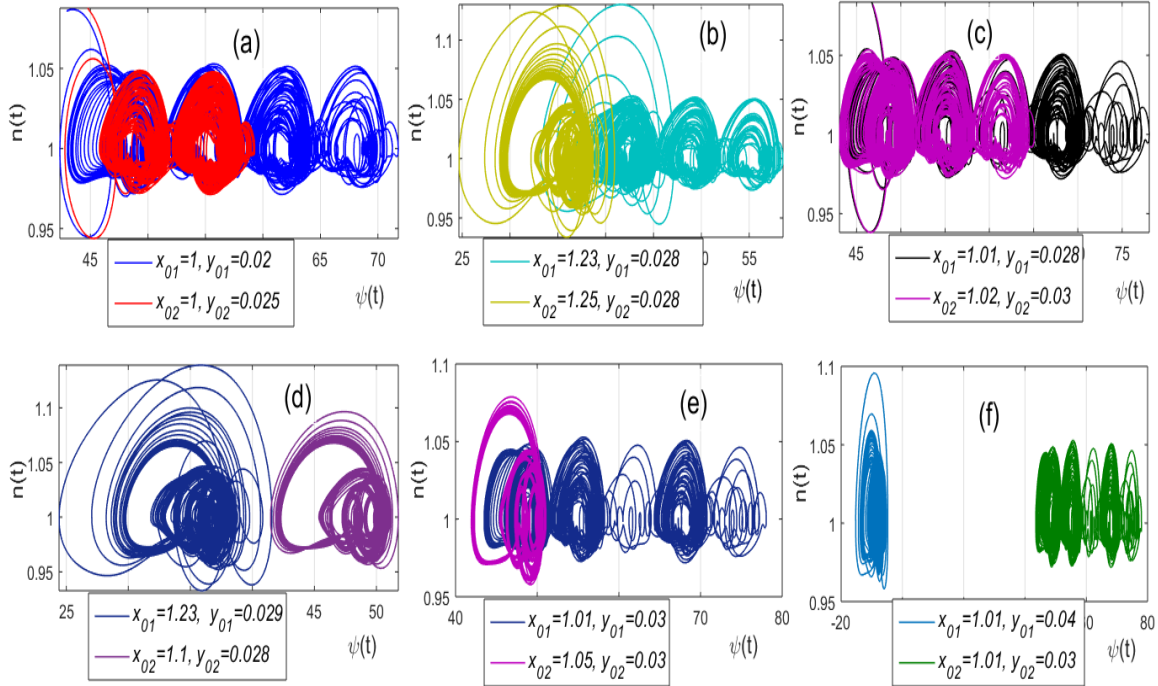


Figure III.28. Phase portraits of coexisting of N-scroll with M-scroll hyperchaotic attractors by adjusting the initial conditions. (a) Coexisting 4-scroll with 2-scroll attractors, (b) coexisting 3-scroll with 1-scroll attractors, (c) coexisting 5-scroll with 3-scroll attractors, (d) coexisting two 1-scroll attractors, (e) coexisting 5-scroll with 1-scroll attractors, (f) coexisting 5-scroll with 1-scroll disconnected attractors.

Multistability Control and Controllable Number of Scroll

Moreover, we use bifurcation diagrams to control and eliminate multistability phenomenon because in many cases of application, this phenomenon is not desirable and need to be controlled. Multistability and generating multiscroll attractors increase grammatically the complexity of the system. Despite high flexibility provided, these phenomenon need to be avoided. For this purpose we firstly, we considered the setting two different initial conditions i.e. $[1, 0.028, 0, -, -, -]$ and $[1, 0.029, 0, -, -, -]$ whereby the trajectories started and we explore the bifurcation diagram and LEs spectrum. When the parameter r is adjusted from 6.6 to 8, the bifurcation diagram presents the maxima of optical output is plotted in Figure III. 29. The trajectories colored in black correspond to the initial conditions $[1, 0.028, 0, -, -, -]$ and those colored in purple correspond to $[1, 0.029, 0, -, -, -]$. Furthermore, this bifurcation demonstrates the emergence of multistability with coexisting multiscroll attractors for selected parameter windows. For instance, the system (II.38) exhibits dynamical behaviors with coexisting multiscroll attractors. Moreover, the system trajectory evolves from coexisting multi scroll attractors toward two scrolls. In addition, the two disconnected single-scrolls evolve toward a single-scroll attractor and finally fall into a single scroll attractor, torus and periodic limit cycle.

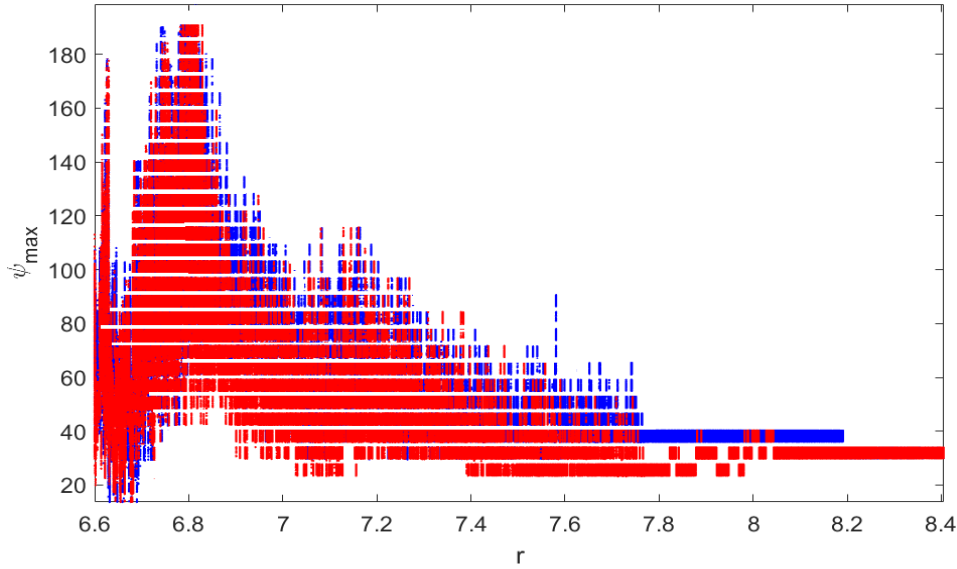


Figure III.29. Bifurcation diagram of coexisting multiscroll attractors of a variable ψ with increasing the resistance r showing a controllable number of scroll in the system (III.38)

In the other hand, the dynamics evolution of the system if plotted in Figure III.30. The system evolves from coexisting multiscroll attractors to one single-scroll and/or periodic limit cycle. The LEs are calculated for 1,600 observations normalized time and step size of 0.01 for the same parameters as in Fig. III.29. When $r = 6.645$, the LEs for the previous ICs are $LE_1 = 0.0019(0.0032)$, $LE_2 = 0.0021(0.001)$, $LE_3 = 0.0000(0.0000)$, $LE_4 = -0.0764(-0.0689)$, $LE_5 = -0.3417(-0.3359)$, $LE_6 = -0.4546(-0.4683)$. In addition, according to Kaplan-York conjecture, the Lyapunov dimensions of this system are $D_L = 6.9111(6.8554)$; which means that the system (II.38) is really defined to by hyperchaotic since at least, two positive LEs are found and the dimension is fractional number. Furthermore, the divergences of the system given onto these conditions are $\Delta V = -\mu(x, n, s) = \sum_{i=1}^6 LE_i = -0.8687(-0.8687) < 0$; which evidences attractors.

From III.30 (a), we can observe the coexistence of corresponding 6-scroll with 9-scroll hyperchaotic attractors for instance. When $r = 6.651$, the system exhibits coexisting 2-scroll with 5-scroll hyperchaotic attractors in Fig. III.30 (b) with corresponding Lyapunov exponents $LE_1 = 0.0028(0.0021)$, $LE_2 = 0.002(0.0004)$, $LE_3 = 0.000(0.000)$, $LE_4 = -0.0834(-0.0725)$, $LE_5 = -0.3419(-0.3465)$, $LE_6 = -0.4490(-0.4530)$ and the Lyapunov dimension of this system is $D_L = 6.9495$ which implies fractional feature. When $r = 6.66$, the system produces coexisting 2-scroll with 4-scroll attractors as depicted III.30 (c) with corresponding Lyapunov exponents $LE_1 = 0.0016(0.0007)$, $LE_2 = 0.0008(0.002)$, $LE_3 = 0.000(0.000)$, $LE_4 = -0.1470(-0.1252)$, $LE_5 = -0.3319(-0.3442)$, $LE_6 = -0.3943(-0.4041)$, the Kaplan-Yorke dimension being $D_L = 6.9495$. From

III.30 (d) the system generates coexisting 1-scroll with 2-scroll attractors when $r = 6.66$. For $r = 6.71$, the system produces coexisting two disconnected coexisting single-scroll as presented in III.30 (e). If we furthermore increase r to 6.73, the two single scroll attractors connect to each other and form a single scroll attractor in III.30 (f). The system produces quasi-periodic torus in Fig. III.30 (g) when $r = 7.2$ and finally the RTD-OISCL system enters into periodic state producing periodic limit cycle in III.30 (h) when $r = 9$ with corresponding Lyapunov exponents $LE_1 = -0.0038(-0.1647)$, $LE_2 = -0.0007(-0.1638)$, $LE_3 = 0.0000(0.0000)$, $LE_4 = -0.1784(-0.1675)$, $LE_5 = -0.3283(-0.1569)$ and $LE_6 = -0.3629(-0.5646)$.

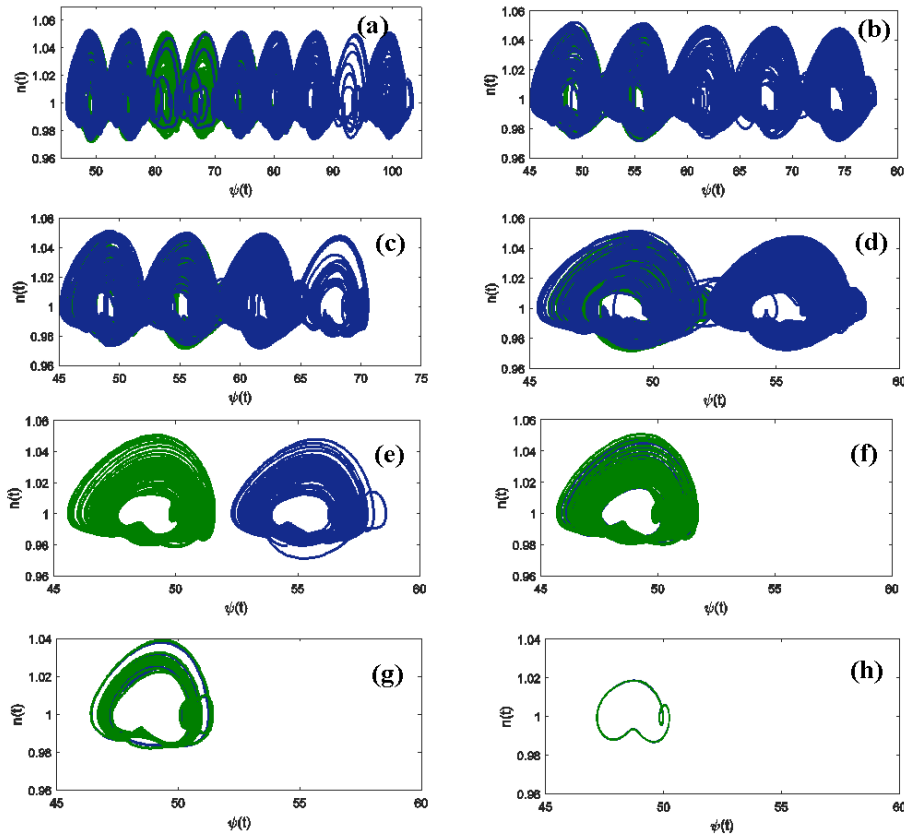


Figure III.30. Control of dynamic evolution from the coexisting N-scroll with M-scroll hyperchaotic attractors to a single one-scroll and to periodic limit cycle. (a) Coexisting 6-scroll with 9-scroll hyperchaotic attractors. (b) Coexisting 2-scroll with 5-scroll hyperchaotic attractors, (c) coexisting 2-scroll with 4-scroll hyperchaotic attractors, (d) coexisting 1-scroll with 2-scroll hyperchaotic attractors, (e) coexisting two disconnected single scroll attractors (f) coexisting two connected single scroll into one scroll, (g) coexisting two connected quasi-periodic torus, (h) periodic limit cycle

Therefore, the parameter r together with v_{dc} lead to the controllable number of scroll and the multistability phenomenon observed in the system (II.38). Obviously, the parameter r refers to the overall resistance of the circuit. Interestingly, this method also applies to v_{dc} parameter. Therefore, it could be promising in hardware experimental realization of these kind of optoelectronic systems because it does not need necessary modifications of system intrinsic parameters values.

A Fast-Slow MMO system

Mixed-mode oscillations (MMOs) describe trajectories of dynamical system that combine a rhythmic alternation of large amplitudes oscillations (LAOs) and small amplitude oscillations (SAOs) [127], [63]. MMOs can be found in different scientific fields, such as physics, chemistry and biology. MMO have been extensively in the hearth of most interdisciplinary research these recent years due to its potential of describing processing information nervous systems for example. Nonlinear systems with MMOs behavior have received too much attention and considerations for instance; mimicking neurological brain dynamics based on low consumption electronic circuit is one of the hot attempts in brain-inspired systems. For example in brain's dynamics, the neuron is quiescent if its membrane potential is at rest or exhibits LAOs (sub-threshold) [128]. Quiescent states of neurons correspond to the closer an equilibrium states while SAOs refer to a small amplitude limit attractor. As more generalized VdP oscillator, RTD-LD Liénard's (optoelectronic hybrid) oscillators are placed to be best candidates to MMO generation. The proposed a neuromorphic photonic circuit of Romeira et al. in [63] and some other examples have been studied previously. Here, we use the L and s numbers denoted in L^s notation to describe the number of local maximum of the LAOs and SAOs. In most existing works relating MMOIBs, $L=1$ and simplest sequences such as $[1^2, 1^1 \times n]$ occur commonly [129]. In electronics, Bonhoeffer-Vander Pol oscillators [130-132] is a most system used to generate MMOIB and Poincaré return map is used to clarify the occurrence of MMOIB [129]. The generalized resulting fast-slow system from a two times scale periodically forced coupled RTD-LD fast-slow system is in the form of Eq. (III.53).

$$\left\{ \begin{array}{l} \dot{x} = y - f(x), \\ \dot{y} = \varepsilon (-x - ry + v_{dc} + v_{ac} \sin \theta), \\ \dot{\theta} = \varepsilon_1 \omega, \\ \dot{n} = \varepsilon_1 \gamma_e \left(\sigma y - n - \frac{n - \delta}{1 - \delta} s \right), \\ \dot{s} = \varepsilon_1 \left(2\beta G(n-1)s + 2\gamma\kappa\sqrt{s} \cos \psi \right), \\ \dot{\psi} = \varepsilon_1 \left(\alpha G(n-1) - \frac{\gamma\kappa}{\sqrt{s(t)}} \sin \psi - \Delta\omega \right), \end{array} \right. \quad (\text{III.53})$$

with $0 < \varepsilon = C/L \ll \varepsilon_1 = L\varepsilon \ll 1$.

This system (II.38) is therefore equivalent to a two-time scale system (III.53) obtained by rescaling T to be equal to t . The variable x refers to the fast variable. Variables y and θ are the slow

variables from electrical subsystem. The parameters n , s and ψ are slow-driven variables from optical subsystem.

Bursting and mixed-mode oscillations

When the system dynamics alternates a quiescent state and a spiking or firing states, its dynamics is said to be *bursting*. The Figure III.31 depicts the bursting phenomenon in optical and electrical outputs. The LD emulates BOs arising from electrical output voltage. In Fig. III.31 (a) and (b), the sequence of firing and resting states refers to periodic BOs. As longer as we further increase the EGC, the system fails into the spiking train with continuous firing exhibition in Figure III.31 (c). The occurrence of BOs and firing in optical output is caused by a smaller external frequency that modulated laser and electrical oscillations.

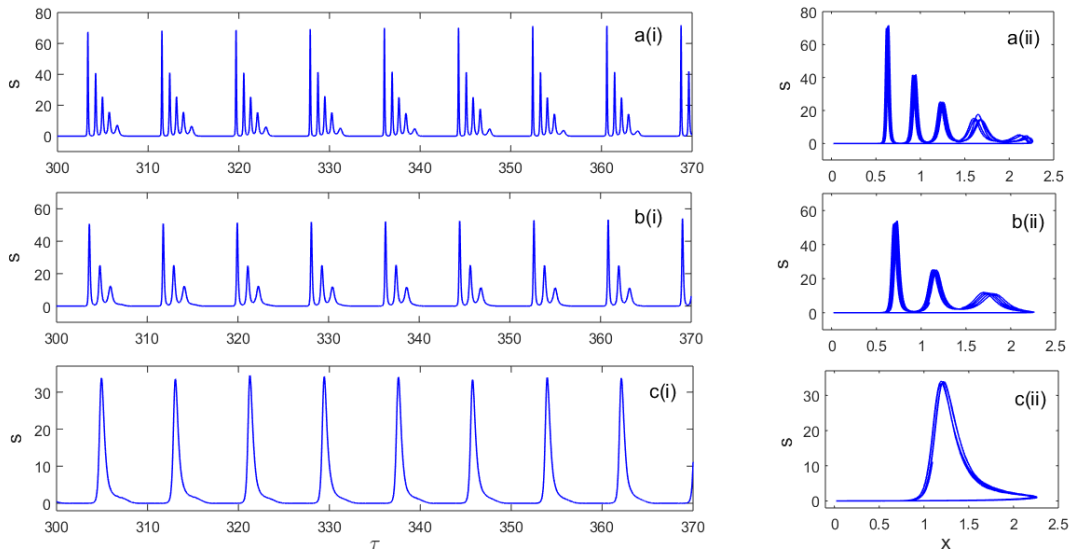


Figure III.31. Square – wave bursting. (i) Time series of optical output $s(t)$ and its corresponding (ii) phase portraits in the light-voltage ($s - x$) planes. (a) Periodic BOs for $\gamma = 0.11$, (b) Periodic BOs for $\gamma = 0.5$ and (c) spiking trains for $\gamma = 0.9$

Chaotic Bursting and Mixed-mode oscillations

A class of BOs, which appears as an alternate sequence of small amplitude and large amplitude oscillations, refers to *mixed-mode oscillations*. In Figure III.32, the time series seem to be periodic and with oscillations within each period. Within each period, this series shows pairs of LAOs combined alternations of SAOs. This means the MMOs behavior. However, corresponding phase portraits in voltage-light ($x - s$) plane reveal the existence of periodic chaotic attractors. The large and smaller orbits of this attractor refer to large amplitude and small amplitude oscillations from time series. Its 3D projection is a Rossler-like chaotic attractor.

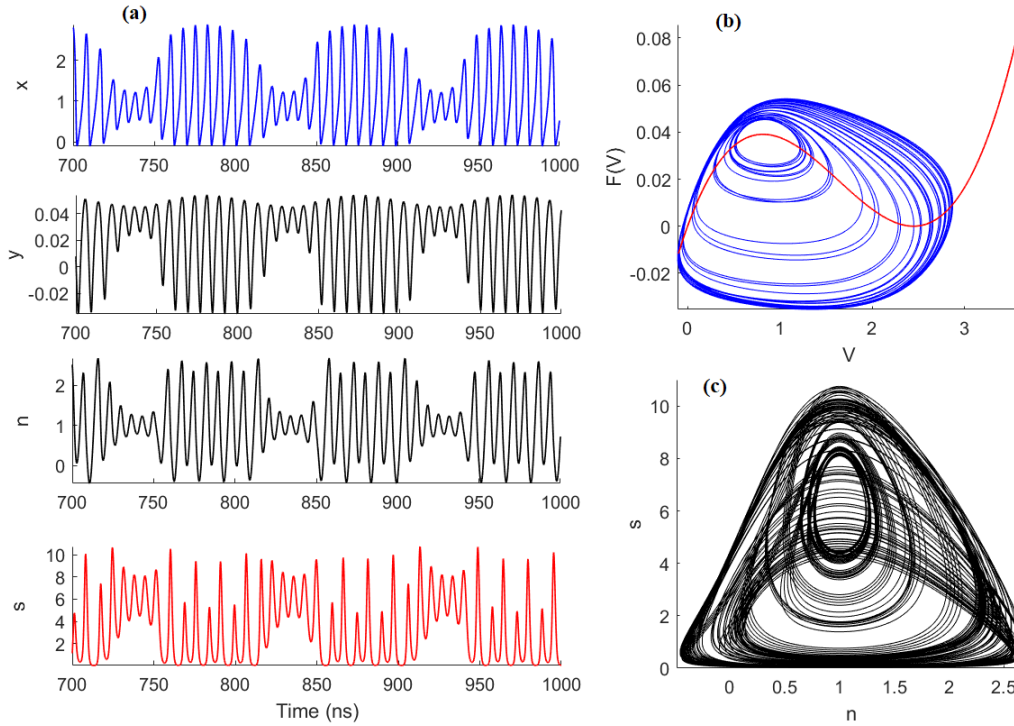


Figure III.32. (a) Time series of chaotic oscillations for voltage $x(t)$ current $y(t)$, carrier density $n(t)$ and optical output $s(t)$ and corresponding phase portraits in the (a) voltage-current ($x - y$) and (b) carrier-photon ($n - s$) planes. The solid red line in (b) corresponds to cubic nonlinear of RTD-LD $I - V$ curve.

In Fig. III.33, we observe simple and complex MMOs achieved in electrical and optical domains for different values of driving sinusoidal force. Phase portraits show magnified views of large and small amplitude oscillations: small oscillations refer to close fix point limit cycles a(ii) and b(ii).

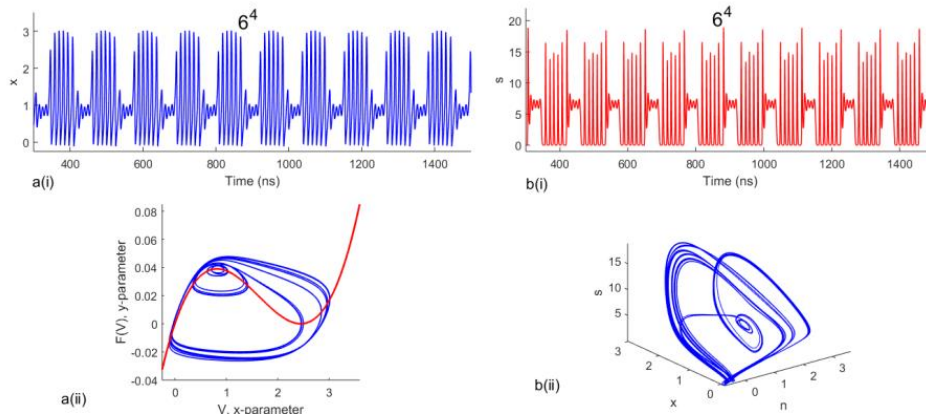


Figure III.33. a(i)-b(i) Time series of simple periodic MMO in voltage and optical output respectively and its corresponding phase portraits in the a(ii) current-voltage and b(ii) 3D carrier-voltage-photon projection.

Mixed-mode oscillation incrementing bifurcation

MMOIBs occur in the manner of the sequence of period doubling generated by the MMO sequence $L^s(L^{s+1})^n$ for successive naturel number n . For instance, the Figure III.34 shows the

optical wave form of an **MMO** after two **MMOIBs**. This **MMO** sequence $15^3(15^4)^2$ represents the **MMOIB** $15^315^415^4$ or $[15^3,15^4 \times 2]$. **MMOIBs** are well known to occur in non-autonomous and autonomous systems. In this section, for **MMOIBs** to occur, the constant parameters are fixed here as $r = 5$, $v_{ac} = 100$, $\omega = 1.2566 \times 10^8$, $\varepsilon = 0.00035$ and $\gamma = 0.97$. We recall that, the system (III.53) has four main bifurcating parameters: ε , r , v_{ac} and ω .

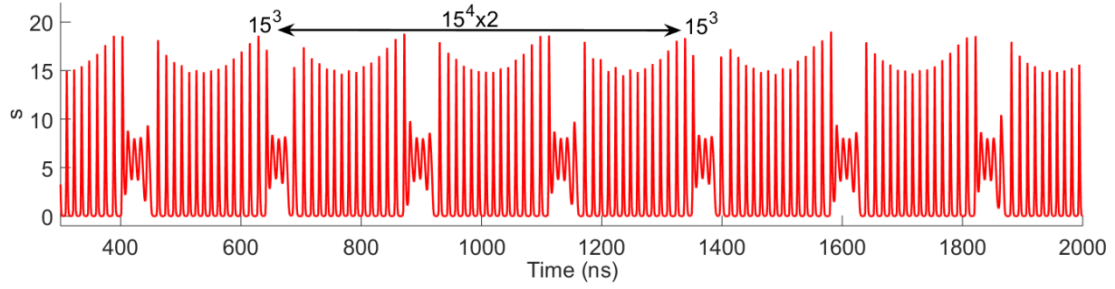


Figure III.34. Optical time series for the sequence of $[15^3,15^4 \times 2]$ MMO after two MMOIBs for $r = 5$, $v_{ac} = 100$, $\omega = 1.2566 \times 10^8$, $\varepsilon = 0.00035$ and $\gamma = 0.97$.

The **EGC** modulates κ -parameter and both merely can be used to modulate the laser output. In the other hand, the bifurcation diagram versus the ration of slow and fast timescales ε as bifurcation parameter is presented in Figure III.35 reveals the resulting a successive generation of period-adding sequences alternated with chaos.

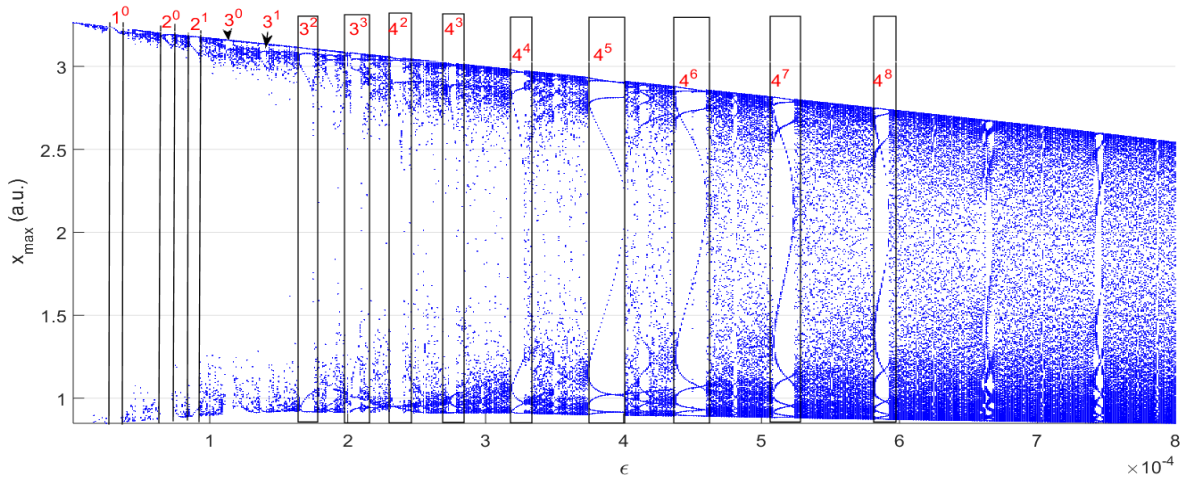


Figure III.35. Bifurcation diagram for $r = 6$, $v_{ac} = 0.110$, $\omega = 0.01\pi \times 10^9$, $0.0000 < \varepsilon < 0.0008$ and $\gamma = 0.97$ with successive $1^0 \rightarrow 2^0 \rightarrow 2^1 \rightarrow 3^0 \rightarrow 3^1 \rightarrow 3^2 \rightarrow 3^3 \rightarrow 4^2 \rightarrow 4^3 \rightarrow 4^4 \rightarrow 4^5 \rightarrow 4^6 \rightarrow 4^7 \rightarrow 4^8$ sequence intervals of MMOs.

Each period-adding window has **LAOs** with **SAOs**. As the parameter is varied, **LAOs** and **SAOs** increase incrementally as $1^0 \rightarrow 2^0 \rightarrow 2^1 \rightarrow 3^0 \rightarrow 3^1 \rightarrow 3^2 \rightarrow 3^3 \rightarrow 4^2 \rightarrow 4^3 \rightarrow 4^4 \rightarrow 4^5 \rightarrow 4^6 \rightarrow 4^7 \rightarrow 4^8$. This refers to **MMOIBs** generation [129].

Influence of r in MMOs evolution

We investigate the influence the parameter r in the dynamics of **MMOs** generation. As r in increasing, by maintaining other parameters as follows, $\gamma = 0.98$; $f_{in} = 0.93GHz$; $\varepsilon = 0.0035$, the system generate **MMOIBs** [$15^3, 15^4 \times 2$] when $r = 5$ [III.36 (a)]. With slight variation of r i.e. $r = 5.1$ in Fig. III.36 (b), the system produces a 15^4 **MMO**.

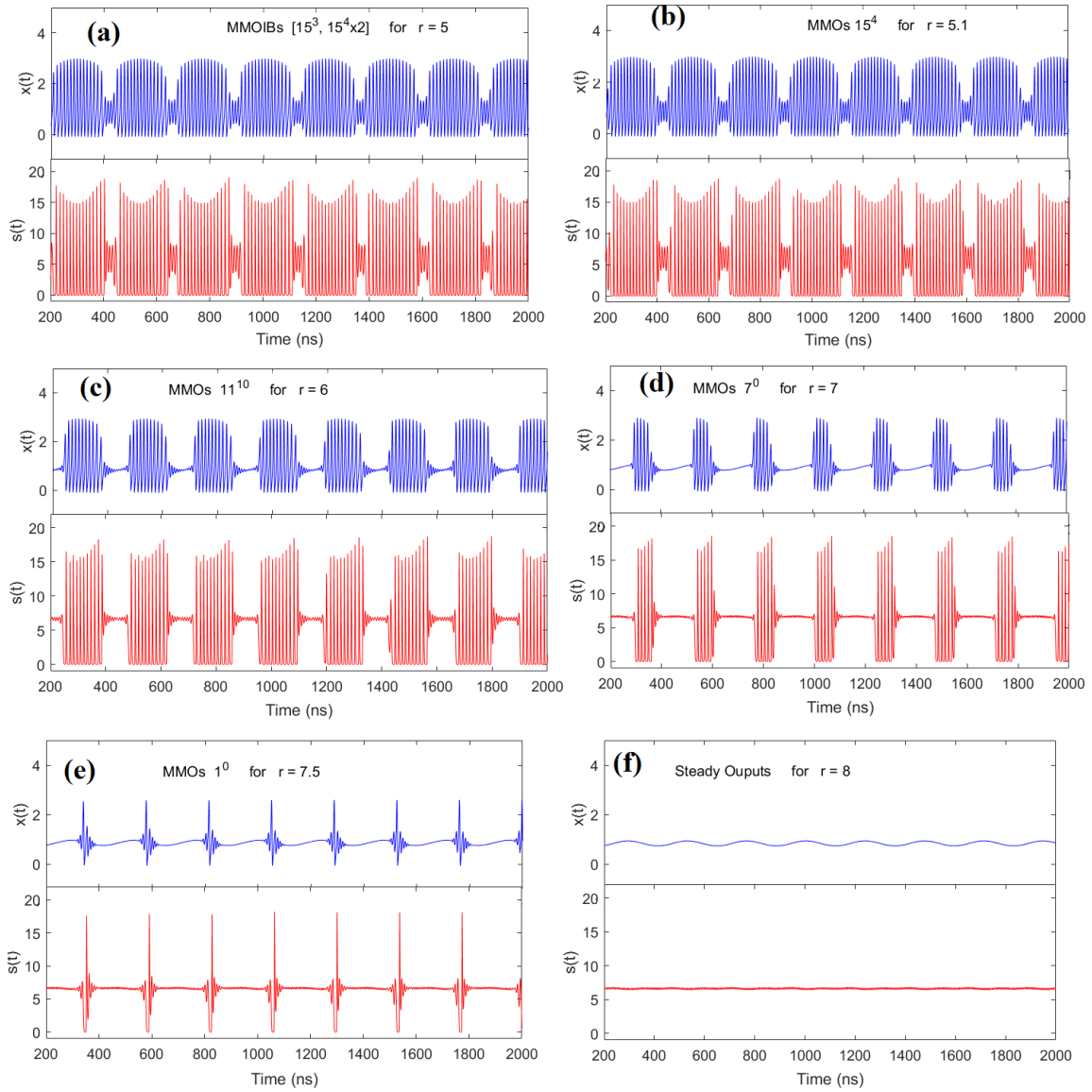


Figure III.36. Evolution of MMOs with variations of overall resistance when $\gamma = 0.98$; $f_{in} = 0.93GHz$; $\varepsilon = 0.0035$. (a) MMOIBs [$15^3, 15^4 \times 2$], (b) 15^4 MMOs, (c) 11^{10} MMOs, (d) 7^0 MMOs, (e) 1^0 MMOs and (f) steady state similar to period-1 oscillations.

As the resistance is increasing, **LAOs** is decreasing while **SAOs** increase up to a certain range of r for which the system exhibits a class of on-off states. Therefore, we have a class of 11^{10} **MMOs** for $r = 6$ in Fig. III.36 (c), on-off oscillations in the manner of 7^0 **MMOs** for $r = 7$ in Fig. III.36

(d), on-off oscillations in the form of 1^0 MMOs for $r = 7.5$ in Fig. III.36 (f) and the system fails down in steady state similar to period-1 oscillations.

Transient Chaos

Transient chaos occurs in this situation if we $r = 7.4$ and $v_{ac} = 0.1$. In this case, chaos appears for the first 525 time iterations as depicted in Figs. III.37 (a) and (b) for electrical and electrical time series respectively. Noise-like appearance in power spectra in Fig. III.37 (c) and as well as attractor in bleu trace from III.37 (d) evidence the occurrence of chaos transient. In addition, the system goes toward period-1 limit for time up to 512 iterations as presented by enlargements from III.37 (a) and III.37 (b), confirmed by one harmonic in power spectra [Fig. III.37 (c)] and period-1 limit cycle traced in red in Fig. III.37 (d).

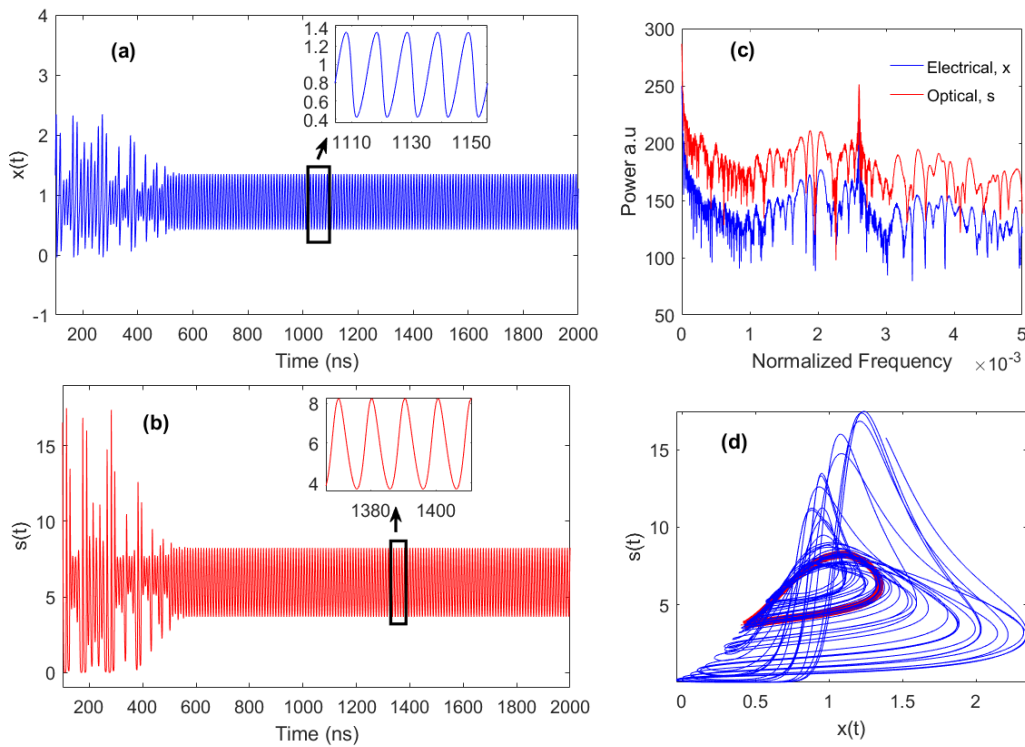


Figure III.37. Transient chaos in (a) electrical and (b) optical outputs. Corresponding power spectrum (c) and (d) projection of chaotic transient attractor (bleu trace) and period-1 limit cycle (red trace) in voltage-light plane.

III.5. Conclusion

In this chapter, noise induced effects in optical injection SCLs that the dynamics includes the EGC as a new control parameter was studied. In addition, we proposed the integration process of this model of lasers with resonant tunnelling diode devices and investigated the dynamical properties the proposal OEHO.

Firstly, theoretical and numerical studies of the transmitted noise in optical injection **SCLs** was carried out by treating the laser rate equations according to the Langevin approach. We unveiled that the **EGC** acts as a modulating and control parameter allowing significant reductions of **RIN** spectra at low frequency from $-110\text{dB}\cdot\text{Hz}^{-1}$ to $-175\text{dB}\cdot\text{Hz}^{-1}$, in addition to the diminution achieved by classic decisive parameters. Moreover, a suitable choice a **ML** with of small phase fluctuations leads to avoiding and eliminating the $1/f$ noise observed in the **RIN** at low frequencies up to by the 1GHz. Next, we proposed a novel formula given the **FWHM** of **SCL** by the mean **EGC** that we called a modified Schawlow–Townes formula.

Next, the stability analysis of the proposed novel **RTD-LD** Liénard oscillator has been investigated in the frame of strong and weak optical injection. It has been demonstrated that the system may provide some stable equilibrium points as demonstrated by the calculation of eigenvalues of the Jacobian matrix and confirmed by the occurrence of a shrunk stable region inside the sea of unstable points through the implementation of the Routh-Hurwitz conditions.

Furthermore, we studied the dynamics properties of the novel **OEIC** and we found that the driven laser diode could exhibit complex dynamics including chaos and hyperchaos. A collection of bifurcation diagrams revealed chaotic and nonchaotic windows including quasi-periodic and non-periodic dynamics for restricted ranges of control parameters. We have shown that the route to chaos can be achieved via cascade period doubling sequences. It has also been observed the phenomenon of antimonotonicity when the resistance r and direct voltage bias v_{dc} are varying. In addition, the **LD** could exhibit strange attractors such as chaotic multiscroll and infinite scroll chaotic attractors. The evidence of the infinite-scroll attractor has been furthermore performed by Simulink implementation with very good accuracy. Moreover, we have observed the multistability phenomenon with coexisting N-scrolls and M-scrolls attractors whose natural numbers M and N are controlled by the resistance r . Furthermore, the present **OEO** has an ability of fast-slow systems generating a class of dynamics memory i.e. bursting on-off sequence oscillations with **BOs**, **MMOs**, square waves and simple **MMOIBs**. Altogether, these results are very promising for the implementation of novel optoelectronic systems free of $1/f$ noise, with low intensity and frequency noises and requiring low modulation voltage/or current and generating complex and utmost nonlinear dynamics

GENERAL CONCLUSION

A. Research Summary

This thesis aimed to study the nonlinear dynamics of optical injection SCLs by focusing on noise effects, its control and suppression using modified rate equations and on non-linear dynamics induced by the integration of novel class of SCLs with RTD devices. We have investigated separately noises and irregular chaotic oscillations as it are of different origins. For this purpose, three chapters have made up this thesis after a general introduction which introduced the general background, motivations and objectives of the study.

First, the Chapter I presented the emergence of laser diodes and laser diode technologies with a focus on optical injection semiconductor lasers and the origins of noise in laser diodes. This chapter has also provided a brief overview of the arguably touted advantages of semiconductor lasers in the global laser market in particular in optical communications and telecommunications. Secondly, tunnel diode devices and mainly resonant tunnel diode, its structures and principles of operation were presented. In addition, we have recalled physical principles that describe the operation of heterostructures based on semiconductors with particular attention in the selection of wavelengths thanks in particular to semiconductor lasers. Finally, we have presented rate equations of optical injection semiconductor lasers model developed by Mengue and Essimbi resulting from the modification of the Lang and Kobayashi equations, an overview of optoelectronic oscillator constituted with negative differential resistance elements.

In Chapter II, we firstly presented theoretical and numerical methods known for their capacity to analyze noise in frequency domain, to represent of the reduced nonlinear functions such as polynomial approximation and the methods to analyses and descriptions for nonlinear systems. Secondly, we have analytically modified the SCL rate equations in terms of photon density $S(t)$, carrier density $N(t)$ and optical phase $\psi(t)$. In this model of equations, the EGC is a new control parameter absent in conventional SCLs rate equations. In addition, we have initiated and proposed the integration process of this model of lasers with a resonant tunnelling diode's optoelectronic oscillator and we have analytically developed deterministic ODEs describing the dynamics evolution of the novel optoelectronic integrated circuit.

The Chapter III was devoted to the presentation and discussion of main results of this thesis. This chapter has been divided in three folders.

The first has treated the effects of noise in optical injection laser systems using Langevin approach and has propose effective and simple means in practice to avoid and eliminate 1/f noise, to reduce intensity and frequency noises in optical injection lasers systems. We have also offered a new formula for the ideal linewidth of semiconductor lasers. This makes it possible to meet the need for low noise lasers without, however, modifying the intrinsic parameters of the laser. Analytical transformations have shown that the master laser noise drastically affects the slave laser. Then, in agreement with the simulations, we have shown a way to avoid and eliminate noise-induced effects. Furthermore, we also shown that FN and RIN depend on the bias current and the effective gain coefficient. It appeared that an increasing in the pumping current leads to a decreasing of intensity and frequency noise. On the other hand, the noise decreases by smoothly decreasing the effective gain coefficient.

The last two parts of this chapter aimed to understand the influence of the RTD current on the stability and dynamics of the optical injection laser diode; by means of different tools combining analytical calculations and simulations presented in chapter II. In our approach, an analytical polynomial model from three models already reported in the literature, was proposed at the beginning of chapter II. It polynomial approximation allowed describing with good precision the N shape of the current-voltage characteristic of the RTD over a wide range of bias current, particularly over the active area of NDR. Despite the great interest of this analytical model, simulations can only understand some local effects outside the active zone. Nevertheless, the study of the complex dynamics of this system being mostly beneficial in NDR region of RTD since outside this zone, the whole system would have a positive resistance and could therefore generate a stable or periodic dynamic, we justified the choice of this model by collected results.

The stability analysis has shown that for laser mode locking to occur, the frequency detuning between the slave and the master should be less than -2GHz and so that the fixe phase should be located between the boundary curves of the gain coefficient effective or injection strength. From Lyapunov methods, it appeared that in the NDR of the RTD, stable equilibrium points are achieved by slightly increasing resistance, polarization and the effective gain coefficient. We used both electrical and optical parameters to control the systems stability and placed this optoelectronic oscillator to belong to next generation optoelectronic systems.

In nonlinear dynamics point of views, we have shown that seven involved parameters can be used as control parameters: m , v_{dc} , r , v_{ac} , γ , k and Ω_{in} using collections of bifurcation

diagrams. However, four of these parameters have been assigned constants all over numerical calculations: $m = 0.0265$, $v_{ac} = 0.145(V_{AC} = 145 \text{ mA})$, $k = 0.0206$ and $\Omega_{in} = 1.1836(f_{in} = 0.9\text{GHz})$ while the rest of parameters v_{dc} , r and γ had served as main bifurcation parameters throughout thesis (V_{DC} , R and the EGC γ). By varying the EGC, the system was capable of generating a scenario of frequency division to chaos with dynamics similar to that displayed in SCLs with optical feedback. Furthermore, the system exhibited complex dynamics such as of chaotic multiscroll attractors. By setting the EGC at 0.68, the resistance at 6.68 and the detuning at -0.32GHz, the system generated an attractor with an infinite number of scrolls whose Lyapunov spectrum has evidenced to be a chaotic attractor because at least one exponent always remained positive. We have verified the effectivity of this attractor by implementing the system under Simulink. Subsequently, we have observed the phenomenon of antimonotonicity created via forward and reverse period-doubling cascades in the parameter space of DC voltage v_{dc} and overall resistance r . Subsequently, coexistence of multiple scroll attractors with contrrollable number of scrolls had been achieved by smoothly adjusting of r parameter. We also transformed this oscillator into a fast-slow system, generating MOs, bursting oscillations, square wave and MMOIBs among others relevant in the description of brain neuron activity.

B. Perspectives of Future Works

As outlooks in short terms, we will explore the following research lines:

1. Use this RTD-LD configuration to investigate the influence of feedback time-delayed looped from a PD by mapping the time delay and optoelectronic feedback strength as control parameters
2. Use this model of RTD-OISCL for two mutually coupled RTD-LD optoelectronic oscillators and investigate synchronization of chaotic laser systems.
3. Extend this study in the point of view of fractional system and investigate experiment results to corroborate fractional analysis by numerical results and experiment results.
4. Make a numerical study of the system including pumping current noise effects in addition two Langevin noise induced by laser working process

APPENDIX

The elements a_1, a_2, a_3, a_4 and a_5 of (4) and (5) are given by

$$\begin{aligned}
 a_0 &= 1, a_1 = -2\beta G_0 \Delta n_0 + mr + 3B_0 m^{-1} (3x_0^2 - 2(a+b)x_0 + ab) + \frac{\gamma_0}{1-\delta} (\sigma B_0 x_0 (x_0 - a)(x_0 - b) - \delta) \quad , \\
 a_2 &= 1 + 3rB_0 (3x_0^2 - 2(a+b)x_0 + ab) + 2\beta G_0 \gamma_0 (\sigma B_0 x_0 (x_0 - a)(x_0 - b) - n_0) + (\alpha G_0 \Delta n_0 - \Delta \Omega)^2 \\
 &\quad + \beta^2 (G_0)^2 (\Delta n_0)^2 - \left\{ mr + 3B_0 m^{-1} (3x_0^2 - 2(a+b)x_0 + ab) \right\} \left\{ 2\beta G_0 \Delta n_0 - \frac{\gamma_0}{1-\delta} (\sigma B_0 x_0 (x_0 - a)(x_0 - b) - \delta) \right\} \\
 &\quad - 2\beta G_0 \gamma_0 \left(\frac{\sigma B_0 x_0 (x_0 - a)(x_0 - b) - \delta}{1-\delta} \right) \Delta n_0 \\
 a_3 &= -2\alpha G_0 \gamma_0 (\alpha G_0 \Delta n_0 - \Delta \Omega) (\sigma B_0 x_0 (x_0 - a)(x_0 - b) - n_0) - 2\beta^2 (G_0)^2 \gamma_0 (\sigma B_0 x_0 (x_0 - a)(x_0 - b) - n_0) \Delta n_0 \\
 &\quad + \frac{\gamma_0}{1-\delta} (\sigma B_0 x_0 (x_0 - a)(x_0 - b) - \delta) \left[1 + 3rB_0 (3x_0^2 - 2(a+b)x_0 + ab) + \beta^2 (G_0)^2 (\Delta n_0)^2 + (\alpha G_0 \Delta n_0 - \Delta \Omega)^2 \right] \\
 &\quad \left\{ + 2\beta G_0 \gamma_0 (\sigma B_0 x_0 (x_0 - a)(x_0 - b) - n_0) - 2\beta G_0 \frac{\gamma_0}{1-\delta} (\sigma B_0 x_0 (x_0 - a)(x_0 - b) - \delta) \Delta n_0 + \right. \\
 &\quad \left. + \beta^2 (G_0)^2 (\Delta n_0)^2 + (\alpha G_0 \Delta n_0 - \Delta \Omega)^2 \right\} \times \left\{ mr + 3B_0 m^{-1} (3x_0^2 - 2(a+b)x_0 + ab) \right\} + \\
 &\quad - 2\beta G_0 \left[1 + 3rB_0 (3x_0^2 - 2(a+b)x_0 + ab) \right] \Delta n_0 \\
 a_4 &= \left\{ -2\alpha G_0 \gamma_0 (\alpha G_0 \Delta n_0 - \Delta \Omega) (\sigma B_0 x_0 (x_0 - a)(x_0 - b) - n_0) \right. \\
 &\quad \left. - 2\beta^2 (G_0)^2 \gamma_0 (\sigma B_0 x_0 (x_0 - a)(x_0 - b) - n_0) \Delta n_0 + \right. \\
 &\quad \left. + \frac{\gamma_0}{1-\delta} (\sigma B_0 x_0 (x_0 - a)(x_0 - b) - \delta) \left[\beta^2 (G_0)^2 (\Delta n_0)^2 + (\alpha G_0 \Delta n_0 - \Delta \Omega)^2 \right] \right\} \times \\
 &\quad \left\{ mr + 3B_0 m^{-1} (3x_0^2 - 2(a+b)x_0 + ab) \right\} + \\
 &\quad \left\{ 2\beta G_0 \gamma_0 (\sigma B_0 x_0 (x_0 - a)(x_0 - b) - n_0) - 2\beta G_0 \gamma_0 \left(\frac{\sigma B_0 x_0 (x_0 - a)(x_0 - b) - \delta}{1-\delta} \right) \Delta n_0 + \right. \\
 &\quad \left. \beta^2 (G_0)^2 (\Delta n_0)^2 + (\alpha G_0 \Delta n_0 - \Delta \Omega)^2 \right\} \times \left\{ 1 + 3rB_0 (3x_0^2 - 2(a+b)x_0 + ab) \right\} \\
 a_5 &= -2\alpha G_0 \gamma_0 (\alpha G_0 \Delta n_0 - \Delta \Omega) (\sigma B_0 x_0 (x_0 - a)(x_0 - b) - n_0) \left\{ 1 + 3rB_0 (3x_0^2 - 2(a+b)x_0 + ab) \right\} \\
 &\quad - 2\beta^2 (G_0)^2 \gamma_0 (\sigma B_0 x_0 (x_0 - a)(x_0 - b) - n_0) \left\{ 1 + 3rB_0 (3x_0^2 - 2(a+b)x_0 + ab) \right\} \Delta n_0 \\
 &\quad - \frac{\gamma_0}{1-\delta} (\sigma B_0 x_0 (x_0 - a)(x_0 - b) - \delta) \left[\beta^2 (G_0)^2 (\Delta n_0)^2 + (\alpha G_0 \Delta n_0 - \Delta \Omega)^2 \right] \left\{ 1 + 3rB_0 (3x_0^2 - 2(a+b)x_0 + ab) \right\}
 \end{aligned}$$

where x_0 and n_0 denote the steady states of the normalized electrical voltage and carrier density respectively.

- [1] A. J. Seeds, *Microwave Photonics*, IEEE Trans. Microwave Theory Technol., **50**, 877–887, 2002.
- [2] G. P. Agrawal, *Fiber-Optic Communications Principles and Practice, 3rd ed.*, Prentice Hall, Essex, England, 2002.
- [3] S. Suzuki, A. Teranishi, K. Hinata, M. Asada, H. Sugiyama, H. Yokoyama, *Fundamental Oscillation up to 831 GHz in GaInAs/AlAs Resonant Tunneling Diode*, Appl. Phys. Express **2**, 054501-1-3, 2009.
- [4] S. Suzuki, M. Asada, A. Teranishi, H. Sugiyama, and H. Yokoyama, *Fundamental oscillation of resonant tunneling diodes above 1 THz at room temperature*, Appl. Phys. Lett. **97**, 242102-1-3, 2010.
- [5] S. Suzuki, M. Asada, A. Teranishi, H. Sugiyama, and H. Yokoyama, *Fundamental oscillation up to 1.08 THz in resonant tunneling diodes with high-indium-composition transit layers for reduction of transit delay*, IECE Electron. Express, **9**, 385-390, 2012.
- [6] M. Feinoy, C. Sydlo, O. Cojocari and O. Meissner, *Resonant-tunneling-diode oscillators operating at frequencies above 1.1 THz*, App. Phys. Lett., **99**, 233506-1-3, 2011.
- [7] P. K. Basu, B. Mukhopadhyay, R. Basu, *Semiconductor Laser Theory*, CRC Press, Boca Rato, 2015.
- [8] R. Dupuis, *An Introduction to the developpement of the semiconductor laser*, IEEE J. Quantum Electron., **QE-23**, 651-657, 1987.
- [9] Amazon.com: Laser Head Diode Dot module WL Red Mini 650nm 6mm 5V...., Jun, 27, 2021.
- [10] En.wavespectrum-laser.com.cn , Jun, 27, 2021.
- [11] J. Ohtsubo, *Semiconductor Lasers Stability, Instability and Chaos*, (Berlin: Springer) , 2017.
- [12] E. N. Lorenz, *Deterministic nonperiodic flow*, J. Atmos. Sci., **20**, 130-140, 1963.
- [13] M. Cattani, I. L. Caldas, S. L. T. de Souza, K. C. Iarosz, *Deterministic chaos theory: Basic concepts*, Rev. Bra. En. Fi., **39**, e1309-1-13, 2017.
- [14] H. Haken, *Analogy between higher instability in fluids and lasers*, Phys. Lett., **53**, 77-78, 1975.
- [15] S. Ayadi, O. Haeberle, *The Lorenz model for single-mode homogeneously broadened laser: analytical determination of the unpredictable zone*, Cent. Europ. J. Phys., **12**, 203-214, 2014.

- [16] M. Sciamanna and K. A. Shore, *Physics and Applications of Laser Diode Chaos*, *Physics and Applications of Laser Diode Chaos*, Nat. photon., **9**, 151-162, 2015.
- [17] K. H. Lee, J. Y. Kim, W. Y. Choi, H. Kamitsuna, M. Ida, M., K. Kurishima, *Low-Cost Optoelectronic Self-Injection-Locked Oscillators*, IEEE Photon. Technol. Lett., **20**, 1151–1153, 2008.
- [18] H. K. Sung, X. Zhao, E. K. Lau, D. Parekh, D., C. J. C. Hasnain, M. C. Wu, *Optoelectronic Oscillators Using Direct-Modulated Semiconductor Lasers Under Strong Optical Injection*, J. Sel. Topics. Quantum Electron., **15**, 572–576, 2009.
- [19] D. S. Lee, J. W. Ryu, Y. J. Park, W. H. Kye, M. S. Kurdoglyan, C. M. Kim, *Stabilization of a chaotic laser and quenching*, Appl. Phys. Lett., **86**, 181104-181106, 2005.
- [20] S. T. Kingni, J. H. Talla Mbé, P. Wofo, *Semiconductor lasers driven by self sustained chaotic electronic oscillators and applications to optical chaos cryptography*, Chaos **22**, 033108-033115, 2012.
- [21] Momo Foutse, S. T. Kingni, B. Nana and P. Wofo, *Edge-emitting semiconductor laser driven by a van der Pol oscillator: analytical and numerical analysis*, Optical and Quantum Electron., **47**, 705-720, 2015.
- [22] B. Romeira and J. M. L. Figueiredo, *Optoelectronic Oscillators for Communication Systems*, L.M. Camaranha-Matos, P. Pereira, and L. Ribeiro(eds.), IFIP Advances in Info. Com. Tech. , **314**, 273–280, 2010.
- [23] X. Y. Yao, L. Maleki, *Optoelectronic Oscillator for Photonic Systems*. IEEE J. Quantum Electron., **32**, 1141–1149, 1996.
- [24] J. M. L. Figueiredo, B. Romeira, T. J. Slight, L. Wang, E. Wasige, C. N. Ironside, *Self-oscillation and period adding from a resonant tunnelling diode – laser diode circuit*, Electron. Lett., **44**, 876–877, 2008.
- [25] T. J. Slight, C. N. Ironside, *Investigation into the integration of a resonant tunnelling diode and an optical communications laser: model and experiment*, IEEE J. Quant. Electron., **43**, 580–587, 2007.
- [26] B. Romeira, J. M. L. Figueiredo, T. J. Slight, L. Wang, E. Wasige, C.N. Ironside, A. E. Kelly, R. Green, *Nonlinear Dynamics of Resonant Tunneling Optoelectronic Circuits for Wireless/Optical Interfaces*. IEEE J. Quant. Electron., **45**, 1436–1445, 2009.
- [27] J.M.L Figueiredo, *Optoelectronic Properties of Resonant Tunnelling Diodes*, (Ph.D Thesis, University of Porto, Portugal), 2000.
- [28] B. Romeira, *Dynamics of resonant tunneling diode optoelectronic oscillators*, (Ph.D. Thesis, Univ. of the Algarve, Portugal), 2012.

- [29] Y. Klofai, B. Z. Essimbi and D. Jager, *An MMIC implementation of FitzHugh-Nagumo neuron using a resonant tunneling diode nonlinear transmission line*, Phys. Scr. , **90**, 025002-1-7, 2015.
- [30] B. Z. Essimbi, A. Stöhr, I. Jäger and D. Jäger, *Neuronlike impulses in a travelling wave structure loaded with resonant tunneling diodes and air bridges*, J. Phys. Commun., **3**, 085010-1-8, 2019.
- [31] I. Jaeger, D. Kalinowshi, A. Stohr, Johan Stiens, Rger Vounckx, Dieter Jager, *Millimeter wave signal using resonant tunneling diodes NLTL-resonators*, Micro. Opt. Techno. Lett., **49**, 2907-2909, 2007.
- [32] The Electromagnetic Spectrum- infinity Theory, www.infinity-theory.com, Jun 27, 2021.
- [33] C.H. Townes, *Optical masers and their possible applications to biology*, Biophys. J., **2**, 325-329, 1962.
- [34] A.L. Schawlow and C.H. Townes, *Infrared and optical masers*, Phys. Rev.**112**, 1940-1949, 1958.
- [35] A. C. Meja, *Stochastic effects in coupled semiconductor and solid-state lasers with coexisting attractors*, Ph.D. Thesis, Centro de Investigaciones en Optica, A.C. 2015.
- [36] A. A. Kaminskii, *Laser Crystals Their Physics and Properties*, (Springer-vergah, New York, NY), 1981.
- [37] J. von Neumans, *Note on the photon-diseauilibrium-amplierf sheme, September 16, 1953*, IEEE J. Quantum Electron, **QE-23**,658-673,1987.
- [38] J. Hecht, *A short history of development*, Appl. Optics, **49**, 091002-F99-F122, 2010.
- [39] C. Masoller, *Semiconductor lasers: dynamcs & appications*,(Univ. Politècnica de Catalunya), www.fisica.edu.uy/~cri/ , ICTP-SAIFR School on Nonlinear Optics and Nanophotonics, Sao Paulo, Brazil, Dec. 03, 2013.
- [40] M. Razeghi, *Technology of quantum devices*, (London: Springer), 2010.
- [41] R. Hall, G. Fenner, J. Kingsley, T. J. Soltys, and R. O. Carlson, *Coherent light emission from GaAs junctions*, Phys. Rev. Lett., **9**, 565-577, 1962.
- [42] G. H. M. van Tartwijk and D. Lenstra, *Semiconductor lasers with optical injection and feedback*, Quantum Semiclass.,**7** 87-143, 1995.
- [43] R. Mostallino, *Development of high-power laser diodes emitting at 975nm with enhanced wall-plug efficiency and wavelength stabilization for optical pumping of doped fibers and realization of fiber lasers*, (Ph.D. Thesis, Univ. Bordeau, France), 2018.
- [44] D. R. Mostallino, J.W. McLaren, D.R. Salomao, T.P. Link, *Retinopathy from a Green Laser Pointer: a Clinicopathologic Study*. Arch. Ophtamol., **123**, 629-633, 2005.

- [45] A. D. Mengue and B. Z. Essimbi, *Complex chaos and bifurcations of semiconductor lasers*, Opt. Quantum Electron., **42**, 389–407, 2011.
- [46] A. D. Mengue and B. Z. Essimbi, *Stability and on–off chaotic states mechanisms of semiconductor lasers with optical injection on the new modified rate equation model*, Phys. Scr., **85**, 025404-1-9, 2012.
- [47] A. D. Mengue and B. Z. Essimbi, *Secure communication using chaotic synchronization in mutually coupled semiconductor lasers*, Nonlinear Dyn., **70**, 1241-1253, 2012.
- [48] A. D. Mengue and B. Z. Essimbi, *Symmetry chaotic attractors and bursting dynamics of semiconductor lasers subjected to optical injection*, Chaos, **22**, 013113-1-10, 2012.
- [49] W. C. S. Wiezorek, *Bifurcations and chaos in semiconductor laser with coherent or noisy optical injection*, Opt. Commun., **282**, 2367-1-10, 2009.
- [50] J. Ling, *Resonant tunneling diodes: theory of operation and applications*, (Univ. of Rochester, Rochester, NY 14627), 2006.
- [51] I. J. S. Coelho and J. F. Martins-Filho, J. M. L. Figuerio J. M. L., C. N. Ironside, *Modeling of light-sensitive resonant-tunneling-diode devices*, J. Appl. Phys., **95**, 8258-8263, 2004.
- [52] E. Buccafurri, *Analytical modeling of silicon based resonant tunneling diode for RF oscillator application*, (Ph.D. Thesis, Inst. Nanotech. Lyon, France), 2010.
- [53] Zhixin Yan and M.J. Deen, *New RTD Large-Signal DC Model Suitable for PSPICE*, IEEE Trans. Comput.-Aided Des. Integr. Circuits Syst., **14**, 167-172, 1995.
- [54] S. F. Nafea and A. A. S. Dessouki, *An accurate large-signal SPICE model for resonant tunneling diode*, (Int. Conf. Microelectron.,), Cairo, 19-22 Dec, pp. 508-510, 2010.
- [55] S. M. Sze and Kwork K. Ng, *Physics of Semiconductor Devices*, (John Willey & Sons, Hoboken, NJ), 2006.
- [56] G. Raphael, A. Cathelin and Y. Deval, *Théorie des oscillateurs verrouillés par injection*, (Confer. Paper Toulouse, France) HAL Id : hal-01552339, May 2016.
- [57] J.P. Sun J.P., Mazumder and J.N. Schulman, *Resonant Tunneling Diodes: Models and Properties*, Proceed. IEEE, **86**, 641-660, 1998.
- [58] J. M. L. Figueiredo, C. N. Ironside and C. R. Stanley, *Electric field switching in a RTD-EAM*, IEEE J. Quantum Electron., **37**, 1547-1552, 2001.
- [59] J. M. L. Figueiredo, C. R. Stanley, A. R. Boyd, C. N. Ironside, S. G. McMeekin, and A. M. P. Leite, *Optical Modulation in a resonant tunneling relaxation oscillator*, Appl. Phys. Lett., **74**, 1197-1199, 1999.

- [60] J. M. L. Figueiredo, C. R. Stanley, A. R. Boyd, C. N. Ironside, S. G. McMeekin, and A. M. P. Leite, *Optical Modulation at around 1550 nm in InGaAlAs optical waveguide containing a In-GaAs/AlAs resonant tunneling diode*, Appl. Phys. Lett., **75**, 3443-3445.
- [61] S. G. McMeekin, M. R. S. Taylor, B. Vögele, C. R. Stanley, and C. N. Ironside, *Franz-Keldysh effect in optical waveguide containing a resonant tunneling diode*, Appl. Phys. Lett., **65**, 1076-1078, 1994.
- [62] T. J. Slight, B. Romeira and L. Wang, *A Liénard Oscillator resonant tunneling diode-laser diode hybrid integrated circuit: model and experiment*, IEEE J. Quantum Electron., **44**, 1158-1163, 2008.
- [63] B. Romeira, J.M. Figueiredo, and Javaloyes, *Delay dynamics of neuromorphic optoelectronic nanoscale resonators: Perspectives and applications*, Chaos **27**, 114323-1-18, 2017.
- [64] B. Romeira et al, *Chaotic Dynamics in Resonant Tunneling Optoelectronic Voltage Controlled Oscillators*, IEEE Photonics Technol. Lett., **21**, 1819-1821, 2009.
- [65] B. Romeira, K. Seunarine, C. N. Ironside, A. Kelly and J. M. L. Figueiredo, *A Self-Synchronized Optoelectronic Oscillator Based on an RTD Photodetector and a Laser Diode*, IEEE Photonics Technol. Lett., **23**, 1148-1150, 2011.
- [66] C. N. Ironside, B. Romeira and J. M. L. Figueiredo, *Resonant Tunneling Diode Photonics*, USA, Morgan & Claypool Publishers, 2019.
- [67] L. A. Coldren and S. W. Corzine, *Diode Lasers and Photonic Integrated Circuits*, (John Wiley & Sons, Inc.), 1995.
- [68] A. D. Mengue, *Dynamics of optically injection semiconductor lasers with application to secure communications*, (Ph. D. Thesis, Univ. Yaounde 1, Cameroon), 2012.
- [69] C. O. Weiss, R. Vilaseca, *Dynamics of lasers*, (VCH, Weinheim), 1991.
- [70] Amitava Kundu and Pritha Das, *Global Stability, Bifurcation, and Chaos Control in a Delayed Neural Network Model*, Hindawi Pub. Corp. Ad. Art. Neur. Systems, **2014**, 369230-1-8, 2014.
- [71] R. Shaw, *Strange attractors, chaotic behavior, and information of flow*, Z. Naturforsch, **36a**, 80-112, 1981.
- [72] N. Stankevch, A. Kazakov, S. Gonchen, *Scenario of hyperchaos occurrence in 4D Rossler system*, Chaos, **30**, 12319-1-15, 2020.
- [73] F. Yang, Y. Cao, L. Chen and Q. Li, *Sequence of route to chaos in a Lorenz-type systems*, Hindawi Disc. Dyn. Nat. Society, **2020**, 3162170-1-10, 2020.
- [74] Characteristics of non-linear systems: *Lorenz Attractor*, ([http:// www.students.uiuc.edu/~ag-ho/choas](http://www.students.uiuc.edu/~ag-ho/choas)), May, 08, 2021.

- [75] C. Çelik, H. Merdan, *Hopf bifurcation analysis of coupled delayed-differential equations*, Appl. Math. Comp. **219**, 6605-6617, 2013.
- [76] P. Blanchard, R. L. Devaney, G. R. Hall, *Differential Equations*, (London: Thompson), 2006.
- [77] S. Sharma, B. C. Etienne, M. H. Lowenberg, S. A. Neild and B. Krauskopf, *Numerical continuation and bifurcation analysis in aircraft design: an industrial perspective*, Phil. Trans. R. Soc. A **373**, 20140406-1-16, 2015.
- [78] S. H. Strogatz, *Nonlinear Dynamics and Chaos*, (Cambridge, Massachusetts, Addison-Wesley), 1994.
- [79] L. Dingjun, W. Xia, Z. Deming & H. maoan, *Bifurcation Theory and Methods of Dynamical Systems*, (World Scientific), 1997.
- [80] J. P. Keener, *Infinite Period Bifurcation and Global Bifurcation Branches*, SIAM J. Appl. Math., **41**, 127–144, 1981.
- [81] R. Rocha, J. Ruthiramorthy and T. Kathamuthu, *Memristive oscillator based on Chua's circuit: stability analysis and hidden dynamics*, Nonlinear Dyn. **88**, 2577-2587, 2017.
- [82] B. C. Bao, Q. Xu, B. H. Bao, M. Chen, *Extreme multistability in a memristive circuit*, Nonlinear Dyn., **81**, 215-226, 2016.
- [83] S. H. Fu, Q. S. Lu, *Set stability of controlled Chua's circuit under a non-smooth controller with the absolute value*, Int. J. Control Autom. Syst., **12**, 507-517, 2014.
- [84] J. J. E. Slotine, W. Li, *Applied Nonlinear Control*, (Prentice-Hall Inc, Englewood Cliffs), 1991.
- [85] [https://math.libretexts.org/Bookshelves/Applied_Mathematics/Book%3A, Introduction to the Modeling and Analysis of Complex Systems DiscreteTime Models Linear Stability Analysis of Discrete-Time Nonlinear Dynamical Systems](https://math.libretexts.org/Bookshelves/Applied_Mathematics/Book%3A_Introduction_to_the_Modeling_and_Analysis_of_Complex_Systems/Discrete-Time_Models/Linear_Stability_Analysis_of_Discrete-Time_Nonlinear_Dynamical_Systems), Nov. 03, 2020.
- [86] T. Akimoto, M. Nakagawa, S. Shinkai and Y. Aizawa, *Generalized Lyapunov exponent as a unified characterization of dynamical instabilities*, Phys. Rev. E **91**, 012926-1-7, 2015.
- [87] W. Ott, M. A. Rivas and J. West, *Observing Lyapunov exponents of infinite-dimensional dynamical systems*, J. Stat. Phys., **161**, 1098-1111, 2015.
- [88] Z. R. Novakovic, *Solving systems of nonlinear equations using the Lyapunov direct method*, Comput. Math. Appl., **20**, 19–23, 1990.
- [89] M. W. Eskew and R. H. Simoyi, *Lyapunov Exponents and the Belousov-Zhabotinsky Oscillator: An Interactive Computational Approach*, S. Afr. J. Chem., **70**, 82–88, 2017.
- [90] E. E. Mahmoud and F. S. Abood, *A New Chaotic Complex Model and Its Complex Antilag Synchronization*, Hindawi Complexity, **2017**, 3848953-1-13, 2017.

- [91] A. Wolf, J. B. Swift, H. L. Swinney and J. A. Vastano, *Determining Lyapunov exponents from time series*, Physica D, **16**, 285-317, 1985.
- [92] G. Byrne and Hindmarsh, *RK methods prove popular at IMA conference on numerical ODE's*, SIA, News, **23/2**, 14-15, 1990.
- [93] J. D. Lambert, *Numerical methods for ordinary differential systems, the initial value problem*, (John Wiley & Sons Ltd), 1991.
- [94] H. Musa, I. Saidu, M. Y. Waziri, *A simplified derivation and analysis of fourth order Runge-Kutta methods*, int. J. comp. applica., **9**, 0975-8887, 2010.
- [95] E. Suli and D. F. Mayers, *An introduction to numerical analysis*, (Cambridge University Press), 2003.
- [96] D. E. Essebe, A. D. Mengue and B. Z. Essimbi, *Stochastic behavior of an external optically injected single-mode semiconductor laser including Langevin noise sources*, Phys. Scr., **94**, 115501-1-12, 2019.
- [97] D. E. Essebe, A. D. Mengue and B. Z. Essimbi, *Multiscroll chaotic attractors in optical injected semiconductor laser driven by a resonant tunneling diode current*, Optik, **212**, 164740-1-8, 2020.
- [98] A. Wolf, J. B. Swift, H. L. Swinney and J. A. Vastano, *Determining Lyapunov exponents from time series*, Physica D, **16**, 285-317, 1985.
- [99] M. Yamada, *Theory of Semiconductor Lasers Stability*, (Japan: Springer), 2014.
- [100] C. H. Henry, *Theory of linewidth of semiconductor lasers*. IEEE J. Quantum Electron., **QE18**, 259-264, 1982.
- [101] I. Fatadin, D. Ives D. and M. Wicks, *Numerical simulation of intensity and phase noise from extracted parameters for CW DFB lasers*, IEEE J. Quantum Electron., **42**, 934-941, 2006.
- [102] M. Yamada, *Mechanism of the noise reduction method by superposition of high-frequency current for semiconductor injection lasers*, IEEE J. Quantum Electron., **27**, 380-388, 1991.
- [103] M. S. Sazzad, Imran, F. F. Tonni and S. I. Sumi, *Numerical Analysis of Intensity and Phase Noise of Solitary AlGaAs Semiconductor Lasers Operating in Multimode*, Int. J. Sci. Eng. Res., **7**, 1026-1033, 2016.
- [104] M. A. Newkirk and K. J. Vahala, *Amplitude-Phase Decorrelation: A Method for Reducing Intensity Noise in Semiconductor Lasers*, IEEE J. Quantum Electron., **27**, 13-22, 1991.
- [105] K. H. Husham, F. A. Ahmad, A. M. Ghafour, A. M. Mohd, S. M. Ahmad, *Relative Intensity Noise Reduction by Optimizing Fiber Grating Fabry-Perot Laser Parameters*, IEEE J. Quantum Electron., **48**, 375-383, 2012.

- [106] W. K. Marshall, J. Paslaski and Yariv, *Reduction of relative intensity noise of the output field of semiconductor lasers due to propagation in dispersive optical fiber*, Appl. Phys. Lett., **68**, 2496-2498, 1996.
- [107] M. Yamada, *Variation of intensity noise and frequency noise with the spontaneous emission factor in semiconductor lasers*, IEEE J. Quantum Electron., **30**, 1511-1519, 1994.
- [108] L.-G. Zei, S. Ebers, J.-R. Kropp, *Noise performance of multimode VCSELs*, J. Lightwave Technol., **19**, 884-892, 2001.
- [109] G. Yabre, G. H. Waardt De, H. P. A. Van der Boom. , *Noise characteristics of single-mode semiconductor lasers under external light injection*, IEEE J. Quantum Electron., **36**, 385-393, 2000.
- [110] F. Mogensen, H. Olesen, and G. Jacobsen, *Locking conditions and stability properties for a semiconductor laser with external light injection*, IEEE J. Quantum Electron., **21**, 784–793, 1985.
- [111] A. Daly, B. Roycroft and B. Corbett, *Stable locking phase limits of optically injected semiconductor lasers*, Opt. Express, **21**, 30126-39, 2013..
- [112] B. Romeira, J. Figueiredo, T. J. Slight, L. Wang, E. Wasige, C. N. Ironside, J. M. Quintana and M. J. Avedillo, *Synchronisation and chaos in laser diode driven by a resonant tunneling diode*, IET Optoelectronics, **2** 211-215, 2008.
- [113] C.H. Wang, H. Xia and L. Zhou, *A memristive hyperchaotic multiscroll jerk system with controllable scroll numbers*, Int. J. Bif. Chaos, **27**, 750091-1-15, 2017.
- [114] X. Xia, Y. Zeng and L. Zhou, *Coexisting multiscroll hyperchaotic attractors generated from a novel memristive jerk system*, Pramana-J. Phys., **91**, 81-1-14, 2018.
- [115] S. Bhalekar, *Infinite-scroll attractor generated by the complex penulum model*, Int. J. Anal., **2013**, 368150-1-3, 2013.
- [116] F. Li, C. Yao, *The infinite-scroll attractor and energy transition in chaotic circuit*, Nonlinear Dyn., **84**, 2305–2315, 2016.
- [117] J. Ma, X. Wu, R. Chu, *Selection of multi-scroll attractors in Jerk circuits and their verification using Pspice*, Nonlinear Dyn, **76**, 1951–1962, 2014.
- [118] J. Ma, P. Zhou, B. Ahmad, G. Ren G and C. Wang, *Chaos and multiscroll attractors in RCL-shunted junction coupled jerk circuit connected by memristor*, PloS one, **13**, e0191120-1–21, 2018.
- [119] D. E. Essebe, A. D. Mengue and B. Z. Essimbi, *Simulink implementation of a new optoelectronic integrated circuit: Stability analysis and infinite-scroll attractor*, Optical and Quantum Electron., **53**, 388-1-16, 2021.
- [120] S. P. Dawson, C. Grebogi, J. A. Yorke, I. Kan, & H. Kocak, *Antimonotonicity: Inevitable reversals of period-doubling cascades*, Phys. Lett. A, **162**, 249–254, 1992.

- [121] J. Kengne, V. R. Folifack Signing, J. C. Chedjou, J. C., & G. D. Leutcho, *Nonlinear behavior of a novel chaotic jerk system: Antimonotonicity, crises, and multiple coexisting attractors*. *Int. J. Dyn. Control*, **6**, 468–485, 2017.
- [122] L. K. Kengne et al. *A broken symmetry approach for the modeling and analysis of antiparallel diodes-based chaotic circuits: a case study*, *Anal. Integr. Cir. Sig. Process.* **104**, 205–227, 2020.
- [123] M. Bier and T. C. Bountis, *Remerging Feigenbaum trees in dynamical systems*, *Phys. Lett. A*, **104**, 239–244, 1984.
- [124] Chlouverakis and Adams, *Antimonotonicity and maximal complexity in optically injected two-section lasers*, *IEEE J. Sel. Top. Quantum Electron.*, **12**, 398-404, 2006.
- [125] A. Bayani, K. Rajagopal, A. J. M. Khalaf, S. Jafari, *Dynamical analysis of a new multistable chaotic system with hidden attractor : antimonotonicity, coexisting multiple attractors, and offset boosting*, *Phys. Lett. A*, **383**, 1450-1456, 2019.
- [126] A.N. Mouelas, T.F. Fozin, R. Kengne, J. Kengne, H.B. Fotsin, B.Z. Essimbi, *Extremely rich dynamical behaviors in a simple nonautonomous Jerk system with generalized nonlinearity : hyperchaos, intermittency, offset-boosting and multistability*, *Int. J. Dyn. Control*, **8**, 51-69, 2018.
- [127] M. Destroches, J Guckenheimer, B. Krauskopt, C. Kuehn, *Mixed-Mode Oscillations with Multiple Time Scales*, *Siam Rev., Soc. for Ind. Appl. Math.*, **54**, 211–288, 2012.
- [128] M. Eugene Izhilevich, *Neural Excitability, Spiking and Bursting*, *Int. J. Bifur. and Chaos*, **10**, 1171-1266, 2000.
- [129] Y. Nagata.T. Endo, H. Kamata S. Kuniyassi, T. Kousaka and N. Inaba, *Mixed-mode oscillations and mixed-mode oscillation-incrementing bifurcations in an extended BVP oscillation with a diode*, *Wold conf. Eng. Comp. Sci.,WCECS*, **2019** 56-60, 2019.
- [130] E. Kutafina, *Mixed mode oscillations in the Bonhoeffer-van der Pol oscillator with weak periodic perturbation*, *Comp. Appl. Math.*, **34**, 81–92, 2015.
- [131] H. Takahashi, T.Kousaka, H. Asahara, N. Stankevich, and N. Inaba, *Mixed-mode oscillation-incrementing bifurcations and a devil's staircase from a nonautonomous, constrained Bonhoeffer–van der Pol oscillator*, *Prog. Theor. Exp. Phys.* **2018**, 103A02-1-16, 2018.
- [132] N. Inaba, T. Kousaka, *Nested mixed-mode oscillations*, *Physica D*, **401**, 132152-1-17, 2020.

List of Publications

- **Essebe DE, Mengue AD. and Essimbi B.Z.**, *Stochastic behavior of an external optically injected semiconductor laser including Langevin noise source*, *Phys. Scr.* **94**, 115501, 2019.
- **Essebe DE, Mengue AD. and Essimbi B.Z.**, *Multiscroll chaotic attractor in optically injected semiconductor laser driven by a resonant tunneling diode current*, *Optik* **212**, 164740, 2020
- **Essebe DE, Mengue AD. and Essimbi B.Z.**, *Simulink implementation of a new optoelectronic integrated circuit: Stability analysis and infinite-scroll attractor*, *Optical and , Quantum Electron*, **53**, 388-1-16, 2021

ACCEPTED MANUSCRIPT

Stochastic behavior of an external optically injected single-mode semiconductor laser including Langevin noise sources

To cite this article before publication: David Essebe *et al* 2019 *Phys. Scr.* in press <https://doi.org/10.1088/1402-4896/ab0c27>

Manuscript version: Accepted Manuscript

Accepted Manuscript is “the version of the article accepted for publication including all changes made as a result of the peer review process, and which may also include the addition to the article by IOP Publishing of a header, an article ID, a cover sheet and/or an ‘Accepted Manuscript’ watermark, but excluding any other editing, typesetting or other changes made by IOP Publishing and/or its licensors”

This Accepted Manuscript is © 2019 IOP Publishing Ltd.

During the embargo period (the 12 month period from the publication of the Version of Record of this article), the Accepted Manuscript is fully protected by copyright and cannot be reused or reposted elsewhere.

As the Version of Record of this article is going to be / has been published on a subscription basis, this Accepted Manuscript is available for reuse under a CC BY-NC-ND 3.0 licence after the 12 month embargo period.

After the embargo period, everyone is permitted to use copy and redistribute this article for non-commercial purposes only, provided that they adhere to all the terms of the licence <https://creativecommons.org/licenses/by-nc-nd/3.0>

Although reasonable endeavours have been taken to obtain all necessary permissions from third parties to include their copyrighted content within this article, their full citation and copyright line may not be present in this Accepted Manuscript version. Before using any content from this article, please refer to the Version of Record on IOPscience once published for full citation and copyright details, as permissions will likely be required. All third party content is fully copyright protected, unless specifically stated otherwise in the figure caption in the Version of Record.

View the [article online](#) for updates and enhancements.

Stochastic Behavior of an External Optically Injected Single-Mode Semiconductor Laser including Langevin Noise Sources

D.E. Essebe⁽¹⁾, A.D. Mengue⁽¹⁾ and B. Z. Essimbi*^(1,2)

⁽¹⁾Department of Physics, Faculty of Science, University of Yaounde I, PO Box 812 Yaounde, Cameroon

⁽²⁾ZHO, Optoelektronik, Universität Duisburg-Essen, D-47048 Duisburg, Germany

ABSTRACT

In this paper stochastic dynamics of an optically injected semiconductor laser (SCL) operating in the single mode are theoretically and numerically investigated in the framework of the Langevin approach. The modified novel analytical expressions of relative intensity noise (RIN) and frequency noise (FN), both for master laser and slave one have been developed. The effective gain coefficient (EGC) parameter of this rate equation model allows achieving noise suppression of 65dB in addition to the diminution of RIN spectra carried out by classic decisive parameters. The modified Schawlow-Townes formula is also proposed for laser linewidth. Moreover the induced modulation of a full width half maximum (FWHM) by the mean EGC allows to more significantly reduce laser linewidth unlike to those of classic SCL when the EGC is lower than 0.5 opening the route to the ideal laser linewidth which is discussed. The impact of linewidth enhancement factor (LEF), spontaneous emission factor (SEF) and EGC is investigated in noise spectra around the threshold current.

Keywords: Semiconductor laser, Langevin noise, effective gain coefficient, relative intensity noise, frequency noise, linewidth, small signal analysis.

PACS codes: 42.55.Px, 42.60.Mi

*Corresponding author

E-mail address: bessimb@yahoo.fr

1
2
3 It is well known that laser optical injection consists in seeding a free running slave laser
4 (SL) with a master laser (ML) beam [1], in a frame of the unidirectional coupling between two
5 lasers. The light from a first laser so-called ML is injected into the cavity of another laser
6 known as slave which represents the transmitting source. Unidirectional coupling is ensured
7 by an optical isolator. Over the past decade, the study of optical injection has attracted many
8 researchers [2] and, single-mode semiconductor laser (SCL) subjected to an external optical
9 injection has shown their great interest leading to the laser injected-locking to be regarded as a
10 high-speed photonic microwave source [3]. This seeding opens a rich variety of dynamical
11 behavior in laser optical wave. In other terms injection-locking improves significantly the
12 performances of slave lasers leading to several benefits for many applications including
13 optical communications, microwave signal generation, all-optical signal processing [1, 4].
14
15
16
17
18
19
20
21
22

23 However some laser systems are likely of generating noise due to intrinsic and extrinsic
24 mechanism such as spontaneous emission, carrier recombination and so on which tend to
25 decrease the performance of optical emission, manifesting in the form of relative intensity
26 noise, frequency noise and widening of laser linewidth [5-7]. Several investigations have
27 proposed the possibilities to reduce noise level in SCLs by carrying out classic decisive
28 parameters. Among which the increasing of laser power or injection biased current [8, 9] the
29 suppression of high frequency current [10], the control of optical feedback [11], noise
30 reduction by the method of amplitude-phase decorrelation based on the variation of the
31 linewidth enhancement factor [12], the control of cavity volume and gain compressor
32 temperature [13] and so on [14]. All of these investigations have been explored using classic
33 rate equations models [1-12].
34
35
36
37
38
39
40
41

42 In 2011, Mengue and Essimbi have developed modified rate equations model of SCLs
43 subject to optical injection [15]. In addition, their recent works have shown that SCLs exhibit
44 the interesting dynamics by the means of effective gain coefficient (EGC) control [16, 17] that
45 classic rate equations models could not display. In other hand it has been shown that the
46 variations of the EGC-parameter control the dynamics generated by classic decisive
47 parameters such as linewidth enhancement factor (LEF) and optical injection rate: which has
48 shown interesting improvement in optics [16, 17]. It has also been shown that, the EGC leads
49 to the generation of hypersensitivity, useful for secure communication systems including
50 chaotic synchronization by coupling two SCLs [18], in addition to the quasi perfect recovery
51 of the encrypted digital message. Knowing that this SCL model has been designated to be
52 connected with optical devices and owing intrinsic random mechanisms, it is obvious that,
53
54
55
56
57
58
59
60

1
2
3 this SCL model is affected by noises. Thus, in this paper we develop modified novel
4 analytical expressions of relative intensity noise (RIN) and frequency noise (FN) for master
5 and slave lasers. The impacts of the EGC-parameter are carried out for noise suppression
6 investigations in addition to the diminution of RIN spectra achieved by classic decisive
7 parameters. Moreover we explore from the mean EGC, the reduction of laser linewidth
8 through the proposed modified Schawlow-Townes formula. This allows envisaging a route to
9 the narrower ideal laser linewidth.

10 The paper is organized as follows. The next section describes the injected SCL rate-equations
11 model for the slave including Langevin noise sources that account the generation of the
12 fluctuations. Section 3 outlines the linearization of the rate equations following the small-
13 signal analysis, with the help of Fourier transformations. Here, mathematical novel
14 expressions of RIN, FN and FWHM both for ML and SL are derived and analyzed. Section 4
15 concludes the paper.

26 2. The injected SCL rate equations

27 We introduce the stochastic single mode rate-equations including few changes on
28 original equations. Based upon Fig.1, the dynamics of the SCL (slave laser) is described from
29 the rate equations for the photon density $S(t)$, the electron density $N(t)$ and optical phase
30 $\psi(t)$ [15]. Note that, the rate equations model from Refs.[15-18] is a predictive description of
31 laser electrical field and optical phase derived from the model depicted in Fig. 1. However,
32 laser output exhibits intensity as well as phase fluctuations. Then, in a strict sense, the
33 stochastic description of rate equations requires to take into account the spontaneous emission
34 noise (SEN) as well as those of Langevin noise. Therefore, one has

$$35 \frac{d}{dt} S(t) = \frac{(1-\gamma)}{(1+\gamma)} [G_N(N(t) - N_{th})] S(t) + 2 \frac{k_{inj}}{\tau_{in}^*} \sqrt{S_{inj} S(t)} \cos[\psi(t) - \varphi_{inj}(t)] + R_{sp}(t) + F_S(t), \quad (1)$$

$$36 \frac{d}{dt} \psi(t) = \frac{1}{2} \alpha \frac{\gamma}{(1+\gamma)} [G_N(N(t) - N_{th})] - \frac{k_{inj}}{\tau_{in}^*} \sqrt{\frac{S_{inj}}{S(t)}} \sin[\psi(t) - \varphi_{inj}(t)] - \Delta\omega + F_\psi(t), \quad (2)$$

$$37 \frac{d}{dt} N(t) = J - \frac{N(t)}{\tau_r} - \left\{ \frac{1}{\tau_p} + [G_N(N(t) - N_{th})] \right\} S(t) + F_N(t), \quad (3)$$

$$38 \psi(t) = \varphi_{inj}(t) - \Delta\omega t, \quad (4)$$

39
40
41
42
43
44
45
46
47
48
49
50
51
52
53
54
55
56
57
58
59
60

$$R_{sp}(t) = \frac{\beta_{sp} \xi N(t)}{\tau_r}. \quad (5)$$

In contrast of the model equations in Ref. [16], here we consider photon density $S(t)$, which is related to the amplitude of electrical field inside the cavity $E(t)$, by $S(t) = |E(t)|^2$. The spontaneous emission noise source is given by R_{sp} ; $\psi(t) = \varphi_{inj}(t) - \Delta\omega t$ is the phase difference between the internal and the injected fields; $\Delta\omega$ is the frequency detuning; S_{inj} is the injected photons number from ML; β_{sp} is the spontaneous emission factor (SEF) representing the fraction of spontaneous emission light coupled to the laser mode; ξ is the confinement factor; the functions $F_x(t)$ with $x = S, N, \psi$ are the Langevin noises sources; J is the pumping parameter corresponding to current density, N_{th} is the carrier density at the threshold, τ_r the carrier lifetime, τ_p the photon lifetime, γ is the effective gain coefficient (EGC), k_{inj} the injection parameter, $\tau_{in}^* = \tau_{in} / \gamma$ is the effective time of light in the laser cavity where the round-trip time inside the laser cavity is τ_{in} .

3. Noise characteristics and discussions

3.1. Master laser noises

Equations (1-5) explicitly show that, slave rate equations include photons density $S_{inj}(t)$ and optical phase $\varphi_{inj}(t)$ from ML. It can seem so clear that, to understand stochastic dynamics of slave, we have to study ML noise contribution [2]. Thus, we do not take into account the injection parameters. The ML is described by the same equations as SL but without optical injection parameters. For better understanding, we refer to ML by the subscript “inj” and assume that ML and SL are identical. Then ML rate equations are linearized taking small-signal analysis around their steady states values for $S_{inj}(t)$, $\varphi_{inj}(t)$ and $N_{inj}(t)$ as follows:

$$x_{inj}(t) = (x_{inj})_0 + \delta x_{inj}(t) \quad (6)$$

where x_{inj} is either S_{inj} , φ_{inj} or N_{inj} .

The spontaneous emission contribution is:

$$R_{sp_{inj}}(t) = \left(R_{sp_{inj}} \right)_0 + \left(\frac{\partial R_{sp_{inj}}}{\partial N_{inj}} \right)_0 \delta N_{inj}(t). \quad (7)$$

Next, the photons number, optical phase, carrier density and spontaneous emission rate are separated into steady states and fluctuations terms,

$$x_{inj}(t) = \left(x_{inj} \right)_0 + \int_{-\infty}^{\infty} \tilde{\delta} x_{inj}(\omega) e^{j\omega t} d\omega; \quad (8)$$

$$R_{sp_{inj}}(t) = \left(R_{sp_{inj}} \right)_0 + \left(\frac{\partial R_{sp_{inj}}}{\partial N_{inj}} \right)_0 \int_{-\infty}^{\infty} \tilde{\delta} N_{inj}(\omega) e^{j\omega t} d\omega \quad (9).$$

Because of their zero means values (due to the stochastic nature of all noises sources), frequency components of Langevin noises for ML are defined by,

$$F_{x_{inj}}(t) = \int_{-\infty}^{\infty} \tilde{F}_{x_{inj}}(\omega) e^{j\omega t} d\omega \quad (10)$$

where x_{inj} is either S_{inj} , φ_{inj} or N_{inj} .

We treat the problem by linearization and we neglect second order fluctuations. Also, we separate continuous and fluctuated terms. Applying Fourier transformations, we get,

$$\left(S_{inj} \right)_0 = \left(J_{inj} - \frac{N_{th_{inj}}}{\tau_{r_{inj}}} \right) \tau_{p_{inj}} = \left(J_{inj} - J_{th_{inj}} \right) \tau_{p_{inj}}, \quad (11a)$$

$$\left(\varphi_{inj} \right)_0 = 0, \quad (11b)$$

$$\left(N_{inj} \right)_0 = N_{th_{inj}}, \quad (11c)$$

$$\left(R_{sp_{inj}} \right)_0 = \frac{\beta_{sp_{inj}} \xi_{inj} \left(N_{inj} \right)_0}{\tau_{r_{inj}}} \quad (11d)$$

$$\begin{bmatrix} \delta \tilde{S}_{inj}(\omega) \\ \delta \tilde{N}_{inj}(\omega) \end{bmatrix} = \begin{bmatrix} j\omega + m_{11} & m_{12} \\ m_{21} & j\omega + m_{22} \end{bmatrix}^{-1} \begin{bmatrix} \tilde{F}_{S_{inj}}(\omega) \\ \tilde{F}_{N_{inj}}(\omega) \end{bmatrix}, \quad (12)$$

$$\delta\tilde{\varphi}_{inj}(\omega) = \frac{1}{j\omega} \left\{ m_{32} \delta\tilde{N}_{inj}(\omega) + \tilde{F}_{\varphi_{inj}}(\omega) \right\}, \quad (13)$$

where

$$m_{11} = 0, \quad (14a)$$

$$m_{12} = - \left\{ \frac{(1-\gamma_{inj})}{(1+\gamma_{inj})} G_{N_{inj}}(S_{inj})_0 + \left(\frac{\partial R_{sp_{inj}}}{\partial N_{inj}} \right)_{(N_{inj})_0} \right\}, \quad (14b)$$

$$m_{21} = \frac{1}{\tau_{p_{inj}}}, \quad (14c)$$

$$m_{22} = \frac{1}{\tau_{r_{inj}}} + G_{N_{inj}}(S_{inj})_0, \quad (14d)$$

$$m_{32} = \frac{1}{2} \alpha_{inj} \frac{\gamma_{inj}}{(1+\gamma_{inj})} G_{N_{inj}}. \quad (14e)$$

Here, $\delta\tilde{S}_{inj}(\omega)$, $\delta\tilde{N}_{inj}(\omega)$, $\delta\tilde{\varphi}_{inj}(\omega)$, $\tilde{F}_{S_{inj}}(\omega)$, $\tilde{F}_{N_{inj}}(\omega)$ and $\tilde{F}_{\varphi_{inj}}(\omega)$ are the Fourier transforms of time functions corresponding to the fluctuation terms $\delta S_{inj}(t)$, $\delta N_{inj}(t)$, $\delta\varphi_{inj}(t)$, $F_{S_{inj}}(t)$, $F_{N_{inj}}(t)$ and $F_{\varphi_{inj}}(t)$, respectively.

Using Cramer's rule, we find the spectral densities for photon density, carrier density and phase density given by the following Eqs. respectively,

$$\langle |\delta\tilde{S}_{inj}(\omega)|^2 \rangle = \frac{1}{|\Delta(\omega)|^2} \left((\omega^2 + m_{22}^2) \langle |\tilde{F}_{S_{inj}}(\omega)|^2 \rangle + m_{12}^2 \langle |\tilde{F}_{N_{inj}}(\omega)|^2 \rangle - 2m_{22}m_{12} \langle \tilde{F}_{S_{inj}}(\omega) \tilde{F}_{N_{inj}}(\omega)^* \rangle \right) \quad (15)$$

$$\langle |\delta\tilde{N}_{inj}(\omega)|^2 \rangle = \frac{1}{|\Delta(\omega)|^2} \left(m_{21}^2 \langle |\tilde{F}_{S_{inj}}(\omega)|^2 \rangle + \omega^2 \langle |\tilde{F}_{N_{inj}}(\omega)|^2 \rangle \right) \quad (16)$$

$$\langle |\delta\tilde{\varphi}_{inj}(\omega)|^2 \rangle = \frac{1}{\omega^2} \left\{ \frac{1}{|\Delta(\omega)|^2} m_{32}^2 \left(m_{21}^2 \langle |\tilde{F}_{S_{inj}}(\omega)|^2 \rangle \right) + \langle |\tilde{F}_{\varphi_{inj}}(\omega)|^2 \rangle \right\} \quad (17)$$

$$|\Delta(\omega)|^2 = (m_{12}m_{21} + \omega^2)^2 + \omega^2 m_{22}^2. \quad (18)$$

Equations (15)-(18) reveal that the spectral characteristics of the ML cannot be determined unless the spectral densities of Langevin noise sources are known. Following the formulas given in Ref. [8] and according to some improvements mentioned in section 2, diffusion coefficient associated with each noise sources can be expressed by taking their correlations [19]. Among these, Langevin terms are given such as,

$$\langle |\tilde{F}_{S_{inj}}(\omega)|^2 \rangle = 2(R_{sp_{inj}})_0 (S_{inj})_0, \langle |\tilde{F}_{\varphi_{inj}}(\omega)|^2 \rangle = \frac{(R_{sp_{inj}})_0}{2(S_{inj})_0}, \langle \tilde{F}_{S_{inj}}(\omega)\tilde{F}_{\varphi_{inj}}(\omega)^* \rangle = 0 \quad (19)$$

$$\langle |\tilde{F}_{N_{inj}}(\omega)|^2 \rangle = 2 \left[(R_{sp_{inj}})_0 (S_{inj})_0 + \frac{N_{th_{inj}}}{\tau_{S_{inj}}} \right], \langle \tilde{F}_{S_{inj}}(\omega)\tilde{F}_{N_{inj}}(\omega)^* \rangle = -2(R_{sp_{inj}})_0 (S_{inj})_0, \\ \langle \tilde{F}_{N_{inj}}(\omega)\tilde{F}_{\varphi_{inj}}(\omega)^* \rangle = 0. \quad (20)$$

A more general expression of the RIN is given by

$$RIN_{inj} = \frac{\langle \langle |\tilde{S}_{inj}(\omega)|^2 \rangle \rangle}{[(S_{inj})_0]^2} \quad (21)$$

From Eqs. (14), (15) and (19), (21) leads to master laser RIN expression,

$$RIN_{inj} = \frac{2(R_{sp_{inj}})_0}{(S_{inj})_0} \times \frac{\omega^2 + m_{22}^2 + m_{12}^2 \left[1 + \frac{N_{th_{inj}}}{\tau_{S_{inj}}(R_{sp_{inj}})_0(S_{inj})_0} \right] + 2m_{12}m_{22}}{(m_{12}m_{21} + \omega^2)^2 + \omega^2 m_{22}^2} \quad (22)$$

where m_{12} , m_{21} , m_{22} and m_{32} are defined in Eqs.(14).

We assume the following numerical values of laser parameters: $\alpha_{inj} = 6$, $G_{N_{inj}} = 8.1 \times 10^{-13} m^3 \cdot s^{-1}$, $\tau_{p_{inj}} = 2ps$, $\tau_{r_{inj}} = 2ns$, $N_{0_{inj}} = 1.1 \times 10^{24} m^{-3}$, $N_{th_{inj}} = 1.7173 \times 10^{24} m^{-3}$, $J_{th_{inj}} = 8.5865 \times 10^{32} m^{-3} \cdot s^{-1}$, $\tau_{in} = 8ps$, $\xi_{inj} = 0.2$. Other parameters used are found on figure captions.

Figure 2(a) shows the spectra of RIN variation curve of ML (free-running laser) for some values of bias current and Fig. 2(b) presents the RIN when EGC changes. The RIN exhibits a resonance phenomenon at the resonance frequency. This will be easier to see by the presence of peaks on illustrative curves, by increasing the injection current, from 1.5 to 12 times the

1
2
3 threshold current (Fig. 2(a)). The RIN spectral is a flat white noise characteristic in low-
4 frequency regime due to the small amplitude of the intensity fluctuation. In the high-
5 frequency regime, the spectra exhibit the well-known carrier photon resonance peak around
6 the resonance frequency. The peaks show that, the stochastic behavior of the laser is affected
7 by the natural resonance of electron and photon populations [20]. The increase of current is
8 associated with an increase in the relaxation oscillation peaks. The fact that the photon
9 number and carrier number in the laser cavity are random variable makes that noise intensity
10 be different from a white noise spectrum. Similar results have been obtained by numerical
11 simulations or observed in experiments [14].

12
13
14
15
16
17
18
19 Moreover, when the laser operating above the threshold (see Fig. 2(b)), varying the EGC
20 values reveals a significant diminution of RIN spectra in the low frequency form -110dB/Hz
21 to -175dB/Hz when EGC moving from 0.99 to 0.1. This noise level is allowed to
22 communication systems [8] for EGC values less than or equal to 0.75 for a bias current two
23 times the threshold. If we need to reduce RIN level we must then increase current. Especially,
24 around the resonance frequencies whose values depend also to the EGC values, the RIN
25 spectra is the same. However, with the same current bias, it is also possible to reduce RIN
26 level through EGC values (see Fig.2 (a) curves (1), (2) and (3)). Over the resonance
27 frequency oscillation (RFO), the convergence of all RIN spectra observed when EGC changes
28 is very quick unlike to the current change values. The peak of intensity noise is reduced down
29 around -25dB/Hz, with the frequency oscillation which is shifted around 0.65GHz when the
30 EGC value is fixed in Fig. 2(a) (see curves from (1) to (5)). Also, in Fig. 2(b) this decrease is
31 only pronounced at the lower frequency (lower than the RFO).

32
33
34
35
36
37
38
39
40
41
42
43 The frequency noise (FN) is given by the relation $f = \frac{1}{2\pi} \frac{d\varphi}{dt}$ which is also expressed as

$$44 \quad \tilde{f}_{inj}(\omega) = \frac{\omega}{4\pi} \delta\tilde{\varphi}_{inj}(\omega) \quad (23)$$

45
46
47
48
49 Thus the frequency noise is given from Eq. (20) as,

$$50 \quad FN_{inj} = \langle |\tilde{f}_{inj}(\omega)|^2 \rangle = \frac{\omega^2}{4\pi^2} \langle |\delta\varphi_{inj}(\omega)|^2 \rangle \quad (24)$$

51
52
53
54
55
56
57
58
59
60 In accordance to Eqs. (13)-(16) and (19) we get,

$$FN_{inj} = \frac{(R_{sp_{inj}})_0}{8\pi^2 (S_{inj})_0} \left\{ 1 + \frac{4m_{32}^2 m_{21}^2 [(S_{inj})_0]^2}{(m_{12} m_{21} + \omega^2)^2 + \omega^2 m_{22}^2} \right\} \quad (25)$$

where m_{12} , m_{21} , m_{22} and m_{32} are defined in Eqs. (14).

The simulated results of the FN is illustrated in Fig. 3 with the same intrinsic parameters values as those used for RIN in Fig. 2. Figure 3(a) shows that, for the injection current rate near above the unit, the FN spectra are flat. Above and far above the unit, the spectra reveal the resonance oscillation frequency around 1GHz and 10GHz when EGC is fixed. If we maintain constant the current and change EGC the repartition becomes the same as with the RIN (see Fig. 3(b)).

The FWHM is derived from the FN. Because of the Lorentzian shape of electrical field, the spectral linewidth is evaluated from the low frequency to the frequency noise as $\Delta f = 2\pi FN(\omega = 0)$ [6, 8]. Using Eqs. (25) and (8), the FWHM is given as,

$$FWHM_{inj} = \frac{(R_{sp_{inj}})_0}{8\pi^2 (S_{inj})_0} \left[1 + \alpha_{inj}^2 \left(\frac{\gamma_{inj}}{1 - \gamma_{inj}} \right)^2 \right] = \frac{(R_{sp_{inj}})_0}{8\pi^2 (J_{inj} - J_{th_{inj}}) \tau_{p_{inj}}} \left[1 + \alpha_{inj}^2 \left(\frac{\gamma_{inj}}{1 - \gamma_{inj}} \right)^2 \right] \quad (26).$$

It is well-known that linewidth of SCL is larger than that of ordinary laser that has an almost negligible linewidth enhancement factor (LEF) α which value is few units [8]. Because of the EGC values range, it is shown from Eq. (26), the induced modulation of the FWHM by the mean EGC (see refs. [15-18] for the mean EGC) which leads to more significantly reduce the laser linewidth. Indeed, the relationship $\alpha_{inj}^2 (\gamma_{inj} / (1 - \gamma_{inj}))^2 < \alpha_{inj}^2$ is maintained valid as long as $0 < \gamma_{inj} < 0.5$. Therefore, the formula (26) known as a Schawlow-Townes formula becomes one of the main point of this paper. We call it the modified Schawlow-Townes formula due to the fact that the EGC-parameter leads to narrower laser linewidth by decreasing EGC values. The Figure 4 plots the corresponding result of the FWHM. Figure 4(a) depicts the variation of the linewidth with bias current ratio $(J_{inj} / J_{th_{inj}})$ for some value of spontaneous emission factor (SEF), and Fig. 4(b) shows the variations of linewidth with EGC. Recent years, the mains way to reduce the FWHM was to reduce LEF or SEF (Fig. 4(a) and Fig. 4(c)). Up to that day, we show that the FWHM can also be controlled with the help of EGC (Fig. 4(b)). The EGC plays a similar role as spontaneous emission factor avoiding an

abrupt increase of FWHM near the threshold [19]. Thus, Fig. 4(b) shows that the decrease of EGC leads to a route to ideal laser linewidth.

We mention that, according with Fig. (2b) and Fig. (4), we may paid more attention to the conditions to get narrow linewidth, keeping the RIN and FN levels always low. Thus, to avoid the increase of FN and RIN spectra keeping narrow linewidth, EGC must stay in the level lower than 0.8 .

3.2 Expression of RIN and FN of slave laser

In this section, to derive the RIN and FN mathematical expressions, we apply successively small-signal analysis around the steady states points (S_0, ψ_0, \bar{N}_0) , linearization and Fourier transformation of Eqs.(1), (2) and (3). Similar to section 3.1, $(x(t) = x_0 + \delta x(t))$, the steady state points are given by the following implicit expressions

$$\psi_0 = -\tan^{-1}\left(\frac{\alpha\gamma}{1-\gamma}\right) + \sin^{-1}\left\{-\frac{\Delta\omega\tau_{in}^*}{k_{inj}}\left[\frac{S_0}{(S_{inj})_0}\right]^{1/2}\frac{1}{\sqrt{1+(\alpha\gamma/(1-\gamma))^2}}\right\},$$

$$S_0 = \frac{J - \bar{N}_0 / \tau_r}{1 / \tau_p + G_N (\bar{N}_0 - N_{th})}, \bar{N}_0 = N_{th} - 2 \frac{1 + \gamma}{G_N (1 - \gamma)} \frac{k_{inj}}{\tau_{in}^*} \left[\frac{(S_{inj})_0}{S_0}\right]^{1/2} \cos(\psi_0). \quad (27)$$

The fluctuation terms are obtained as solutions following system,

$$\begin{bmatrix} \delta\tilde{S}(\omega) \\ -2S_0\delta\tilde{\psi}(\omega) \\ \delta\tilde{N}(\omega) \end{bmatrix} = \begin{bmatrix} j\omega + b_{11} & b_{12} & b_{13} \\ -b_{12} & j\omega + b_{22} & b_{23} \\ b_{31} & 0 & j\omega + b_{33} \end{bmatrix}^{-1} \begin{bmatrix} \tilde{f}_S(\omega) \\ \tilde{f}_N(\omega) \\ \tilde{f}_\psi(\omega) \end{bmatrix}, \quad (28)$$

with

$$b_{11} = -\left(\frac{1-\gamma}{1+\gamma} G_N (\bar{N}_0 - N_{th}) + \frac{k_{inj}}{\tau_{in}^*} \left[\frac{(S_{inj})_0}{S_0}\right]^{1/2} \cos(\psi_0)\right), b_{12} = -\frac{k_{inj}}{\tau_{in}^*} \left[\frac{(S_{inj})_0}{S_0}\right]^{1/2} \sin(\psi_0),$$

$$b_{13} = -\left(\frac{1-\gamma}{1+\gamma} G_N S_0 + \left[\frac{\partial R_{sp}}{\partial N} \right]_{\bar{N}_0} \right), b_{21} = -b_{12} = \frac{k_{inj}}{\tau_{in}^*} \left[\frac{(S_{inj})_0}{S_0} \right]^{1/2} \sin(\psi_0),$$

$$b_{22} = \frac{k_{inj}}{\tau_{in}^*} \left[\frac{(S_{inj})_0}{S_0} \right]^{1/2} \cos(\psi_0), b_{23} = \alpha \frac{\gamma S_0}{1+\gamma} G_N, b_{31} = \frac{1}{\tau_p} + G_N (\bar{N}_0 - N_{th}) \text{ and } b_{33} = \frac{1}{\tau_r} + G_N S_0$$
(29)

The functions \tilde{f}_S , \tilde{f}_N and \tilde{f}_ψ expressed in Eqs. (30), (31) and (32) are equivalent to the total fluctuations of photons density, carriers density and optical phase respectively inside the slave laser cavity whose expressions are,

$$\tilde{f}_S(\omega) = \tilde{F}_S(\omega) + S_0 b_{22} \frac{\delta \tilde{S}_{inj}(\omega)}{(S_{inj})_0} - 2S_0 \delta \tilde{\varphi}_{inj}(\omega), \quad (30)$$

$$\tilde{f}_N(\omega) = \tilde{F}_N(\omega), \quad (31)$$

$$\tilde{f}_\psi(\omega) = -2S_0 \left(\tilde{F}_\psi(\omega) + \frac{1}{2} b_{12} \frac{\delta \tilde{S}_{inj}(\omega)}{(S_{inj})_0} + b_{22} \delta \tilde{\varphi}_{inj}(\omega) \right), \quad (32)$$

where S_0 , \bar{N}_0 and ψ_0 are average values for photons density, carriers density and optical phase of SL, respectively. The fluctuations components $\delta \tilde{S}(\omega)$, $\delta \tilde{\psi}(\omega)$ and $\delta \tilde{N}(\omega)$ are obtained as solution of Eq.(28). After arrangements we get

$$\delta \tilde{S}(\omega) = \left\{ -[b_{22}b_{33} - \omega^2 + j\omega(b_{22} + b_{33})] \tilde{f}_S(\omega) + [b_{12}b_{33} + j\omega b_{33}] \tilde{f}_\psi(\omega) + [-b_{12}b_{23} + b_{13}b_{22} + j\omega b_{13}] \tilde{f}_N(\omega) \right\} \div \tilde{Y}(\omega), \quad (33)$$

$$\delta \tilde{\psi}(\omega) = \frac{1}{2S} \left\{ [b_{12}b_{33} + b_{23}b_{31} + j\omega b_{12}] \tilde{f}_S(\omega) + [b_{11}b_{33} - b_{31}b_{13} - \omega^2 + j\omega(b_{33} + b_{11})] \tilde{f}_\psi(\omega) + [-b_{11}b_{23} + b_{13}b_{12} + j\omega b_{23}] \tilde{f}_N(\omega) \right\} \div \tilde{Y}(\omega), \quad (34)$$

$$\delta \tilde{N}(\omega) = \left\{ [b_{22}b_{31} + j\omega b_{31}] \tilde{f}_S(\omega) - [b_{31}b_{12}] \tilde{f}_\psi(\omega) + [-b_{11}b_{22} + b_{12}^2 - \omega^2 + j\omega(b_{22} + b_{11})] \tilde{f}_N(\omega) \right\} \div \tilde{Y}(\omega). \quad (35)$$

$$\begin{aligned} \tilde{Y}(\omega) = & \left\{ -b_{31}b_{12}b_{23} + b_{31}b_{13}b_{22} - b_{12}^2b_{33} - b_{11}b_{22}b_{33} + (b_{11} + b_{22} + b_{33})\omega^2 \right\} + \\ \text{with} & \left\{ \omega^3 + \omega(b_{31}b_{13} - b_{12}^2 - b_{11}b_{33} - b_{11}b_{22} - b_{22}b_{33}) \right\} \end{aligned} \quad (36)$$

We need to know the cross-correlations and correlations of \tilde{f}_S , \tilde{f}_N and \tilde{f}_ψ functions in order to express RIN and FN of slave. For simplification, Yabre *et al.* [2] assumed that the Langevin noise sources of \tilde{F}_S , \tilde{F}_ψ and \tilde{F}_N are not to be correlated with photon density $\delta\tilde{S}_{inj}(\omega)$ and optical phase $\delta\tilde{\varphi}_{inj}(\omega)$ fluctuations of the ML is given as solutions of Eqs.(12) and (13). From Eq. (33), the power spectral densities for intensity and phase noise can be obtained as follows, respectively

$$\begin{aligned} \langle |\delta\tilde{S}(\omega)|^2 \rangle = & \left\{ \left[(b_{22}b_{33} - \omega^2)^2 + \omega^2(b_{22} + b_{33})^2 \right] \langle |\tilde{f}_S(\omega)|^2 \rangle + \left[b_{12}^2b_{33}^2 + \omega^2b_{33}^2 \right] \langle |\tilde{f}_\psi(\omega)|^2 \rangle + \right. \\ & + \left[(b_{13}b_{22} - b_{12}b_{23})^2 + \omega^2b_{13}^2 \right] \langle |\tilde{f}_N(\omega)|^2 \rangle + 2(\omega^2 - b_{22}b_{33})(b_{13}b_{22} - b_{12}b_{23}) \langle \tilde{f}_S(\omega)\tilde{f}_N(\omega)^* \rangle + \\ & + 2b_{12}b_{33}(\omega^2 - b_{22}b_{33}) \Re \left[\langle \tilde{f}_S(\omega)\tilde{f}_\psi(\omega)^* \rangle \right] + \\ & \left. + 2b_{12}b_{23}(b_{13}b_{22} - b_{12}b_{23}) \langle \tilde{f}_\psi(\omega)\tilde{f}_N(\omega)^* \rangle \right\} \div |\tilde{Y}(\omega)|^2 \end{aligned} \quad (37)$$

$$\begin{aligned} \langle |\delta\tilde{\psi}(\omega)|^2 \rangle = & \frac{1}{4(S_0)^2 |\tilde{Y}(\omega)|^2} \left\{ \left[(b_{12}b_{33} + b_{23}b_{31})^2 + \omega^2b_{12}^2 \right] \langle |\tilde{f}_S(\omega)|^2 \rangle + \right. \\ & + \left[(b_{11}b_{33} - b_{31}b_{13} - \omega^2)^2 + \omega^2(b_{11} + b_{33})^2 \right] \langle |\tilde{f}_\psi(\omega)|^2 \rangle + \\ & + \left[(b_{11}b_{23} + b_{13}b_{12})^2 + \omega^2b_{23}^2 \right] \langle |\tilde{f}_N(\omega)|^2 \rangle + \\ & + 2(b_{12}b_{33} + b_{23}b_{31})(b_{11}b_{33} - b_{31}b_{13} - \omega^2) \Re \left[\langle \tilde{f}_S(\omega)\tilde{f}_\psi(\omega)^* \rangle \right] + \\ & \left. - 2(b_{12}b_{33} + b_{23}b_{31})(b_{11}b_{23} + b_{13}b_{12}) \langle \tilde{f}_S(\omega)\tilde{f}_N(\omega)^* \rangle \right\} \end{aligned} \quad (38)$$

Using \tilde{f}_S , \tilde{f}_ψ and \tilde{f}_N expressions according with $\delta\tilde{S}_{inj}(\omega)$, $\delta\tilde{N}_{inj}(\omega)$ and $\delta\tilde{\varphi}_{inj}(\omega)$, we obtained spectral density of slave fluctuations as

$$\langle |\tilde{f}_S(\omega)|^2 \rangle = 2(R_{sp})_0 S_0 - \frac{4(R_{sp_{inj}})_0 (S_0)^2 m_{21}m_{32}b_{12}b_{22}}{|\Delta(\omega)|^2} + (S_0)^2 b_{22}^2 \frac{\langle |\delta\tilde{S}_{inj}(\omega)|^2 \rangle}{[(S_{inj})_0]^2} + 4(S_0)^2 b_{12}^2 \langle |\delta\tilde{\varphi}_{inj}(\omega)|^2 \rangle \quad (39)$$

$$\langle |\tilde{f}_\psi(\omega)|^2 \rangle = 4(S_0)^2 \left[\frac{(R_{sp})_0}{2S_0} + \frac{2(R_{sp_{inj}})_0 m_{21} m_{32} b_{12} b_{22}}{|\Delta(\omega)|^2} + \frac{1}{4} b_{12}^2 \frac{\langle |\delta\tilde{S}_{inj}(\omega)|^2 \rangle}{[(S_{inj})_0]^2} + b_{22}^2 \langle |\delta\tilde{\varphi}_{inj}(\omega)|^2 \rangle \right], \quad (40)$$

$$\langle |\tilde{F}_N|^2 \rangle = 2 \left[(R_{sp})_0 S_0 + \frac{\bar{N}_0}{\tau_r} \right], \quad (41)$$

$$\langle \tilde{F}_S(\omega) \tilde{F}_N(\omega)^* \rangle = -2(R_{sp})_0 S_0, \quad (42)$$

$$\langle \tilde{F}_N(\omega) \tilde{F}_\psi(\omega)^* \rangle = 0, \quad (43)$$

where

$$\Re \left\{ \langle \tilde{f}_S(\omega) \tilde{f}_\psi(\omega)^* \rangle \right\} = -2(S_0)^2 \left[\frac{2(R_{sp_{inj}})_0 m_{21} m_{32}}{|\Delta(\omega)|^2} (b_{22}^2 - b_{12}^2) + \frac{1}{2} b_{12} b_{22} \frac{\langle |\delta\tilde{S}_{inj}(\omega)|^2 \rangle}{[(S_{inj})_0]^2} - 2b_{22} b_{12} \langle |\delta\tilde{\varphi}_{inj}(\omega)|^2 \rangle \right], \quad (44)$$

Using the definition of RIN and substituting Eqs. (39) - (44) in Eq. (37), the RIN of slave laser can be written as

$$\begin{aligned} RIN = \frac{2(R_{sp})_0}{S_0 |\tilde{Y}(\omega)|^2} & \left\{ \left[1 - \frac{S_0}{2R_{sp_0}} \left(\frac{4(R_{sp_{inj}})_0 m_{21} m_{32} b_{12} b_{22}}{|\Delta(\omega)|^2} + b_{22}^2 RIN_{inj} + 4b_{12}^2 \left(\frac{2\pi}{\omega} \right)^2 FN_{inj} \right) \right] \times \right. \\ & \left[(b_{22} b_{33} - \omega^2)^2 + \omega^2 (b_{22} + b_{33})^2 \right] + \\ & + [b_{12}^2 b_{33}^2 + \omega^2 b_{33}^2] \left[1 + \frac{2S_0}{(R_{sp})_0} \left(\frac{2(R_{sp_{inj}})_0 m_{21} m_{32} b_{12} b_{22}}{|\Delta(\omega)|^2} + \frac{1}{4} b_{12}^2 RIN_{inj} + b_{22}^2 \left(\frac{2\pi}{\omega} \right)^2 FN_{inj} \right) \right] \\ & + \left[1 + \frac{\bar{N}_0}{\tau_r (R_{sp})_0 S_0} \right] \left[(b_{13} b_{22} - b_{12} b_{23})^2 + \omega^2 b_{13}^2 \right] - 2(\omega^2 - b_{22} b_{33})(b_{13} b_{22} - b_{12} b_{23}) \\ & \left. - \frac{2b_{12} b_{33} S_0}{(R_{sp})_0} (\omega^2 - b_{22} b_{33}) \left[\frac{2(R_{sp_{inj}})_0 m_{21} m_{32}}{|\Delta(\omega)|^2} (b_{22}^2 - b_{12}^2) + \frac{1}{2} b_{12} b_{22} RIN_{inj} - 2b_{22} b_{12} \left(\frac{2\pi}{\omega} \right)^2 FN_{inj} \right] \right\} \quad (45) \end{aligned}$$

From the previous definition giving the expression of FN in Eq. (24) and Eq.(37), we derived the slave laser FN expression as follows

$$\begin{aligned}
 FN = & \frac{\omega^2}{16\pi^2 (S_0)^2 |\tilde{Y}(\omega)|^2} \left\{ 2 \left[\left(R_{sp} \right)_0 S_0 + \frac{\bar{N}_0}{\tau_r} \right] \left[(b_{11}b_{23} + b_{13}b_{12})^2 + \omega^2 b_{13}^2 \right] + \right. \\
 & + 4 \left(R_{sp} \right)_0 S_0 (b_{12}b_{33} + b_{23}b_{31})(b_{11}b_{23} + b_{13}b_{12}) + \\
 & + \left. \left[(b_{12}b_{33} + b_{23}b_{31})^2 + \omega^2 b_{12}^2 \right] \left[2 \left(R_{sp} \right)_0 S_0 - \frac{4 \left(R_{sp_{inj}} \right)_0 (S_0)^2 m_{21} m_{32} b_{12} b_{22}}{|\Delta(\omega)|^2} + (S_0)^2 b_{22}^2 RIN_{inj} + \frac{16\pi^2 (S_0)^2 b_{12}^2}{\omega^2} FN_{inj} \right] \right\} + \\
 & + 4 (S_0)^2 \left[(b_{11}b_{33} - b_{31}b_{13} - \omega^2)^2 + \omega^2 (b_{33} + b_{11})^2 \right] \left\{ \left[\frac{\left(R_{sp} \right)_0}{2S_0} + \frac{2 \left(R_{sp_{inj}} \right)_0 m_{21} m_{32} b_{12} b_{22}}{|\Delta(\omega)|^2} + \frac{b_{12}^2}{4} RIN_{inj} + \frac{4\pi^2 b_{22}^2}{\omega^2} FN_{inj} \right] + \right. \\
 & \left. - 4 (S_0)^2 (b_{12}b_{33} + b_{23}b_{31})(b_{11}b_{33} - b_{31}b_{13} - \omega^2) \left[\frac{2 \left(R_{sp_{inj}} \right)_0 m_{21} m_{32}}{|\Delta(\omega)|^2} (b_{22}^2 - b_{12}^2) + \frac{b_{12} b_{22}}{2} RIN_{inj} - \frac{8\pi^2 b_{22} b_{12}}{\omega^2} FN_{inj} \right] \right\}
 \end{aligned} \tag{46}$$

The functions RIN_{inj} and FN_{inj} derived from Eq.(22) and Eq. (25) are intensity noise and phase noise from the ML respectively.

3.3 Illustrative Curves and Discussion

a) The RIN

We recall that noises of the SL are influenced by noises from ML, and therefore Eq. (45) and Eq. (46) agree with fact, because RIN and FN of the slave are expressed as dependent functions of intensity noise RIN_{inj} and frequency noise FN_{inj} from ML. Owing to the large number of parameters involved in these expressions, in order to reduce the level of frequency noise and intensity noise, those parameters that can significantly affect noise levels will only be examined. The choice brought to these parameters and especially to the EGC can be best understood through RIN and FN spectra by turning to the next figures for SL relative intensity and frequency noise.

Indeed Fig.5 (a) and Fig. 5(b) show the abrupt decrease of intensity noise with appearance of two relaxation peaks. That decrease is similar to the shot noise limit in Ref.[19] or to the famous $1/f^\alpha$ noise. The first peak corresponds to free-running laser relaxation frequency (drop representations). Thus, all these peaks are perfectly at the same relaxation frequency as

those of optically injected laser (fat representations). However for $-20dB$ injection rate (Fig. 5(a) and Fig 5(c)), at all frequencies the both spectra level RIN are highest to free-running level noise. Near the RFO and above RFO these levels become reduced of more than $5dB/Hz$ compared to the master levels. At RFO the reduction is more than 10dB. But, we can establish in Fig. 5(d) that for $40dB$ injection rate, slave RIN level leaves above that of master laser on all frequencies repartition: on that conditions, intensity fluctuation from the SL is greatly enhanced by the optical injection from the ML.

It remains that, the appearance on second peak has also been reached as in Ref. [2]. That peak can be understood with accordance to Eq. (45) and in connection with the fact that the noise characteristics of ML are included in the determination of the SL noise in the stable-locking condition.

b) The effect of ignoring master laser optical phase noise contribution on RIN

To avoid the abrupt decrease of RIN observed in low frequencies reducing RIN levels, we may need here more careful choice of parameters involved and we must suppose for simplicity that, the ML phase fluctuations are small enough to be taking into account. The term $\delta\tilde{\varphi}_{inj}(\omega)$ in Eq. (30) could be neglected. Figure 5(c) and Fig. 5(d) show the effect of neglecting ML optical phase noise contribution. The frequency spectra show an almost flat profile at lower frequencies whatever the injections rate $(S_{inj})_0/S_0$. Figure 5(d) is the main important case of intensity noise reduction. Indeed, we have a little more $40dB$ reduction in the RIN spectrum comparatively to the free-running slave. We pay attention to the choice of the physical parameter values by supposing that slave and master lasers are to be almost identical and keeping SCL linewidth narrow. Then, we have restricted to work on these conditions: injection parameters are to be $(S_{inj})_0/S_0 \in]-4dB \ 45dB[$, EGC in ranges $]0 \ 0.88[$ and $]0.4 \ 0.99[$ for ML and SL respectively. On these conditions, the SL bias current is more or equal to two times his threshold current. Exact values of main parameters are given in the captions. When the master bias current is increased, the RIN decreases. However when that current becomes at five times the threshold current (for $40dB$ injection parameter) and at ten times (for $-20dB$ injection parameter) (see Fig. 6(a) and Fig. 6(b) respectively) or above, the stochastic dynamics of slave change. RIN and FN spectra become very interesting. We can observe clearly the gradual disappearance of the first relaxation peak. Intensity spectrum of slave behaves almost identically as those of ML (see Fig. (6)). That fact is supported by the

1
2
3 slave laser frequency noise Fig.7(a) to which we also have the gradual disappearance of first
4 pic relaxation corresponding to the SL when $J_{inj} = 12 \cdot J_{inj_{th}}$ and in Fig. 7(b) for $\gamma = 0.45$. These
5 observations indicate that the ML parameters and noise could provide drastic change on
6 characteristic of SL noise spectrum. Figures 8 and 9 show the effect EGC on the FN and RIN
7 spectra when the ML and SL bias currents and other injections parameters are fixed. By
8 increasing the EGC of the slave, the FN is reduced. Sometime, if master laser EGC becomes
9 near the unit, master laser FN takes the lead and noise becomes also more intense in RFO
10 (Fig. 8(a) for $\gamma = 0.3$; $\gamma_{inj} = 0.99$). Figure 8(b) presents the effect of master laser EGC in FN
11 when slave laser EGC is fixed, it provides FN reduction when master laser EGC is decreasing.
12 When $\gamma_{inj} = 0.55$, whatever $\gamma > 0.3$, we have dual pronounced peaks in noise spectra Fig. 9(a).
13 However, the level easily decreases on low frequencies domain and display convergence after
14 RFO by increasing EGC of slave laser when EGC of master laser is fixed (see Fig. 9 (b)). The
15 RIN and FN profiles show that stochastic behavior of the SL can be identical to that of free-
16 running laser or injected laser by the adapted choice of EGC values. Figure 9(b) reveals the
17 sensitivity of the nonlinear dynamics of the SCL used in this paper. Indeed for small
18 variations of EGC, the RIN spectrum presents a very new particular stochastic dynamics, for
19 $0.65 \leq \gamma \leq 0.69$, the profiles present hollows in points A and B (see Fig. 9(b)) at low
20 frequencies (before resonance) which are connected with the change of RIN sign observed in
21 Ref. [12]. When $\gamma = 0.578$, the variation of the RIN becomes almost flat. In Fig. 10(a), it is
22 clearly observed that, when the injection rate is positive (dB unit) the slave RIN to master
23 RIN ratio (RIN/RIN_{inj}) is smaller than the unit (see Fig.10 (a)). This confirms, in agreement
24 with the Fig 5(a) and Fig. 5(c) that the RIN of slave is higher than those of master. However
25 in Fig.10 (b), the phenomenon is reversed. For better understanding, we have to note that,
26 RIN and RIN_{inj} have negative values and the interpretation of Fig. 10(a) and Fig. 10(b)
27 requires the consideration of these negative signs.
28
29
30
31
32
33
34
35
36
37
38
39
40
41
42
43
44
45
46
47
48
49
50
51
52

53 4. Conclusion

54 In this paper, we analytically and numerically presented the stochastic behavior of a
55 single-mode SCL under external optical injection. Using the small signals analysis, we
56 derived the novel expressions for the RIN and the FN from the master and the slave lasers.
57 The effective gain coefficient (EGC) parameter of this rate equations model allows a drastic
58
59
60

1
2
3 diminution of RIN spectra in the low frequency from -110dB/Hz to -175dB/Hz in addition to
4 the diminution of RIN spectra carried out by classic decisive parameters. Moreover the
5 induced modulation of FWHM by the mean EGC leads to more significantly reduce laser
6 linewidth which has opened the route to the ideal laser linewidth by reducing EGC-values
7 through the proposed modified Schawlow-Townes formula. In addition, we have envisioned
8 as a solution to avoid abrupt decrease of slave RIN on low frequency regime, a suitable choice
9 of small phase fluctuations from the master laser. Numerical analysis of intensity, phase noise
10 and linewidth of this SCL rate equations model is under way and will achieve the full study of
11 this system under in consideration.
12
13
14
15
16
17
18
19
20
21
22
23
24
25
26
27
28
29
30
31
32
33
34
35
36
37
38
39
40
41
42
43
44
45
46
47
48
49
50
51
52
53
54
55
56
57
58
59
60

References

- [1] Pramod M S et al 2014 Eur. Phys. J. D. **68** 186
- [2] Yabre G S et al 2000 IEEE J. Quantum Electronics **36** 385
- [3] Sze-Chun C 2010 IEEE J. Quantum Electronics **46** 421
- [4] Fu X et al 2010 J. of Electromagn. Wave and Appl. **24** 849
- [5] Agrawal G P 2002 Fiber-Optic Communication Systems (Wiley, John & Sons)
- [6] Yamada M 2014 Theory of Semiconductor Lasers (Springer Japan)
- [7] Bijoya Paul et al 2014 ARPN Journal of Science and Technology **4** 12
- [8] Ohtsubo J 2006 Semiconductor Lasers Stability, Instability and Chaos (Berlin : Springer-Verlag)
- [9] Fatadin I et al 2006 IEEE J. Quantum Electronics **42** 9
- [10] Yamada M et al 2001 IECIE Trans. Electron **E84-C** 10
- [11] Sazzad M S et al 2014 J. Laser Opt. Photonics **1** 106
- [12] Newkirk M A and Vahala K J 1991 IEEE J. Quantum Electronics **27** 13
- [13] Husham K H et al 2012 IEEE J. Quantum Electronics **48** 385
- [14] Marshall W K et al 1996 Appl. Phys. Lett. **68** 1996
- [15] Mengue A D and Essimbi B Z 2011 Opt. Quantum Electron **42** 389
- [16] Mengue A D and Essimbi B Z 2012 Phys. Scr. **85** 025404.
- [17] Mengue A D and Essimbi B Z 2012 American Institute of Physics Chaos **22** 013113
- [18] Mengue A D and Essimbi B Z 2012 Nonlinear Dyn. **70** 1241
- [19] Yamada M 1994 IEEE J. Quantum Electronics **30** 1511
- [20] Sazzad M S I et al 2016 Int. J. Scientific & Engineering Research **7** 1026

Figure captions

Fig.1. Scheme of optical injection. The slave laser is submitted to optical injection by the master laser. Unidirectional coupling is ensured by and optical isolator.

Fig.2. RIN of the master laser as function of frequency; (2a) when $\gamma_{inj}=0.5$ for several bias current conditions (1) $J_{inj} = 2 \cdot J_{th_{inj}}$, (2) $J_{inj} = 2.5 \cdot J_{th_{inj}}$, (3) $J_{inj} = 4 \cdot J_{th_{inj}}$ and (4) $J_{inj} = 12 \cdot J_{th_{inj}}$; (2b) when $J_{inj} = 2 \cdot J_{inj_{th}}$, for several value of EGC (1) $\gamma_{inj} = 0.00$, (2) $\gamma_{inj} = 0.25$, (3), $\gamma_{inj} = 0.5$. (4) $\gamma_{inj} = 0.65$. (5) $\gamma_{inj} = 0.99$.

Fig.3. FN of the master laser as function of frequency; (a) when $\gamma_{inj} = 0.45$ for several bias current conditions; (b) when $J_{inj} = 2 \cdot J_{inj_{th}}$ for several values of EGC.

Fig.4. Variation of linewidth with injection current ratio. Curves show the rapid narrowing of linewidth with increasing current ration. By decreasing the following parameters: (a) SEF, (b) EGC, (c) LEF.

Fig.5. RIN variation for the following rate injection. (a) -20dB and (b) 40dB when phase fluctuations of master laser are considered. (c) -20dB and (d) 40dB when phase fluctuations are neglected.

Fig.6. Effects of ML increasing current in the slave RIN spectrum for the following rate injections. (a)for 40dB, (b)-20dB.

Fig.7. Slave laser FN. (a) for some values of current, (b) for some values of EGC.

1
2
3 Fig.8. Frequency-variation of FN of the slave laser, with the following injection parameters

4
5 $\Delta\omega = -20 \times 10^9 \text{ Hz}$, $k_{inj} = 1 \times 10^{-1}$, $S_0 = 10^{-2} (S_{inj})_0$; $J_{inj} = 2.5 \cdot J_{inj_{th}}$. (a) When the master laser and
6
7 slave laser EGCs change, (b) when slave laser EGC is fixed.

8
9
10
11
12 Fig.9. Influence of EGC and other injection parameters on RIN. (a) When EGC of master laser
13
14 is fixed to 0.55, (b) when both EGC of ML and SL change.

15
16
17
18
19 Fig.10. Slave RIN to master RIN ratio. (a) When EGC of master laser is fixed, (b) when EGC
20
21 of master laser changes and $\gamma = 0.8$.

22
23
24
25
26
27
28
29
30
31
32
33
34
35
36
37
38
39
40
41
42
43
44
45
46
47
48
49
50
51
52
53
54
55
56
57
58
59
60

Accepted Manuscript

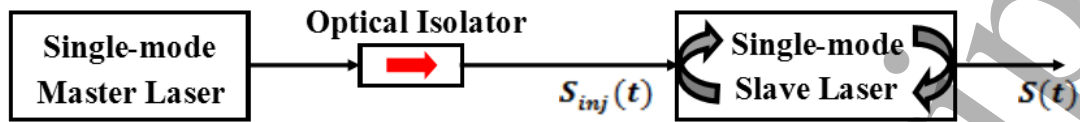


Fig. 1. David Essebe E. Noise.

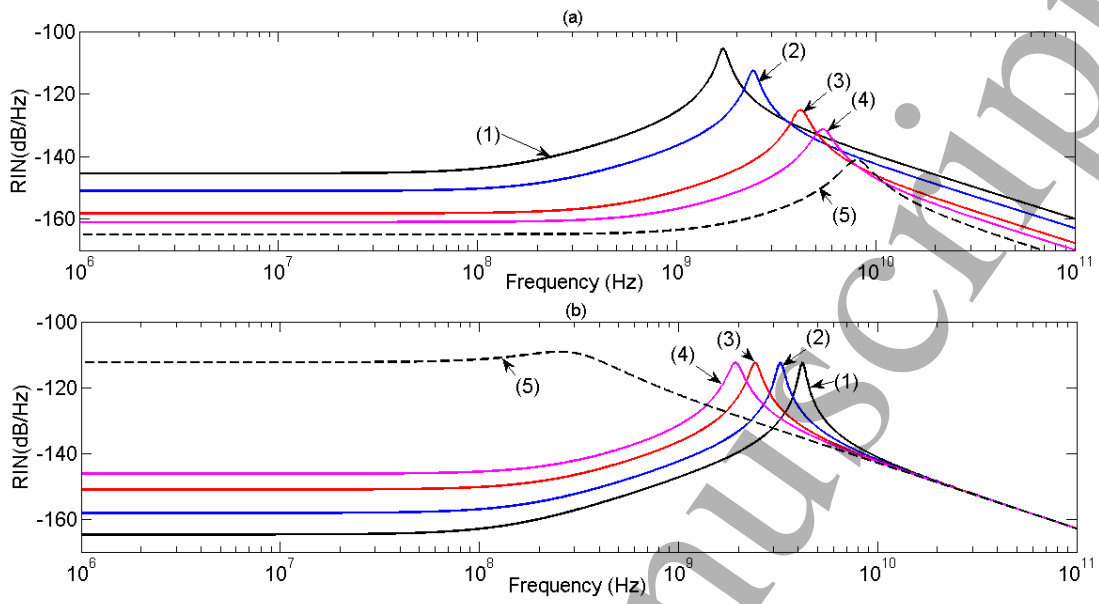


Fig. 2. David Essebe E, et al. Noise.

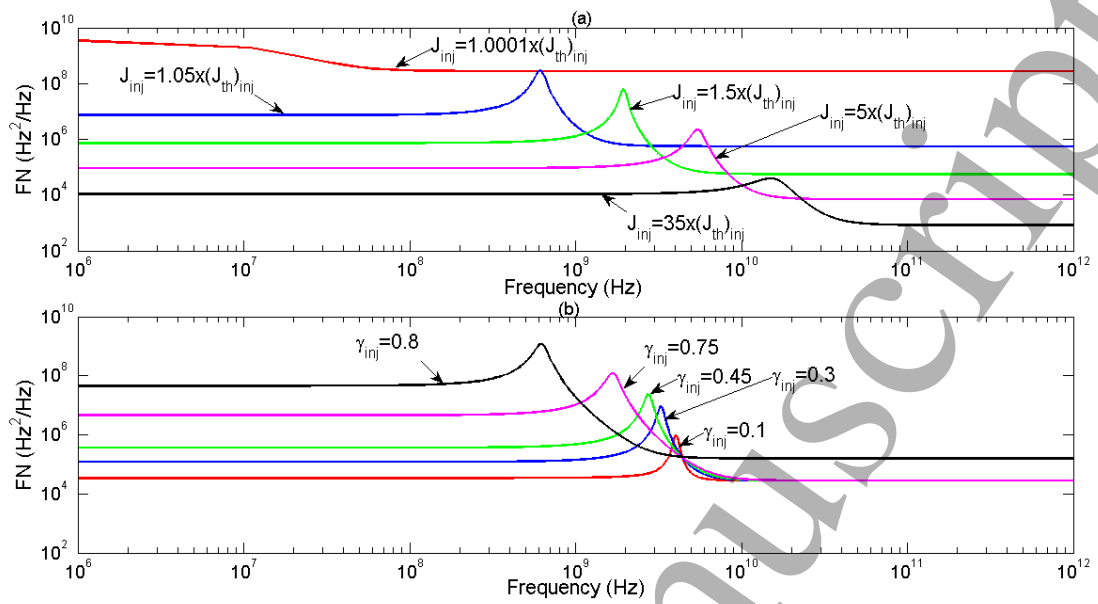


Fig. 3. David Essebe E. et al. Noise.

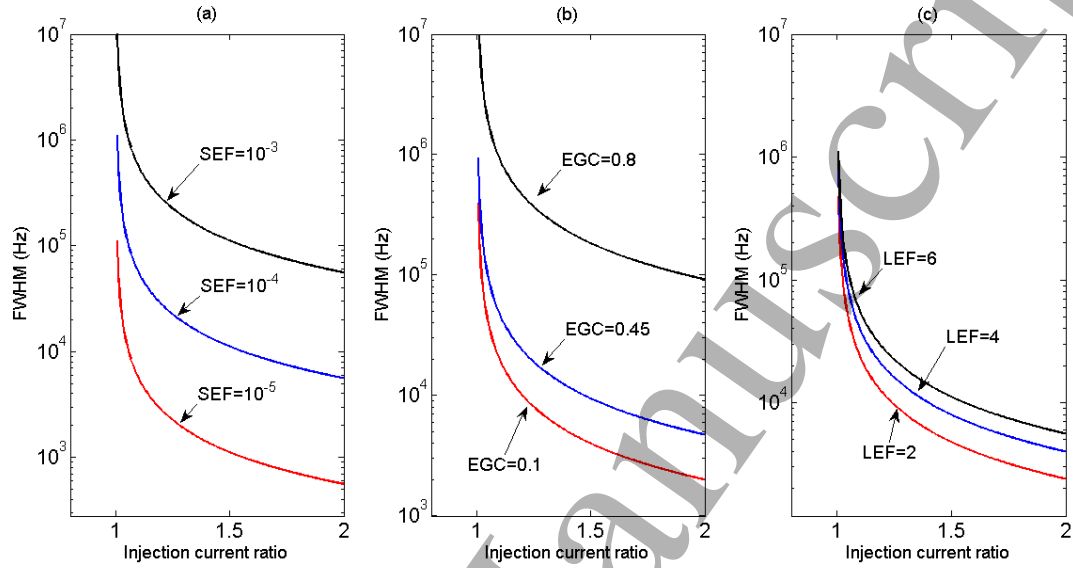


Fig. 4. David Essebe E. et al. Noise.

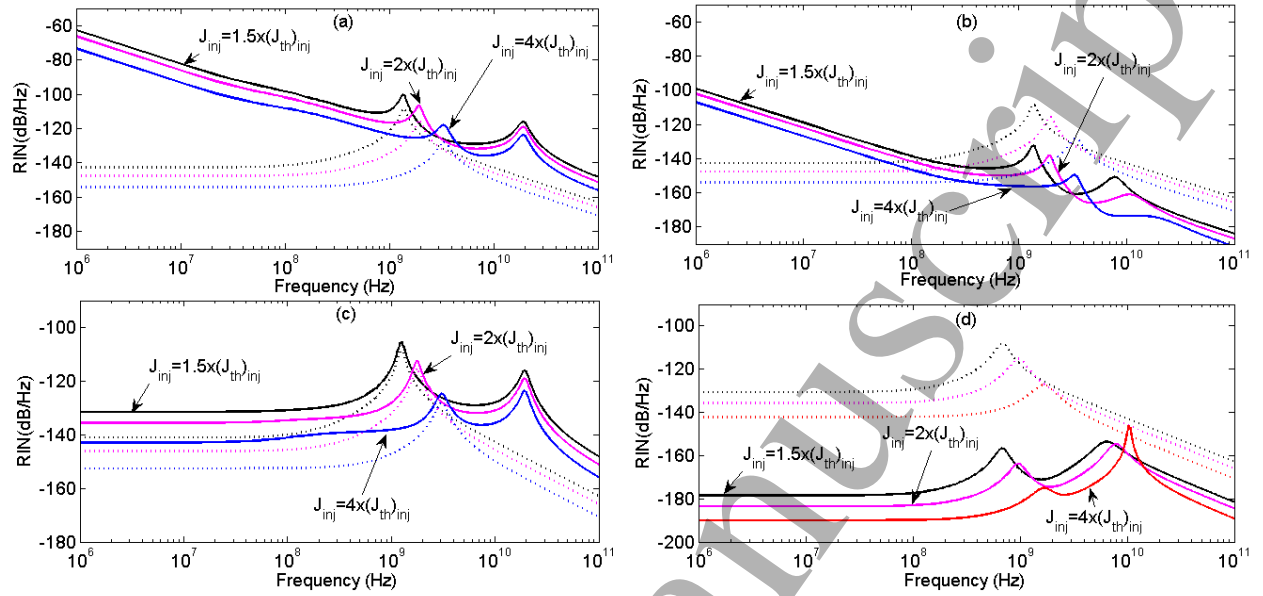


Fig. 5. David Essebe E. et al. Noise.

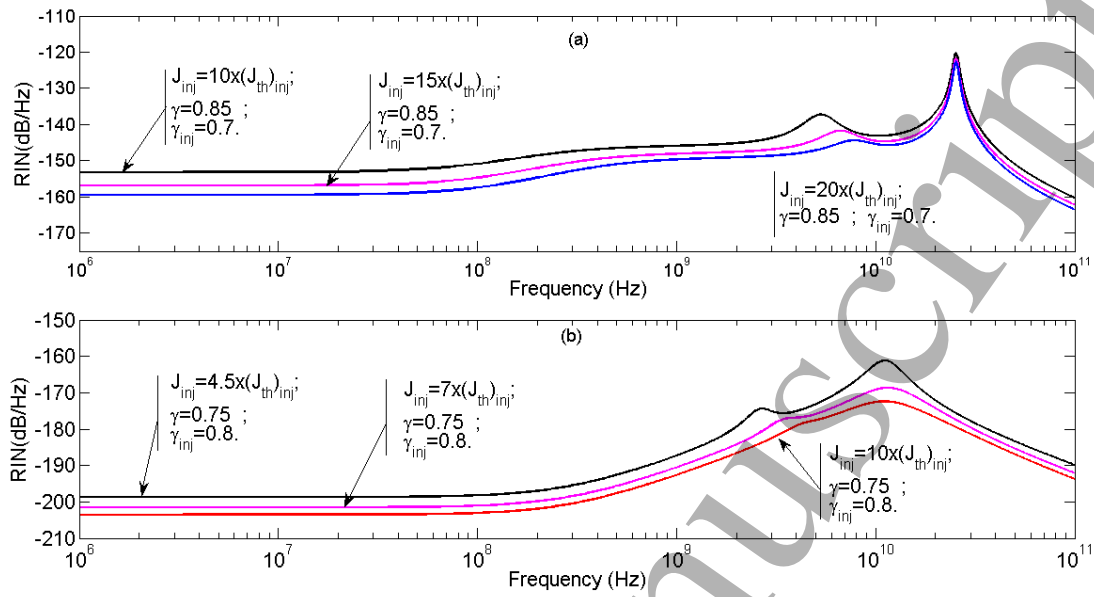


Fig. 6. David Essebe E. et al. Noise.

1
2
3
4
5
6
7
8
9
10
11
12
13
14
15
16
17
18
19
20
21
22
23
24
25
26
27
28
29
30
31
32
33
34
35
36
37
38
39
40
41
42
43
44
45
46
47
48
49
50
51
52
53
54
55
56
57
58
59
60

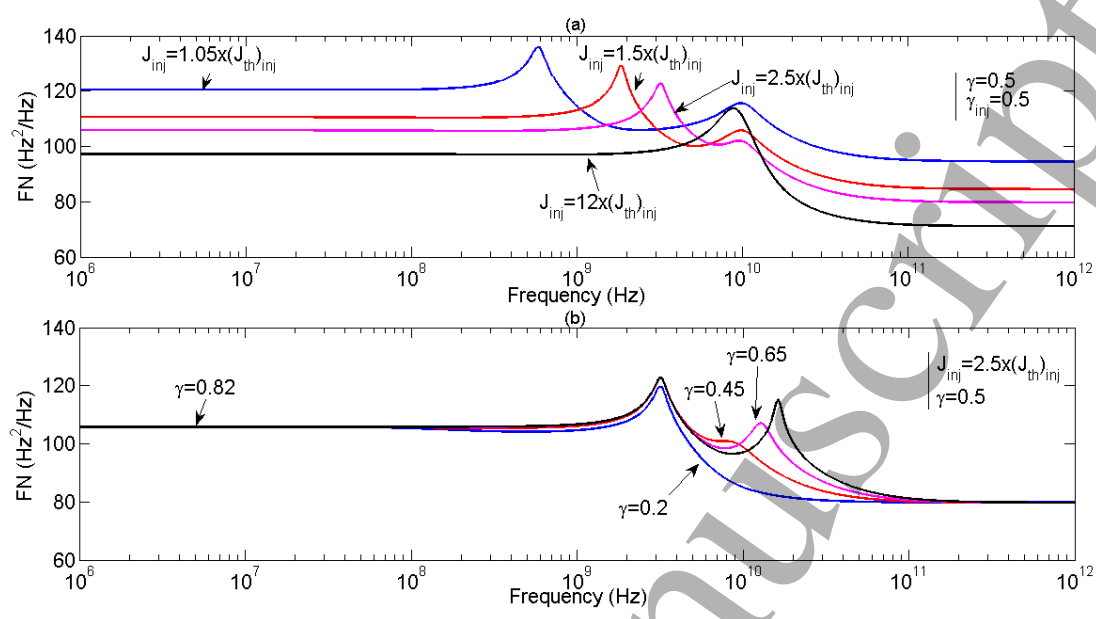


Fig. 7. David Essebe E. et al. Noise.

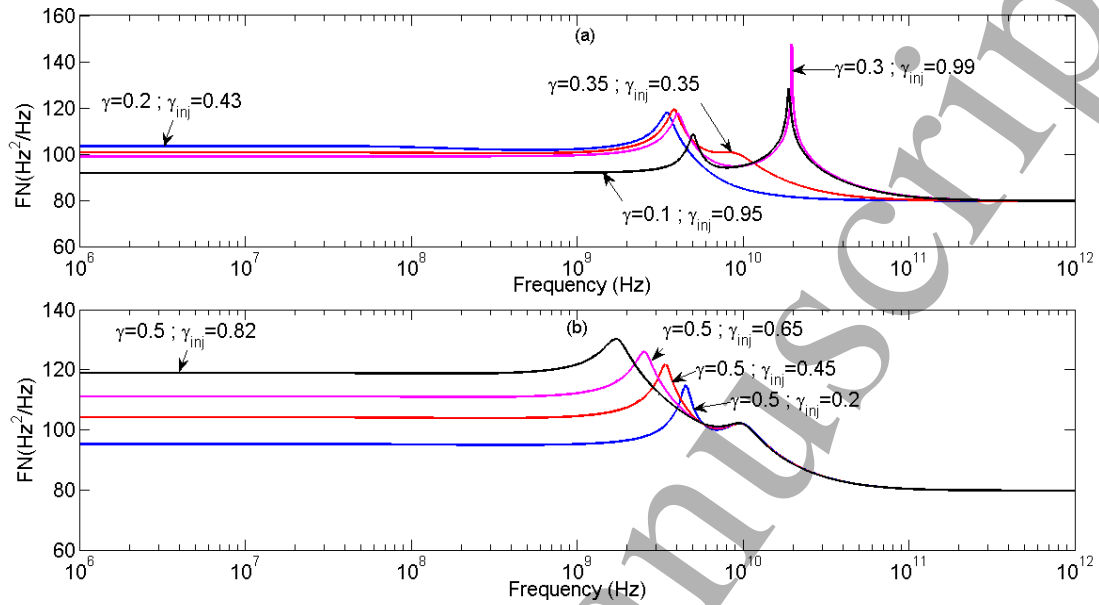


Fig. 8. David Essebe E. et al. Noise.

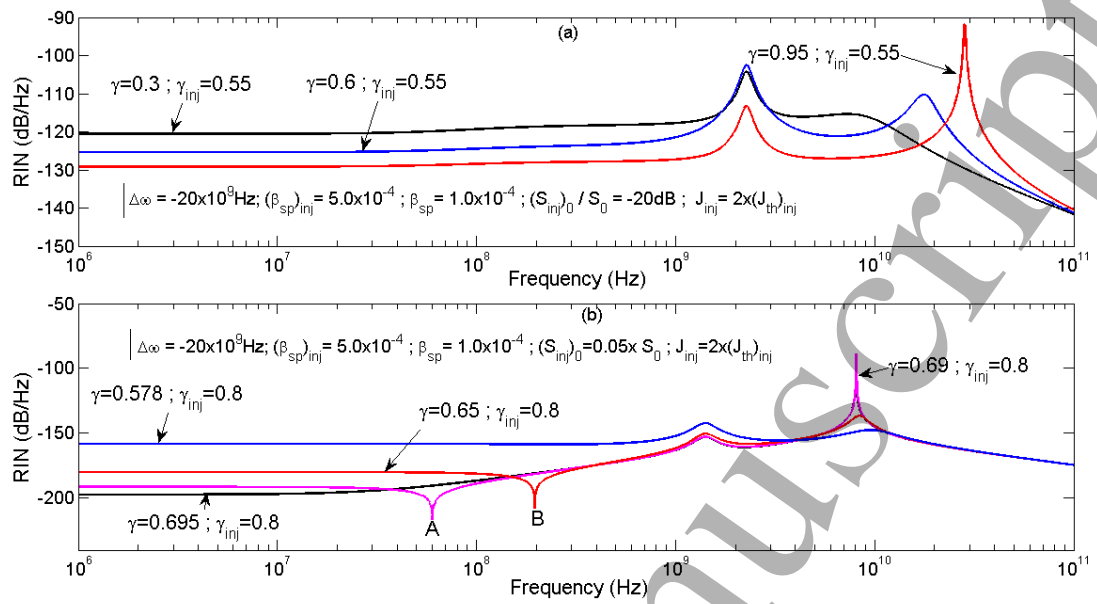


Fig. 9. David Essebe E. et al. Noise.

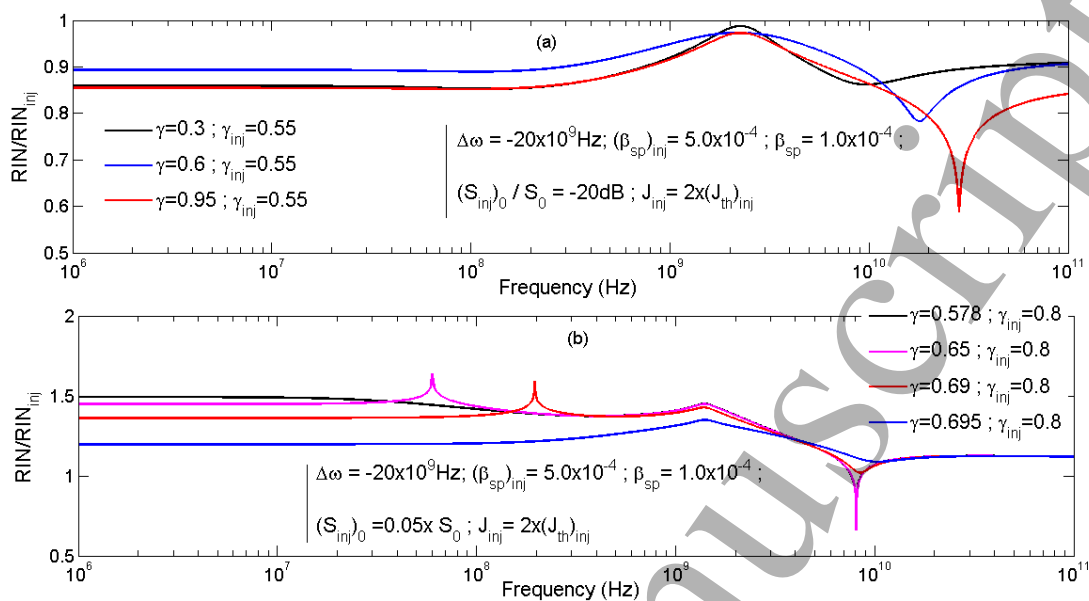


Fig. 10. David Essebe E. et al. Noise.

Accepted Manuscript



Contents lists available at ScienceDirect

Optik

journal homepage: www.elsevier.com/locate/ijleo

Original research article

Multiscroll chaotic attractors in Optical Injected Semiconductor Laser Driven by a Resonant Tunneling Diode Current

David Essebe Eba^a, Armand Didier Mengue^{b,*}, Bernard Essimbi Zobo^{a,c}^a Department of Physics, Faculty of Science, University of Yaounde I, PO Box 812, Yaounde, Cameroon^b EE Department, Faculty of Engineering and Technology, University of Buea, PO Box 63, Buea, Cameroon^c ZHO, Optoelektronik, Universität Duisburg-Essen, D-47048, Duisburg, Germany

ARTICLE INFO

PACS:
42.81

Keywords:

Optoelectronic circuit
resonant tunneling diode
chaotic attractors
semiconductor laser
optical injection

ABSTRACT

This paper shows a complex nonlinear dynamics of an optically injected laser diode (LD) directly modulated by electrical current from a resonant tunneling diode (RTD) circuit. The LD model evolves a new control parameter called effective gain coefficient (EGC) and can switch between a free-running laser and a perturbed laser. A bifurcation diagram analysis sustained Lyapunov exponents' spectra reveals chaotic and quasi-periodic dynamics for restricted ranges of the frequency f_{in} and by EGC variations, including the generation of the hyperchaotic regime and multiscroll chaotic attractors through a cascade of periodic oscillations to the chaos. Moreover, an implementation of this new coupled system also shows that when an AC signal $V_{ac} \sin(2\pi f_{in} t)$ is added to the DC voltage bias, the LD outputs show several optical signals such as periodic, coherence collapse and chaotic regimes with different strange complex attractors which are devoted to more improve secure optical telecommunications.

1. Introduction

Since the discovery of chaos in 1963 by Lorenz, several attempts are made in many research fields in order to improve the complexity of dynamical system behaviors, leading to the chaos control. Nowadays, the study of chaotic systems is one of the main topics in nonlinear dynamics. Particular interest of chaos in optoelectronic circuits is to increase of specific performances of secure communication systems [1]. Semiconductor lasers are well-known as three-dimensional nonlinear systems for electrical field $E(t)$, carrier densities $N(t)$ and optical phase $\psi(t)$ mainly used in electronic/optical communications. However, these lasers are very sensitive to external perturbations such as optical feedback, optoelectronic feedback or optical injection[2,3]which can induce various instabilities such as extreme events, unforeseen effects complex nonlinear dynamical behaviors including chaos generation and so on in laser optical emission[4,5]. Therefore optically injected laser diodes (ILDs) are classified as complex nonlinear dynamics systems.

In addition, it has been proved that when driven by nonlinear current, the laser can operated with complicated dynamics[6]. Numerous driving nonlinear circuits are built by negative differential resistance elements for example Van der Pol oscillator, RTD circuits [7,8]and so on. In these last recent years, RTD circuits have received considerable attention due the broad-bandwidth negative differential resistance (NDR) region up to hundreds of GHz that RTDs provide[9]. Due to their narrow depletion region, RTDs can generate quantum effects such as phenomenon of tunneling effect; indeed the flow of electron (current) can easily tunnel through the quantum-well structure (QWS), manifesting itself by giving rise to the NDR. Major breakthroughs in RTD optoelectronic

* Corresponding author.

E-mail address: didier_mengue@yahoo.fr (A.D. Mengue).<https://doi.org/10.1016/j.ijleo.2020.164740>

Received 20 February 2020; Accepted 11 April 2020

0030-4026/ © 2020 Elsevier GmbH. All rights reserved.

hybrid circuits' (OEHCs) research have presented the possibility to easily integrate a RTD with others optoelectronic or optical devices such as photo-detector (RTD-PD) [9,10], electroabsorption modulator (RTD-EAM), laser diode (RTD-LD) or photodiode-laser diode (RTD-PD-LD) [7,10]. In these integrated circuits, RTD-LD modules act as hybrid optoelectronic devices which preserve the high-nonlinearity of RTD's current voltage (I-V) [4,8]. That is the starting reaping benefit of this coupling.

In recent works on RTDs-based circuits, the voltage-dependence current of RTD is modelled by the physics-based representation of Schulman et al.[7,8]or those of Brown et al[11]. Most of these works are focused on the single mode free-running laser whose rate equations describe the photon S and carrier N densities motions on the laser cavity[7,8]. Nevertheless, it is very interesting to know how the RTD-LD optoelectronic circuit acts by using an optically injected laser especially controlled by a novel chaotic parameter; the so-called effective gain coefficient (EGC) which is acknowledged to improve the secure communications and optical stability with or without noise and renders more complex the fractal dimension of relevant chaotic attractors[5,12]. Therefore, this paper describes for the first time the RTD and optically injected semiconductor laser coupling, using new rate equations model given by Mengue et al [2] and several interesting investigations carried out by the means of new decisive parameter-EGC and by the integration of the RTD driving. It is proven here that this approach leads to a novel sort of nonlinear complex laser systems whose dynamical behaviors seems richer than those of free-running laser diodes and the laser is capable of switching between a free-running laser and a perturbed laser. Therein, when an external AC driving voltage is added to de DC-bias, the injected laser diode (ILD) outputs a rich variety of dynamics including period adding to chaos, coherence collapse and different strange chaotic attractors for low modulating DC-biased voltage around 1.1V. This investigation carries interest in optical communication systems requiring low modulation current, frequency synthesizer and encryption information using controlled chaos generators.The article is organized as follows. In the tracking section, we present the equivalent electrical circuit of RTD-ILD optoelectronic oscillator and ILD rate equations. Section III presents numerical results and discusses about laser emissions by exploring series time evolutions and bifurcation diagrams of carrier and photon densities. It also discusses about, strange attractor shape obtained in carrier-photon space, Poincaré maps and evolutions of Lyapunov exponents. Finally, we conclude our paper in section IV.

2. Equivalent RTD-ILD lumped circuit description and laser model

The equivalent lumped circuit of the system is shown in Fig. 1(a) consisting of an RTD connected in series with a semiconductor laser subjected to the optical injection. The dynamics of RTD-based oscillator is described by the output voltage $V(t)$ across the capacitance C and electrical current $I(t)$ flowing in the inductor L .The resistor R is the overall resistance due to ohmic contacts and the circuit is well known as a forced Liénard oscillator [8,10]. Since the series connection of RTD with LD preserves the RTD shape current-voltage $I-V$ characteristic [4],we use the cubic nonlinear term $F(V)$ (Eq. (1)) modeling a mathematical representation of current-voltage characteristic of RTD-ILD whose graphic is given in Fig. 1(b). The factor B , a and b are positive constants.

Throughout numerical calculations, we have used the following parameter values: $B = 0.01796 \times 10^{-3} A/V^3$, $a = 2.451 \times 10^{-3} V$ and $b = 2.446 \times 10^{-3} V$, and therefore

$$F(V) = BV(V - a)(V - b) \tag{1}$$

Using Kirchoff's rules to the circuit presented in Fig. 1(b),we obtain the set of first order ordinary differential Eq. (2) giving the current modulation of the LD; $I(t)$ and the voltage $V(t)$ across RTD-ILD series connected. For the sake of simplicity, we could also admit RTD-LD instead of RTD-ILD.

$$\begin{aligned} \frac{dV(t)}{dt} &= \frac{1}{C}[I(t) - F(V)], \\ \frac{dI(t)}{dt} &= \frac{1}{L}[V_{dc} - RI(t) - V(t) + V_{ac} \sin(2\pi f_{in}t)]. \end{aligned} \tag{2}$$

In order to study the dynamical behavior of the driven ILD, we use the single mode semiconductor laser rate equations for the photon density $S(t)$, the electron density $N(t)$ and the optical phase $\psi(t)$ as given in Ref.[12] without stochastic terms,

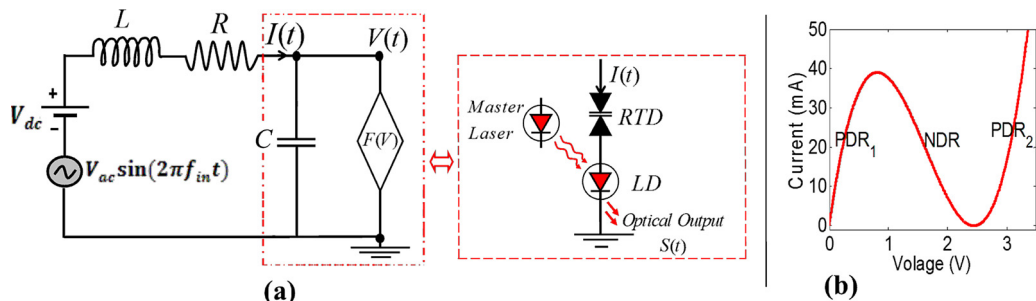


Fig. 1. XXX.

$$\begin{aligned}
 \frac{d}{dt}N(t) &= \frac{\eta_i I(t)}{q\mathfrak{V}} - \frac{N(t)}{\tau_r} - \left\{ \frac{1}{\tau_p} + [G_N(N(t) - N_{th})] \right\} S(t), \\
 \frac{d}{dt}S(t) &= \frac{(1 - \gamma)}{(1 + \gamma)} [G_N(N(t) - N_{th})] S(t) + 2 \frac{k_{inj}}{\tau_{in}^*} \sqrt{S_{inj} S} \cos \psi(t), \\
 \frac{d}{dt}\psi(t) &= \frac{1}{2} \alpha \frac{\gamma}{(1 + \gamma)} [G_N(N(t) - N_{th})] - \frac{k_{inj}}{\tau_{in}^*} \sqrt{\frac{S_{inj}}{S(t)}} \sin \psi(t) - \Delta\omega, \\
 \psi(t) &= \varphi(t) - \Delta\omega t.
 \end{aligned} \tag{3}$$

$I(t)$ is the modulating current given by numerical calculations of Eq. (2), η_i is the optical efficiency, q the electronic charge, \mathfrak{V} the laser diode active region volume, τ_r the carrier life time, τ_p the photon lifetime, the constant G_N is the modal gain, N_{th} the carrier density at the threshold, γ the effective gain coefficient (EGC), k_{inj} the injection parameter, $\tau_{in}^* = \tau_{in}/\gamma$ is the effective time of light in the laser cavity where the round-trip time inside the laser cavity is τ_{in} , $\psi(t) = \varphi(t) - \Delta\omega t$ represents the phase difference between the internal and the injected fields where $\Delta\omega$ is the frequency detuning.

For the purpose of algebraic transformations and numerical simulations, Eqs. (1)–(3) are normalized in order to work with small quantity values.

Thus, the variables are rescaled by the mean of constant values of optoelectronic system $(V_0, I_0, N_{th}, S_0)^T$, with $V_0 = 1\text{ V}$, $I_0 = 1\text{ A}$, $N_{th} = N_0 + 1/(G_N \tau_p)$, $S_0 = N_{th} \tau_p / (G_N \tau_p)$. The subscript $(...)^T$ indicates the transpose. Thus the dimensionless voltage $x(t)$, current $y(t)$, photon $s(t)$ and carrier $n(t)$ densities are defined by $x(t) = V(t)/V_0$, $y(t) = I(t)/I_0$, $n(t) = N(t)/N_{th}$ and $S(t) = s(t)/S_0$ respectively.

The rate coupled equations corresponding to dimensionless quantities $(x, y, z, n, s, \psi)^T$ for the dimensionless rescaling time variable $\tau = \omega_0 t$ are given as follows:

$$\begin{cases}
 \dot{x}(t) = m^{-1}[y(t) - f(x)] \\
 \dot{y}(t) = m[v_{dc} - ry(t) - x(t) + v_{ac} \sin(z(t))] \\
 \dot{z}(t) = \Omega_{in} \\
 \dot{n}(t) = \gamma_0 \left[\frac{1}{i_{th}} y(t) - n(t) - \frac{n(t) - \delta}{1 - \delta} s(t) \right] \\
 \dot{s}(t) = 2G_0(\gamma^{-1} - 1)(n(t) - 1)s(t) + 2\gamma k \sqrt{s(t)} \cos(\psi(t)) \\
 \dot{\psi}(t) = \alpha G_0(n(t) - 1) - \gamma k \frac{1}{\sqrt{s(t)}} \sin(\psi(t)) - \Delta\Omega
 \end{cases} \tag{4}$$

The normalized parameters are defined by $m = \sqrt{C/L}$, $\tau_0 = \omega_0 \tau_r$, $\gamma_0 = 1/\tau_0$ and $\Omega_{in} = 2\pi f_{in}/\omega_0$ is the normalized frequency of external AC perturbation, $G_0 = G/\omega_0$ with G the normalized differential gain[2], $\omega_0 = 1/\sqrt{LC}$ is the dimensionless natural angular-frequency of forced RTD circuit, $\Delta\Omega = \frac{\Delta\omega}{\omega_0}$ and $k = \frac{k_{inj}}{\omega_0 \tau_{in}} \sqrt{\frac{S_{inj}}{S_0}}$ refer to normalized frequency detuning and injection strength, respectively. Without lack the generality and for simplification, we choose $S_{inj} = S_0$. For numerical calculation we assume that the laser threshold current is around $I_{th} = 5.1\text{ mA}$ ($i_{th} = 5.1$), R-parameter around $6.6\ \Omega$, $C = 5.6\text{ pF}$ and $F = 8.0nH$.

3. Numerical Results and Discussion

3.1. Bifurcation diagrams and proposed control parameters

Since the semiconductor laser is perturbed by an external periodic AC voltage with frequency f_{in} and an optical injection signal characterized by k_{inj} parameter or γ from S_{inj} according to semiconductor LD here used model, we propose to use an RTD driver oscillator parameter f_{in} and laser EGC parameter γ as control parameters of laser dynamics.

Fig. 2 plots bifurcation diagrams of LD driving current corresponding to normalized $y(t)$ parameter (Fig. 2(a)) and photon density in Fig. 2(b) with the variation of f_{in} respectively. It is found that these bifurcation diagrams present chaotic regions separated by quiescent regions when f_{in} is moving from around 0 GHz to 2.35 GHz maintaining EGC constant at 0.5 , $V_{dc} = 1.145\text{ V}$ and $V_{ac} = 150\text{ mV}$. Chaotic regions are known as unsynchronized windows and quiescent regions describe the possible synchronization between driving current and laser emission corresponding to period- n oscillations[7]. It is also found that the nature of driving current is emulated by laser photon number through the perfect replications of different windows corresponding to bifurcation diagrams infrequency domain. So we also highlight this fact through the times series evolutions stood for in Fig. 5.

The bifurcation diagram of laser output with increasing EGC is presented in Fig. 3 for $f_{in} = 1.3\text{ GHz}$. According to certain values of EGC as depicted in Fig. 6. It is clearly shown that the laser evolves from chaotic dynamical behavior for $\gamma \leq 0.37$ to periodic orbits for γ equal to 0.4 , 0.6 or near 0.8 as presented by zooming in Fig. 6 and far near to 0.97 EGC values. However there are narrower chaotic regions between periodic windows.

According to bifurcation diagrams in Figs. 3 and 4 f_{in} and EGC, γ can be used as to control chaotic dynamics. In addition, bifurcation diagrams depicted in Fig. 4 show that the amplitude of the periodic perturbation V_{ac} also allows the control of chaos. Therefore, various dynamics that bifurcation diagrams reveal leads to choose f_{in} , γ and V_{ac} like control parameters whose numerical values are given on different captions.

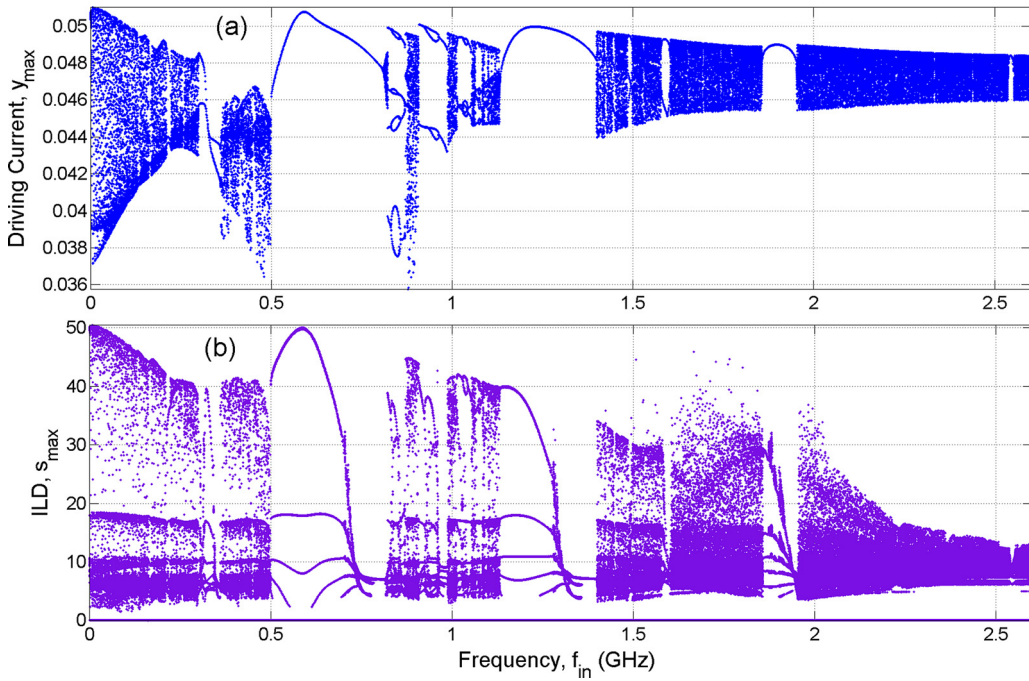


Fig. 2. XXX.

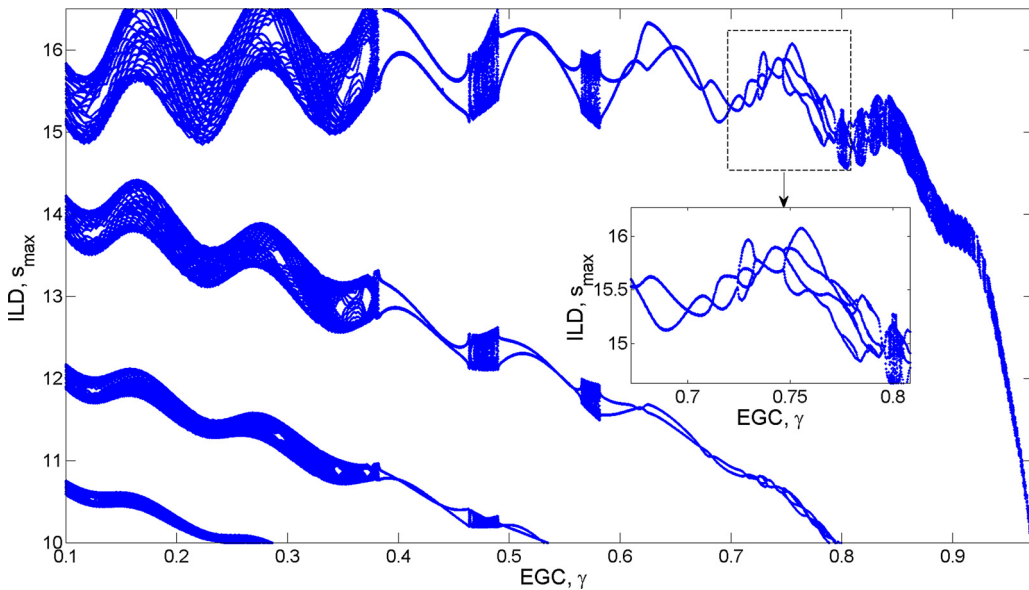


Fig. 3. XXX.

3.2. Time series and phase portraits

In optical communications, the driving oscillatory current $I(t)$ information is converted into optical output via the laser in order to be coupled to conventional channel such as optical fiber until its extraction at the receiver. We present through Fig. 4, series time evolutions of driving current and optical outputs, when EGC is fixed to 0.65, without frequency detuning, with $k_{inj} = 0.0078$, $V_{dc} = 1.145 V$ and $V_{ac} = 120 mV$, for different values of f_{in} mainly $f_{in} = 0 GHz$ (Fig. 4(a)), $f_{in} = 0.42 GHz$ (Fig. 4(b)) and $f_{in} = 1.9 GHz$ (Fig. 4(c)). It appears conspicuous to observe for laser emissions, carriers and photons evolutions emulate the driving current (y variable), confirming the earlier mentioned fact that the RTD current waveforms directly modulate the optically ILD even when laser outputs are chaotic (Fig. 4(b) and (c)). The emulation phenomenon means that laser diode rationally converts electrical signal into optical signal.

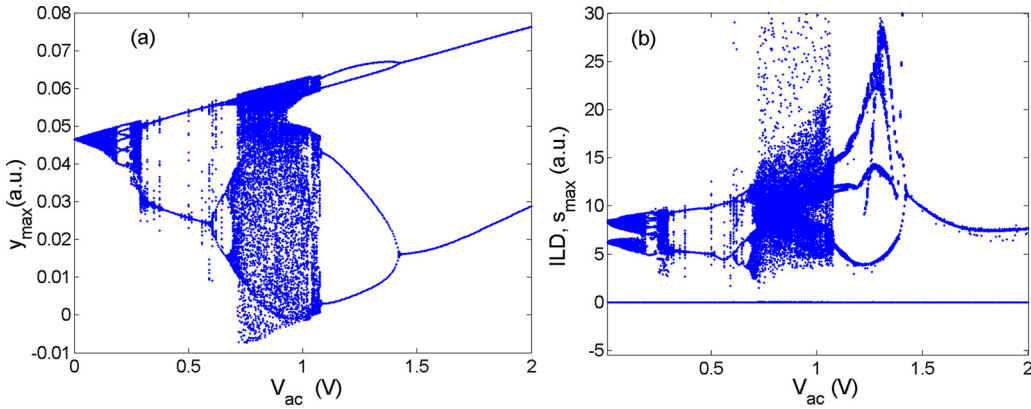


Fig. 4. XXX.

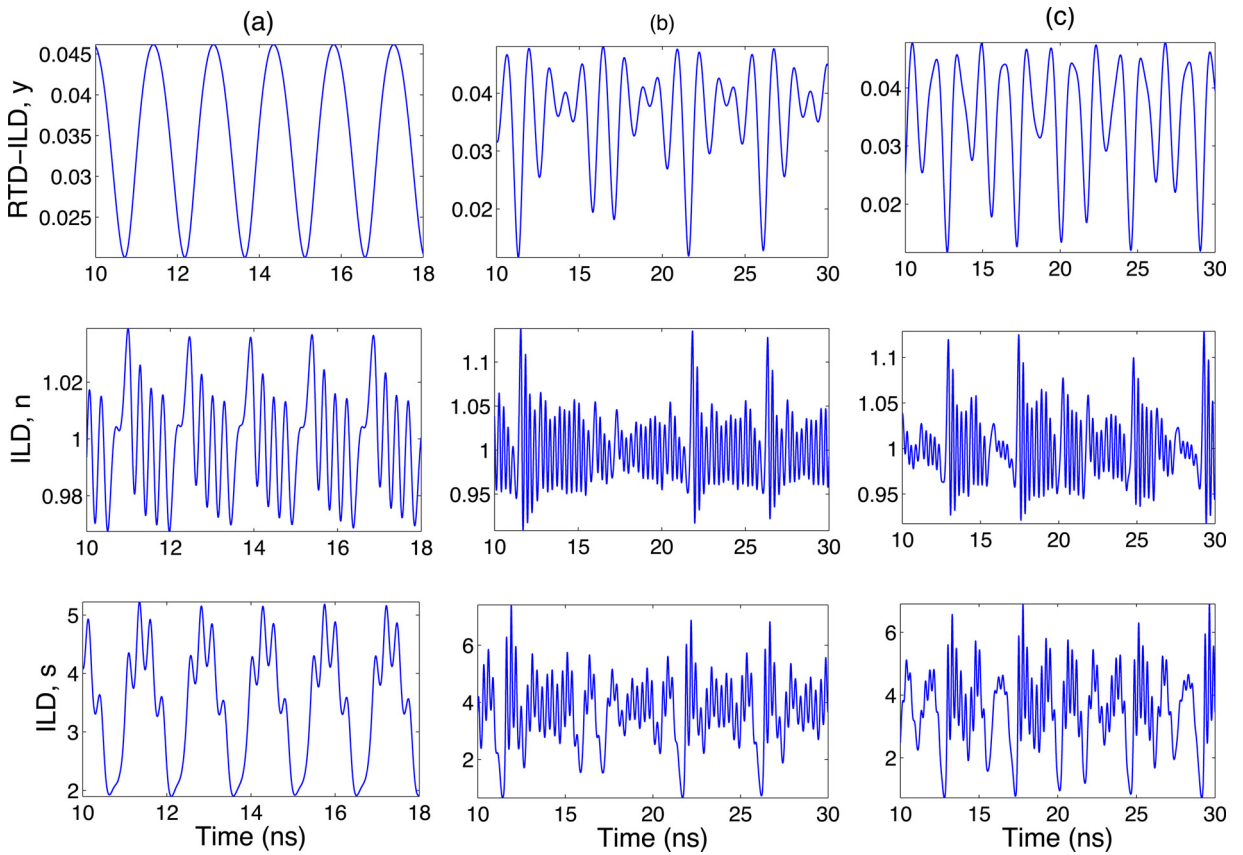


Fig. 5. XXX.

In addition, with particular values of both optical and electrical perturbation (optical injection and AC voltage excitation, respectively), corresponding to injection strength $k_{inj} = 2 \times 10^{-3}$ for frequency $f_{in} = 1.3 \text{ GHz}$, at 1.145 V DC bias, we reproduce some dynamical behaviors of the LD through phase portraits limit cycles in Fig. 6 for certain values of EGC, namely $\gamma = 0.99$, $\gamma = 0.9$, $\gamma = 0.75$, $\gamma = 0.4$, $\gamma = 0.3$ and $\gamma = 0.25$. We notice that a period-1 oscillation occurs when $\gamma = 0.99$ and a period-2 close $\gamma = 0.9$. When EGC $\gamma = 0.75$ and $\gamma = 0.4$, the laser displays a period-3 and a period-6 attractors respectively. The dynamics becomes chaotic as long as γ is decreasing from 0.41 to 0.1. According to the bifurcation diagram depicted in Fig. 3, we clearly observe the γ -control chaos in laser oscillations in Fig. 6. In these conditions, γ -variations carry away a route to chaos like those displayed in certain optical feedback systems [13].

We notice in addition that, the frequency detuning shift from 2 GHz to 30 GHz , while other parameter values are constant as in the previous figure, the LD outputs various different shapes of attractors for certain values of EGC and these attractors are strange at

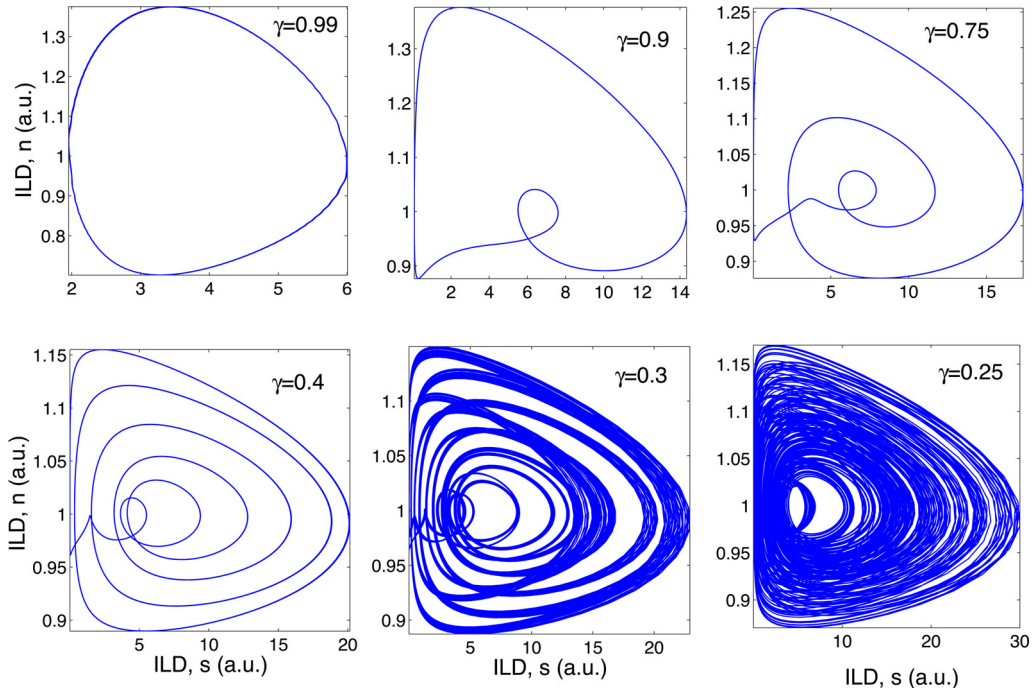


Fig. 6. XXX.

lower γ -values at 0.4 as presented in Fig. 7.

A paramount result of this coupled system is also exhibited in Fig. 7(a) with the emergence of novel multiscroll chaotic attractors rarely observed in semiconductor lasers dynamics which appear through a scenario of 2-period attractor, 3-period attractor and multiscroll chaotic attractor in the photon-carrier phase plane by decreasing the EGC. In addition in Fig. 7(b), we stand for the 3D-projection (s, n, ψ) of a multiscroll attractor near to the upper limit value of EGC ($\gamma = 0.099$).

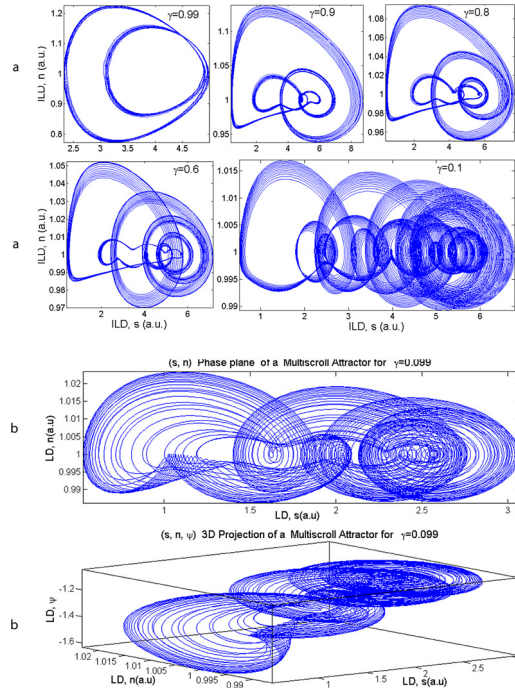


Fig. 7. XXX.

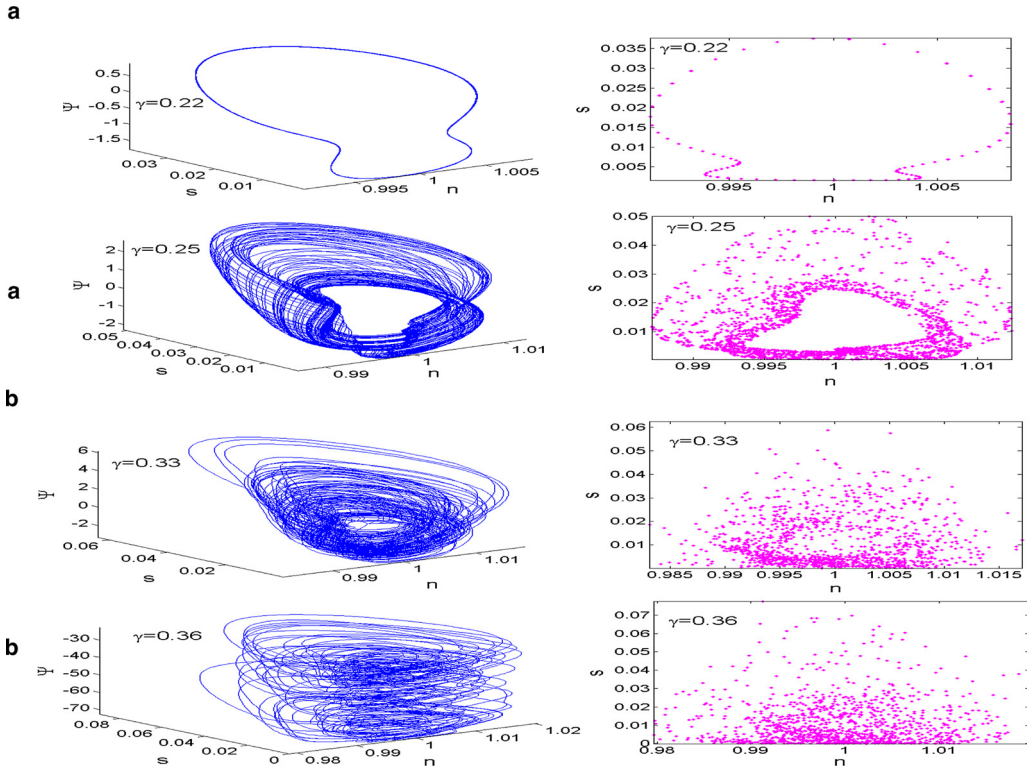


Fig. 8. XXX.

3.3. Poincaré maps and Lyapunov exponent spectra

In this subsection we study the rich dynamics of the coupled system by successively showing Poincaré maps and Lyapunov exponent evolutions for different values of control parameters. The Poincaré section is obtained from the topological behavior of phase space portrait. Its simplest idea is to suppose a particular proper surface (plan (P)) on phase space. One observes the set of intersection points between the plane (P) and states of the trajectories of variables. The Poincaré map is then created with this set of crossing points [14–16]. Fig. 8 depicts the 3D behavior of carrier-light-phase attractors and the corresponding Poincaré maps by sampling the phase space portrait stroboscopic following the plane (s-n) when the RTD-RLC-LD circuit is biased at high voltage around $V_{dc} = 2.38 V$ (but always in the RTD-LD negative differential resistance region), for the amplitude of AC voltage $V_{ac} = 2 mV$ and $f_{in} = 910 MHz$. The displayed 3D strange shapes in (n, s, ψ) plan (left panel) and corresponding Poincaré map (right panel) indicate that laser operations are highly affected by variations of EGC. When $\gamma = 0.22$, the laser exhibits a quasi-periodic oscillation due the corresponding closed curve shown by Poincaré map. It appears a strange attractor for $\gamma = 0.25$ in Fig. 8(a). However, in Fig. 8(b) we show a coherence collapse regime for γ -values higher than 0.25 in particular increasing of γ from 0.33 to 0.36 and corresponding Poincaré maps.

We finally examine the sensitivity of laser with control parameters f_{in} and γ by evaluating the predicted quantity (number) that measures the exponential rate of separation or attraction of two close trajectories in the phase space. In Fig. 9, we compute the evolutions of Lyapunov exponents. It is found that at least one of the Lyapunov exponents evolutions corresponding for the photon density λ_s , the carrier density λ_n or the optical phase λ_ψ is positive when $f_{in} \in]0 GHz, 2.6 GHz[$ (Fig. 9(a)) or for $\gamma \in]0, 0.85[$ (Fig. 9(b)): It is a strong hallmark of chaotic signals generated by the laser. Furthermore, by looking into Fig. 9(a), we note two positive Lyapunov exponents for f_{in} lower than 1.2 GHz and a narrower frequency region with two positive Lyapunov exponents for $f_{in} \in]0.5 GHz, 0.7 GHz[$. It points up of the hyperchaotic regime in the complex dynamics the semiconductor laser-tunnel diode coupling. These kind of systems are primordial in secure optical communications due to fractal dimension of aforementioned attractors in the complete chaotic synchronization [5,17].

4. Conclusion

In this study, we have analyzed dynamics of semiconductor lasers driven by a current from an RTD oscillator. Owing to the large number of parameters involved, we have explored the evolution of the laser rate equations through bifurcation analysis of proposed control parameters i.e. the frequency f_{in} , the effective gain coefficient γ or the external periodic voltage amplitude V_{ac} . We demonstrated that the laser exhibits a rich variety of complex dynamics including chaos which was firstly proved by displayed shapes of strange attractors on photon-carrier space. One of main results of the study is the multi-switching of lasers which behave as electro/

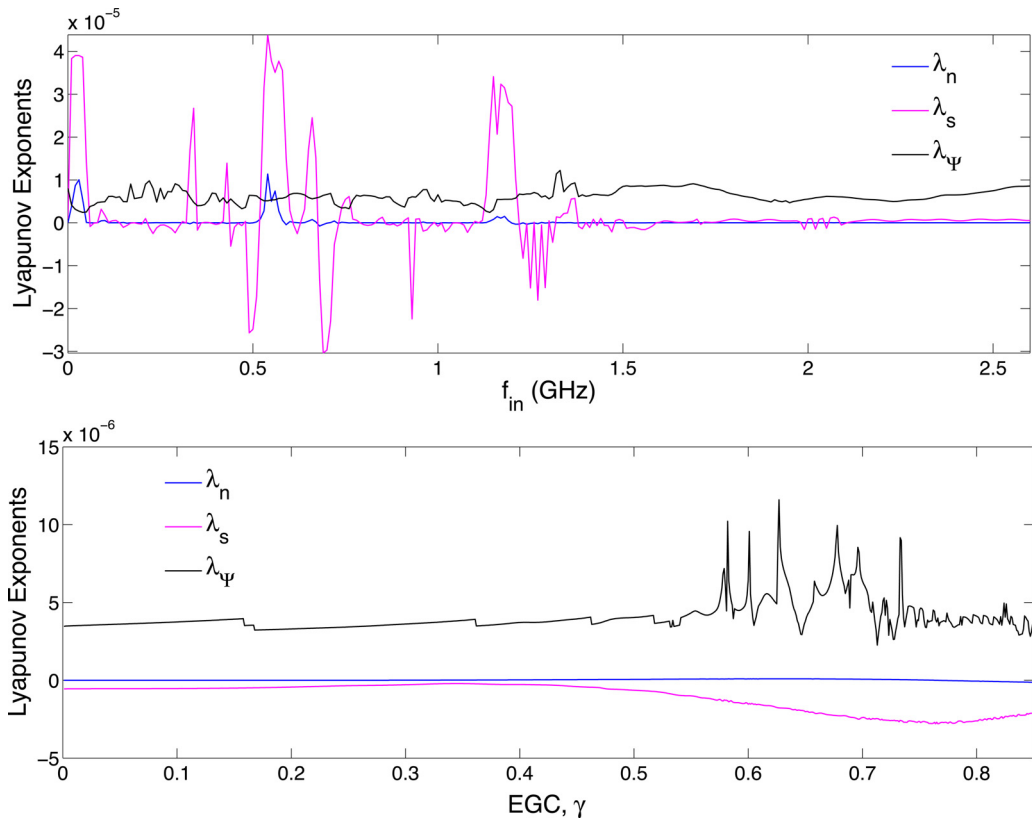


Fig. 9. XXX.

optical converter under peculiar conditions. We have investigated the route of the multiscroll chaotic attractors and proving the existence of the hyperchaotic regime in laser dynamics at a limited frequency interval. Altogether, these results are very promising for the implementation of novel optoelectronic systems requiring low modulation current with an utmost nonlinear dynamics.

Declaration of Competing Interest

The following authors declare that the paper is an original work and it is not submitted to another journal.

References

- [1] M.Z. De la Hoz, L. Acho, Y. Vidal, A modified Chua chaotic oscillator and its application to the secure communications, *Applied Mathematics and Computation* 247 (2014) 712–722.
- [2] A.D. Mengue, B.Z. Essimbi, Complex chaos and bifurcations of semiconductor lasers subjected to optical injection, *Opt Quant Electron* 42 (2011) 389–407.
- [3] P. Kumar, F. Grillot, Control of dynamical instability in semiconductor quantum nanostructures diode lasers: Role of phase-amplitude coupling, *Eur. Phys. J.* 222 (2013) 813–820.
- [4] B. Romeira, J.M.L. Figueiredo, T.J. Slight, L. Wang, E. Wasige, C.N. Ironside, *Optoelectronic Integration of a Resonant Tunneling Diode and a Laser diode*, Eindhoven, The Netherlands, *Optoelectronic* (2008) 211–215.
- [5] A.D. Mengue, B.Z. Essimbi, Secure communication using chaotic synchronization in mutually coupled semiconductor lasers, *Nonlinear Dyn.* 70 (2012) 1241–1253.
- [6] L. Illing, M.B. Kennel, Shaping Current Waveforms for direct Modulation of Semiconductor Lasers, *IEEE J. Quantum Electron.* 40 (2004) 445–452.
- [7] B. Romeira, J.M.L. Figueiredo, T.J. Slight, L. Wang, E. Wasige, C.N. Ironside, J.M. Quintana, M.J. Avedillo, Synchronisation and chaos in a laser diode driven by a resonant tunnelling diode, *IET Optoelectron.* 2 (2008) 211–215.
- [8] B. Romeira, J.M.L. Figueiredo, T.J. Slight, L. Wang, E. Wasige, C.N. Ironside, Resonant tunneling diode optoelectronic integrated circuits, *Proc. of SPIE* 60 (2010) 7608 quantum sensing and nanophotonic VII, 760801 (22 January 2010).
- [9] J.M.L. Figueiredo, B. Romeira, T.J.S. light, L. Wang, E. Wasige, Self-Oscillation and period adding from resonant tunneling diode-laser diode circuit, *Electronics Letters* 44 (2008) 876–878.
- [10] B. Romeira, K. Seunarine, C.N. Ironside, A.E. Kelly, J.M.L. Figueiredo, Self-synchronized optoelectronic oscillator based on an RTD photo-detector and a laser diode, *IEEE Technol. Lett.* 23 (2011) 1048–1058.
- [11] L.J.S. Coelho, J.F. Martins-Filho, J.M.L. Figueiredo, C.N. Ironside, Modeling of light-sensitive resonant-tunneling-diode devices, *J. Appl. Phys.* 95 (2004) 8258.
- [12] E.D. Essebe, A.D. Mengue, B.Z. Essimbi, Stochastic Behavior of an External Optically Injected Single-Mode Semiconductor Laser including Langevin, Noise Sources, *Phys. Scr.* 94 (2019) 115501.
- [13] J. Ohtsubo, *Semiconductor Laser: Stability, Instability and Chaos*, Second edition, (2007) Springer series in Optical Sciences 111.
- [14] A.D. Mengue, B.Z. Essimbi, Symmetry chaotic attractors and bursting dynamics of semiconductor lasers subjected to optical injection, *Chaos* 22 (2012) 10 013113.
- [15] A.D. Mengue, B.Z. Essimbi, Stability and on-off chaotic states mechanisms of semiconductor lasers with optical injection on the new modified rate equation model, *Phys. Scr.* 85 (2012) 9 025404.
- [16] A.B. Özer, E. Akin, Tools for detecting chaos, *SAÜ Fen Bilimleri Enstitüsü Dergisi*, (2005), pp. 60–66 Cilt, 1. Sayı 9.
- [17] G. Dong, R. Du, L. Tian, Q. Jia, A novel autonomous system with different multilayer chaotic attractors, *Physics Lett. A* 373 (2009) 3838–3845.



Simulink implementation of a new optoelectronic integrated circuit: stability analysis and infinite-scroll attractor

D. E. Essebe¹ · A. D. Mengue² · B. Z. Essimbi^{1,3}

Received: 30 October 2020 / Accepted: 1 June 2021

© The Author(s), under exclusive licence to Springer Science+Business Media, LLC, part of Springer Nature 2021

Abstract

In this paper a 6-D optoelectronic system consisting of an optical injected semiconductor laser driven by a resonant tunneling diode is reported. A stability analysis of the hybrid system is analytically and numerically performed and paramount role of the effective gain coefficient is stuck out in the framework of new stability control. As a result, this parameter allows improving the accuracy of the stability study by circumscribing locked and unlocked regions. Besides, a narrow area of stability is pointed up within the sea of unstable points from which a complex fractal attractor so-called infinite-scroll attractor is highlighted. Thereby, Simulink shows generation effectiveness of infinite-scroll attractor erratically interspersed by laminar phases. Also dynamics of Lyapunov exponents has confirmed that it refers to a strange fractal attractor. Moreover chaos control is structurally carried out by direct current polarisation.

Keywords Infinite-scroll attractor · Stability · Chaos control · Simulink implementation · Tunneling diode · Laser

1 Introduction

Chaos is a rich nonlinear phenomenon characterized by interesting properties such as unpredictability, ergodicity, mixing property, complicated structure dynamics, deterministic dynamics, high sensitivity to initial condition (Abdullah et al. 2018) to name a few. Many natural and non-natural systems are commonly modeled by nonlinear differential equations exhibiting chaos. So, nonlinear process plays as a cornerstone in developing and understanding novel complex systems as well it has received significant attentions in various fields. Chaotic systems have been also attracted in several scientist fields and usually play a relevant role improving their performances. There are many

✉ A. D. Mengue
didier_mengue@yahoo.fr

¹ Department of Physics, Faculty of Science, University of Yaounde I, PO Box 812, Yaounde, Cameroon

² Department of Electrical and Electronic Engineering, Faculty of Engineering and Technology, University of Buea, PO Box 63, Buea, Cameroon

³ ZHO, Optoelektronik, Universität Duisburg-Essen, D-47048 Duisburg, Germany

reasons why the nonlinear dynamics have been intensively studied in recent years. For example in physics to mention merely a few, nonlinear dynamics offers a great opportunity to improve memristive systems (Wang et al. 2017; Ma et al. 2018), circuit-systems (Li and Yao 2016; Ma 2014; Sun et al. 2011) lasers (Mengue and Essimbi 2012a; Daly et al. 2013) RTD optoelectronic based-systems (Figueiredo 2008), etc.

In recent years, several studies have been reported in the field of optoelectronic related to resonant tunneling diode-laser diodes (RTD-LD) systems with very interesting potential in improving laser features (Romeira 2008, 2013; Romeira et al. 2017; Ironside et al. 2019). However, the two-rate equations have been used to model the LD dynamics. Recently, Essebe et al. (Essebe et al. 2020) have taken into account the modified RTD-LD systems including a semiconductor laser with optical injection modeled by Mengue and Essimbi (Mengue and Essimbi 2011). This has led to a 6-D optoelectronic system with furthermore complex dynamical behavior such as the generation of multiscroll chaotic attractors, coherent collapse, as well as hyperchaotic dynamics controlled by the effective gain coefficient and other parameters (Essebe et al. 2020).

As well-known, in nonlinear chaotic systems, a slight variation of parameters or initial conditions can give rise to different outputs dynamics due to instabilities for example (Abdullah, et al. 2018). In addition in lasers' dynamics, optical injection, optical feedback, electrical current modulation or other external excitation provides additional degree of freedom (Ohtsubo 2006; Mengue and Essimbi 2012b). Hence, despite interesting behavior which occurs in laser output due to additional degree of freedom, the system may be subject to undesired phenomena such as relaxation oscillations, coherence collapse, instabilities, bursting oscillation (Mengue and Essimbi 2012a), etc. that can deteriorate the laser outputs (Ohtsubo 2006). Stability analysis may provide suitable conditions improving the features of those systems. Understanding instabilities of nonlinear systems is important to access their performance or to control their dynamics. Stability analysis deals better with nonlinear systems (Daly et al. 2013; Ohtsubo 2006; Mengue and Essimbi 2012b). The stability analysis control includes the phase portrait analysis, Lyapunov stability theory using eigenvalues or Lyapunov exponents and Routh-Hurwitz criterion to name a few.

In this paper, the Routh-Hurwitz stability criterion, Simulink implementation and Lyapunov exponents' dynamics are applied to various control parameters to investigate the oscillatory behavior of this system. Using theoretical and numerical calculations, we investigate the effects of main parameters such as DC bias, optical injection strength and the effective gain coefficient (EGC) on dynamical behavior. The purpose of this paper is to study the stability analysis and infinite-scroll attractor behavior of this novel model. The control of the system is provided through bifurcation diagram to furthermore improve functionalities of RTD-LD oscillators. In recent years, Matlab-Simulink environment has taken growing consideration in the simulation and implementation of chaotic systems (Abdullah et al. 2018) and in designing new chaotic maps for secure communication/transmission (Hamsa 2018) with accuracy. So, in this paper, Matlab/Simulink implementation will be built to understand well the formation of infinite scroll attractors.

The paper proceeds as follows: in Sect. 2 we present the optoelectronic model equations and the stability analysis according to Routh-Hurwitz criterion. Section 3 provides its infinite-scroll attractor and Simulink implementation. Section 4 discusses the results and the effect of main parameters of dynamical behavior and the last section is devoted to conclusion.

2 Optoelectronic model

Recently starting from the classical RTD-LD Liénard oscillator (Figueiredo 2008; Romeira 2008,2013; Romeira et al. 2017), we have derived the time dependent equations of a novel 6-D optoelectronic hybrid oscillator by replacing the 2-D LD by 3-D LD from Essebe et al. (2019). The model’s circuit is presented in Fig. 1. From Ref. (Essebe et al. 2020), the normalized dimensionless differential equations of the system are given by Eqs. (1)

$$\begin{cases} \dot{x}(t) = m^{-1} [y(t) - f(x)] \\ \dot{y}(t) = m [v_{dc} - ry(t) - x(t) + v_{ac} \sin(z(t))] \\ \dot{z}(t) = \Omega_{in} \\ \dot{n}(t) = \gamma_0 \left[\sigma y(t) - n(t) - \frac{n(t) - \delta}{1 - \delta} s(t) \right] \\ \dot{s}(t) = 2G_0\beta(n(t) - 1)s(t) + 2\gamma k \sqrt{s(t)} \cos(\psi(t)) \\ \dot{\psi}(t) = \alpha G_0(n(t) - 1) - \gamma k \frac{1}{\sqrt{s(t)}} \sin(\psi(t)) - \Delta\Omega \end{cases} \quad (1)$$

Let us note that, the triplet (n, s, ψ) represents the optical output subsystem where n, s and ψ are normalized carrier density, photon density and optical phase respectively. Equation (1) is obtained rescaling parameters as follows: $x(t) = V(t)/V_0, y(t) = I(t)/I_0, N(t) = N(t)/N_{th}$ and $s(t) = S(t)/S_0, \sigma = 1/i_{th}$. The normalized parameter m is equal to $m = \sqrt{C/L}$; $\tau_0 = \omega_0 \tau_r$ ($\gamma_0 = 1/\tau_0$) and $\Omega_{in} = 2\pi f_{in}/\omega_0$ is the normalized frequency of external AC perturbation. $G_0 = G/\omega_0$, with G the normalized differential gain, $\omega_0 = 1/\sqrt{LC}$ is the normalized natural angular-frequency of forced RTD circuit, $\Delta\Omega = \Delta\Omega/\omega_0$ and $k = \frac{k_{inj}}{\omega_0 \tau_{in}} \sqrt{\frac{S_{inj}}{S_0}}$ refer to normalized frequency detuning and injection strength respectively. The parameter β is the mean EGC (Essebe et al. 2020). The RTD consists of 2 AlAs barriers each 2 nm thick and 6 nm InGaAs quantum with measured values of valley-to-peak voltage difference of around 0.8 V and peak current densities up to 18 kAcm⁻². The device emitted in the 1550 nm optical communications window and can achieve up to 28 dB optical modulation in a 200 μm active length device area InGaAlAs RTD, with 500 nm as the width of the low doped layer on the collector side of the RTD (Figueiredo et al. 2001). The tunable semiconductor diode Laser with external cavity from 635 to 2450 nm, output power up to 1mW and high fiber coupling efficiency (Mengue and Essimbi 2011).

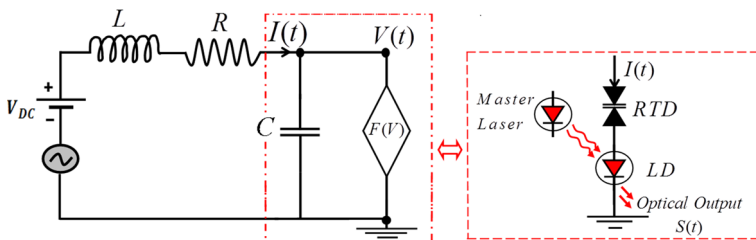


Fig. 1 Equivalent circuit of the optoelectronic RTD-LD oscillator

3 Theory

3.1 Analytical study of stability

The N-shape of the RTD is approximated by a current–voltage cubic law which presents a negative differential resistance region (Essebe et al. 2020), as depicted in Fig. 2. Here, we denote the first positive differential resistance PDR1, the negative differential resistance NDR and the second positive differential resistance PDR2. Also, the area (between the curve and V-axis) under the RTD current–voltage characteristic is S_1 and that above is S_2 . Later we shall discuss the dynamic of the system when $S_1 \approx S_2$ (Fig. 2a), $S_1 < S_2$ (Fig. 2b) $S_1 > S_2$ (Fig. 2c). The number of equilibria points will be analyzed as follows. Let $\dot{x} = \dot{y} = \dot{z} = \dot{s} = \dot{h} = \dot{\psi} = 0$, so we get the non-trivial steady states. This leads to numerical calculation of equilibria points solving the Eqs. (2) giving the relationships between fixed points successively

$$\begin{cases} rf(x_0) + x_0 - v_{dc} = 0 \\ y_0 = f(x_0) \\ z_0 = 0 \\ A_3(\Delta n_0)^3 + A_2(\Delta n_0)^2 + A(\Delta n_0) + A_0 = 0 \\ s_0 = (\sigma y_0 - n_0)(1 - \delta)/(n_0 - \delta) \\ \psi_0 = -\arctan(\alpha/\beta) + \sin^{-1}\left(-\Delta\Omega\sqrt{s_0}/\gamma k\sqrt{1 + (\alpha/\beta)^2}\right) \end{cases} \quad (2)$$

with $y_0 = B_0x_0(x_0 - a)(x_0 - b)$, $\Delta n_0 = n_0 - 1$, $\beta = 1 - \gamma$, $A_0 = -(\Delta\Omega)^2(\sigma y_0 - 1) + \gamma^2k^2$, $A_1 = \frac{\gamma^2k^2}{1-\delta} + (\Delta\Omega)^2 + 2\alpha G_0\Delta\Omega(\sigma y_0 - 1)$, $A_2 = -\alpha^2(G_0)^2(\sigma y_0 - 1) - \beta^2(G_0)^2(\sigma y_0 - 1)2\alpha G_0\Delta\Omega$ and $A_3 = \alpha^2(G_0)^2 + \beta^2(G_0)^2$.

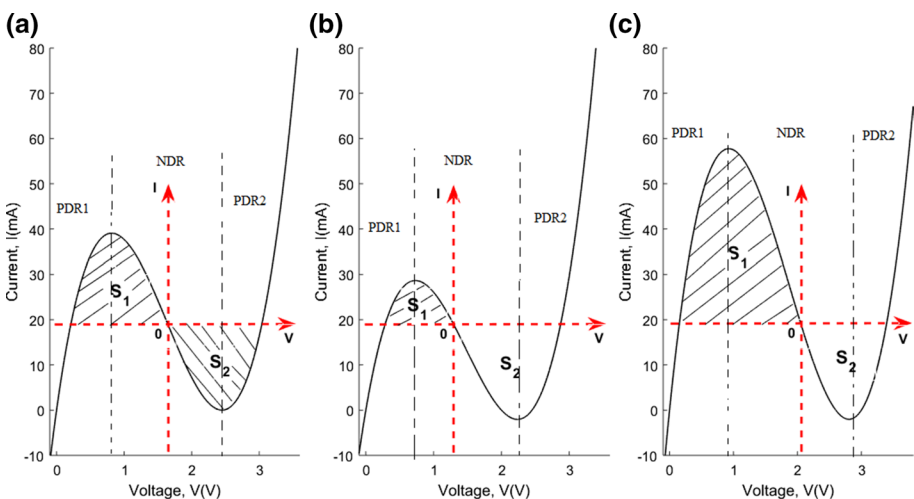


Fig. 2 Current–voltage (I-V) characteristics of RTD corresponding to $S_1 \approx S_2$ (a), $S_1 < S_2$ (b) and $S_1 > S_2$ (c)

From the relation $S(t) = (E_0(t))^2$ (where $E_0(t)$ is the magnitude of the complex optical field), s_0 must always be a positive value i.e. $\sigma y_0 > n_0$. Numerical calculation of Eqs. (2) shows that this conditions is satisfied if and only if the frequency detuning obeys $\Delta\Omega \leq 2GHz$ i.e. $\Delta\Omega \leq 0.41952$. In addition, according to the boundary of sine function, the necessary condition for optical locking requires the following relation $\Delta\Omega = \pm(\gamma k/\sqrt{s_0})\sqrt{1 + (\alpha/\beta)^2}$. For constant biased laser, we found in Ref. (Mengue and Essimbi 2012b) that all the points situated in space ($\Delta\Omega = \pm\gamma k/\sqrt{s_0}$) inside two curves are in locking region. However for the described driven laser, the condition $\Delta\Omega \leq 0.41952$ is added to insure that the photon number s_0 should be positive. Then possible locking regions can be found as presented in Fig. 3. From Eqs. (2), z_0 is always equal to zero due to the t-component from non-autonomous system. The steady state solutions x_0 and y_0 can be numerically calculated, and therefore we can obtain the corresponding n_0, s_0 and ψ_0 by solving numerically Eqs. (2) for each other variable.

The Jacobian matrix of the system around the equilibrium set of point $M_0(x_0, y_0, z_0, n_0, s_0, 0, \psi_0)$ is defined by

$$J_{M_0} = \begin{bmatrix} -m^{-1}f'(x_0) & m^{-1} & 0 & 0 & 0 & 0 \\ -m & -mr & mv_{ac} & 0 & 0 & 0 \\ 0 & 0 & 0 & 0 & 0 & 0 \\ 0 & \gamma_0\sigma & 0 & -\gamma_0\left(1 + \frac{s_0}{1-\delta}\right) & -\gamma_0\left(\frac{n_0-\delta}{1-\delta}\right) & 0 \\ 0 & 0 & 0 & 2\beta G_0 s_0 & 2G_0\beta(n_0 - 1) + \frac{\gamma k}{\sqrt{s_0}} \cos(\psi_0) & -2\gamma k\sqrt{s_0} \sin(\psi_0) \\ 0 & 0 & 0 & \alpha G_0 & \frac{\gamma k}{2(s_0)^{3/2}} \sin(\psi_0) & -\frac{\gamma k}{\sqrt{s_0}} \cos(\psi_0) \end{bmatrix} \tag{3}$$

where $f'(x_0) = B_0(3x_0^2 - 2(a + b)x_0 + ab)$.

The corresponding characteristic equation of the system (3) can be written as

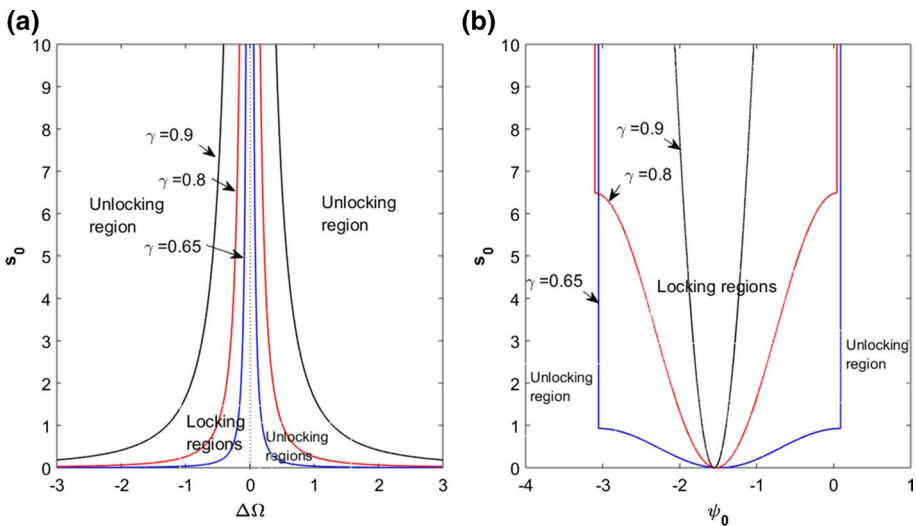


Fig. 3 **a** Unlocking and locking regions. The blue, red and black solid lines are plotted for $\gamma = 0.65, \gamma = 0.8$ and $\gamma = 0.9$ respectively; **b** Range of fixed optical phase ψ_0 for $\Delta\Omega$ situated in locking region between the bleu solid line and dote black line from (a)

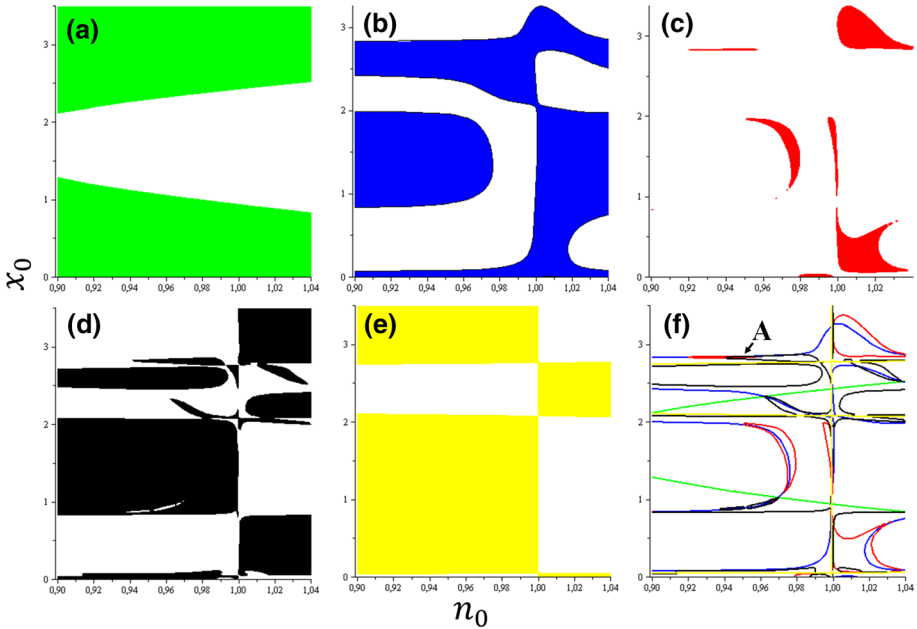


Fig. 4 Stability boundaries calculated from the Routh-Hurwitz stability criterion given by Eq. (6) for the first minor (a), the second minor (b), the third minor (c), the fourth minor (d) and the fifth minor (e) of the Hurwitz matrix. The intersecting figure (f) shows that there exists a shrunk stable locking region which satisfies Routh conditions

$$E(\lambda) = \lambda(a_0\lambda^5 + a_1\lambda^4 + a_2\lambda^3 + a_3\lambda^2 + a_4\lambda + a_5) \tag{4}$$

The coefficients a_1, a_2, a_3, a_4 and a_5 are given in Appendix.

The Hurwitz matrix associated to Eq. (4) is given by the Eq. (5).

$$H = \begin{bmatrix} a_1 & a_0 & 0 & 0 & 0 \\ a_3 & a_2 & a_1 & a_0 & 0 \\ a_5 & a_4 & a_3 & a_2 & a_1 \\ 0 & 0 & a_5 & a_4 & a_3 \\ 0 & 0 & 0 & 0 & a_5 \end{bmatrix} \tag{5}$$

Equation (4) can then be solved in order to capture the type of fixed point stability. In the same way, from the Routh-Hurwitz criterion, the equilibria $M_0(x_0, y_0, 0, n_0, s_0, \psi_0)$ are stable if all roots of Eq. (4) have negative real parts; otherwise they are unstable fix points. The necessary condition for stability is satisfied if and only if all the principal minors of (5) are positive. Since the coefficient $a_0 = 1$, this implies the following Routh-Hurwitz criterion stable locked solutions condition:

$$\begin{cases} a_1 > 0 \\ a_1 a_2 - a_3 > 0 \\ a_1 a_2 a_3 - (a_1)^2 a_4 - (a_3)^2 + a_5 a_1 > 0 \\ a_1 a_2 a_3 a_4 - a_1 (a_2)^2 a_5 + 2 a_1 a_4 a_5 - (a_1 a_4)^2 - (a_3)^2 a_4 + a_2 a_3 a_5 - (a_5)^2 > 0 \\ a_5 > 0 \end{cases} \tag{6}$$

In this stage, we can solve Eqs. (6) graphically using Maple software and the result is depicted in Fig. 4.

3.2 Dissipativity

The divergence of the system (1) is

$$\begin{aligned} \Delta V &= \partial \dot{x} / \partial x + \partial \dot{y} / \partial y + \partial \dot{z} / \partial z + \partial \dot{n} / \partial n + \partial \dot{s} / \partial s + \partial \dot{\psi} / \partial \psi \\ &= -mr - m^{-1} abB_0 - \gamma_r - 2\beta G_0 + (-m^{-1} B_0 x(3x - 2a - 2b) - \gamma_r s / (1 - \delta) + 2\beta G_0 n) \end{aligned} \tag{7}$$

It is hard to directly determine this dissipativity because of its dependence to the system variables (x, n, s) . However, as $a, b, B_0, m, \gamma_r, \delta$ (with $\delta < 1$), r, β and G_0 are positive, the variables (x, n, s) have always positive values and n is nearly equal to one. Hence, it clearly appears that the divergence $\nabla V = -\mu(x, n, s)$ is less than zero for convenient values of (x, n, s) such as $-\mu(x_0 = 1, n_0 = 0.99, s_0 = 6.4751) = -0.78516$ wherein s_0 is determined by using Eq. (2).

In this respect, the system (1) could be dissipative (as we have shown in tracking section that $\mu \approx 0.87$) and the element volume of the system is contracted at time t by the flow in the volume $V_0 e^{-\mu t}$. This means that the asymptotic solution settles into an attractor in the 6-D phase space. We denote that the selected maps will not be the 6-D, 5-D or 4-D but the projection of the attractor of the system in 2-D or 3-D spaces generated by adjusting selective control parameters such the EGC, frequency detuning and r-parameter.

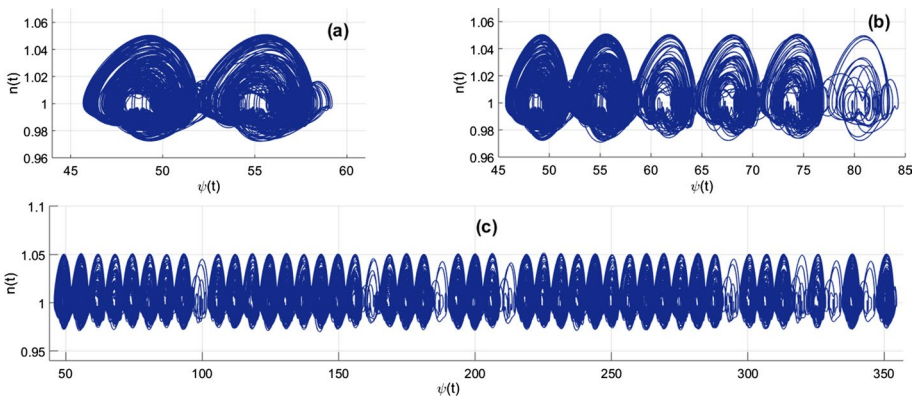


Fig. 5 The formation of *infinite-scroll* attractor: **a** Two-scroll attractor ($t = 1,000$), **b** Five-scroll attractor ($t = 3,000$) and **c** Forty one-scroll attractor with eight laminar phases ($t = 20,000$)

3.3 The Infinite-scroll attractor and Matlab/Simulink implementation

In this section, we use the fourth order Runge–Kutta (RK4) in the rate equation system (1) to generate the infinite scroll attractor and verify its effectiveness using MATLAB/Simulink implementation.

Let us recall that there is not non-chaotic system that exhibits multiple scrolls. Multiscroll attractors can be found either the system is chaotic or hyperchaotic (Ma et al. 2018). In this section, we set the parameters as $\alpha = 0.0264$, $r = 6.65$, $\gamma = 0.68$, $\sigma = 1/i_{th} \approx 196$, $\delta = 0.1512$, $v_{dc} = 1.145v$ and $v_{ac} = 0.1441$ and the system (1) being under relative strong external optical injection $k = 0.020637$. We choose the normalized time varying and numerical implementations are implemented using the RK4 algorithm in Matlab. After an initial transient, the solution settles into irregular and non-periodic oscillation that never repeats exactly in time. The trajectories in phase diagram when the optical phase $\psi(t)$ is plotted against the carrier density $n(t)$ in Fig. 5 show that, an attractor which the number of scroll that increases while the calculating time increasing. The system generates: two-scroll, five-scroll, and forty one-scroll attractors as the time is increasing, respectively in Fig. 5a–c. This stands for the infinity-attractor. We recall in addition that, according to refs. (Ma 2014) and (Ma et al. 2018), the number of scroll increases the complexity of the systems; it is useful that this number be stabilized to a fixed number. This fact is possible to be carried out by choosing $\gamma > 0.68$ when others parameters are fixed as indicated above or by decreasing the optical injection parameter k .

The MATLAB/Simulink implementation is used in addition in normalized system (1). A complex scheme is designed in a chip simply by choosing essentially small building blocks of Simulink such as multipliers, gains, summations, constants, functions, integrators, etc. as shown in Fig. 6. The behavior of (1) through Simulink scheme is investigated for same parameter values as in Fig. 5.

The first step is to verify the generation of infinite-scroll attractor. Simulink observations referring to the formation of infinite-scroll attractor, in the $\psi - n$ plane from XY Graph3 is depicted in Fig. 7a. Figure 7a (i) shows a three scroll attractor for $t = 2,226$, Fig. 7a (ii) presents a four scroll for $t = 2,410$, a five scroll attractor in Fig. 7a (iii) for $t = 3,000$ and a six scroll attractor in Fig. 7a (iv) for $t = 3,360$. It is shown that, the number of scrolls generated increases by the time of implementation. The Simulink observations confirm the RK4 numerical simulation results and the effectiveness of the infinite scroll attractor.

Second step consists to present optoelectronic attractors for other different parameters. It is interesting to discuss the optoelectronic phase portrait using the triplet (x, n, s) which is implied in the divergence in Sect. 3.2. Figure 7b–d depict the current–voltage, the light–voltage (optoelectronic) and the carried-photon projection of the chaotic attractors respectively.

Let us mention in addition that, the chaotic behavior of the infinite-scroll attractor is confirmed in respect to the frame of Lyapunov exponent dynamics. As depicted in Fig. 8, we have at least one positive Lyapunov exponent so; the system (1) the generated infinite-scroll is chaotic.

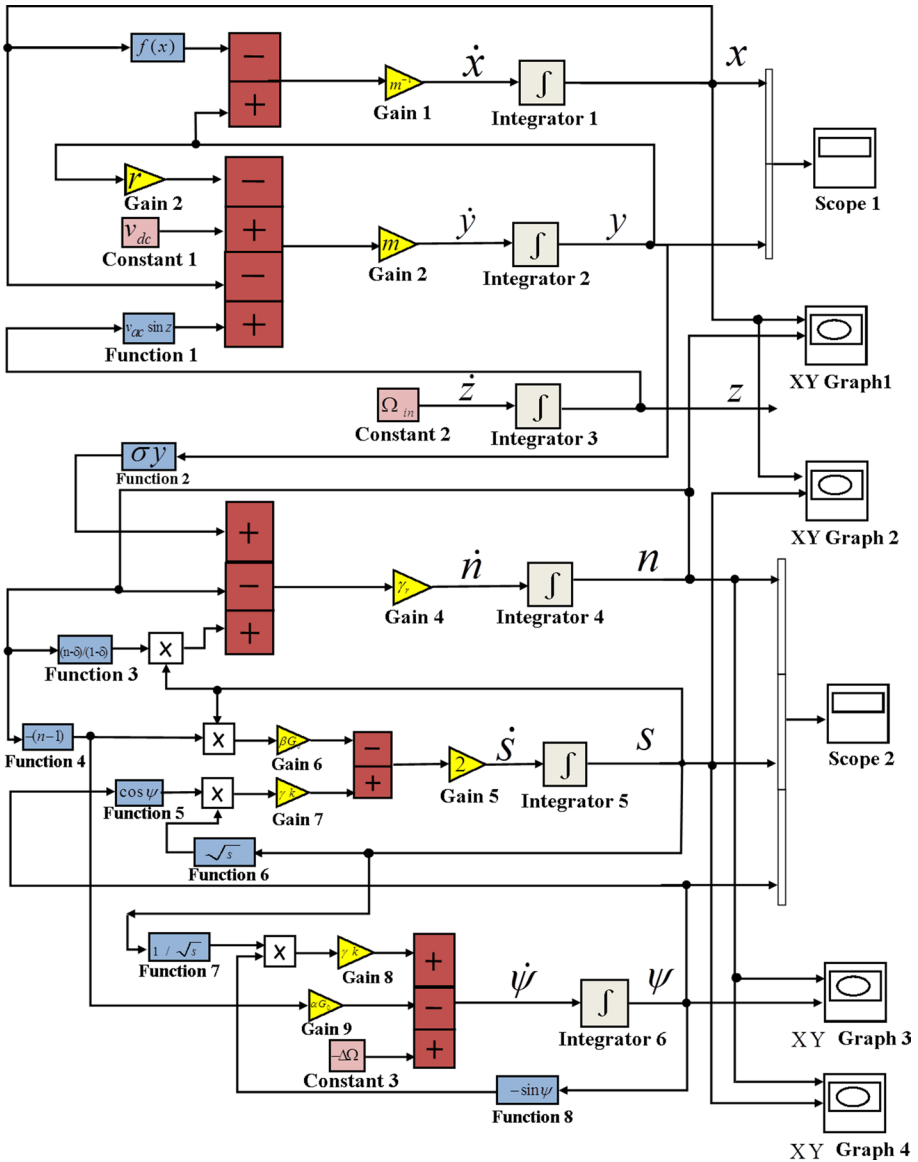


Fig. 6 Simulink implementation scheme of RTD-LD hybrid optoelectronic oscillator

4 Results and discussions

4.1 Improved linear stability and dynamics of infinite-scroll

In this section, the stability properties of the optically injected semiconductor laser (LD) driven by a resonant tunneling diode (RTD) current is numerically investigated and

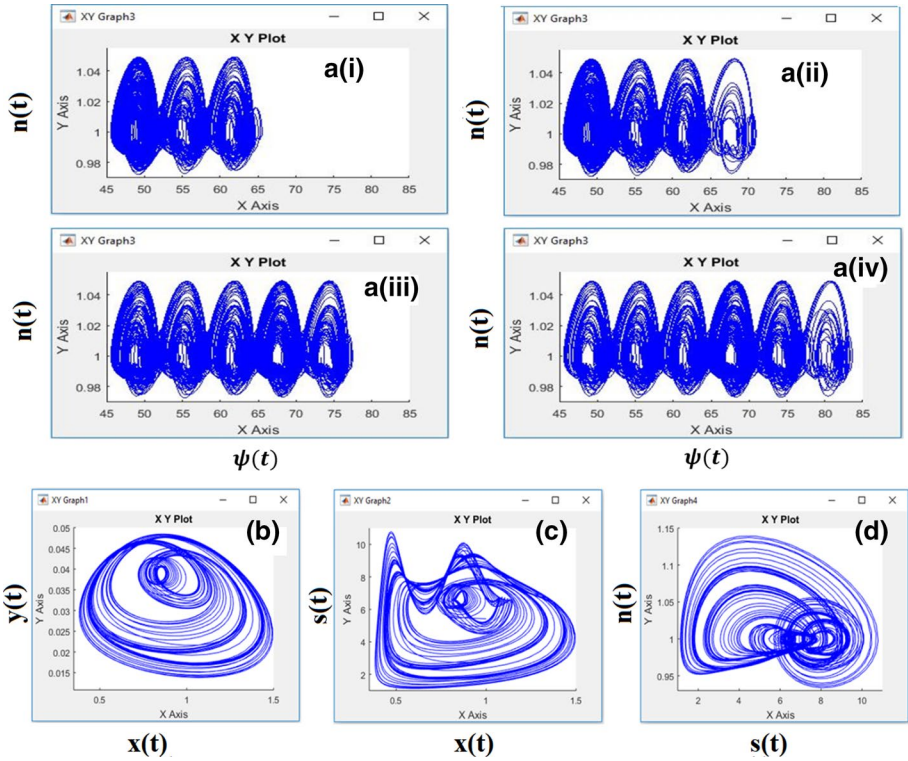


Fig. 7 a Simulink observations referring to formation of Infinite-scroll attractor: the projection on $\psi - n$ plane from XY Graph3 given for the simulating time show three-scroll **a(i)** $t=2,226$, **four-scroll a(ii)** $t=2,410$, **five-scroll a(iii)** $t=3,000$ and **six-scroll a(iv)** $t=3,360$ attractors. Projections of chaotic attractor from Simulink simulation in (b) current–voltage, (c) light–voltage and (d) carrier–photons plane from XY Graph1, XY Graph2 and XY Graph4 respectively when $r = 6.65$, $\gamma = 0.7$, $v_{dc} = 1.145$, $v_{ac} = 0.1441$ and $k = 0.020637$

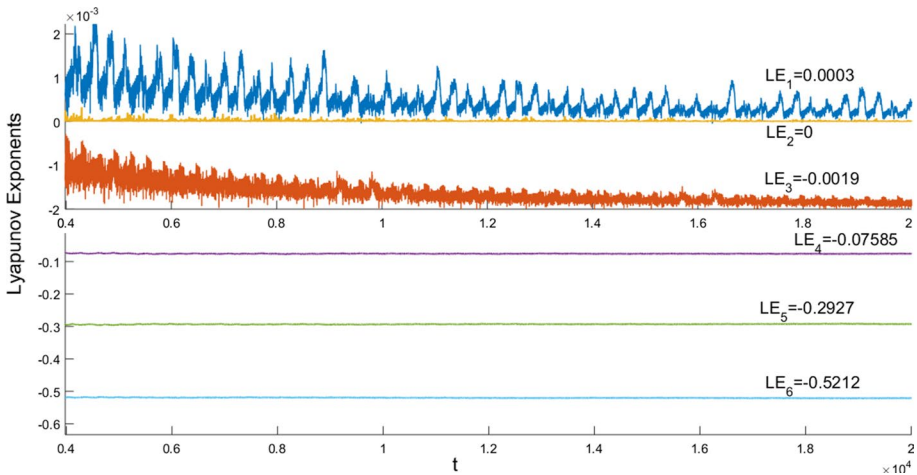


Fig. 8 Lyapunov exponents' dynamics of infinite-scroll of system (1) with the same fixed parameters as in Fig. 5

dynamic implementation of these stability properties is performed.

In Fig. 3a it is shown that the locking regions extend when EGC increases from a certain value. EGC acts as a control stability parameter and enables to improve the accuracy of the stability study further. From Fig. 3b almost all possible values of ψ_0 are negative. Their number should be larger as γ decreasing. Additionally, under weak injection strength and according to Eq. (2), $\psi_{0_{\min,\max}} = \pm\pi/2 - \arctan(\alpha/\beta)$ and under strong injection, $\psi_{0_{\min,\max}} = \pm\pi/2$ similar to the Ref. (Daly et al. 2013). As $\beta = \gamma^{-1} - 1$, the stable phase condition at the boundaries of EGC γ will be such that, when $\psi_{0_{\min,\max}}(\gamma < 0) = \pm\pi/2$ and $\psi_{0_{\min,\max}}(\gamma < 1) = -\pi$ or 0.

Note that, according to Eq. (6) the stable region corresponding to the frequency detuning in locking region shall be given from voltage-carrier steady states ($x_0 n n_0$) as all states can be connected from Eq. 2. In Fig. 4 we illustrate the Routh condition for the first minor Fig. 4a, the second minor Fig. 4b, the third minor Fig. 4c, the fourth minor Fig. 4d and the fifth minor Fig. 4e from the Hurwitz matrix (5). Figure 4f illustrates the superposition of aforementioned figures corresponding to all combined parts of Eq. (6). It is obvious to observe that, Fig. 4f does not display a wide intersecting region which satisfies Eq. (6). Nevertheless, it exists a shrunk region where the system has stable fixe points; this tiny region is circumscribed by a stability boundary denoted by the line A in Fig. 4f. Thereby, the study reveals a shrunk area of the system from which nonlinear dynamics can be undertaken as attraction basin and a sea of points in which the system drops to instability.

Let us in addition mentioned that, the local stability of all steady-state points for a given set of decisive parameters values (v_{dc}, r, γ) can be evaluated from Eq. (4) directly. For the simplicity we set $\Delta\Omega \approx 0$ according to the limit of locking region for low frequency detuning as depicted in Fig. 3. The pick of the control parameter for stability response through eigenvalues of the Jacobian matrix J_{M_0} for different equilibria points are illustrated in Table 1. Each equilibrium point has at least two complex-conjugate eigenvalues. Then Routh criterion applied to different control parameters indicates that all fixed points are almost unstable, and the system (1) may exhibit either chaotic or hyperchaotic dynamics. However for appropriate pick of control parameters, there exist stable fixed points. For instance when the RTD is biased in NDR, stable fixed points A_1 and A_2 the Table 1 have x_0 and n_0 values which effectively belong to the shrunk stable region too close to the line A on in Fig. 4f. So, it is obviously to point out that stable fixed points A_1 and A_2 also belong to stable phase locking regions from Fig. 3.

Moreover, in Fig. 5, when the time increases, optical phase values upgrade and the number of attractor scrolls infinitely grows. With this framework, the system depicts two-scroll attractor in Fig. 5a for ($t=1,000$), five-scroll attractor in Fig. 5b for ($t=3000$) and forty one-scroll attractor in Fig. 5c for ($t=20,000$). We notice that scrolls are interspersed to laminar phases which firstly appear after the fifteen scroll, as the time evolves they erratically appear and after a relative longtime their appearance becomes flat before falling again. This aforementioned study proves that it refers to a so-called an infinite-scroll chaotic attractor therein the number of generated scrolls depend to time calculation and non-periodic reproduction of infinite-scroll as the time evolves in regard to laminar phases. So the system (1) generates an infinite-scroll attractor. Indeed the transformation $M_0(x_0, y_0, z_0, n_0, s_0, \psi_0) \rightarrow M_0(x_0, y_0, z_0, n_0, s_0, \psi_0 + 2k\pi)$, where $k = 0, \pm 1, \pm 2, \pm 3, \dots$ is an invariant since trigonometric functions involved in optical phase give rise to infinitely many equilibrium points that provide infinite-scroll attractor. Nowadays, infinite-scroll attractor is not mostly reported in nonlinear dynamical systems for the best knowledge of the authors.

Table 1 The equilibrium point and their stability evaluated from system typical parameters values

Current-voltage regions	Values of (r, γ)	Equilibrium point $(x_0, y_0, z_0, n_0, \psi_0, \psi_0)$	Type of equilibrium point $\lambda_i (i = 1, 2, 3, 4, 5 \text{ or } 6)$	
<i>NDR</i>				
$v_{dc} = 1.1$	(8, 0.95)	(0.78783, 0.039022, 0, 7.6444, 0.00078157, -1.562)	$\lambda_{1,2} = -0.15323 \pm 0.9984i; \lambda_3 = 0; \lambda_4 = -0.10636; \lambda_{5,6} = 10.527 \pm 0.70709i$	Unstable focus
$v_{dc} = 1.5$	(3, 0.995)	(1.419, 0.027012, 0, 5.2921, 0.00071814, -1.57)	$\lambda_{1,2} = -0.59831 \pm 0.73601i; \lambda_3 = 0; \lambda_4 = -0.20143; \lambda_{5,6} = 0.71287 \pm 0.81117i$	Unstable focus
$v_{dc} = 2.8$	(6.68, 0.5)	$A_1 = (2.7664, 0.0050225, 0, 0.92163, 0.069603, -1.5708)$	$\lambda_{1,2} = -0.72469 \pm 0.83547i; \lambda_3 = 0; \lambda_4 = -0.37477; \lambda_5 = -1.2257; \lambda_6 = -1.7413$	Stable
	(6.68, 0.8)	$A_2 = (2.7664, 0.0050225, 0, 0.92067, 0.07074, -1.5708)$	$\lambda_{1,2} = -0.72469 \pm 0.83547i; \lambda_3 = 0; \lambda_4 = -0.901153; \lambda_{5,6} = -0.15062 \pm 0.47136i$	Stable
	(6.68, 0.95)	(2.7664, 0.0050225, 0, 0.91877, 0.073015, -1.5674)	$\lambda_{1,2} = -0.72469 \pm 0.83547i; \lambda_3 = 0; \lambda_4 = -0.63775; \lambda_{5,6} = 0.21123 \pm 0.50306i$	Unstable focus

4.2 Influence of the areas of RTD current–voltage curve and chaos control bifurcation

In this section, we investigate the dynamical behavior of the system for three different cases; when $S_1 \approx S_2$, $S_1 < S_2$ and $S_1 > S_2$. For the comparison purposes, we investigate the phase portrait diagrams in $(n - s)$ plane when others parameters are set as in Ref. (Essebe et al. 2020). Throughout all above sections, the case $S_1 \approx S_2$ has been used. It is important to show by the current–voltage characteristic of the RTD; $F(V) = BV(V - a)(V - b)$ that, there is invariance by changing a-parameter to b-parameter. In Fig. 9, we give prediction of the driven laser dynamics firstly when $S_1 \approx S_2$ in Fig. 9a, secondarily for $S_1 < S_2$ in Fig. 9b and finally when $S_1 > S_2$ in Fig. 9c. We use in addition the EGC γ as bifurcation parameter in order to magnify the influence of the areas S_1 and S_2 in the system (1). It is shown in Fig. 9a that the complexity of (1) decreases while γ is increasing. For example, the laser exhibits three-scroll chaotic attractor for $\gamma = 0.6$ in Fig. 9a(i), two-scroll attractor for $\gamma = 0.75$ in Fig. 9a(ii) and fails down unto one-scroll attractor for $\gamma = 0.9$ in Fig. 9a(iii). However in the case $S_1 < S_2$ we can observe relaxation dynamics for $\gamma = 0.6$ in Fig. 9b(i), a non-oscillatory dynamics for $\gamma = 0.75$ in Fig. 9b(ii) and crisis when $\gamma = 0.9$ in Fig. 9b(iii). When $S_1 > S_2$, the system generates merely periodic limit cycles whatever the value of the EGC γ as depicted in Fig. 9c(i), 9c(ii), and 9c(iii). We find very important to highlight that as one of the area S_1 gradually increasing the system evolves from chaos to periodic dynamics as depicted from Fig. 9a and c. Nevertheless a more careful observation of Fig. 2 reveals that the overall shape of RTD current–voltage characteristics is not changed but everything suggests that a shift in the axes has occurred. Therefore, interestingly the

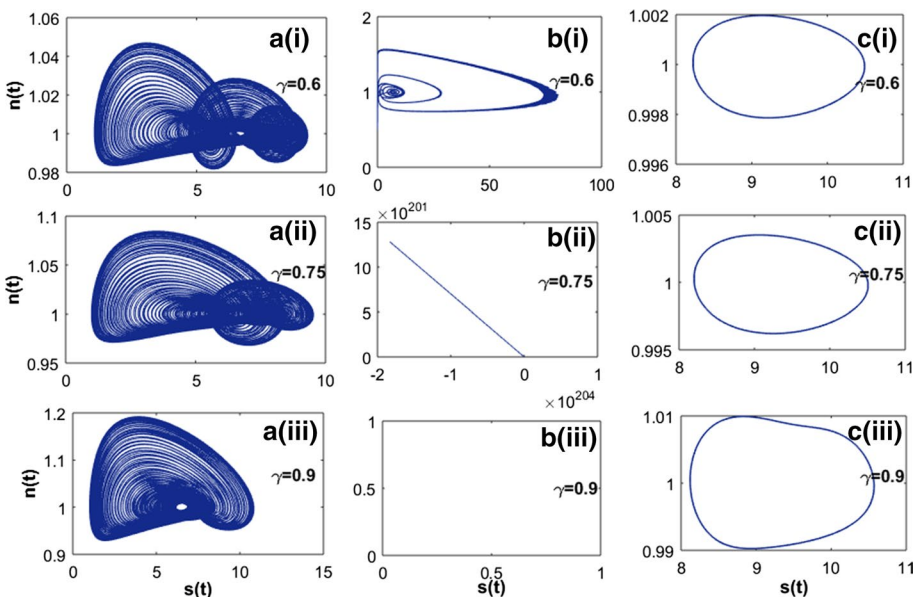


Fig. 9 Influence of RTD current–voltage (I-V) characteristics with EGC γ . **a**-When $S_1 \approx S_2$: **a(i)** Three-scroll chaotic attractor, **a(ii)** Two-scroll attractor and **a(iii)** One-scroll attractor. **b**- When $S_1 < S_2$: **b(i)** relaxation dynamics, **b(ii)** non-oscillatory dynamics and **b(iii)** crisis. **c**- When $S_1 > S_2$, the system generates periodic limit cycles whatever the value of γ . **c(i)**, **c(ii)**, and **c(iii)**

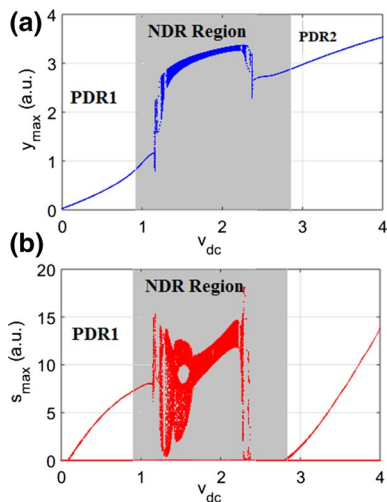
stabilization resistor and voltage biased could be adjusted to get a desired dynamics such as chaos, hyperchaos or periodic oscillations resulting from each of the investigated cases namely $S_1 \approx S_2$, $S_1 < S_2$ and $S_1 > S_2$ according to the threshold characteristics of the semiconductor laser.

Since chaos has a strong dependence on the initial conditions, its time-future oscillations being unforeseen, chaos control becomes a very useful tool in nonlinear dynamics. In this section we also apply an external control using the polarization control technique to stabilize electrical and optical outputs so as to control chaos. We investigate to the bifurcation diagram of y -state variable with the variation of DC polarisation v_{dc} and fixed AC excitation v_{ac} . From Fig. 10 we can notice that periodic and aperiodic oscillations occur in electrical current Fig. 10a and in optical output Fig. 10b if the system is biased in the NDR of the RTD. When the DC biasing is beyond the NDR region (PDR1 or PDR2 region), the dynamical behavior becomes periodic. However, the system could exhibit either slight chaotic or periodic windows in NDR region. This sticks out the relevance of DC polarisation on the chaos control in optoelectronic systems.

5 Conclusion

We have investigated stability analysis of a novel OEIC in the framework of weak and strong optical injection. An analytical study has been performed from Hurwitz matrix and by using Routh-Hurwitz criterion to highlight some stable fixed points within the shrunk stable region inside the sea of unstable points. Besides, dissipativity of the system has been analytically exemplified to firm divergence of Lyapunov exponents and nonlinear dynamics characteristic of the system. Numerical implementation has allowed to show that the laser locking regions are drastically affected by slight variations of EGC-parameter and DC bias. Moreover, from numerical calculations, the system displays stable and unstable equilibria points for negative or low frequency detuning values. Later on, generation and complexity of an infinite-scroll chaotic attractor has been discussed and stick out by using Lyapunov

Fig. 10 DC bias control of system dynamics (1): **(a)** and **(b)** bifurcation diagrams of electrical driving current and optical output, respectively



exponents' dynamics and Simulink implementation. At last, RTD current–voltage characteristics is studied under slight variations of control parameters namely the areas under and above the curve, further bifurcation diagrams and phase portraits are used to control DC polarization of the system. The momentous role played by EGC (a new decisive parameter for this kind of OEIC) so as to improve the accuracy of stability analysis and the chaos control outlined prove that this study can be relevant for experimental implementations of optoelectronic devices.

Appendix

The elements a_1, a_2, a_3, a_4 and a_5 of (4) and (5) are given by.

$$a_0 = 1, a_1 = -2\beta G_0 \Delta n_0 + mr + 3B_0 m^{-1} (3x_0^2 - 2(a + b)x_0 + ab) + \frac{\gamma_0}{1 - \delta} (\sigma B_0 x_0 (x_0 - a)(x_0 - b) - \delta),$$

$$a_2 = 1 + 3rB_0 (3x_0^2 - 2(a + b)x_0 + ab) + 2\beta G_0 \gamma_0 (\sigma B_0 x_0 (x_0 - a)(x_0 - b) - n_0) + (\alpha G_0 \Delta n_0 - \Delta \Omega)^2 + \beta^2 (G_0)^2 (\Delta n_0)^2 - \{mr + 3B_0 m^{-1} (3x_0^2 - 2(a + b)x_0 + ab)\} \left\{ 2\beta G_0 \Delta n_0 - \frac{\gamma_0}{1 - \delta} (\sigma B_0 x_0 (x_0 - a)(x_0 - b) - \delta) \right\} - 2\beta G_0 \gamma_0 \left(\frac{\sigma B_0 x_0 (x_0 - a)(x_0 - b) - \delta}{1 - \delta} \right) \Delta n_0$$

$$a_3 = -2\alpha G_0 \gamma_0 (\alpha G_0 \Delta n_0 - \Delta \Omega) (\sigma B_0 x_0 (x_0 - a)(x_0 - b) - n_0) - 2\beta^2 (G_0)^2 \gamma_0 (\sigma B_0 x_0 (x_0 - a)(x_0 - b) - n_0) \Delta n_0 + \frac{\gamma_0}{1 - \delta} (\sigma B_0 x_0 (x_0 - a)(x_0 - b) - \delta) \left[1 + 3rB_0 (3x_0^2 - 2(a + b)x_0 + ab) + \beta^2 (G_0)^2 (\Delta n_0)^2 + (\alpha G_0 \Delta n_0 - \Delta \Omega)^2 \right] + \left\{ 2\beta G_0 \gamma_0 (\sigma B_0 x_0 (x_0 - a)(x_0 - b) - n_0) - 2\beta G_0 \frac{\gamma_0}{1 - \delta} (\sigma B_0 x_0 (x_0 - a)(x_0 - b) - \delta) \Delta n_0 + \beta^2 (G_0)^2 (\Delta n_0)^2 + (\alpha G_0 \Delta n_0 - \Delta \Omega)^2 \right\} \times \{mr + 3B_0 m^{-1} (3x_0^2 - 2(a + b)x_0 + ab)\} + -2\beta G_0 [1 + 3rB_0 (3x_0^2 - 2(a + b)x_0 + ab)] \Delta n_0$$

$$a_4 = \left\{ -2\alpha G_0 \gamma_0 (\alpha G_0 \Delta n_0 - \Delta \Omega) (\sigma B_0 x_0 (x_0 - a)(x_0 - b) - n_0) - 2\beta^2 (G_0)^2 \gamma_0 (\sigma B_0 x_0 (x_0 - a)(x_0 - b) - n_0) \Delta n_0 + \frac{\gamma_0}{1 - \delta} (\sigma B_0 x_0 (x_0 - a)(x_0 - b) - \delta) \left[\beta^2 (G_0)^2 (\Delta n_0)^2 + (\alpha G_0 \Delta n_0 - \Delta \Omega)^2 \right] \right\} \times \{mr + 3B_0 m^{-1} (3x_0^2 - 2(a + b)x_0 + ab)\} + \left\{ 2\beta G_0 \gamma_0 (\sigma B_0 x_0 (x_0 - a)(x_0 - b) - n_0) - 2\beta G_0 \gamma_0 \left(\frac{\sigma B_0 x_0 (x_0 - a)(x_0 - b) - \delta}{1 - \delta} \right) \Delta n_0 + \beta^2 (G_0)^2 (\Delta n_0)^2 + (\alpha G_0 \Delta n_0 - \Delta \Omega)^2 \right\} \times \{1 + 3rB_0 (3x_0^2 - 2(a + b)x_0 + ab)\},$$

$$a_5 = -2\alpha G_0 \gamma_0 (\alpha G_0 \Delta n_0 - \Delta \Omega) (\sigma B_0 x_0 (x_0 - a)(x_0 - b) - n_0) \{1 + 3rB_0 (3x_0^2 - 2(a + b)x_0 + ab)\} - 2\beta^2 (G_0)^2 \gamma_0 (\sigma B_0 x_0 (x_0 - a)(x_0 - b) - n_0) \{1 + 3rB_0 (3x_0^2 - 2(a + b)x_0 + ab)\} \Delta n_0 + \frac{\gamma_0}{1 - \delta} (\sigma B_0 x_0 (x_0 - a)(x_0 - b) - \delta) \left[\beta^2 (G_0)^2 (\Delta n_0)^2 + (\alpha G_0 \Delta n_0 - \Delta \Omega)^2 \right] \{1 + 3rB_0 (3x_0^2 - 2(a + b)x_0 + ab)\}.$$

where x_0 and n_0 denote the steady states of the normalized electrical voltage and carrier density respectively.

Declarations

Conflict of interest The authors declare that they have no known competing interests and the work covered in this manuscript has been conducted with the ethical approval.

References

- Daly, A., Roycroft, B., Corbett, B.: Stable locking phase limits of optically injected semiconductor lasers. *Opt. Express* **21**, 30126–30139 (2013)
- Essebe, D.E., Mengue, A.D., Essimbi, B.Z.: Stochastic behavior of an external optically injected single-mode semiconductor laser including Langevin noise sources. *Phys. Scr.* **94**, 115501-1-30 (2019)
- Essebe, D.E., Mengue, A.D., Essimbi, B.Z.: Multiscroll chaotic attractors in optical injected semiconductor laser driven by a resonant tunneling diode current. *Optik* **212**, 164740-1-8 (2020)
- Figueiredo, J.M.L., et al.: Self-oscillation and period adding from resonant tunnelling diode-laser diode circuit. *Electron. Lett.* **44**, 876–877 (2008)
- Figueiredo, J.M.L., Ironside, C.N., Stanley, C.N.: Electric field switching in a resonant tunneling diode electroabsorption modulator. *IEEE J. Quant. Electr.* **37**, 1547–1552 (2001)
- Gokyildirim, A., et al.: A weak signal detection application based on hyperchaotic Lorenz system. *Tech. Gazette* **25**, 701–708 (2018)
- Hamsa, A., et al.: A new chaotic map for secure transmission. *Telkomnika* **16**, 1135–1142 (2018)
- Ironside, C., Romeira, B., Figueiredo, J.: *Resonant Tunneling Diode Photonics: Devices and Applications*. Iop Concise Physics, Concise edition (2019)
- Li, F., Yao, C.: The infinite-scroll attractor and energy transition in chaotic circuit. *Nonlinear Dyn.* **84**, 2305–2315 (2016)
- Ma, J., et al.: Selection of multi-scroll attractors in Jerk circuits and their verification using Pspice. *Nonlinear Dyn.* **76**, 1951–1962 (2014)
- Ma, J., Zhou, P., Ahmad, B., Ren, G., Wang, C.: Chaos and multi-scroll attractors in RCL-shunted junction coupled Jerk circuit connected by memristor. *PloS one* **13**(1), e0191120-1-21 (2018)
- Mengue, A.D., Essimbi, B.Z.: Complex chaos and bifurcations of semiconductor lasers subjected to optical injection. *Opt. Quant. Electron.* **42**, 389–407 (2011)
- Mengue, A.D., Essimbi, Z.B.: Symmetry chaotic attractors and bursting dynamics of semiconductor lasers subjected to optical injection. *Chaos* **22**, 013113-1-10 (2012a)
- Mengue, A.D., Essimbi, B.Z.: Stability and on-off chaotic states mechanisms of semiconductor lasers with optical injection on the new modified rate equation model. *Phys. Scr.* **85**, 025404 (2012b)
- Ohtsubo, J.: *Semiconductor Lasers Instability and Chaos*. Springer, Berlin (2006)
- Romeira, B., et al.: Synchronisation and chaos in a laser diode driven by a resonant tunnelling diode. *IET Optoelectron.* **2**, 211–215 (2008)
- Romeira, B., et al.: Delayed feedback dynamics of Liénard-type resonant tunneling-photo-detector optoelectronic oscillators. *IEEE J. Quant. Electro.* **49**, 31–42 (2013)
- Romeira, B., Figueiredo, J., Javaloyes, J.: Delay dynamics of neuromorphic optoelectronic nanoscale resonators: perspectives and applications. *Chaos* **27**, 114323-1-18 (2017)
- Sun, G., et al.: Generating multi-scroll chaotic attractors via switched fractional systems circuits. *Syst. Sign. Process.* **30**, 1183–1195 (2011)
- Wang, C.H., Xia, H., Zhou, L.: A memristive hyperchaotic multiscroll jerk system with controllable scroll numbers. *Int. J. Bifurcat. Chaos* **27**, 1750091-1-15 (2017)

Publisher's Note Springer Nature remains neutral with regard to jurisdictional claims in published maps and institutional affiliations.